UNIVERSITY OF SOUTHAMPTON
FACULTY OF SCIENCE
DEPARTMENT OF PHYSICS

POSITION-SENSITIVE SCINTILLATION COUNTERS

by

Andrew Truman

A thesis submitted for the degree of Doctor of Philosophy

March 1996

UNIVERSITY OF SOUTHAMPTON

ABSTRACT

FACULTY OF SCIENCE

PHYSICS

Doctor of Philosophy

POSITION-SENSITIVE SCINTILLATION COUNTERS

by Andrew Truman

This thesis considers recent developments in γ-ray scintigraphy, and presents the current state-of-the-art in nuclear medicine imaging techniques. Stimulated by these advances, we consider the possibility that valuable performance advantages could be realised by employing an extremely compact camera in closer proximity to the patient, enabling an improvement in the spatial resolution of the camera. Position-sensitive photodetectors, suitable for inclusion within a compact gamma camera are considered, and the two most promising devices are evaluated in a series of laboratory tests. The importance of careful scintillation crystal selection, and the optimisation of the crystal geometry has been quantified using Monte Carlo simulations to model the optical photon transport, and the γ-ray interactions within the detector crystal.

Measurements have been obtained of the energy and spatial resolution of a number of compact gamma cameras based upon the (R2487) 3 inch square, and the (R3292) 5 inch diameter circular position-sensitive photomultiplier tube (PSPMT), using different readout methods. These tubes viewed a variety of continuous and segmented scintillation crystals, with event localisation provided by parallel hole collimators. The R2487 PSPMT was used to view a sealed 5 mm thick continuous NaI(Tl) detector crystal, and the position resolution has been determined to be 2.7 mm FWHM at 122 keV. When viewing a segmented CsI(Tl) crystal array, with elemental dimensions of 2 mm, and a crystal separation of 0.5 mm, the uncertainty in the reconstructed position has been determined to be only 1.5 mm FWHM at 122 keV. The larger R3292 PSPMT was used to view a 3 mm thick, continuous CsI(Na) detector crystal, and the position resolution was determined to be 2.9 mm FWHM at 122 keV. The imaging performance of each of these three cameras has been qualitatively estimated by viewing a ^{57}Co (122 keV) thyroid contrast phantom source. In addition, a prototype auroral x-ray imager has been developed based upon the R2487 PSPMT, viewing a two-dimensional segmented CsI(Tl) crystal array, having elemental detector dimensions of 2 mm, and a crystal separation of 0.5 mm, in combination with a pin-hole collimator. Qualitative images of extended sources, similar in morphology to that expected from an auroral arc have been acquired at 60 keV and 122 keV.

A prototype hybrid photodiode (HPD) tube based upon a position-sensitive diode (PSD) anode structure has also been evaluated and its performance characteristics presented. In addition, the performance of a compact scintillation counter based upon a single-anode HPD has been evaluated in conjunction with a range of potentially suitable scintillation materials. The results of these studies together with the optical photon counting performance of the HPD when integrated within a gamma camera are presented, and the excellent potential of these novel photodetectors for future applications in nuclear medicine is discussed. In addition, a scaled down version of the Anger Camera based upon a prototype 19 pixel HPD with the detector crystal coupled via a lightguide to the entrance window of the tube is currently being developed, and will also be introduced.

To Diane and the girls

for your love

Publications During Ph.D Study

Conference Papers:

1. A.Truman, A.J.Bird, D.Ramsden, Z.He, 'Pixellated CsI(Tl) Arrays with Position-Sensitive PMT Readout', Conference Proceedings of the 1994 Symposium on Radiation Measurements and Applications, Ann Arbor, Michigan, U.S.A., pp 375-378, May 16-19.

2. Z.He, A.Truman, S.V.Guru, D.K.Wehe, G.F.Knoll, D.Ramsden, 'Portable Wide- Angle Gamma-Ray Vision Systems', Conference Proceedings of the 1994 IEEE Nuclear Science Symposium and Medical Imaging Conference, Norfolk, Virginia, U.S.A., pp 863-867, October 30-November 5.

3. A.Truman, M.J.Palmer, P.T.Durrant, A.J.Bird, D.Ramsden, J.Stadsnes, 'A Broad-Band Auroral X-Ray Imager', Conference Proceedings of the 1994 IEEE Nuclear Science Symposium and Medical Imaging Conference, Norfolk, Virginia, U.S.A., pp 648-652, October 30-November 5.

4. A.Truman, D.Ramsden, 'A Portable High Resolution Gamma Camera System', Conference Proceedings of the 1995 Canadian Organisation of Medical Physicists AGM, Montréal, Quebec, Canada, pp 59-60, June 4-7.

5. P.T.Durrant, A.Truman, C.Datema, D.Ramsden, 'A Gamma Camera Probe with Hybrid Photodiode Readout', Conference Proceedings of the 1995 IEEE Nuclear Science Symposium and Medical Imaging Conference, San Francisco, California, U.S.A. October 21-28.

Refereed Publications:

6. A.Truman, A.J.Bird, D.Ramsden, Z.He, 'Pixellated CsI(Tl) Arrays with Position-Sensitive PMT Readout', Nuclear Instruments and Methods in Physics Research, Vol. A353, pp 375-378, (1994).

7. Z.He, A.Truman, S.V.Guru, D.K.Wehe, G.F.Knoll, D.Ramsden, 'Portable Wide-Angle Gamma-Ray Vision Systems', IEEE Transactions on Nuclear Science, Vol.42(4), pp 668-674, (1995).

8. A.Truman, M.J.Palmer, P.T.Durrant, A.J.Bird, D.Ramsden, J.Stadsnes, 'A PSPMT Based Auroral X-Ray Imager', Nuclear Instruments and Methods in Physics Research, Accepted for publication (1995).

Reports & Book Chapters:

9. 'Radiation Detectors - A Review of Recent Developments', Report Prepared for British Nuclear Fuels Limited, July 1995.

ACKNOWLEDGEMENTS

I am deeply indebted to my supervisor, Dr. David Ramsden, for his continual guidance, encouragement and support throughout this work. The timely completion of this work could not have been achieved without his invaluable ideas and comments which have contributed to make this thesis possible.

Also I would like to thank Prof. A.J.Dean, Dr. M.J.Coe, Dr. I.McHardy, Dr. T.Marsh and Dr. M.Merrifield for their help, advice and many fruitful discussions. Dr. A.J.Bird has collaborated and commented on several published works during this time. Indeed I have on many occasions benefited from his advice and experience for which I am extremely grateful.

Thanks are also due to Dr. I.Cullum, and staff at the Institute of Nuclear Medicine, UCL Middlesex Hospital, for their assistance and use of facilities in the clinical trials of the two cameras described in this work.

I would also like to thank Dr. Riccardo DeSalvo of INFN Pisa, for his invaluable help and advice relating to the operation of the hybrid photodiodes (HPD's) described in this work, and for the loan of two prototype multi-anode HPD's.

I would like to add my personal thanks to all the members of the Astronomy and Space Science group at Southampton, both past and present, for their help and advice during the last three years. I believe the following (in no particular order) deserve special mention for their achievements: Harbie, Zhong, Steve M, Laurence, Tony C, Fan, Andy, Graham, Max, Paul, Cor, Iossif, Ian P, and Ian J. Thanks also go to Tony Gomm, Graham Chadwick, Steve Holder, and the staff of both the mechanical and electronics workshops for their excellent technical support.

Finally, I would like to thank the following:

- Dr. P.Lanchester and Dr. D.Ramsden for the use of departmental facilities.
- The Engineering and Physical Sciences Research Council for the award of a CASE research studentship.
- Financial and technical support provided by Electron Tubes Limited.
- The EPSRC for the computing support provided by the Starlink Project.

PREFACE

The author was responsible for the Monte Carlo modelling and measurements performed to optimise the detector crystal geometry for direct coupling to the entrance window of each position-sensitive photomultiplier (PSPMT) based imaging system described. He also demonstrated a novel multiwire readout of the PSPMT using prototype MXRP and HX-2 hybrid charge integrating readout electronics developed at the Daresbury Rutherford Appleton Laboratory (DRAL). The author was further responsible for the design and testing of a dedicated HX-2 multiwire signal processing board for acquiring data from the R2487 PSPMT. The technician support provided by Mr. G.Chadwick in developing and debugging the prototype HX-2 boards is hereby acknowledged.

The camera based upon the R2487 PSPMT was designed by the author, and constructed to these specifications under his direction. The camera based upon the R3292 PSPMT was designed jointly between the author (Southampton), Dr. A.J.Bird (Southampton), and Dr. I.Cullum (UCL). Trials of camera designs based upon these tubes were conducted with the assistance of Dr. I.Cullum and Miss F.Christie at the UCL Middlesex Hospital. In addition, the camera based upon the R2487 PSPMT was further tested at Southampton for an application in auroral imaging. The support of Mr. M.Palmer in developing the necessary software to conduct these measurements, and the considerable collaborative support received from Dr. J.Stadsnes of the University of Bergen, Norway in developing the collimator for this application is hereby acknowledged.

In addition to the development of various compact gamma cameras based upon the PSPMT, the author collaborated with his CASE sponsor, Electron Tubes Limited, Ruislip, to construct a position-sensitive scintillation counter based upon the development of a novel proximity focused hybrid photodiode tube (HPD), which offered potential for inclusion within a compact gamma camera. The photodetector was designed jointly between the author, Dr. D.Ramsden (Southampton), and Dr. R.McAlpine (ETL). The author was responsible for conducting a range of measurements using a small duolateral position-sensitive diode (PSD), and a number of newly developed 'flip-chip' diodes to assess their suitability for inclusion within such a device.

The measurements with single-anode and multi-anode HPDs from DEP described in Chapter 7 were carried out in conjunction with Mr. C.Datema, a research assistant formerly from the University of Gronningen, Netherlands, funded by the E.C. through the Human Capital and Mobility Program.

Contents

1 Introduction **1**

2 Nuclear Medicine Imaging Techniques **5**

2.1 Introduction 5

2.2 The Discovery of X-Rays and Gamma-Rays 6

2.3 Gamma-Rays in Nuclear Medicine 8

2.3.1 Principle of In Vivo Imaging of Gamma-Rays 9

2.3.2 The Radioactive Decay Process 9

2.3.3 Some Common Radiopharmaceuticals 11

2.3.4 Radiopharmaceutical Uptake 14

2.4 Localization of γ-Rays in Nuclear Medicine 16

2.4.1 Parallel Multihole Collimators 16

2.4.2 Converging and Diverging Collimators 17

2.4.3 Electronic Collimation 18

2.5 Planar Imaging in Nuclear Medicine 19

2.5.1 The Rectilinear Scanner 20

2.5.2 The Anger Camera 21

2.6 Tomography in Nuclear Medicine 25

2.6.1 Computerized Tomography (CT) 25

2.6.2 Single Photon Emission Computed Tomography (SPECT) 29
2.6.3 Positron Emission Tomography (PET) 29
2.7 Conclusions 32
3 Detectors for Gamma-Ray Imaging **35**
3.1 Introduction 35
3.2 Considerations for the Design of Scintillation Detectors 35
3.3 Characteristics of Some Common Scintillators 37
3.3.1 Properties of Some Classic Inorganic Scintillators 37
3.3.2 Summary of Some Classic Inorganic Scintillators 41
3.3.3 Properties of Some Recent Inorganic Scintillators 42
3.3.4 Summary of Some Recent Inorganic Scintillators 43
3.4 Scintillation Counting Devices 44
3.4.1 Principle of Operation 44
3.4.2 The Photomultiplier Tube 45
3.4.3 The Position-Sensitive Photomultiplier Tube (PSPMT) 49
3.4.4 The Photodiode 52
3.4.5 The Hybrid Photodiode Tube (HPD) 57
3.5 Conclusions 58
4 Design of a PSPMT Based Compact Gamma Counter **61**
4.1 Introduction 61
4.2 Continuous Detector Crystals 63
4.3 Segmented Detector Crystal Arrays 66
4.4 Choice of Scintillator for a PSPMT Based Gamma Camera 67

4.5 Readout Method ... 69
4.5.1 Resistive Charge-Division Readout ... 69
4.5.2 Centroiding Method of Image Reconstruction ... 70
4.5.3 Multiwire Readout ... 71
4.5.4 Peak Fitting Method of Image Reconstruction ... 72
4.6 Results ... 73
4.6.1 Spatial Resolution ... 75
4.6.2 Position Linearity ... 78
4.6.3 Energy Resolution ... 79
4.7 Low Energy Detection Threshold ... 79
4.8 The HX-2 Readout ... 81
4.9 A Dedicated HX-2 Readout Board for the 3 inch Square PSPMT ... 83
4.10 Conclusions & Future Work ... 89
5 Modelling of the Detector Crystal Design **92**
5.1 Introduction ... 92
5.2 The GEANT 3 Monte Carlo ... 93
5.3 GEANT 3 Monte Carlo Models of Detector Crystal Geometry ... 94
5.4 The GUERAP V Optical Monte Carlo ... 99
5.5 Optical Monte Carlo Models of Detector Crystal Geometry ... 100
5.6 Conclusions & Future Work ... 107
6 Preliminary Trials of a Compact Gamma Camera **109**
6.1 Introduction ... 109
6.2 Clinical Applications of a Compact Gamma Camera ... 109

6.3 Images Obtained with a Segmented Detector 112

6.4 Images Obtained with a Continuous Detector 114

6.5 Trials of a 5 in. Diameter PSPMT and Continuous Detector 116

6.6 Conclusions and Future Work 127

7 A Prototype Auroral X-Ray Imager 128

7.1 Imaging Auroral X-Rays 128

7.2 A PSPMT Based Auroral X-Ray Imager 128

7.3 Experimental Setup 129

7.4 Detector Crystal Design 130

7.5 Readout System 131

7.6 The Optical Monte Carlo 132

7.7 Detector Response 133

7.8 Low Energy Detection Threshold 135

7.9 Imager Performance 136

7.10 A Proposed Auroral Imager 137

7.11 Conclusions and Future Work 138

8 The Potential of a Position-Sensitive Hybrid Photodiode 139

8.1 The Need For a New Approach 139

8.2 History of the HPD 140

8.3 Principle of Operation 141

8.4 A New Detector Based Upon the HPD Principle 146

8.5 Anode Structures 146

8.6 Tests of a 1 cm^2 Duolateral PSD 152

8.6.1 Experimental Procedure 152

8.6.2 Signal Processing 155

8.6.3 Energy Resolution 156

8.6.4 Spatial Resolution 158

8.6.5 Position Linearity 159

8.6.6 Diode Characteristics 160

8.6.7 Typical Characteristics of an 'Ideal' PSD 161

8.7 Design Considerations for the HPD 163

8.7.1 Development of a single-pixel 'Flip-Chip' PiN Diode for the HPD 163

8.7.2 Development of the Ceramic Enclosure 164

8.7.3 The Assembly Process 165

8.8 Outcome of Investigation 166

8.8.1 Development of the 'Flip-Chip' Silicon PiN Diode 166

8.8.2 Development of the Ceramic Enclosure 169

8.9 Conclusions & Future Work. 170

9 A Single-Anode Hybrid Photodiode for Scintillation Counting 172

9.1 Introduction 172

9.2 The HPD Development 173

9.2.1 Electrostatically Focused 173

9.2.2 Tube Characteristics 174

9.2.3 Proximity Focused 174

9.2.4 Tube Characteristics 175

9.3 Tests of an Electrostatically Focused Single-Pixel HPD 175

9.3.1 Experimental Procedure 176

9.3.2 Charge Gain 176

9.3.3 Energy Resolution 177

9.3.4 Optical Photon Counting 180

9.3.5 Low Energy Detection Threshold 181

9.4 Applications of the HPD 183

9.4.1 Gamma-Ray Spectroscopy 183

9.4.2 Gamma Camera Probe with Hybrid Photodiode Readout 183

9.4.3 Miniature SPECT 184

9.5 Conclusions & Future Work 185

A The Interaction of Gamma-Rays with Matter **187**

A.1 Introduction 187

A.2 Photoelectric Absorption 189

A.3 Compton Scattering 191

A.4 The Scintiliation Process 194

Bibliography **198**

List of Figures

Figure 2.1: *An early advertisement following the discovery of x-rays*

Figure 2.2: *Localization of radiopharmaceutical activity by a mechanical aperture*

Figure 2.3: *The Compton camera*

Figure 2.4: *Reconstructed image of a ^{60}Co calibration source*

Figure 2.5: *The rectilinear scanner*

Figure 2.6: *Rectilinear scans of the thyroid gland*

Figure 2.7: *The Anger Camera*

Figure 2.8: *Distorted light spread function due to Compton scatter*

Figure 2.9: *Principle of operation of CT scanner*

Figure 2.10: *A brain study using CT imaging techniques*

Figure 2.11: *Principle of coincidence detection*

Figure 2.12: *Parameters affecting position resolution in PET*

Figure 3.1: *Transmission of various thicknesses of CsI(Na) dead layer*

Figure 3.2: *A typical pulse height spectrum from a NaI(Tl) - PMT based scintillation counter*

Figure 3.3: *The spectral sensitivity of a range of photocathode materials*

Figure 3.4: *The electron multiplication process*

Figure 3.5: *Principle of the mesh dynode (Barone et al. [10])*

Figure 3.6: *A typical scintillation counter*

Figure 3.7: *The Hamamatsu family of PSPMTs*

Figure 3.8: *Schematic representation of the PSPMT*

Figure 3.9: *Schematic arrangement for a scintillator -photodiode combination*

Figure 3.10: *Principle of a proximity focused HPD*

Figure 4.1: *Light transport in a continuous crystal*

Figure 4.2: *Data collection system used*

Figure 4.3: *Schematic diagram showing the original data acquisition system*

Figure 4.4: *Contour plot of all detectors viewed together by the R2487 3 in. PSPMT, illuminated with 122 keV (57Co). Crystal sizes from top to bottom are 1.25 mm, 2 mm, and 3 mm.*

Figure 4.5: *16 crystal elements each 1.25 mm, illuminated with 122 keV (^{57}Co) with conventional readout. Mean position resolution = 1.3 mm FWHM.*

Figure 4.6: *16 crystal elements each 1.25 mm, illuminated with 122 keV (^{57}Co) with multiwire readout. Mean position resolution = 0.9 mm FWHM.*

Figure 4.7: *Plot of spatial linearity of the R2487 PSPMT*

Figure 4.8: *Electron distribution profiles*

Figure 4.9: *A schematic diagram of the prototype HX-2 test board*

Figure 4.10: *Waveform diagram for the prototype HX-2 test board*

Figure 4.11: *A schematic diagram of the modified HX-2 board*

Figure 4.12: *Waveform diagram of modified board*

Figure 4.13: *A photograph detailing the modified HX-2 board*

Figure 4.14: *Schematic diagram of EPROM based HX-2 board*

Figure 4.15: *Waveform diagram of EPROM based HX-2 board*

Figure 5.1: *Energy deposited as a function of depth for NaI(Tl) and CsI(Tl) at 140 keV*

Figure 5.2: *Trade-off between detection efficiency and light output for CsI(Tl)*

Figure 5.3: *Multiple bar interaction probability as a function of cross-section of CsI detector crystal elements with virtual cuts, 40 keV threshold*

Figure 5.4: *Multiple bar interaction probability as a function of cross-section of CsI detector crystal elements separated by 500 μm of epoxy, 1 keV threshold*

Figure 5.5: *Optical Monte Carlo simulation illustrating the effect of glass window thickness upon light spread when viewing continuous detector crystals*

Figure 5.6: *Optical Monte Carlo simulations illustrating the effect of crystal dimensions upon light spread*

Figure 5.7: *Optimisation of optical coupling compound*

Figure 5.8: *Optical Monte Carlo simulation illustrating the effect of a small air gap upon light spread*

Figure 5.9: *Effect of aspect ratio upon light collection for 2 mm x 2 mm CsI(Tl) crystal*

Figure 5.10: *Effect of cladding upon light output for a 2 mm x 2 mm CsI(Tl) crystal*

Figure 6.1: *The compact gamma camera*

Figure 6.2: *Segmented CsI(Tl) detector used to view a thyroid phantom source*

Figure 6.3: *Continuous NaI(Tl) detector used to view a thyroid phantom source*

Figure 6.4: *Count-rate response of camera in real time*

Figure 6.5: *Energy response as a function of radial position*

Figure 6.6: *Position and energy spectra of R3292 PSPMT viewing a 3 mm thick CsI(Na) image plate illuminated by 122 keV (^{57}Co)*

Figure 6.7: *Image of an extended ^{57}Co source without pulse-height discrimination*

Figure 6.8: *Image of an extended ^{57}Co source without pulse-height discrimination*

Figure 6.9: *Transmission phantom images of 4 mm, 3.5 mm, 3 mm, and 2.5 mm bars*

Figure 6.10: *Pie transmission phantom images*

Figure 6.11: *Images obtained with the PSPMT based camera and an Anger Camera*

Figure 6.12: *Image of a thyroid contrast phantom*

Figure 7.1: *Arrangement of rotating x-ray source and imager*

Figure 7.2: *A compilation of available auroral x-ray spectra*

Figure 7.3(a): *Optical montecarlo simulations illustrating the effect of glass window thickness on light spread.*

Figure 7.3(b): *Optical montecarlo simulations illustrating the effect of crystal dimensions on light spread.*

Figure 7.4: *3 mm crystals illuminated by 122 keV (^{57}Co) with conventional readout. Detector response is 2.1 mm FWHM.*

Figure 7.5: *3 mm crystals illuminated by 122 keV (^{57}Co) with multi-wire readout. Detector response is 1.5 mm FWHM.*

Figure 7.6: *2 mm crystals illuminated by 122 keV (^{57}Co) with conventional readout. Detector response is 1.5 mm FWHM.*

Figure 7.7: *2 mm crystals illuminated by 122 keV (^{57}Co) with multi-wire readout. Detector response is 1.2 mm FWHM.*

Figure 7.8: *Response function of CsI(Tl) ladder illuminated with 22 keV x-rays*

Figure 7.9: *Raw data of extended 60 keV and 122 keV x-ray source*

Figure 7.10: *Extended 60 keV and 122 keV x-ray source after smoothing*

Figure 7.11: *A proposed imager for auroral x-rays*

Figure 8.1: *An image intensifier tube with a silicon anode*

Figure 8.2: *HPD gain characteristics as a function of contact layer thickness and transverse magnetic field*

Figure 8.3: *Normalized HPD response as a function of transverse magnetic field*

Figure 8.4: *Effect of magnetic field angle upon HPD response*

Figure 8.5: *Layout of a silicon micro-strip detector*

Figure 8.6: *Three typical configurations of wedge and strip detectors*

Figure 8.7: *Various one-dimensional and two-dimensional PSDs*

Figure 8.8: *The structure of a duolateral PSD*

Figure 8.9: *The structure of a tetralateral PSD*

Figure 8.10: *Pin-cushion distortion in the duolateral and tetralateral PSD*

Figure 8.11: *Simulated count rate at detector as a function of source-detector separation*

Figure 8.12: *Diagram illustrating the vacuum chamber*

Figure 8.13: *Schematic diagram of the PSD test system*

Figure 8.14: *A dedicated four channel signal processing board*

Figure 8.15: *Energy spectrum of ^{241}Am α-particle deposit in a duolateral PSD*

Figure 8.16: *Intensity plot of 5.5 MeV α-particles, source-detector separation = 3 mm*

Figure 8.17: *Intensity plot of 5.5 MeV α-particles, source-detector separation = 100 mm*

Figure 8.18: *Position linearity of a duolateral PSD*

Figure 8.19: *PSD leakage current as a function of reverse bias*

Figure 8.20: *PSD capacitance as a function of reverse bias*

Figure 8.21: *Characteristics of an 'ideal' PSD*

Figure 8.22: *The structure of a 'flip-chip' silicon PiN photodiode*

Figure 8.23: *Design of the ceramic enclosure*

Figure 8.24: *Performance characteristics of the 'flip-chip' diode*

Figure 8.25: *A leak on one of the leadthroughs of an assembled HPD*

Figure 8.26: *Micro-cracking in the corners of the ceramic assemblies*

Figure 9.1: *Schematic representation of a 7 segment anode HPD*

Figure 9.2: *Energy spectra of CsI(Na) viewed by HPD*

Figure 9.3: *Spectra demonstrating single optical photon counting ability of an HPD*

Figure 9.4: *Energy spectrum of ^{55}Fe with CsI(Tl) coupled to HPD*

Figure 9.5: *Hybrid photodiode silicon PiN diode characteristics*

Figure 9.6: *Anode structure of the multi-anode HPD*

Figure A.1: *Relative contribution of gamma-ray interaction processes*

Figure A.2: *Energy dependence of gamma-ray attenuation in sodium iodide*

Figure A.3: *The photoelectric absorption process*

Figure A.4: *The Compton scattering process*

Figure A.5: *Some cross-sections for Compton scatter*

Figure A.6: *π-electron energy structure of an organic molecule*

Figure A.7: *Luminescence in (a) a pure alkali halide crystal, (b) a crystal with added impurity*

Figure A.8: *Temperature dependence of light output from inorganic crystals*

List of Tables

Table 2.1:	*Decay product characteristics*
Table 2.2:	*Characteristics of some common radionuclides used in nuclear medicine*
Table 2.3:	*Radiopharmaceuticals in routine clinical use*
Table 3.1:	*Summary of the properties of classic inorganic scintillators*
Table 3.2:	*Summary of properties of some recently developed scintillators*
Table 3.3:	*Typical NaI(Tl) Energy Resolution Values, source Harshaw Catalogue*
Table 3.4:	*Performance characteristics of CsI(Tl) - photodiode detectors*
Table 4.1:	*Mean PSF characteristics as a function of energy and crystal size for the R2487 PSPMT. Numbers in brackets indicate the performance of the larger R3292 tube type. All measurements are in mm.*
Table 4.2:	*Mean PSF characteristics and peak-to valley ratio as a function of crystal size for the R2487 PSPMT with multiwire readout. Numbers in brackets indicate the performance for conventional readout.*
Table 4.3:	*Energy resolution measurements with the 3 in. square R2487 PSPMT*
Table 5.1:	*Effect of surface finish upon light output*
Table 8.1:	*Leakage current characteristics when probed at Southampton*
Table 8.2:	*Leakage current measurements performed at ETL*
Table 9.1:	*Spectral performance of the HPD with quartz entrance window*
Table 9.2:	*Relative spectral performance of the HPD compared with other scintillation counting devices*
Table A.1:	*Properties of scintillators at 20° C*

Chapter 1

Introduction

Medical Physics is a specialist activity that, over a period of almost a century, has integrated several imaging modalities, together revolutionising medicine and clinical diagnostic procedures. Almost all of the electromagnetic spectrum is now used in an effort to identify the minute anatomical and physiological changes within the human body which accompany various states of disease. Currently used imaging techniques include thermography, ultrasound, electrical impedance tomography, nuclear magnetic resonance imaging (MRI), x-ray radiography, computed axial tomography (CT), single photon emission computed tomography (SPECT), positron emission tomography (PET), and γ-ray scintigraphy. Each offers particular performance advantages and limitations, and there is considerable overlap between them.

Since its invention by Hal Anger at the University of California almost fifty years ago, the gamma camera with its modest spatial resolution has enabled gamma-ray scintigraphy studies to be performed non-invasively, yielding insight into the *in vivo* physiological functions of the organs within the body. The thick NaI(Tl) scintillation crystal used to detect the radiation emerging from the patient is efficiently shielded from sources outside of the field-of-view by surrounding the camera with large quantities of lead, increasing both the dimensions and the mass of the camera. A process of continuous development by gamma camera manufacturers has ensured that the effect of this additional weight is minimised, and few practical problems are presented in general clinical operation.

Concentrating upon the development of novel imaging systems for new applications in nuclear medicine, this thesis considers the design requirements of compact gamma cameras suitable for imaging 140 keV in a range of clinical studies. Apart from these applications in nuclear medicine, we have also considered the design requirements for a broad-band camera that is suitable for imaging auroral x-rays.

Recently proposed scintigraphic studies could potentially enable the field of clinical nuclear medicine to be extended to encompass both intraoperative imaging, and breast imaging. However, at the present time both the dimensions and the mass of conventional gamma cameras remain incompatible with these applications, and it is therefore expected that further hardware development will be necessary. However, two recently developed photodetectors have been identified that appear to be compatible with the necessary reduction of scale for the construction of a compact camera for the imaging of γ-rays.

The first of these photodetectors is the family of position-sensitive photomultiplier tubes (PSPMTs). This work will demonstrate that the optimisation of both the detector crystal geometry and the signal processing electronics can provide sub-millimetric intrinsic spatial resolution for incident γ-ray energies of 122 keV. In addition, a recent reduction in the size of these tubes will enable a new generation of gamma cameras to be constructed on a scale compatible with recent advances towards truly intraoperative applications in nuclear medicine. Consideration has been given to the optimisation of such a design.

The second of these photodetectors is based upon the recently developed hybrid photodiode tube (HPD). This work will confirm the ability of these new devices to count single optical photons, and will investigate the possibility of using the HPD as a compact scintillation counter for applications in nuclear medicine. The energy resolution performance of the HPD is determined for a range of incident γ-ray energies, and compared with other photodetectors commonly used in scintillation counting. Consideration has also been given to the design and construction of a new style of position-sensitive, proximity focused device for which two representative applications have been identified in nuclear medicine and auroral imaging. Finally, a design for a 'hand-held' gamma camera based upon a segmented-anode HPD will be proposed and its potential application as a position-sensitive gamma camera in nuclear medicine discussed.

In **Chapter 2**, a brief review of nuclear medicine imaging techniques will be presented. Following a description of the discovery of x-rays and γ-rays, the focus turns towards the uptake of radioisotopes within the human body, and the principles which permit their detection. Techniques used to localise and code the γ-ray flux incident upon the scintillation detector, and the general principles of operation of the nuclear medicine imaging systems used to detect the incident radiation will be reviewed here.

Chapter 3 introduces the principal considerations when coupling a scintillation crystal to a photodetector for applications in nuclear medicine. The physical characteristics of several commonly available scintillator materials used for the detection of γ-rays are reviewed. The principle of operation of four photodetectors suitable for inclusion within a compact position-sensitive scintillation counter will be presented, and their potential for applications in nuclear medicine imaging discussed.

Chapter 4 advances the argument that the intrinsic spatial and energy resolution performance characteristics of a position-sensitive scintillation counter could be influenced by the geometry of the detector crystal. The possibility therefore exists that a worthwhile improvement in the performance of the detector might be achieved through the careful optimisation of the scintillation crystal geometry. It is proposed that the PSPMT be used to investigate these ideas experimentally. Two contrasting readout techniques will be presented, and their relative performance compared. Both the energy and spatial characteristics will be evaluated for the 3 inch square R2487, and the 5 inch diameter circular R3292 tubes viewing a range of segmented and continuous detector crystals. The suitability of each configuration for applications in nuclear medicine, and auroral imaging will be discussed. A board offering dedicated multi-channel signal processing for the R2487 tube is also presented.

Chapter 5 describes the optimisation of the detector design using the GUERAP V, and the GEANT 3 Monte Carlo simulation algorithms to model both the optical performance of each scintillation crystal geometry, and the probability of Compton scatter between adjacent discrete detector crystals. This chapter considers a range of detector crystal geometries which might be suitable for inclusion within a compact gamma camera for either application.

Chapter 6 documents the results of preliminary tests conducted upon two PSPMT based detectors for nuclear medicine imaging applications, in collaboration with the Institute of Nuclear Medicine at the UCL Middlesex Hospital.

Chapter 7 presents the results of measurements made using a PSPMT based prototype broad-band position-sensitive scintillation counter for the detection of auroral x-rays.

Chapter 8 introduces the operational characteristics exhibited by the HPD. Further, the development of a square proximity focused HPD, together with the necessary modifications to the anode which enable position-sensitivity are considered. Tests of a small duolateral position-sensitive diode used to detect alpha-particles will be discussed, and the basic characteristics of this device as a charged particle detector will be presented. The outcome of this novel HPD detector development will be reported.

Chapter 9 discusses several types of HPD which have been developed by DEP. Tests of an electrostatically focused single-pixel HPD will be reported which illustrates the low energy threshold and single optical photon counting capability of this device. Further tests will be reported which demonstrate the excellent energy resolution of this device when used for γ-ray spectroscopy. A possible design for a gamma camera probe based upon a prototype 19 pixel HPD will also be presented here.

Chapter 2

Nuclear Medicine Imaging Techniques

2.1 Introduction

The scope of this chapter is to review the principal techniques currently used in nuclear medicine imaging, enabling the relative strengths and weaknesses of each to be identified. This chapter should therefore be considered to be a contextual point of reference for the author's work described in the remaining chapters. The two main themes which have influenced the direction of this research project can be summarised as being the development of new imaging systems for applications in nuclear medicine, and auroral imaging.

- The primary focus of this work is to develop a camera for applications in nuclear medicine. Recently, several groups have identified new applications in nuclear medicine which require a very compact position-sensitive scintillation counter. It is expected that such a small camera would offer comparable energy resolution to the conventional Anger Camera, whilst perhaps offering some modest improvement in intrinsic spatial resolution.

- There also exists a requirement to develop a position-sensitive scintillation counter which is capable of covering a broad band of energies from approximately 2 keV through to about 200 keV. Such a detector would be suitable for inclusion within the payload complement of ENVISAT II, and would enable detailed investigative studies to be performed into the complex interactions between highly energetic charged particles and the magnetosphere which result in the generation of auroral x-rays.

After a short summary of the events leading to the discovery of x-rays and γ-rays, this chapter will consider the principles and techniques used in nuclear medicine for the imaging of γ-rays *in vivo*. The clinical application of a wide range of commonly used radiopharmaceuticals and their uptake within the body will be discussed. Consideration will be given to techniques used to localize or code the γ-ray photon flux at the detector plane which enable the formation of an image. The present status of imaging in nuclear medicine and diagnostic radiology will be illustrated with a review of a number of planar and tomographic imaging detector systems, with particular emphasis placed upon their relative performances and limitations when considering new applications in medical physics.

2.2 The Discovery of X-Rays and Gamma-Rays

Last year marked the centenary of the discovery of x-rays, and the invention of the radiograph as a clinical procedure to externally observe anatomical features from within the body.

On Friday, November 8, 1895, Professor Wilhelm Conrad Röentgen was preparing to conduct a series of experiments with a high vacuum Crookes' tube at the Königliche University of Würzburg. The objective of these experiments was to identify the "invisible high-frequency rays" that Hermann Ludwig Ferdinand von Helmholtz had predicted from the Maxwell theory of electromagnetic radiation. As Röentgen tested his apparatus in preparation for this work, he noticed a shimmering light in the darkness coming from a barium platinocyanide-coated fluorescent screen placed on a bench a metre or so away from the tube. Had he not seen that faint fluorescence at the end of his laboratory bench as he tested his equipment, he would surely have noticed the screen glow brightly a few minutes later, since he had intended to place the screen next to the face of his black-cardboard-covered cathode-ray tube. However, chance favours those who are prepared to see, and his observation of that first glimmer in the darkness could hardly be described today as a purely accidental event in the history of scientific achievement.

Röentgen studied this intriguing phenomenon tirelessly, working long hours and even taking his meals in the laboratory. Finally, his wife Bertha demanded to know why he was so obsessed. Röentgen invited her to his laboratory where he demonstrated his experiments and took the first human radiograph of her hand.

On December 28, 1895, Röentgen presented a paper to the secretary of the Würzburg Physical and Medical Society entitled "*eine neue Art von Strahlen*" [96]. Translated, this paper spoke of "a new kind of rays", and describes his observations of bones surrounded by transparent flesh when exposed to these new, invisible rays, which Röentgen referred to as *X-strahlen*, or X-rays ("X" for unknown).

On New Year's day Röentgen sent copies of his article and radiographs to colleagues. The Vienna Free Press heard of the breakthrough and carried it as front page news on January 5, 1896.

It was not long before the phenomenon also received widespread publicity in the professional journals of the time, and advertisements for the technology needed to produce a beam of x-rays suitable for taking clinical images appeared. One such advertisement appeared in the *Electrical Engineer* only four months after the announcement of Roentgen's discovery (see Figure 2.1).

News of his success spread rapidly, and in the weeks following the discovery many scientists and physicians around the world began to repeat Roentgen's experiments in their own laboratories and hospitals. Within months of the discovery more efficient x-ray tubes became available, and diagnostic radiology, as it would later be termed, quickly became a common feature of medical practice in hospitals world-wide. For his pioneering and revolutionary work on the discovery and application of x-rays to medicine, Röentgen was awarded the first ever Nobel Prize in physics.

Figure 2.1: *An early advertisement following the discovery of x-rays*

In France a year later, Becquerel was investigating the effect of sunlight upon certain minerals. He hoped to prove his hypothesis that sunlight would cause certain minerals to emit x-rays which he could then detect with film contained within a light-tight envelope. Unknown to Becquerel, the minerals that he was using were naturally radioactive, and upon developing his film he found, just as he had expected, darkening due to x-rays. Later, however, he accidentally repeated the test without the presence of sunlight, and quite unexpectedly observed a similar positive result. It gradually became clear that he had observed the effects of natural radioactivity. In 1905 Becquerel received the Nobel Prize in physics for his work.

Both medical physics, and in particular the field of radiology have developed as a direct result of these two brilliant, if somewhat serendipitous, achievements which together have revolutionised our understanding of science and its application in medicine. The very penetrating nature of x-rays and γ-rays, and the wide range of radiopharmaceuticals now available, facilitate the routine, non-invasive, imaging of most anatomical features and physiological processes within the human body. Once formed, these images can be used to assist the physician in the diagnosis of a wide range of medical conditions.

2.3 Gamma-Rays in Nuclear Medicine

One of the primary methods used to investigate the *in vivo* biochemical function of organs within the body is through nuclear medical imaging techniques. Nuclear medicine relies upon the ability to detect the penetrating x-ray or γ-ray radiation emitted from within a patient after the administration of small amounts of radionuclide-labelled substances, called tracers. Organ function and metabolism can be measured in healthy and progressively diseased states with the resulting images being complementary to the purely anatomical information gained from radiographic film, ultrasound, x-ray CT and MRI imaging modalities.

Two γ-ray photon counting applications are routinely performed in nuclear medicine, each requiring detectors which offer very different characteristics. The determination of the amount of radioactivity in a given sample or volume (usually an organ), is commonly known as *organ counting*. Here position-sensitivity is not usually required, but excellent sensitivity and energy resolution are important. However, the determination of the distribution of radioactivity within the body, known as *imaging*, requires either intrinsic position-sensitivity, or the integration of many similar detectors to define an imaging plane, usually in two dimensions.

2.3.1 Principle of In Vivo Imaging of Gamma-Rays

The most useful radionuclides for use in nuclear medicine are those that emit γ-rays above 100 keV, since they can easily penetrate several cm of tissue and be detected from outside the body. Once the radionuclide-labelled tracer has been administered to the patient, it immediately begins to be *taken up* and metabolised by the organs and tissue within the body. Tracers are chosen that label a specific biochemical function and consequently larger amounts of the radionuclide will be metabolised by the organ whose function is to be studied, allowing some contrast in the image. Radionuclides used to label organs in this way are unstable isotopes which release energy from their nuclei in the form of photons or particles. The photons produced from many radioactive decays or positron annihilations from within a volume element radiate isotropically. Providing these γ-rays are sufficiently energetic and are not lost through internal Compton scatter and the photoelectric effect, they will penetrate the human body where they may be externally detected by several types of instrument. The point of origin of these emergent photons can be determined by using parallel hole collimators to localize those γ-rays which are normally incident on the detector, and generate images mapping the *in vivo* distribution of the radionuclide within the region of interest. This yields information relating to the location, uptake and metabolic function of that organ.

2.3.2 The Radioactive Decay Process

A particular radionuclide may emit charged particles in the form of alpha-particles (α), or beta-particles (β^-), or photons in the form of x-rays or γ-rays, or. Alpha-particles and γ-rays emitted from a given radionuclei have fixed energies, whereas beta-particles have a continuous range of energies up to a maximum value that is characteristic of the radionuclide. The fundamental properties of these decay products are briefly summarized in Table 2.1.

Decay Product	Symbol	Rest Mass (kg)	Charge	Typical Penetration Depth
Alpha-Particle	α	6.6×10^{-27}	+2	Varies with Kinetic Energy <10 cm in Air[1]
Beta-Particle	β	9×10^{-31}	-1	Absorbed by Several mm of Tissue
Gamma-Ray	γ	Zero	0	Absorbed Exponentially

1 Alpha-particles emitted by ^{241}Am yielding 5.5 MeV have a mean range of ~ 4 cm in air (Knoll [68])

Table 2.1: *Decay product characteristics*

A particular element will have a given number of protons and a varying number of neutrons contained within its nucleus. Nuclei of a particular element with different numbers of neutrons are called *isotopes* of the element. There are many naturally occurring, unstable or *radioactive* elements known as *radioisotopes*. Each radioisotope decays, obeying the laws of conservation of energy, momentum and charge, and energy is transported away from the nucleus (see Table 2.2).

Element	Radioisotope	Emission or Decay Mode [1]	Main Photon Energy (keV)	Half-Life
Carbon	^{11}C	β^+	511	20 minutes
Nitrogen	^{13}N	β^+	511	10 minutes
Oxygen	^{14}O	β^+, γ	511, 2312	71 seconds
	^{15}O	β^+	511	2 minutes
	^{19}O	β^-, γ	197	29 seconds
Fluorine	^{18}F	β^+, ec	511	110 minutes
Phosphorus	^{32}P	β^-	no photons	14.5 days
Chromium	^{51}Cr	ec, γ	320	28 days
Iron	^{52}Fe	β^+, ec, γ	165, 511	8 hours
Cobalt	^{57}Co	ec, γ	122, 136	270 days
Gallium	^{67}Ga	ec, γ	93, 184, 296, 388	78 hours
	^{68}Ga	β^+, ec	511	68 minutes
Krypton	^{81m}Kr	IT, γ	190	13 seconds
Rubidium	^{81}Rb	β^+, ec, γ	253, 450, 511	4.7 hours
Technetium	^{99m}Tc	IT, γ	140	6 hours
Indium	^{113m}In	IT, γ	393	102 minutes
Iodine	^{123}I	ec, γ	159	13 hours
	^{125}I	ec, γ, IT	28, 35	60 days
	^{131}I	β^-, γ	364	8 days
Xenon	^{133}Xe	β^-, γ	81	5.3 days
Ytterbium	^{169}Yb	ec, γ	57, 110, 131, 177, 198, 308	31 days
Gold	^{198}Au	β^-, γ	412	2.7 days
Mercury	^{197}Hg	ec, γ	69	65 hours
	^{203}Hg	β^-, γ	279	47 days
Thallium	^{201}Tl	ec, γ	81, 135, 167	73 hours

1 ec refers to electron capture; IT refers to isomeric transition

Table 2.2: *Characteristics of some common radionuclides used in nuclear medicine*

A daughter isotope is formed having less mass than its parent, but is often also unstable and will decay further until finally a stable isotope is formed. Most elements do not have naturally occurring radioisotopes at all, but those that do tend to be heavier. However, it is now possible to artificially synthesise radioisotopes of all elements in a particle accelerator or nuclear reactor, and more than 1400 different isotopes are now known of which about 80% are unstable. A number of these unstable isotopes are sufficiently abundant, and of the right energy to be extremely useful for applications in nuclear medicine.

2.3.3 Some Common Radiopharmaceuticals

The application of radionuclides to clinical nuclear medicine depends upon the widespread availability of suitable radiopharmaceuticals. These chemical compounds, administered to the patient with one of many radionuclides attached, are chosen taking into account the physiology and biochemistry of the organ which is to be studied (see Table 2.3a).

A whole new branch of the science of pharmacy has developed to meet the demands of modern nuclear medical imaging. Because the half-life of most radionuclides chosen for use in nuclear medicine is short, radiopharmaceutical techniques have evolved which enable the production and supply of fresh batches of tracer as they are required for clinical use.

A considerable range of radionuclide-labelled compounds are now available for applications in diagnostic nuclear medicine. The most common radionuclide currently being used is Technetium (^{99m}Tc) which has been incorporated into a wide variety of radiopharmaceuticals and is used to identify specific biochemical functions *in vivo* in virtually every human organ (see Table 2.3a). Similarly, Fluorine (^{18}F) a positron emitter with a half-life of 109 minutes, has found widespread use for imaging glucose metabolism *in vivo* in the form of the compound Fluorodeoxyglucose (FDG), an analogue of glucose. FDG is primarily used in PET studies of ambulatory cardiac function, and in brain studies. In addition, FDG has been used successfully in SPECT studies of ambulatory cardiac function together with a 511 keV collimator. However, the lower energy gamma-rays emitted from Thallium (^{201}Tl) usually enable SPECT studies of cardiac perfusion to be performed without the problems of septal penetration associated with the use of FDG. Hence ^{201}Tl, a γ-ray emitter with a half-life of 73 hours is often used in place of FDG, either for initial ambulatory studies of cardiac function, or where no PET detector is available to perform the scan.

Chemical Form	Investigation	Injected Activity (MBq)	Organ Dose (mGy)	Whole-Body Dose (mSv)
^{99m}Tc-Labelled Compounds				
Pertechnetate	Thyroid Scan	80	10	
Pertechnetate	Brain Scan	500	35 (Stomach)	12
Pertechnetate	Salivary Gland	80	10 (Thyroid)	
Pertechnetate	Meckel's Diverticulum	150	20 (Thyroid)	
Pertechnetate	Hemodynamic Studies	750	50	17
Microspheres	Lung Scan	80	8	
Tin Colloid	Liver Scan	150	13	2
IDA $_1$	Dynamic Liver Study	150	15	
Methyldiphosphonate	Bone Scan	600	14	
Pyrophosphate	Cardiac Infarct Scan	500	13	
Red Cells/Albumin	Cardiac Angiography	600		14
DMSA $_2$	Renal Scan	100	90	
DTPA $_3$	Dynamic Renal Study	100-500	8-40	
Various Foods	Gastric Emptying	80	3	
^{111}In-Labelled Compounds				
White Cells	Abscess	40	50 (Spleen)	
DTPA $_3$	Cisternography	30	6	
^{113m}In-Labelled Compounds				
Colloid	Liver Scan	80	9	
^{201}Tl-Labelled Compounds				
Thallium Salt	Cardiac Scan	100		3.6
^{75}Se-Labelled Compounds				
Methyl Cholesterol	Adrenal Scan	9	145	
Methionine	Pancreas Scan	9	60 (Liver)	25
^{51}Cr-Labelled Compounds				
Red Cells	Red Cell Mass	1	10 (Spleen)	
Chromic Chloride	Gut Protein Loss	4	20 (Spleen)	1.7
EDTA $_4$	Renal Clearance	4	22	

1 IDA, imidoacetate 2 DMSA, dimercaptosuccinate 3 DTPA, diethylenetriaminepentaacetate

4 EDTA, ethylenediaminetetraacetate

Table 2.3a: *Radiopharmaceuticals in routine clinical use (Phys. in Med. Biol. Encl. [90])*

Chemical Form	Investigation	Injected Activity (MBq)	Organ Dose (mGy)	Whole-Body Dose (mSv)
^{131}I-Labelled Compounds				
Iodide	Thyroid Scan	1	560	22
Cholesterol	Adrenal Scan	50	200	
Iodohippurate	Probe Renography	1	0.6	
Polyclonal Antibody	Cancer	40	100	
^{123}I-Labelled Compounds				
Iodide	Thyroid Scan	20-50	100-250	
Iodohippurate	Dynamic Renal Study	30-80	2-5 (Bladder)	
Fatty Acid	Cardiac Study	40	110 (Thyroid)	0.5
Monoclonal Antibody	Cancer	80	20	
n-isopropyl-*p*-iodoamphetamine	Brain Study	200	6 (Lung)	1.5
^{125}I-Labelled Compounds				
Fibrinogen	Deep Vein Thrombosis	4	1.5	
Albumin	Plasma Volume	0.2	0.14	
^{67}Ga-Labelled Compounds				
Citrate	Abscess	150	36 (Colon)	
^{81m}Kr-Labelled Compounds				
Gas	Lung Ventilation	500 min^{-1}	0.45	
^{133}Xe-Labelled Compounds				
Gas	Lung Ventillation	40 l^{-1} [1]	0.6	
^{57}Co-Labelled Compounds				
Vitamin B_{12}	Vitamin B_{12} Absorption	0.04	1.6 (Liver)	
^{58}Co-Labelled Compounds				
Vitamin B_{12} + Intrinsic Factor	Vitamin B_{12} Absorption	0.04	2.8 (Liver)	
^{59}Fe-Labelled Compounds				
Iron Salts	Ferrokinetics	0.4	14	
^{14}C-Labelled Compounds				
Tripalmitin	Gut Absorption Tests	0.4	0.5	

1 rebreathed for 2 min

Table 2.3b: *Radiopharmaceuticals in routine clinical use (Phys. in Med. Biol. Encl. [90])*

One of the earliest radiopharmaceuticals used is sodium iodide labelled with ^{131}I, having a γ-ray photon energy of 360 keV and a half-life of 8 days (see Table 2.3b). Its 8 day half-life enables ^{131}I-labelled radiopharmaceuticals to be used a great distance from where the radionuclide was synthesised, and weekly shipments are normally adequate for most medical facilities. However, this tracer is no longer extensively used because its long half-life and beta particles combine to give a relatively large radiation dose to the patient. Since long-lived beta or gamma emitting radionuclides give a larger radiation exposure to the patient than one with a shorter half-life and emissions of similar energy, they are avoided if a suitable alternative is available.

2.3.4 Radiopharmaceutical Uptake

The principles involved in the uptake of radiopharmaceuticals by the human body are well illustrated by the metabolism of the thyroid gland. The thyroid gland comprises two main lobes, one on either side of the trachea at the base of the neck, each consisting of follicles containing a jelly-like substance called colloid. The function of the thyroid is to concentrate iodine from the blood for the production of the iodine-containing hormones thyroxine and tri-iodothyronine which are stored in the colloid. Both the secretory activity and growth of the thyroid is controlled by the pituitary gland at the base of the brain through the secretion of the thyrotrophic hormone. In turn, thyrotrophic hormone production by the pituitary is controlled by the amount of thyroxine in the blood; when the blood thyroxine level falls, thyrotrophic hormone production is increased leading to the production of more thyroxine. This increased thyroxine concentration in the blood triggers a reduction of the pituitary gland's production of thyrotrophic hormone. Usually, equilibrium is maintained through this feedback control mechanism.

Thyroxine has a very powerful affect upon the body's metabolic rate and growth of all tissues. In man, thyroid underactivity in the infant results in a condition called *cretinism*; a cretin fails to attain adult stature or sexual maturity and is often grossly obese and is mentally subnormal. Thyroid underactivity in the adult produces a condition called *myxoedema*, characterized by a peculiar puffiness of the face and a thickening of the skin. The individual becomes slow witted, and because of the lowered metabolic rate they become very sensitive to the cold. The treatment to reverse these effects is to administer thyroxine to the patient.

Thyroid overactivity also occurs, often observed in middle-aged women, producing the condition known as *thyrotoxicosis* or *exopthalmic goitre*. Here many of the symptoms are caused by the raised metabolic rate and include weight loss, nervousness and irritability, quickened heart rate and insensitivity to cold. There is a swollen thyroid in the neck and the eyes protrude because of the accumulation of fatty material in the orbit behind the eyeball. The condition is probably due to the failure of the feedback mechanism; the pituitary is no longer so sensitive to the circulating thyroxine and therefore large amounts of thyrotrophic hormone are produced despite a high level of thyroxine in the blood. The treatment can be the partial removal of the thyroid gland in an operation known as *thyroidectomy*.

If there is insufficient intake of iodine in the diet, thyroxine production is reduced and there is a subsequent overproduction of thyrotrophic hormone by the pituitary gland. The thyroid gland grows, but is still unable to produce thyroxine because there is insufficient iodine in the diet. This type of enlargement is called *simple goitre* and is sometimes referred to as *Derbyshire neck* due to its prevalence at that location. Table salt is now often iodized to ensure an adequate intake of iodine in the diet.

This discussion of our understanding of the physiological function of the thyroid gland suggests that diagnostic nuclear medicine can provide information which will assist the clinician to identify these physiological changes within both the thyroid and the body. It has been found that chemical compounds labelled with a radionuclide are metabolised in exactly the same way as their stable counterparts, and minute quantities ($< 1\ \mu g$) of radiopharmaceutical have not demonstrated any disturbance in the normal physiological functioning of the body. Early work identified sodium iodide labelled with ^{131}I administered intravenously to be quickly taken up by the thyroid gland. Hence the measurement of ^{131}I-uptake gives some indication of thyroid activity. If the thyroid is underactive, causing the patient's metabolic processes to slow down, the amount of ^{131}I taken up is less than usual. When the thyroid is hyperactive, causing an increased metabolic rate (and resultant cardiac and eye disorders), the amount of ^{131}I taken up by the thyroid is greater than normal. Conversely, if part of the thyroid is abnormal due to the growth of a tumour or cyst, little or no ^{131}I activity will be observed from this region. However, as previously discussed in section 2.3.3, ^{131}I presents a greater risk to the health of the patient than some alternative radionuclides, and medical centres now tend to use ^{99m}Tc pertechnetate in preference. The pertechnetate ion has some similar physical characteristics to the iodide ion, but although the thyroid is able to trap it from the blood it is unable to incorporate it into the thyroid hormones. An image of the thyroid may be obtained using a gamma camera 20 minutes after intravenous injection of 100-150 MBq of ^{99m}Tc sodium pertechnetate, the distribution of the tracer within the organ yielding important information relating to its function and state of health.

In addition to ^{99m}Tc pertechnetate, ^{123}I is a recently introduced radionuclide offering the benefit of a much lower radiation dose than ^{131}I for thyroid imaging. This radionuclide has a photon energy of 160 keV and a half-life of 13 hours with no β^- emission, and has higher specificity for thyroid tissue than pertechnetate. The thyroid can be imaged 2-4 hours after intravenous administration of 200 MBq of ^{123}I.

2.4 Localization of γ-Rays in Nuclear Medicine

In most clinical studies in nuclear medicine, it is important that only γ-rays from within the region of interest are detected. Photons originating outside of this region increase the number of background γ-rays detected, reducing both the sensitivity and the contrast in the image. For this reason high-Z materials are used which limit the field-of-view and shield against unwanted counts. Information relating to the origin of the incident γ-ray flux must also be preserved in order to form an image whose x, y co-ordinates relate to the x, y co-ordinates of a two-dimensional projection of the object (Anger [3, 4, 5]). Several techniques for either directly localizing, or coding the incident photons upon the detector are currently used.

2.4.1 Parallel Multihole Collimators

Often referred to as low energy general purpose (LEGP) collimators, these mechanical collimators are specially designed shields placed within the field-of-view, in intimate contact with the detector. The collimator is usually constructed from a plate of approximately 2 cm thickness of high Z material, such as lead or tungsten, in which an array of parallel apertures ~ 2 mm diameter are formed. Through its careful geometric design, the LEGP collimator mechanically confines the counting volume to γ-ray photons which are almost normally incident upon the detector, and thereby localizes the site of the emitting radioactive sources (see Figure 2.2).

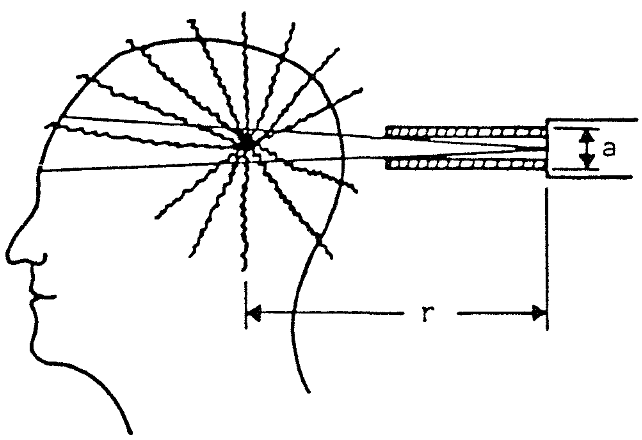

Figure 2.2: *Localization of radiopharmaceutical activity by a mechanical aperture*

These mechanical forms of collimation are simply based upon restricting the angle of acceptance such that the solid angle Ω is very small and is given by the relationship:

$$\Omega = \frac{\pi(a/2)^2}{4\pi r^2} \qquad 2.1$$

where a is the aperture diameter, and r the distance between the object and the detector. For typical values of a = 0.2 cm, and r = 10 cm, Ω approximates to 0.000025%. This is a considerable reduction in the original flux affecting both the sensitivity of the detector, and exposure time taken to acquire the image. In order to reduce this exposure time, either the aperture size or the injected activity could be increased. Increasing the dose to the patient is usually undesirable, whilst both the collimator resolution and the overall resolution that can be achieved by the scintillation camera would be affected by such a modification to the collimator.

Collimator resolution is dependent upon the diameter and length of each aperture, and the distance between the object being imaged and the collimator. This may be defined in terms of a point-spread function whose full-width may be determined from the expression:

$$R_c = \frac{d(1+b)}{l} \qquad 2.2$$

where d and l are the diameter and length of each aperture, and b is the distance of the point source from the outer surface of the collimator. Typically the collimator resolution is ~ 1 cm at a distance of 10 cm from the collimator, which represents a typical source depth within the patient. Therefore, the contribution of the collimator to the overall resolution of a scintillation camera is significant, making R_c the dominant factor in determining the resolution of a scintillation camera.

Most clinical examinations in nuclear medicine are conducted using an LEGP collimator because it provides a combination of adequate resolution and sensitivity for most regions of the body with no geometrical distortion. However, it can be seen from this discussion that the resolution can be significantly improved by reducing the distance between the object being imaged and the detector plane.

2.4.2 Converging and Diverging Collimators

For certain applications in nuclear medicine, it is desirable to angulate these apertures to form converging or diverging collimators. This modification to the parallel-hole design described previously, enables the detector to be adapted to image relatively small regions (converging collimator), or relatively large regions (diverging collimator), with a corresponding magnification or minification of the image formed at the detector. Alternatively, a similar result to the converging collimator can be achieved with a simple single, or multi-pinhole collimator which is particularly useful for imaging very small regions or small organs such as the thyroid gland. Due to the very penetrating nature of high-energy γ-rays, focused collimators must be designed for specific energies. Most are optimised for the 140 keV γ-rays from ^{99m}Tc.

2.4.3 Electronic Collimation

As figure 2.2 illustrates, mechanical collimation suffers from fundamentally poor sensitivity due to the very small solid angle which defines the counting volume. Only a small fraction (~0.000025%) of γ-rays emitted isotropically from the object are transmitted through the apertures to produce counts in the detector. Furthermore, for incident γ-ray energies in excess of about 250 keV, the increased septal thickness, length, and diameter of the apertures required for effective collimation, deteriorate the spatial resolution, uniformity, and sensitivity to the point where imaging becomes impractical. For this reason, many radioisotopes in the 250 keV region have either not been considered or are imaged under less than optimum conditions.

To overcome these fundamental disadvantages, an electronic alternative to mechanical collimation has been proposed by Singh et al. in 1977 [116]. The principle of electronic collimation depends upon the coincident detection of γ-rays which Compton scatter from one detector into a second detector.

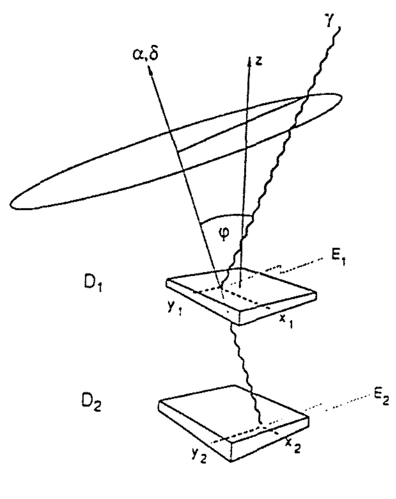

Figure 2.3: *The Compton camera*

The position of interaction and the energy deposited is measured in each detector, and by applying the well understood physical principles of Compton scattering, information relating to the origin of the γ-ray may be determined. The basic concept of electronic collimation is illustrated in Figure 2.3.

It can be found that each coincident count originates from activity lying somewhere on a hollow cone whose vertex, axis, and angle are known with an accuracy which is dependent upon the relative positions of the two detectors and their energy resolution.

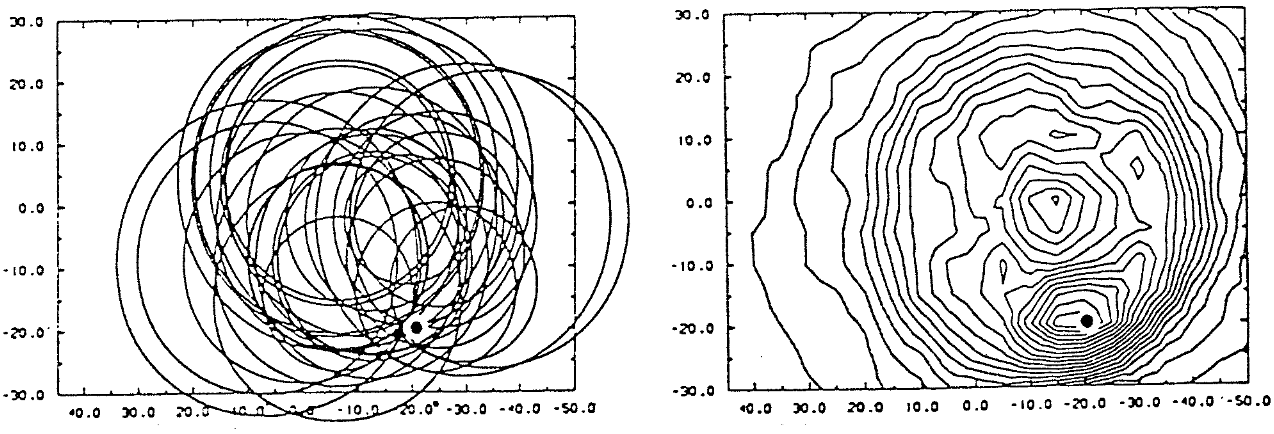

Figure 2.4: *Reconstructed image of a ^{60}Co calibration source*

Electronic collimation therefore localizes incident γ-rays to a region defined by the surface of a cone crossing the object. For repeated γ-ray photons incident upon the detector, a large number of intersecting conical surfaces will be defined from which the two-dimensional activity distribution can be mapped (see Figure 2.4). However, it should be noted that off-axis sources will lie somewhere along the path of an ellipse generated by the intersection of a cone inclined to the detector plane. This causes the point-spread function to vary as a function of scattering angle.

2.5 Planar Imaging in Nuclear Medicine

In planar imaging, penetrating radiation passes through the body and is projected onto an imaging plane, and a two-dimensional image of the three-dimensional object is produced. This section examines several planar imaging techniques which are used to reconstruct the spatial distribution of incident radiation from this projection data.

2.5.1 The Rectilinear Scanner

In 1950, Cassens developed the first mechanical scanner which became known as the *rectilinear scanner*. Typically, a converging collimator is used to localize the γ-rays incident upon a 12.7 cm diameter by 5 cm thick NaI(Tl) detector crystal which is coupled to a photomultiplier tube. The region of interest (ROI) is scanned in a raster pattern, recording the count rate at each position (see Figure 2.5).

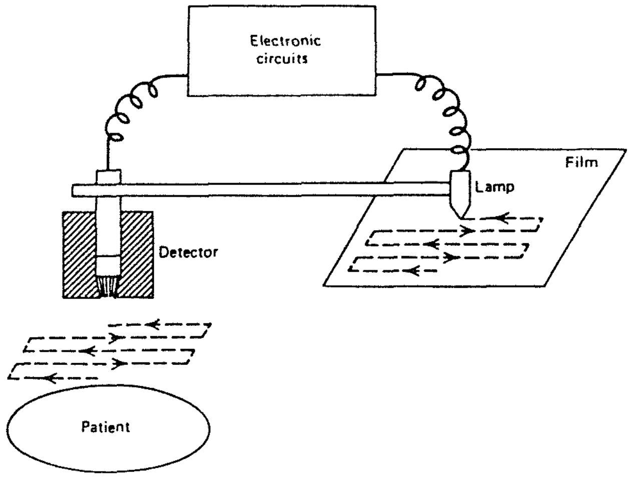

Figure 2.5: *The rectilinear scanner*

The movement of the scintillation detector is synchronously coupled to a lamp, the intensity of which is modulated according to the activity detected by the scintillation counter. As the detector scans the ROI, the lamp records the amount of radioactivity detected at each position by exposing the film corresponding to that position. The intensity of the lamp increases with activity, producing a pattern of dark regions on the film, and can be modified electronically to enhance count rate differences in areas of particular clinical interest. Usually a second image is made and stored electronically which can later be analysed using computational techniques to provide a quantitative image. The raster scan rate, the line spacing, and the area covered by the scan, can all be adjusted to suit the organ size, and the activity of the organ. Whilst early scanners covered areas of 36 cm by 43 cm, many modern scanners can perform whole-body scans, with the resulting image minified to fit on a standard 36 cm by 43 cm film. Some scanners have been adapted to accommodate two detectors facing each other so that both sides of the patient can be scanned simultaneously. This helps to determine the distribution of the radioactivity with greater accuracy. Illustrated in Figure 2.6 is a rectilinear scan of the thyroid gland in both normal and diseased states of health, taken from Cameron and Skofronick [21].

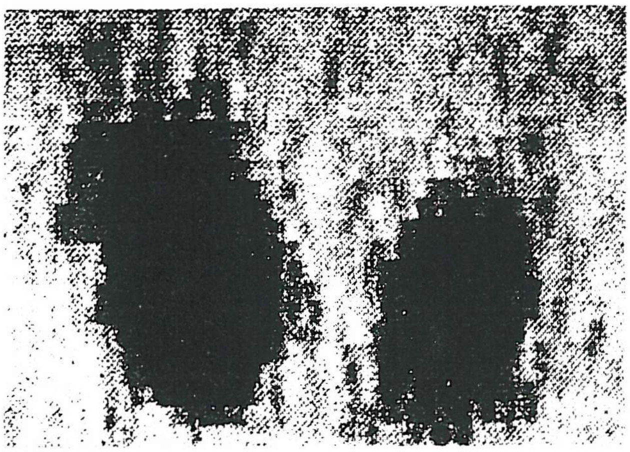

(a) *Scan showing healthy thyroid*

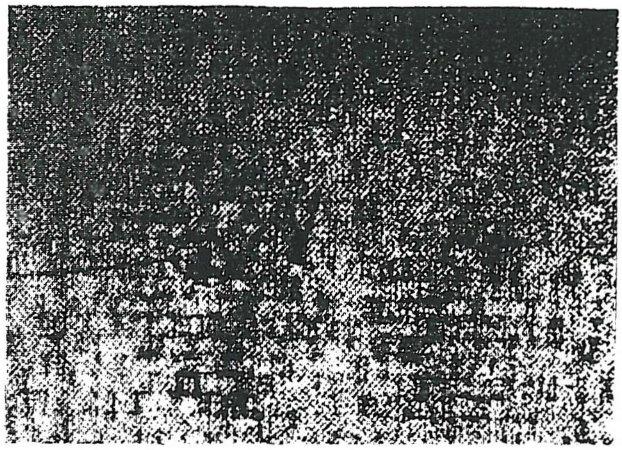

(b) *Scan showing thyrotoxicosis*

Figure 2.6: *Rectilinear scans of the thyroid gland*

This technique yields information relating to both anatomy and physiology. However, the spatial resolution is low (~5 mm FWHM), and the detail in the image is poor. In addition, scanning in this way is a very inefficient imaging technique, as only a very small fraction of activity is used at any one time with the consequence that the patient dose is higher than would be necessary to obtain the same image with a non-scanning imaging system. Each scan can last as long as 30 minutes during which time the patient must remain motionless. Motion artifacts from the heart, diaphragm, and liver therefore cause blurring of the image. Despite these disadvantages, this method of imaging still finds use for some studies in several hospitals in the UK.

2.5.2 The Anger Camera

In 1956, Hal Anger of the University of California invented the *gamma camera*, later known as the Anger Camera [3]. This now well established technique has found particular application in diagnostic nuclear medicine, and is widely used as one of the primary clinical tools for imaging γ-rays in the detection of tumours and other physiological disorders. Several authors have conducted detailed investigations of the performance characteristics of the Anger Camera (Short [112], and Webb [131]), in an attempt to improve upon the original design for a range of applications in nuclear medicine.

A typical Anger Camera comprises as many as 91 small hexagonal photomultiplier tubes of between 4 cm and 6 cm A/F grouped concentrically. These view a NaI(Tl) scintillator of 1 cm thickness and up to 50 cm in diameter, through a glass lightguide having a thickness of between 1 cm and 2 cm (see Figure 2.7).

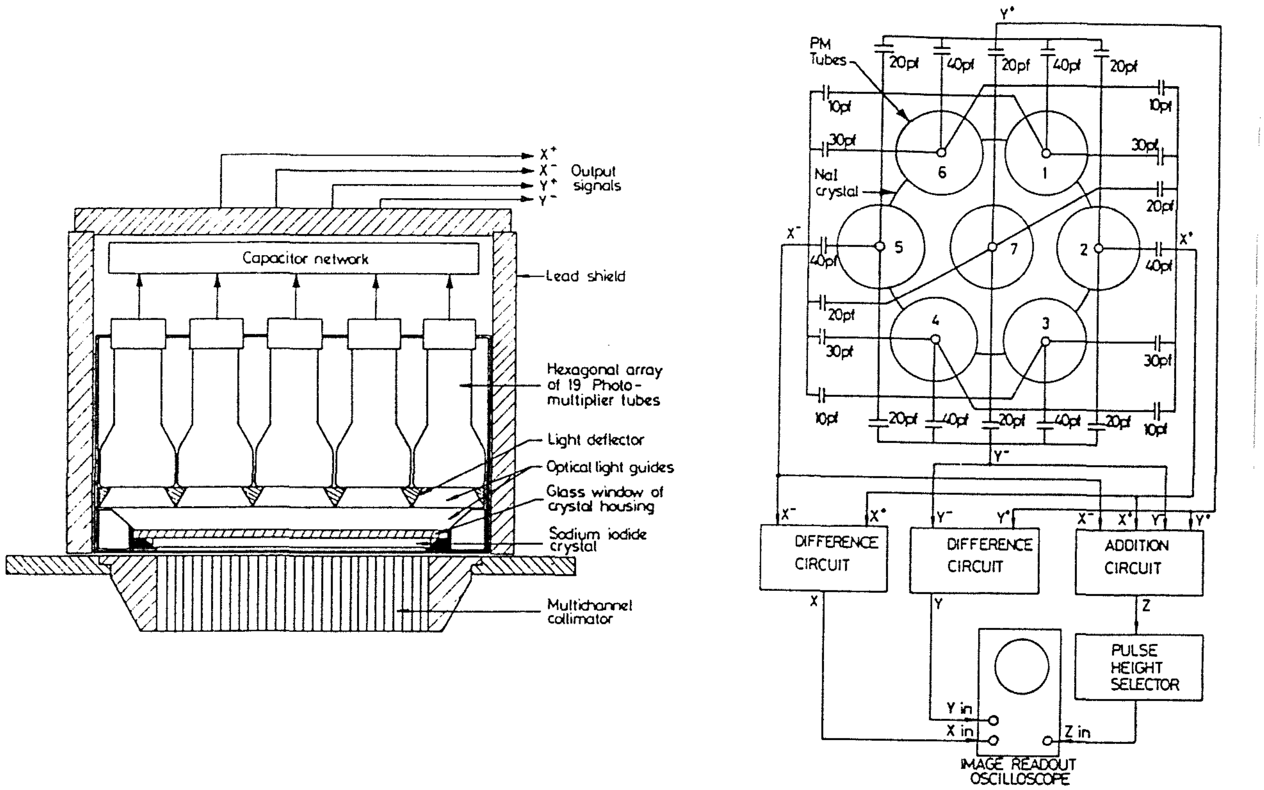

Figure 2.7: *The Anger Camera*

Photons emitted isotropically from within the patient are mechanically collimated, and incident γ-rays interacting within the detector generate scintillation photons which themselves propagate isotropically through the crystal from their point of interaction. Those photons falling within a cone of acceptance defined by Snell's law, will be captured by the glass lightguide where they will continue to spread out as they propagate further. Eventually, the flux will be incident upon an array of several tubes, producing a large signal in the tube closest to the point of interaction, and weaker signals in those further away. The resulting electronic signals are read out by a resistive charge-division network from which the light spread function can be found computationally using an interpolating algorithm.

Photons not meeting the criteria for transmission from the detector crystal into the lightguide will be trapped within the crystal where they will continue to propagate, and will subsequently undergo many diffuse reflections until they reach the edge of the crystal. Here they are absorbed by an absorbing black coating which is applied to the edge of the detector crystal, and they play no further part in the operation of the gamma camera. In fact this is an over simplification, and the effect of the diffuse background in the detector crystal upon camera performance will be explored further later in this section, and in Chapter 4.

This imaging technique exploits the excellent SNR characteristics of PMTs, to provide clear images above the electronic noise. However, the centroiding readout and image reconstruction technique used to read out the Anger Camera place limitations upon the usable sensitive area for imaging applications. The centroid of the light-spread function for γ-rays whose point of interaction is located towards the edge of the detector crystal, would suffer reconstruction errors due to edge effects. In order that this can be avoided, the outermost ring of photomultiplier tubes lies outside of the sensitive area of the camera, enabling better sampling and accurate determination of the centroid of the light pool. The original gamma camera exploited the simplicity of pinhole collimation, and although the parallel multihole collimator is now favoured, the pinhole collimator is still used for some studies where a frame-filling image of a small organ such as the thyroid gland is required. The imaging time for a gamma camera will obviously depend upon such factors as the injected activity, the specificity of the radiopharmaceutical, and the distance between the source and the detector plane. However, for typical nuclear medicine studies this is of the order of a few minutes, and it is therefore possible to conduct dynamic physiological studies using this technique that cannot be achieved with the rectilinear scanner. Radionuclides with half-lives as short as 2 minutes or less can also be imaged using the Anger Camera. For clinical studies in nuclear medicine using ^{99m}Tc at 140 keV, the Anger Camera offers a detection efficiency of 97%, and a spatial resolution slightly better than the rectilinear scanner at between 3 mm and 4 mm FWHM, although this will be very dependent upon the collimator resolution. Typical energy resolution of 15% FWHM has been achieved with ^{57}Co at 122 keV, and the Anger Camera has a low energy detection threshold of about 40 keV.

The performance of a scintillation camera can be characterized in terms of its resolution, sensitivity, and intrinsic non-linearities. The resolution R of scintillation imaging is primarily determined by the *intrinsic resolution* of the camera R_i, and the *collimator resolution* R_c. The net resolution can be obtained by the quadratic sum of these two terms:

$$R^2 = R_i^2 + R_c^2 \qquad 2.3$$

Intrinsic Resolution is the cameras ability to locate the point of interaction of the incident γ-ray photon. Generally, the more photomultiplier tubes that are used for a given camera size, the better the intrinsic resolution. However, fluctuations in the output voltages due to fluctuations in the number of photons collected by each photomultiplier tube ($N \pm \sqrt{N}$), will tend to limit the improvement in position resolution that might be achieved by greatly reducing tube size. Since N is a linear function of the incident energy E, contributions to the intrinsic resolution are also due to Poisson statistics ($1/\sqrt{E}$), with resolution improving as energy increases. The intrinsic resolution is further limited by the accuracy with which the point of interaction can be located from the light pool which is incident upon the array of photomultiplier tubes. There is some research underway to estimate the depth of the interaction from a knowledge of the shape of the light spread function (Rogers et al. [99]). This should eventually lead to improvements in the intrinsic spatial resolution of commercially available gamma cameras. In addition to this, single or multiple Compton scatters followed by photoelectric absorption at some distance from the site of the original Compton scatter will produce a distorted light spread function (see Figure 2.8).

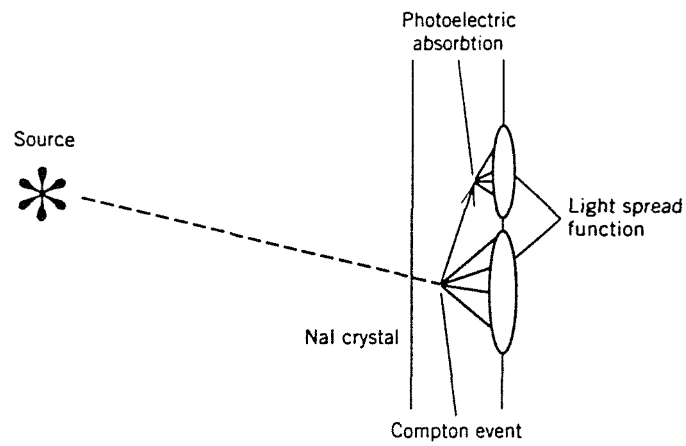

Figure 2.8: *Distorted light spread function due to Compton scatter*

This leads to centroid reconstruction errors in determining the original position of interaction within the crystal which cannot so far be corrected for in the conventional gamma camera.

Non-linearities cause the response function of the Anger Camera to be spatially variant as a function of position of interaction. Variations in the photocathode response of photomultiplier tubes within the array cause point-to-point fluctuations greater than those expected by photon counting statistics. These non-uniformities can be corrected by imaging a flood source with good statistics and then normalizing subsequent images with the flood source image. In addition, the resolution is non-uniform across the sensitive area of the camera due to the weighting effect caused by the diffuse background within the detector crystal. Correction of resolution distortions are more difficult, and can only be achieved in the conventional gamma camera through repeated calibration of the camera, and the subsequent application of a lookup table. Pulse pileup due to high count rates either distort the image, or are not counted resulting in a dead time. Currently the usable count rate is in the 100,000-200,000 cps range, although some cameras have been designed to operate at count rates as high as 500,000 cps.

2.6 Tomography in Nuclear Medicine

In 1917, Radon postulated that objects could be represented by a series of line-integrals which could subsequently be combined to reconstruct slices of the original object [94]. In 1963 Cormack further developed this idea, suggesting that Radon transformations could be applied to obtain 3-dimensional distributions of radiographic density within the human body [29]. This technique, better known as *tomography*, was later to demonstrate improved contrast over the conventional radiograph.

Since then, this technique has been widely applied, enabling 2-dimensional images of sections through the body to be generated. Considerable advances in computer processor speed, data storage, and data handling capability has also recently enabled the 3-dimensional reconstruction of surfaces within the body. This section considers the various imaging modalities in both diagnostic radiology and nuclear medicine where this technique is commonly applied, and discusses the performance characteristics of each.

2.6.1 Computerized Tomography (CT)

This technique combines the data acquired over a number of projection angles about the patient to generate 2-dimensional cross-sectional images of the body. The principle of computerized tomography (CT) was first demonstrated in 1972 when Houndsfield of EMI in England developed a CT system, based upon the principles first proposed by Cormack nine years earlier, for imaging the head [57]. Both Houndsfield and Cormack later received the Nobel Prize for their work. In the original unit, two pencil beams of 140 keV x-rays scan linearly across a patients head. The intensities of the transmitted beams are sampled by two detectors positioned diametrically opposite, whose motion is synchronized with that of the beams. The linear scan data is stored in the computer, the detectors are rotated through 1°, and the process repeated until after approximately 4 minutes, 180 sets of projection data have been acquired (see Figure 2.9).

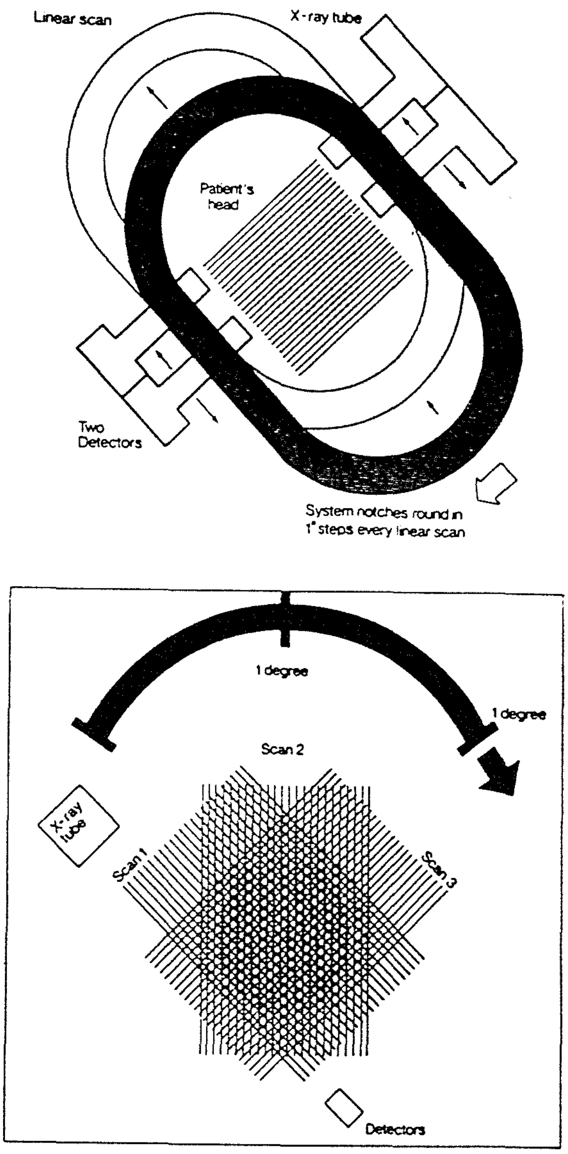

Figure 2.9: *Principle of operation of CT scanner*

By reducing the 180 sets of projection data to a series of linear equations, Houndsfield determined the distribution of densities within the slice by applying an iterative reconstruction algorithm to determine their solution by successive approximations. The resulting solution can be displayed as a greyscale image from which variations in density as small as 1% can be observed.

Modern CT imaging systems have scan times enabling the possibility of dynamic studies, and can be used to image any part of the body. The most common image reconstruction algorithm currently used in CT is that of *filtered back-projection* (FB), which is easily and rapidly implemented by digital computer and which can reconstruct an image more quickly than Houndsfield's original method. Illustrated in Figure 2.10 is a brain study taken recently showing the fine detail that can be achieved using this technique.

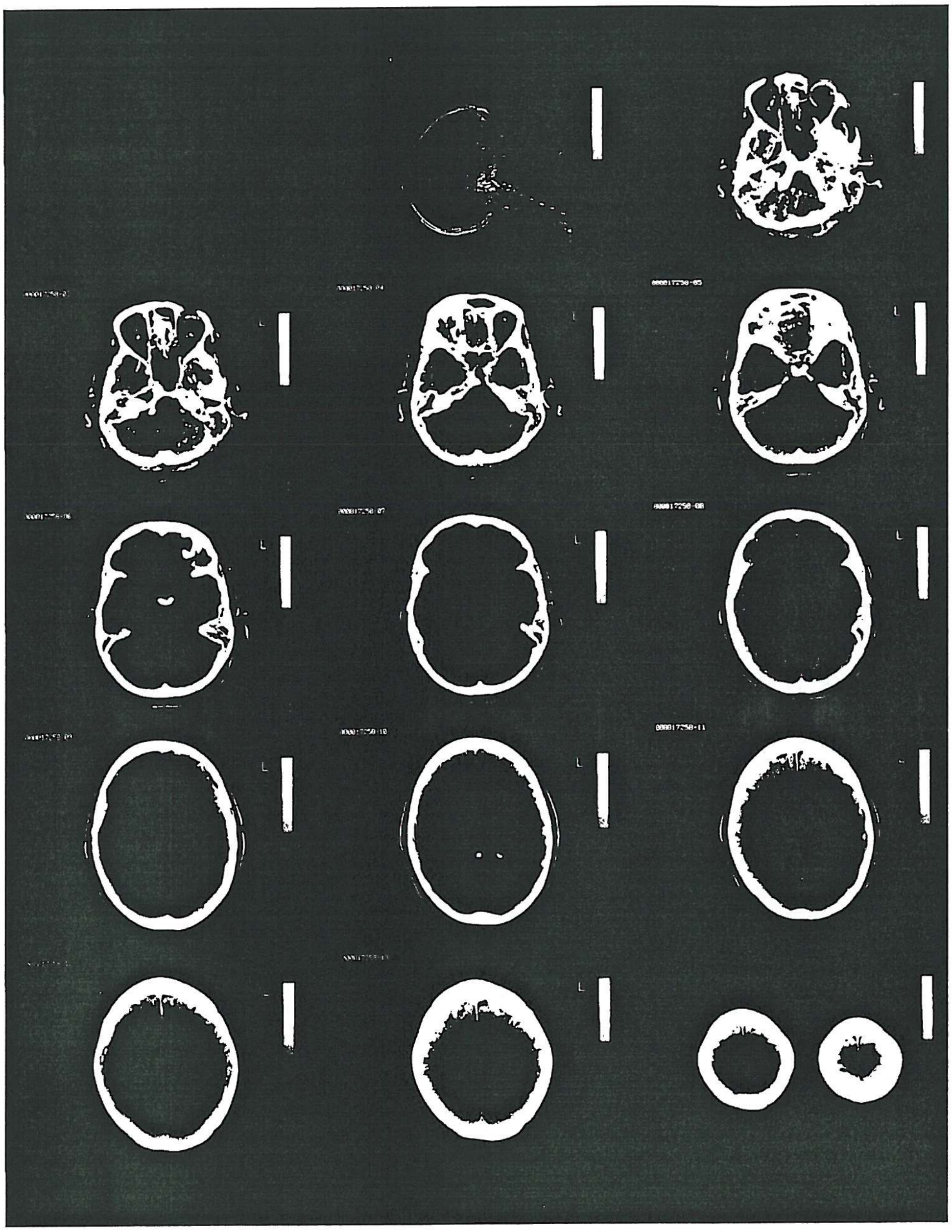

Figure 2.10(a): *A brain study using CT imaging techniques*

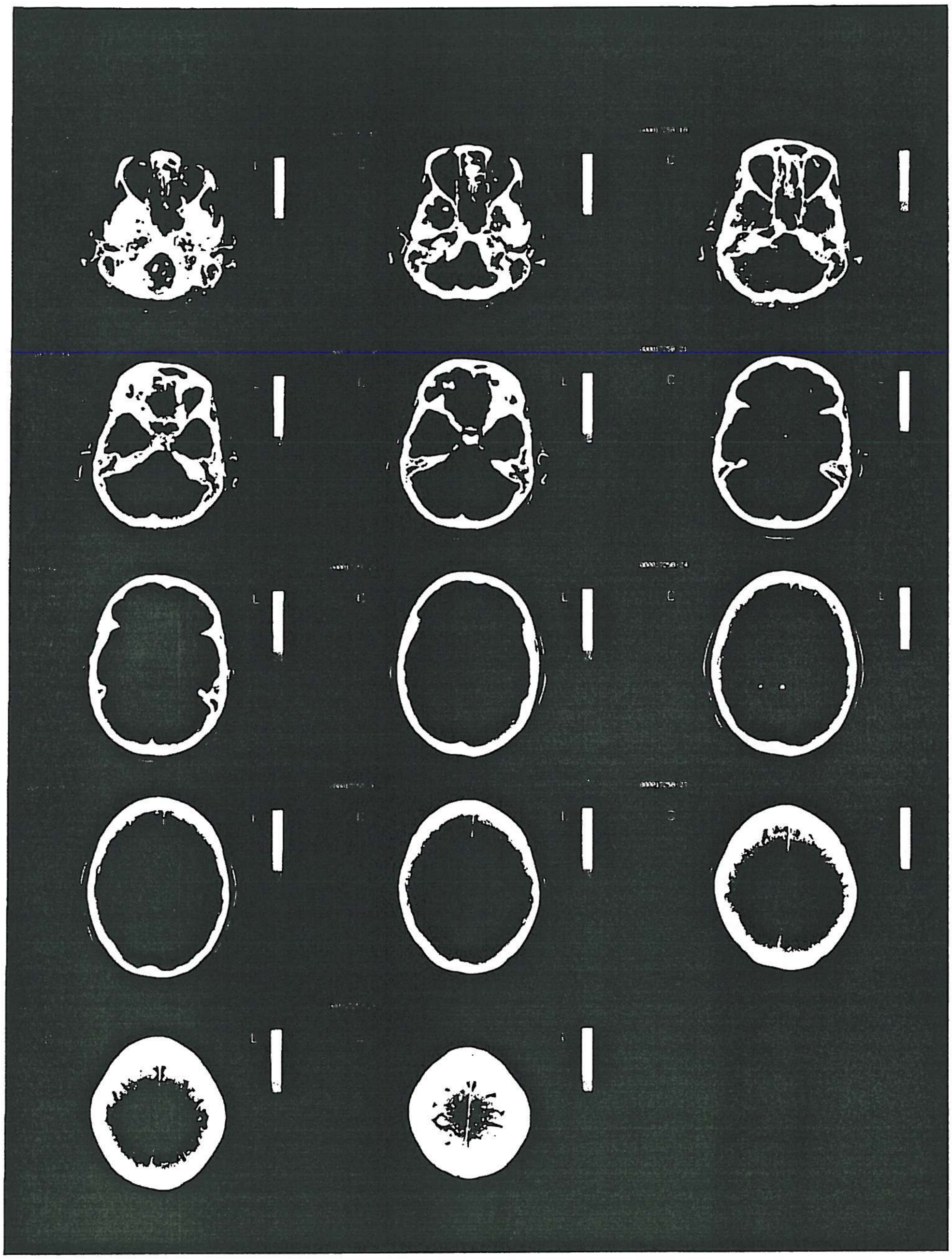

Figure 2.10(b): *A brain study using CT imaging techniques*

2.6.2 Single Photon Emission Computed Tomography (SPECT)

The tomographic imaging technique can also be applied to nuclear medicine studies, to provide an *in vivo* quantitative estimate of the 3-dimensional distribution of radionuclide within the patient. A gamma camera of the type described previously is used together with a mechanical collimator to localize the γ-ray photons along a narrow region analogous to the pencil beam used in x-ray CT. One obvious advantage of SPECT is the ability of the gamma camera to simultaneously acquire projection data along many axes. However, the poor intrinsic sensitivity of the gamma camera due to the small solid angle defined by the collimator, places a statistical limitation upon the temporal resolution that can be achieved with SPECT. In addition, other intrinsic non-uniformities exhibited by the gamma camera described previously will manifest themselves in the SPECT image. Recently, three headed camera systems have been developed to improve the sensitivity of SPECT, enabling four revolutions in data acquisition mode to be performed per minute. This yields a theoretical temporal resolution of 5 seconds, although in practice this is limited by photon statistics to approximately 30 seconds. Spatial resolution of the order of 2 cm FWHM can be achieved using this technique.

Due to the relatively modest cost of single and multi-head gamma cameras, and the ability to study the relationship between anatomy and physiology using readily available radiopharmaceuticals, this imaging modality has found widespread use.

2.6.3 Positron Emission Tomography (PET)

Although the principle of positron imaging was recognised as early as the 1950s, it was not until the development of x-ray CT in 1972 that the potential of PET could start to be realised.

Physical characteristics exhibited by positron emitting radionuclides enables PET to offer a uniquely valuable diagnostic procedure for clinical imaging in nuclear medicine. The most important characteristic is the near collinearity of the two photons generated in the annihilation process, enabling the path along which the annihilation event took place to be localized without resorting to the application of mechanical collimation techniques. This is achieved in practice through the use of a coincidence detection circuit which records only those annihilation events where two 511 keV γ-ray photons are detected within a period of 10^{-8} second or less (see Figure 2.11).

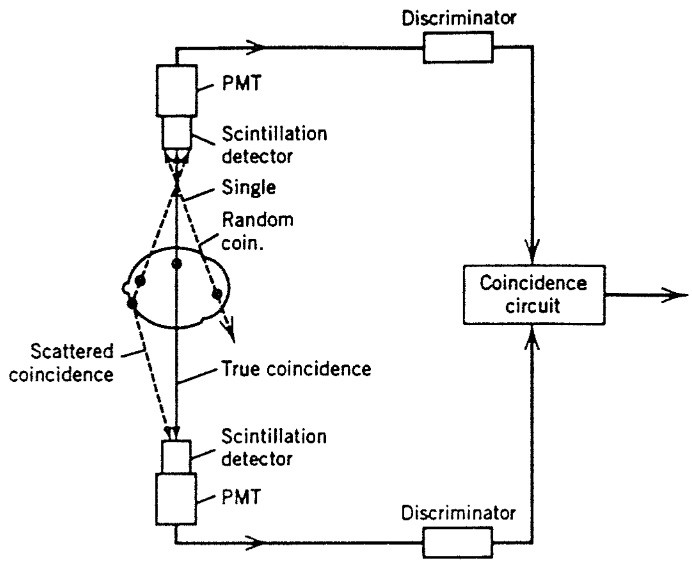

Figure 2.11: *Principle of coincidence detection*

Since the two detectors recording the coincidence events can only record annihilations from a volume in space which is defined by a column which is subtended between the two detectors, a very uniform collimation characteristic is observed compared to that of SPECT. Since this form of *electronic collimation* alone is employed to localize the incident γ-rays, the sensitivity exhibited by PET is also correspondingly better than SPECT. Using the tomographic techniques previously discussed, line-integral projection data are acquired from a large number of detectors at different views. The distribution of the activity within the slice or volume can then be measured quantitatively using filtered back-projection reconstruction algorithms to produce an image of the slice.

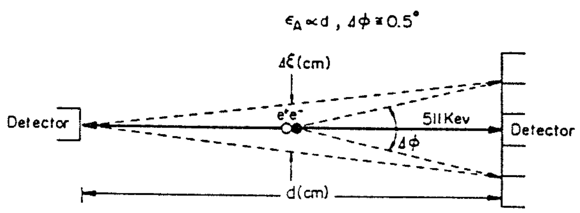

(a) Effect of angular uncertainty of positron annihilation upon position resolution

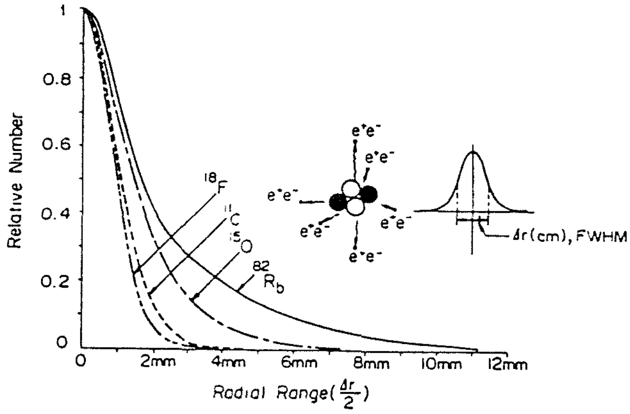

(b) Effect of positron range upon position resolution

Figure 2.12: *Parameters affecting position resolution in PET*

The accuracy with which the position of interaction can be reconstructed is limited by two physical characteristics of the positron annihilation process (see Figure 2.12). Firstly, there will be some uncertainty due to the non-perfect collinearity of the annihilation photons. In addition, there will be some uncertainty in the annihilation position caused by the range of positrons within the body. Modern PET detectors offer spatial resolution between 2 mm and 3 mm FWHM depending upon detector size, the separation distance between the detectors, and the radionuclides used. Despite these limits placed upon the spatial resolution that can be achieved with this technique, PET has both the highest resolution, and the highest sensitivity of any detector used for imaging in nuclear medicine.

It is theoretically feasible to improve the spatial performance of PET by encoding the depth of each annihilation occurring within the region of interest. Although difficult in practice, this might be achieved by exploiting the very small time of flight (TOF) differences between "coincident" γ-ray photons as they are incident upon the ring of detectors. For axially propagating photons within the detector, TOF differences are directly proportional to the radial distance of the annihilation within the detector.

By encoding these timing differences, and knowing the column which is subtended between two detectors, it will be possible to reconstruct the exact point of origin in three dimensions. The TOF concept in PET therefore appears to be useful in low-resolution PET systems, where additional TOF information can be of value in enhancing the resolution and improving the signal-to-noise ratio of the imaging. However, for this technique to be practically achievable, the decay constant of the scintillator must be significantly shorter than the minimum TOF difference that is to be resolved. For axially propagating photons, the TOF difference can be determined from the expression:

$$TOF\ difference = \frac{2r}{c} \qquad 2.4$$

where r is the radial distance of the annihilation event from the centre of the detector ring, and c is the velocity of light in a vacuum. For a radial distance of 1 cm, the TOF difference approximates to 6.67 x 10^{-11} seconds. For a system comprising scintillators coupled to photomultiplier tubes, the variance in the response of the two detectors can be described by the following expression:

$$\sigma_{t,t}^{*2} = 2\frac{\tau^2 + \sigma_t^2}{\bar{n}_{k,s}} \qquad 2.5$$

where τ is the decay constant of the scintillator, σ_t is the standard deviation of the fluctuations in the transit time, and $\bar{n}_{k,s}$ is the mean number of photoelectrons per scintillation event. In order that these two γ-ray photons will be resolved at the detector, scintillators with a decay constant less than 100 picoseconds should be used. This is usually very difficult to achieve through existing detectors and associated electronics. Whilst the recent development of a few fast scintillation crystals, such as CsF and BaF_2, are encouraging, such excellent timing characteristics are not yet common, and for this reason depth encoding based upon TOF differences generally remains speculative.

2.7 Conclusions

We have examined the role played by radionuclides and radiopharmaceuticals in diagnostic nuclear medicine, together with a number of systems used for their detection. Existing knowledge of the physiological changes associated with various states of disease in the thyroid gland has illustrated how nuclear medicine is currently able to offer procedures which are of clinical benefit to the patient. Several radiopharmaceuticals offering higher specificity and lower patient dose have been developed which enable improved contrast in the image, whilst at the same time offering improvements in radiation safety. These developments have created the possibility for a range of innovative nuclear medicine studies such as nuclear mammography which is currently being considered by several groups (Pani [86], and Thompson [122]).

Whilst the preferred alternative for most nuclear medicine studies at low energies is the conventional gamma camera, the very large size of these systems is incompatible with an application such as nuclear mammography where, in order to be effective, the camera needs to be in intimate contact with the breast-bone of the patient. Moreover, the performance of these cameras is limited by the collimator resolution, the intrinsic resolution of the camera, and more importantly by Compton scatter within the patient. Better energy resolution could in theory offer improved results through scatter rejection.

Mechanical collimation systems currently used in nuclear medicine have the advantage of simplicity and, for most clinical investigations, they offer acceptable spatial resolution combined with adequate, if somewhat modest, sensitivity. However, to minimize the radiation dose to which the patient is exposed, a reduction in the injected radiopharmaceutical activity is increasingly desirable. The relatively modest sensitivity performance of all forms of mechanical collimation make such a development improbable without migrating to alternative methods of source flux localisation. The very high sensitivity that can be achieved using electronic collimation techniques clearly offers the potential to overcome some of these problems, although the development of a Compton Camera for applications in nuclear medicine is non-trivial, and it is probable that these imaging systems will not be available for a considerable time.

Clearly, the tomographic imaging modalities that have been discussed in this chapter are extremely powerful diagnostic techniques that offer potential benefits in clinical radiology. Many of these imaging modalities are developing steadily, and have yet to fully realise their potential.

Investigation of the physiology of organs within the body can be performed using SPECT. The widespread use of gamma cameras perhaps makes this the most practical and most cost-effective choice of the two modalities described here. However, image quality is modest, and the spatial resolution and sensitivity are both poor using this technique. Both attenuation and scatter correction for this technique are non-trivial, and considerable effort has been expended in trying to improve the performance of SPECT. Work is currently being conducted to investigate the feasibility of performing dynamic SPECT (Limber et al. [77]).

Perhaps the most interesting development discussed here is that of PET. This technique offers excellent spatial resolution and a uniformly high sensitivity over the whole of the detector, enabling the accurate compensation of the attenuation within the patient. Organ function can be studied using radioisotopes which have a very strong physiological affinity for the human body combined with very short half-lives, facilitating imaging combined with a considerable reduction in the radiation dose received by the patient. An example is ^{15}O with a half-life of 2.05 minutes, which because of its close relationship with metabolic processes in human physiology offers the possibility of performing dynamic brain studies. However, both the detector, and the cyclotron needed to produce the radioisotopes are expensive, and this technique is being evaluated at only a few medical centres at present, largely as a research tool. Work is currently being conducted into a depth encoding form of the PET detector (Moisan et al. [83], and Rogers [100]).

It seems clear from this discussion that whilst PET has the capability to offer superior resolution and sensitivity, the clinical gamma camera will remain in widespread use for both planar imaging and SPECT for a considerable time. For many applications a more compact camera could potentially offer performance advantages over conventional gamma cameras where improved resolution could be achieved by positioning the camera in much closer proximity to the patient. Thyroid and breast imaging studies are good examples where improved resolution could be realised if the desired reduction in scale could be achieved.

Chapter 3

Detectors for Gamma-Ray Imaging

3.1 Introduction

A range of scintillation detector materials suitable for the detection of γ-rays in nuclear medicine will be presented, and photodetectors which offer the possibility of developing a position-sensitive scintillation counter are reviewed in this chapter. Their performance characteristics and suitability for inclusion within a small gamma camera will be discussed.

3.2 Considerations for the Design of Scintillation Detectors.

There are many factors to be considered when deciding which scintillator has the most suitable qualities for a particular application in nuclear medicine. Seldom do the operational characteristics of the scintillator crystal and the photodetector match perfectly when the two are combined in a scintillation counter. Therefore the choice will always be a compromise, weighing those scintillator qualities which are considered to be of greatest importance against the most desirable performance features of the detector design.

In conventional γ-ray scintigraphy for example, where the expected count rate at the detector is unlikely to exceed 25,000 cs^{-1} , a moderately fast scintillator is perfectly adequate. A high detection efficiency is required in order to reduce the radiation dose to which the patient is exposed, and high contrast, determined by a high SNR, is important to delineate physiological and anatomical features in the image. Thallium doped sodium iodide - NaI(Tl), a high light yield scintillator with moderate density, and modest timing characteristics is generally accepted as the best compromise for this particular application. However, for other applications in nuclear medicine, this compromise almost always involves a trade-off between decay time, light output matched to the spectral response of the detector, and detection efficiency, although there are several other qualities which must also be taken into consideration. Listed below are the most important characteristics which should be considered:

Detection efficiency depends upon the interaction cross-section at a particular energy. It will vary as a function of density and the atomic number. Ideally this should be chosen to be as high as possible, particularly for high-energy applications such as PET, where Compton scatter dominates.

Light output depends upon the efficiency with which incident γ-rays are converted into optical photons, and should be linear as a function of deposited energy. Increased light output improves spatial, and energy resolution due to improved Poisson statistics.

Decay time depends upon the half-life of activator excited states before de-exciting to the activator ground state. This value should be well defined for a particular crystal. The speed of decay will be of greatest significance where fast timing is required for either high count-rate applications, veto detection, or applications such as time of flight PET. Scintillators with different decay times can be used in a *phoswich* configuration to distinguish between energy deposits in different crystals.

Afterglow or phosphorescence occurs because some electron excited states within the crystal have long half-lives due to forbidden transitions. It is often possible to anneal the crystal and temporarily eliminate this source of photons. However, in high count rate applications, or if centroiding is used to reconstruct the position of interaction, crystals that are known to suffer from afterglow should be avoided.

Peak emission depends upon the bandgap energy between the activator excited state and the vibrational ground state. The material should ideally have high transparency to the light which is emitted, and the peak wavelength of emission should be well matched to the response function of the photodetector in order to maximise the light collection efficiency.

Refractive index is of primary importance in any γ-ray scintillation counting detector. Ideally, the scintillator crystal should be carefully matched to the photodetector, and any other optical components of the detector system. A poorly matched optical system will severely inhibit the light collection efficiency through a combination of increased total internal reflection and a reduction in the cone of acceptance for meeting the criteria for transmission.

Mechanical stability can be particularly important for applications where the scintillator crystal is required to be machined into a particular geometrical configuration.

Chemical stability should be considered if the scintillation crystal is to remain unprotected from the environment in which it is to be used. Ingress of moisture under normal atmospheric conditions can severely degrade the performance of hygroscopic crystals necessitating either complete mechanical encapsulation, or the application of a non-porous conformal coating material such as Parylene-C (Day et al. [34]).

3.3 Characteristics of Some Common Scintillators

Almost half a century has elapsed since early crystalline inorganic scintillators were first used to detect ionising radiation in nuclear medicine. In that time several new materials have been found to scintillate, and a wide range of performance characteristics can now be chosen which closely match both the spectral response of the photodetector, and the desired temporal performance for many applications in nuclear engineering and medical physics. Recent research using computer modelling to develop a range of *designer* scintillators has yielded a great many more scintillating materials (Blasse [19], and Lecoq et al. [74]).

Scintillators can generally be separated into two main groups, organic and inorganic. Inorganic crystals are characterised by high photon yield, high stopping efficiency, and good linearity. However, with only a few exceptions this group of scintillators are relatively slow. Conversely, organic scintillators are characterised by low photon yield, low stopping efficiency, but are very fast. Generally, inorganic scintillators are most suitable for applications in nuclear medicine due to their higher stopping efficiency and light yield. The discussion in this section will therefore concentrate almost wholly upon the performance characteristics of a variety of inorganic scintillation crystals, and their particular suitability for applications in nuclear medicine.

3.3.1 Properties of Some Classic Inorganic Scintillators

Crystalline inorganic scintillators have been commercially available for many decades during which time their properties have been optimised through extensive research. Further improvement in the characteristics of this group of scintillators seems unlikely at the present time, although the search for the ideal fast, bright, high density scintillator material continues unabated. Included on the following page is a discussion of the principal materials against which some of the more recently developed scintillators are compared, and Table 3.1 provides a summary of the properties of these and several other classic inorganic scintillators.

NaI(Tl) has since the early 1950s remained the most popular choice for use in the clinical Anger Camera due to its high photon yield per MeV and close match with the spectral response of the bialkali photocathode. Being strongly hygroscopic, this material rapidly forms a layer of sodium hydroxide when exposed to air which seriously degrades its performance, necessitating mechanical encapsulation. It suffers from phosphorescence, with 9% of the total light yield being emitted with a characteristic decay time of 150 μs. Whilst this is not a major problem in γ-ray scintigraphy, this material is unsuitable for higher count rate applications such as PET [12, 54, 55, 68]. Polycrystalline NaI(Tl), produced through the recrystallization of single crystals under heat and pressure, offers an alternative material exhibiting identical scintillation properties to the single crystal form. The resulting structure yields improved mechanical strength, permitting the construction of complex geometries requiring only a minimum of machining. Other inorganic scintillators are also available in polycrystalline form. Current development hopes to overcome the problems associated with the hygroscopic characteristic of this scintillator enabling the manufacture of segmented arrays. It is possible that the non-porous conformal coating material Parylene-C might be used, enabling the crystals to be directly optically coupled to the window of the PSPMT. Commercially available crystals are expected within the next six months (Day et al. [34]).

CsI(Tl) has a photon yield per MeV which is far higher than NaI(Tl), but when viewed by a photomultiplier tube its performance is significantly worse due to poor matching of its peak emission wavelength with the spectral response of most photocathodes [12, 55, 68]. However, the improved match between this wavelength, and the spectral response of high quality silicon photodiodes has recently found widespread application of this material (Grassman et al. [41]). Since CsI(Tl) is only slightly hygroscopic no mechanical encapsulation is necessary. This enables a variety of crystal configurations to be constructed, including a wide range of segmented arrays. Despite the relatively poor PMT quantum efficiency at the peak emission wavelength of CsI(Tl), segmented arrays of this material viewed by the position-sensitive photomultiplier tube (PSPMT) have yielded encouraging results. The material has only moderate mechanical stability, and polished surfaces can easily sustain damage.

When irradiated with γ-rays, CsI(Tl) has two principle decay components of 0.6 μs (54%) and 3.4 μs (46%) with the slower component having a higher peak emission wavelength than the fast component (Gong et al. [40], Grassman et al. [42], Rossner et al.

[102], and Schotanus et al. [108]). When viewed by photodiodes, the rise-time of the output signal due to the scintillation crystal is observed to be in excess of 10 μs. For maximum light collection a long integration time is therefore required. In practice however, a more modest integration time of the order of 3 μs is chosen as the optimum value (Bird et al. [15], and Carter et al. [25]). Since the spectral response of the bialkali photocathode peaks at much shorter wavelengths, the slow decay component is not detectable, and an integration time of the order of 1 μs is typically chosen when viewed by a PMT.

The varying decay time for different exciting particles is a characteristic of this material making it very interesting for applications where pulse shape discrimination techniques are used to distinguish between types of incident particle (Bird et al. [17]).

CsI(Na) has a total photon yield per MeV which is slightly higher than NaI(Tl) but not as high as CsI(Tl). The peak emission is well matched to the spectral response of the photomultiplier tube, resulting in a figure being quoted for the relative light output of this material of between 85% and 115% of NaI(Tl), viewed by a bialkali photocathode. CsI(Na) is mildly hygroscopic, and for most applications mechanical encapsulation is not required [12, 54, 55, 68]. Ingress of moisture into the surfaces of the crystal, reacts with the sodium activator sites causing a sodium hydroxide *dead layer* to be formed to a depth of between 200 μm and 600 μm from the crystal surface (Lewis [76]).

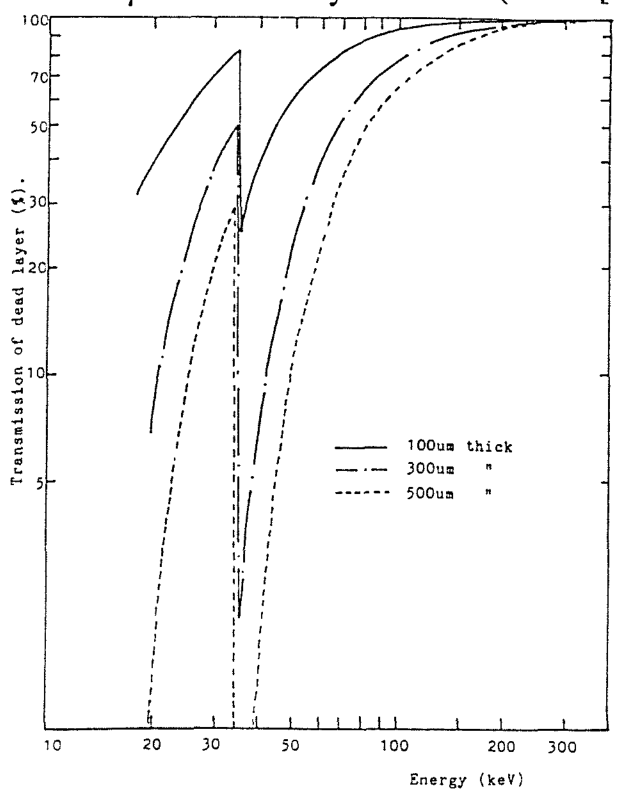

Figure 3.1: *Transmission of various thicknesses of CsI(Na) dead layer (Lewis [76])*

Low energy γ-rays absorbed within this layer will fail to produce scintillation light, and more energetic photons that are absorbed below this layer have their light output degraded through attenuation and absorption (see Figure 3.1). The layer of sodium hydroxide, once formed, acts as a barrier preventing further degradation of the material. Since there is no permanent damage to the crystal, it can be repolished to remove the sodium hydroxide layer prior to coupling. Despite these problems, Ito et al. [59], have reported excellent results using a CsI(Na) scintillation plate to acquire high resolution images. However, difficulties have been encountered in the production of consistently high quality crystals that exhibit a uniform response function. This is particularly marked in the case of segmented arrays, and recent measurements performed on samples of these detector arrays has demonstrated that the variance in the light output between adjacent elements can be as high as 60%. Assuming a dead layer growth to a depth of 500 μm, the transmission of γ-rays at energies of 140 keV is as high as 85%, making this a suitable material for applications in nuclear medicine. However, this dead layer is believed to also affect the transmission of optical photons, and further critical investigation into the absorption of optical photons in this dead layer is required. Communications with scintillator crystal manufacturers have recently tentatively suggested that many of the problems associated with the formation of sodium hydroxide on the surface of hygroscopic NaI(Tl), and CsI(Na) crystals will shortly be overcome by the application of conformal coating materials. However, further investigation is needed before this is realised (Day et al. [34]).

BGO is a dense scintillator material exhibiting high stopping efficiency combined with modest light output with decay components of 60 ns (10%) and 300 ns (90%), and no significant phosphorescence [12, 54, 55, 68]. The peak emission wavelength is better matched to the spectral response of photodiodes than it is to the majority of photocathodes, although both types of photodetector are used to view the scintillation light. This material demonstrates excellent mechanical and chemical stability compared with either CsI(Tl) or NaI(Tl), but the significantly lower light output makes it most useful at high energies. It is often chosen for nuclear medicine applications such as PET where the count rate is high, Compton scatter dominates, and high detection efficiency is consequently desired (Yamashita et al. [134]).

$ZnWO_4$ exhibits properties which are comparable to those of BGO and consequently this material is used for similar applications, such as nuclear medicine and PET. Its stopping efficiency and light output are slightly higher, but its decay time is significantly slower [12, 55].

Pure Alkyl Halides, in particular NaI and CsI deserve special mention. Both of these materials exhibit strong temperature dependence, and although at room temperature their performance is disappointing, at liquid nitrogen temperatures their scintillation efficiency increases considerably (Knoll [68]). However, the operation of photomultiplier based systems at these low temperatures has proven difficult for most practical applications in clinical nuclear medicine.

3.3.2 Summary of Some Classic Inorganic Scintillators

Material	Density ($g\ cm^{-3}$)	Att. Length [2] μ^{-1} (cm)	Light Yield (Photons per MeV)	Principal Decay Constant (ns)	Refract. Index	Peak λ (nm)	Rel. Light Output [1] (%)
CsI [3]	4.51	2.43	126500	600	1.79	400	220
NaI [3]	3.67	3.05	76000	60	1.85	303	200
NaI(Tl)	3.67	3.05	38000	230	1.85	415	100
CsI(Na)	4.51	2.43	39000	630	1.79	420	85
CaF_2(Eu)	3.18	3.72	19000	940	1.40	435	50
CsI(Tl)	4.51	2.43	52000	1000	1.79	550	45
LiI(Eu)	4.08	2.73	11000	1400	1.96	470	35
$CdWO_4$	7.90	1.21	15000	15000	2.30	470	25 - 30
						540	
GSO(Ce)	6.71	1.50	10000	60	1.85	440	20 - 25
$ZnWO_4$	7.87	1.19	10000	5000	2.20	480	28
$CaWO_4$	6.10	1.50	6000	6000	1.92	430	16
BGO	7.13	1.11	8200	300	2.15	480	15 - 20
BaF_2	4.88	2.29	10000	630	1.50	310	16
			1800	0.8	1.54	220	5
Li-glass	2.50			75	1.55	395	10
CsF	4.64	2.69	2500	3	1.48	390	5 - 7
CsI	4.51	2.43	2300	16	1.79	315	4 - 6
CeF_3	6.16	1.77	4200	27	1.62	340	3

1 Relative pulse height measured using a PMT with bialkali photocathode
2 Attenuation length (in cm) for 511 keV photons
3 At liquid nitrogen temperature

Table 3.1: *Summary of the properties of classic inorganic scintillators*

3.3.3 Properties of Some Recent Inorganic Scintillators

In addition to the materials already considered, there are several scintillation materials that have only been commercially available for a short time. Many of them are still being improved in the continued search for the ideal combination of characteristics of high speed, high light output, and high density, with excellent properties of mechanical and chemical stability. Here we discuss many promising new inorganic and polycrystalline materials against which some of the very recently developed scintillators can be compared. Table 3.2 provides a summary of the properties of these and several other recently developed inorganic scintillators.

Lu_2SiO_5 (Ce) yields a light output of approximately 70% of NaI(Tl), making this material of particular interest. It demonstrates a fast decay time and is both chemically and mechanically very stable. Cerium doped Leutetium Oxyorthosilicate (LSO) has two decay components of 12 ns and 42 ns, producing 35% and 65 % respectively of the total light yield, approximating to a single decay time of 40 ns (Melcher [80]). However, these very useful qualities are somewhat overshadowed by several undesirable characteristics and the expense of the raw materials used in its production. Approximately 2.6% of naturally occurring Lu is in the form of ^{176}Lu, a radioactive isotope which gives rise to self-excitation of the crystal with characteristic photoelectric absorption peaks at 89 keV, 202 keV, and 307 keV at a rate of approximately 200 $cs^{-1}cm^{-3}$. In addition, it has been demonstrated that this material exhibits a non-linear response to incident energies between 5 and 60 keV, which is thought to be responsible for poorer than expected resolutions at energies up to 662 keV (Suzuki [118]). This new material is also strongly excited by ultraviolet, resulting in phosphorescence with a very long half-life, and the light output is strongly temperature dependant (Visser [128]). Continuing research is seeking ways of overcoming these various problems whilst preserving the excellent light output and timing characteristics of the material.

$YAlO_3$(Ce) provides significantly better light output than BGO and has a fast decay time. Cerium doped yttrium aluminate (YAP:Ce) has good radiation hardness, but because of it's lower density it has poorer stopping efficiency than BGO (Baccaro et al. [9]). In order to improve the stopping power, the *Crystal Clear* collaboration are investigating the possibility of increasing the density by replacing yttrium with isoelectronic cations such as ytterbium [54, 110].

$PbWO_4$ is the most promising new scintillator currently under development, and the high density and atomic number of this material provides the highest stopping efficiency of any known scintillator. The fast decay time and modest light output of this material, combined with its excellent mechanical and chemical stability is expected to attract considerable interest in this material for a wide range of applications in nuclear engineering and nuclear medicine imaging applications such as PET. It is however still a very recently developed material, and further investigation into its scintillating properties is continuing [54]. Crystals of high quality $PbWO_4$ are expected to become commercially available shortly.

3.3.4 Summary of Some Recent Inorganic Scintillators

Material	Density ($g\ cm^{-3}$)	Att. Length [1] μ^{-1} (cm)	Light Yield (Photons per MeV)	Principal Decay Constant (ns)	Refract. Index	Peak λ (nm)	Mechanical Stability
YSO(Ce)	4.50	2.70	45000	370, 82	1.80	420	high
LSO(Ce)	7.40	1.22	30000	40	1.82	420	high
YAP(Ce)	5.35	2.24	19700	31	1.94	390	high
YAG(Ce)	5.00	2.63	11000	65	1.82	550	high
GSO(Ce)	6.71	1.50	10000	60	1.85	440	high
CeF_3	6.16	1.77	4200	27	1.62	340	high
LaF_3(Ce)	5.94	1.85	220, 1890, 90	3, 26.5, 185	1.70	290 340	high
LaF_3(Nd)	5.94	1.85	1800	6	1.70	173	high
CdS(Te)	4.82	2.39	190, 3170, 13640	18, 270, 30,000		640	high
BSO	7.13	1.06	1200	100	2.06	480	high
CdF_2	6.64	1.76	200	10	1.55	540	poor
CsCl	3.99	2.79	1800	880	1.64	245, 270	poor
$PbSO_4$	6.40	1.28		135	1.85	340	high
$PbCO_3$	6.60	1.16		2, 15, 92	1.80 2.04	475	high
$PbWO_4$	8.20	0.90	2000	4.5, 10.2		430	high

1 Attenuation length (in cm) for 511 keV photons

Table 3.2: *Summary of properties of some recently developed scintillators*

3.4 Scintillation Counting Devices

This section considers the often complex problems encountered when combining the characteristics of a range of modern photodetectors which are suitable for coupling to scintillation crystals for photon counting in the x-ray and γ-ray regime. Whereas for many years scintillators have been almost exclusively viewed by arrays of discrete photomultiplier tubes, recent developments in the field of photonics have provided a far wider variety of position-sensitive devices. These photodetectors are presented here, and the suitability of each for inclusion within a compact position-sensitive scintillation counter which will offer spatial resolution of 1-2 mm is discussed.

3.4.1 Principle of Operation

Because inorganic scintillation crystals are ~2000 times more dense than the gas used in gas proportional counters, they make very efficient detectors for stopping γ-rays. They can be fabricated in a variety of geometries, and there is virtually no limit upon the collection depth as is often the case with semiconductors. The intensity of the weak scintillation flash produced when an incident γ-ray deposits energy in the crystal is proportional to the energy deposited. Hence, if the incident γ-ray photon is totally photoelectrically absorbed within the crystal, the light yielded by the crystal will also be proportional to the energy of the incident γ-ray. This weak scintillation flash is detectable by a number of quite different photodetectors. The purpose of the photodetector is simply to collect the optical photons from the scintillator, and convert this optical signal into an electronic signal that can subsequently be amplified and processed. The resulting pulses can either be counted directly, or more usually are passed to a pulse height analyser (PHA) and *windowed* before determining the number of counts at the γ-ray energy of the administered radionuclide.

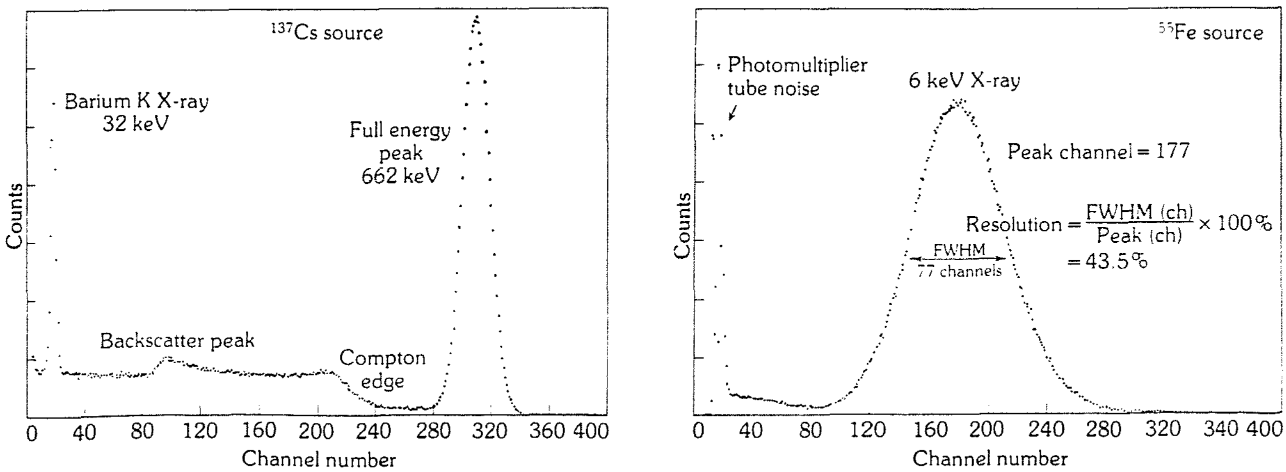

Figure 3.2: *A typical pulse height spectrum from a NaI(Tl) - PMT based scintillation counter*

For certain purposes it is desirable to determine the pulse height distribution of all of the pulses from the detector. This is most conveniently performed with a multi-channel analyser (MCA), which bins the pulses according to their amplitude into 256 or 512 channels. An energy spectrum of a NaI(Tl) detector used to view a monoenergetic γ-ray source is shown in Figure 3.2.

3.4.2 The Photomultiplier Tube

Since about 1950, the standard photomultiplier tube (PMT) has provided charge gain between the γ-ray interaction process in the scintillation crystal and the readout electronics. A handful of companies now dominate in the mass manufacture of PMTs for a range of applications. However the supply of small hexagonal tubes for inclusion within Anger Cameras for clinical nuclear medicine forms the largest sector of the total demand for PMTs. These tubes, whilst not intrinsically position-sensitive, tessellate very well to form a group of typically 91 hexagonal tubes, each measuring approximately 6 cm A/F, which define the area of the imaging plane. Position-sensitivity can then be easily achieved by reading out the signals from a group of seven adjacent tubes using a resistive charge-division network, and subsequent use of an interpolating algorithm to determine the centroid of the event. Photomultiplier tubes are also coupled to spectroscopy crystals and used to determine the specific activity within a given volume of the body.

The principle of operation of the PMT is dependent upon an internal, multi-stage charge multiplication process. Photons are first converted into primary photoelectrons with a quantum efficiency of typically 15-25% which will vary depending upon the type of photocathode employed and the wavelength of the scintillation light (see Figure 3.3).

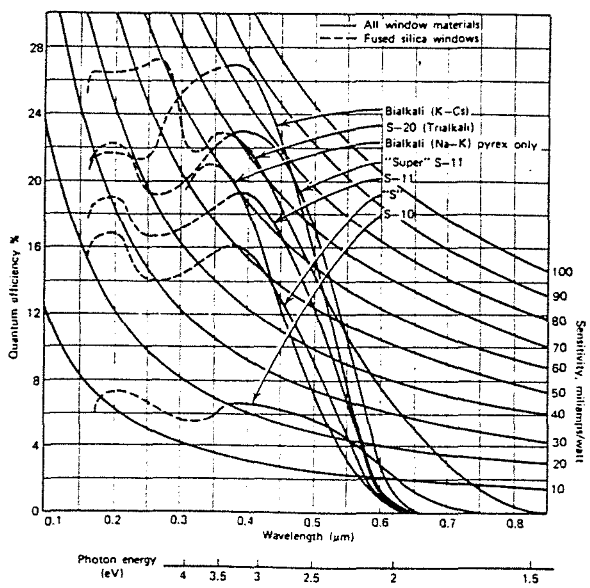

Figure 3.3: *The spectral sensitivity of a range of photocathode materials*

A high negative potential (typically ≤ 1000 Volts) is applied between the photocathode and the collection anode of the PMT. This potential is distributed between the photocathode and a series of dynode structures using a simple potential divider circuit with each successive dynode at a more positive potential than that preceding it. Primary photoelectrons ejected from the photocathode are therefore accelerated towards the first dynode where they deposit their acquired kinetic energy. For each incident primary photoelectron, many more secondary photoelectrons are emitted which in turn are accelerated towards the next dynode stage. This successive process of amplification is repeated between 10 and 15 times providing a typical charge gain of 10^5-10^6, and finally the amplified signal is collected by an anode plate at the base of the PMT. The charge deposited upon this anode is subsequently read out by the data acquisition system used to analyse measure the energy deposited within the scintillator (see Figure 3.4).

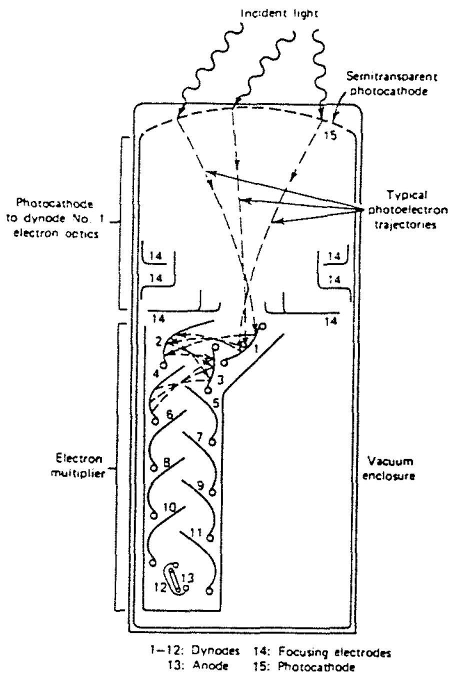

Figure 3.4: *The electron multiplication process*

Examples of two basic photomultiplier tube designs in common use employ dynode structures known as the *Venetian-blind* and the *box-and-grid*, and these are described in greater detail:

Venetian-blind dynodes comprise parallel strips slanted with respect to the axis of the tube and stacked parallel to the photocathode. The large surface of the first dynode makes it possible to use a fairly simple electron-optical input system. This arrangement permits high collection efficiency and good gain stability. However, only moderate temporal characteristics can be achieved, the response time being slow due to the low electric field at the surface of the dynodes.

Box-and-grid dynodes also have a large collection area at the first dynode, and hence have good collection efficiency, but the low electric field at the internal surface of the boxes does not contribute to good time characteristics. These tubes are of course available in a wide range of sizes and are commonly used in many applications where spectroscopic or photon counting information is desired.

More recently developed dynode structures include the *mesh dynode*. These consist of parallel mesh planes of thin wire which through their careful construction constrain the spread of the photoelectron cloud (see Figure 3.5).

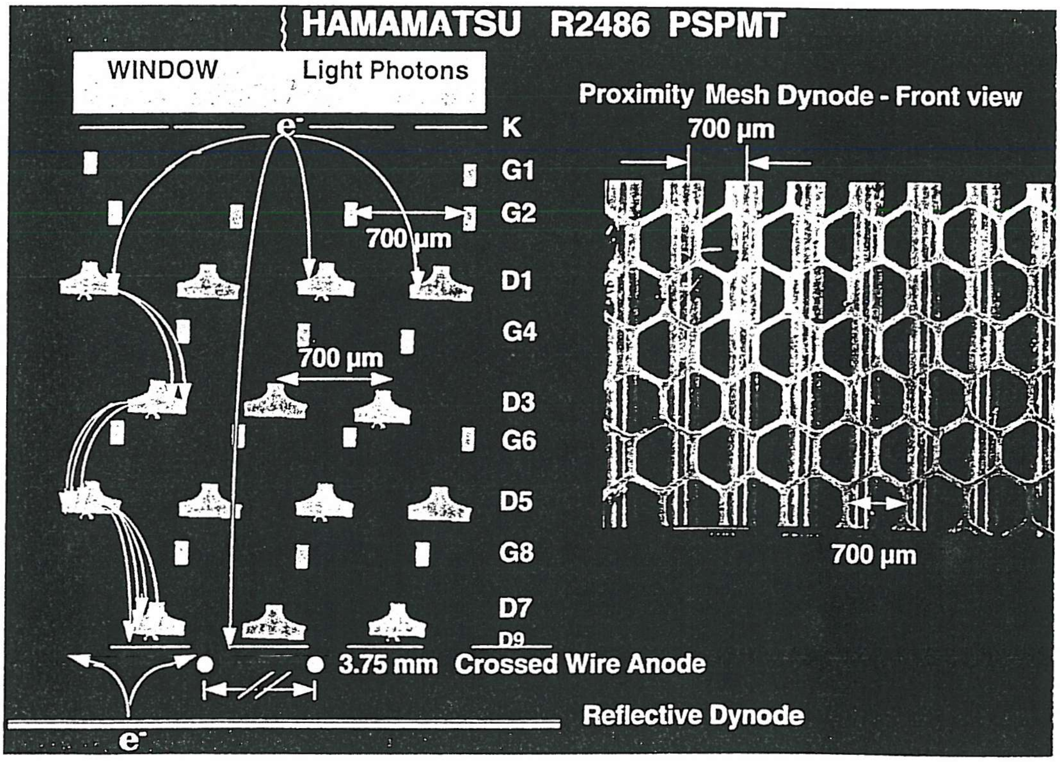

Figure 3.5: *Principle of the mesh dynode (Barone et al. [10])*

Mesh dynodes have found particular application in recently developed position-sensitive photomultiplier tubes (PSPMTs). Because of the high crosstalk, the spatial position of an event must be found by centroiding over many channels, and consequently these tubes demonstrate modest timing response. Their collection efficiency from dynode to dynode is low due to the relatively small collection areas which contributes to an effective reduction in the gain. Despite this, the mesh dynode has been used successfully in the Hamamatsu family of PSPMTs, which provides a gain of approximately 10^5 for 10 stages of mesh dynodes, and an applied bias potential of 1150 Volts. Variations of these tubes have been operated in magnetic fields of about a Tesla, and although the gain is reduced in fields of this magnitude, it is still approximately 10^4 for a 16-stage tube.

A process of continuous development over several decades has facilitated the commercial availability of tubes having very modest dimensions, with many manufacturers recently developing TO8 packaged devices to complement their product range. In addition to their standard range of photomultipliers, both Hamamatsu and Philips currently offer a wide variety of photomultiplier tubes which exhibit intrinsic position-sensitivity. Hamamatsu Photonics offer their family of PSPMT employing mesh dynode structures [45, 46, 47], whilst Philips Photonics provide several variations which employ foil dynode structures [89].

PMT based organ counters are typically comprised of a scintillation crystal directly coupled to the window of a standard configuration non position-sensitive photomultiplier tube. Generally, since only limited position information can be obtained by scanning a region of interest, these systems are primarily used with specially designed collimators for detailed spectroscopic studies of single organs, where high detection efficiency and energy resolution are required. Typically, 12 and 14 stage venetian blind tubes are used which offer the benefit of high gain at the expense of a relatively slow response, and these tubes are well suited to view large NaI(Tl) scintillation crystals for most clinical applications (see Figure 3.6).

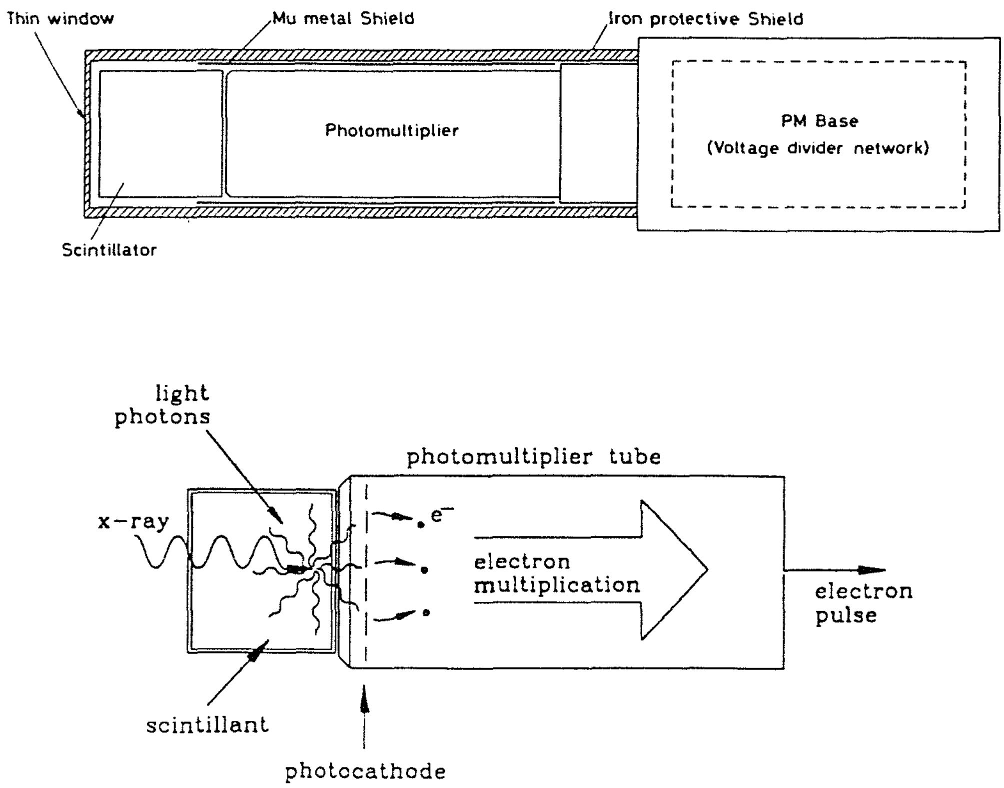

Figure 3.6: *A typical scintillation counter*

The performance of these scintillation-counter systems will depend upon several factors. The spectral sensitivity of the PMT should be chosen to match the peak emission wavelength of the scintillator as closely as possible. Generally, scintillators with higher light yield will offer superior energy resolution due to improved counting statistics. Gain stability and pulse height resolution determine the performance of a γ-ray spectrometer. Pulse height resolution is dependant upon the photocathode uniformity, the photocathode sensitivity, and the first dynode secondary emission ratio. The detection efficiency of a γ-ray spectrometer is a measure of how much of the incident radiation is absorbed within the scintillation crystal and converted into optical photons. To be useful as a spectrometer, a scintillation material should exhibit a high probability for the complete absorption of the incident radiation.

Isotope	**Energy (keV)**	**Typical Energy Resolution (FWHM %)**	**Best Energy Resolution (FWHM %)**
^{55}Fe	5.9	60	45
^{129}I	30	40	30
^{241}Am	60	30	15
^{57}Co	122	25	15
^{137}Cs	662	9	7

Table 3.3: *Typical NaI(Tl) Energy Resolution Values, source Harshaw Catalogue [49]*

The interaction cross-section for 140 keV γ-rays emitted by a ^{99m}Tc being fully absorbed by a 1 cm thick crystal of NaI(Tl) is very high, and these crystals offer unsurpassed light yield at a peak emission wavelength which almost exactly matches the optimum sensitivity response of the bialkali photocathode. For this reason, NaI(Tl) crystals are currently the most widely used detectors for applications in nuclear medicine. Table 3.3 illustrates the energy resolution performance of a typical NaI(Tl) gamma spectrometer.

3.4.3 The Position-Sensitive Photomultiplier Tube (PSPMT)

Position-sensitive photomultiplier tubes (PSPMT's) are particularly suitable as modular scintillation detectors for gamma-ray imaging applications in which both good spatial and energy resolution are required. Applications have been proposed in astronomy, particle physics, nuclear medicine, computed tomography, and neutron scattering measurements. More recent applications include nuclear contamination monitoring (He et al. [52], and Redus et al. [96]), and auroral imaging (Truman et al. [126]). Described here are two types of device which each offer intrinsic position-sensitivity. The first from both Philips and Hamamatsu uses multiple discrete anode arrays in order to sample the photoelectron cloud, and the second from Hamamatsu uses a series of orthogonally crossed wire anodes.

As discussed in the previous section, one possible way of providing charge gain between the scintillation process and the amplifier is by using a conventional photomultiplier tube. However, there have recently emerged several modifications to the basic design of the photomultiplier which enable these devices to exhibit truly intrinsic position-sensitivity. Philips have developed an equivalent version of the patented mesh dynode, named the *foil dynode* which consists of perforated metal foils with well defined apertures, and is used with a multi-channel anode design of either 16 or 64 elements [89]. Their collection area is high and their collection efficiency from dynode to dynode is about the same as that of venetian blind dynodes. They can work in magnetic fields of some tens of mT and their low crosstalk allows them to be used in position-sensitive multi-channel tubes in which all signals are read out in parallel. It is this parallel readout and its associated requirement for many channels of signal processing electronics and ADC channels which is perhaps the biggest drawback with this type of device used as a position-sensitive scintillation counter for applications in nuclear medicine where count rates are relatively high. Despite this apparent drawback, several authors have recently reported encouraging results with this photodetector for a number of applications where the detection and reconstruction of low light level events is required such as scintigraphy (Boutot et al. [20]).

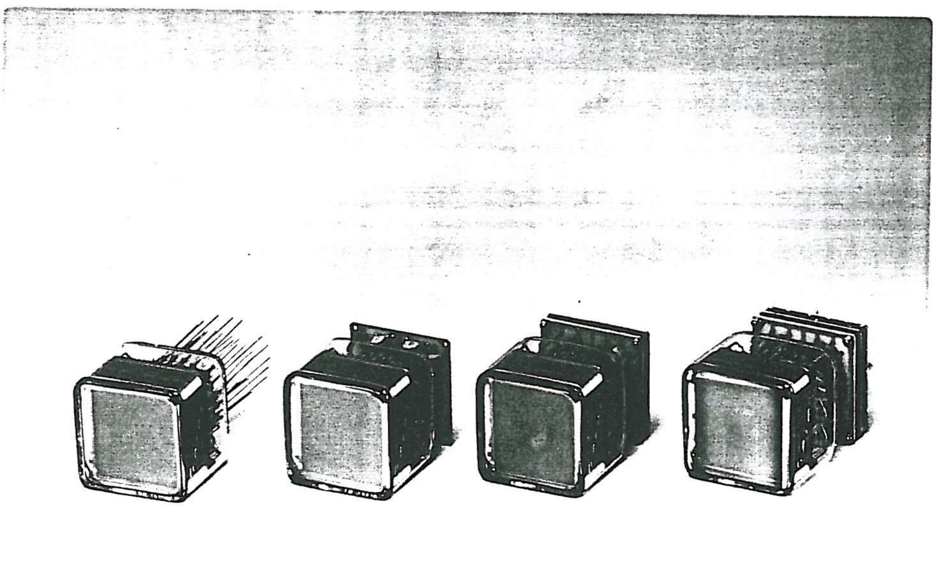

Figure 3.7: *The Hamamatsu family of PSPMTs*

However, the most successful of these position-sensitive devices has come from Hamamatsu with their large family of position-sensitive photomultiplier tubes, hereafter referred to as the PSPMT (see Figure 3.7). The operation of the Hamamatsu PSPMT relies upon their intrinsic ability to control the spatial distribution of the photoelectron cloud throughout the multiplication process using a series of mesh dynode structures, with subsequent charge collection by a position-sensitive anode. The anode employed by these tubes comprises a series of orthogonally crossed wires to sample the distribution of the photoelectron charge (see Figure 3.8).

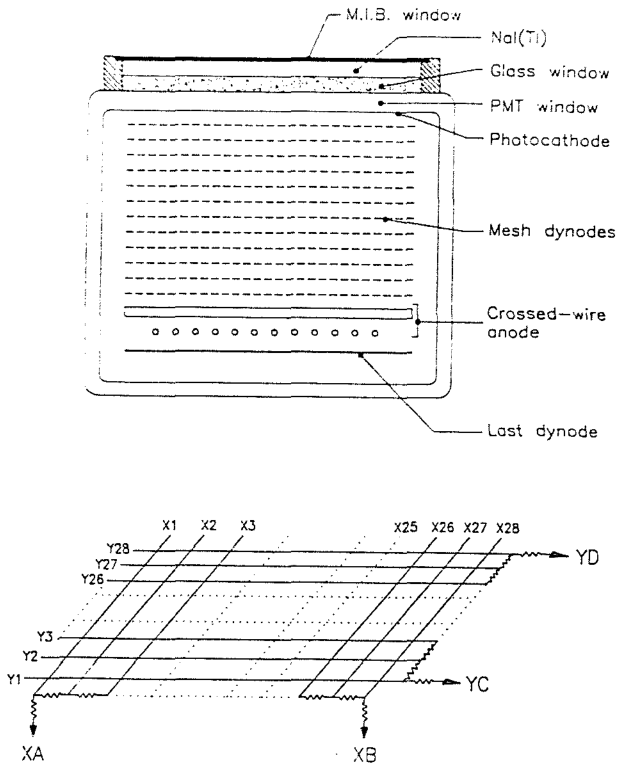

Figure 3.8: *Schematic representation of the PSPMT*

The anode of the 3 in. square R2487 PSPMT for example consists of two orthogonal layers of 18 wires in the X axis and 17 in the Y axis, with a pitch of 3.75 mm. The design of the mesh dynode structure included within the PSPMT provides quite a high degree of electrostatic spreading of the photoelectrons, enabling the charge cloud at the anode wires to be fully sampled by the application of a simple centroiding technique thus preserving as much spatial information as possible. For certain extremely high count rate applications this readout technique might be considered slow. Yet despite this apparent limitation, the Hamamatsu PSPMT is increasingly being chosen as the principal photodetector in PET detector systems under development (Watanabe et al. [129]). Because of the range of sensitive areas offered by these devices, the interest in the PSPMT for nuclear medicine applications has steadily increased over the past decade.

Recently proposed applications in nuclear medicine has continued to fuel this interest, and several investigators have clearly identified the PSPMT as a suitable photodetector for the development of a compact camera for γ-ray scintigraphy (Barone et al. [10], Bird [14], Hayashi [50], Kume et al. [70], Matthews et al. [78], Moore et al. [84], and Yasillo et al. [137, 138]). Several authors have recently suggested a development based upon the PSPMT to provide an imaging system capable of performing accurate nuclear mammography studies (Pani et al. [86, 87], and Thompson et al. [122]). In addition, the prospect of new procedures in intraoperative nuclear medicine have precipitated several suggested detector designs based upon the PSPMT (Chen et al. [27], Daghighian et al. [31], Moore et al. [84], Redus et al. [95], Saffer et al. [104], and Tornai et al. [123]).

Clearly, significant interest has been paid to the PSPMT by investigators around the world, which has resulted in a variety of beta-particle, and gamma-ray imaging systems which are currently under development. It would appear that this photodetector shows excellent potential for many applications where imaging and spectroscopy combined with the advantages of photon counting capability are desired. Measurements of the position and energy response of these devices when coupled to either continuous or segmented scintillation crystals have yielded encouraging results for energies ranging from a few keV to several hundred keV. A process of continuous improvement has facilitated a reduction in the dimensions of the PSPMT enclosure to only 28 mm x 28 mm x 20 mm, whilst improving the performance characteristics of the device (Watanabe et al. [129]). In addition, experimental position-sensitive devices have recently been developed by Kawarabayashi et al. [65], which demonstrate a high tolerance to strong magnetic fields, within an even more compact enclosure.

3.4.4 The Photodiode

For many years, photomultipliers have been the principal devices used in scintillation counting systems. However, in the past decade silicon photodiodes have increasingly been used as the principal photodetector for viewing those scintillators whose peak emission is above 450 nm, and for which the spectral response of the photomultiplier tube is inadequate. The high quantum efficiency of photodiodes (~90 %) compared with photomultiplier tubes (~20 %) results in better carrier statistics, and implies that better energy resolution should theoretically be possible.

Photodiodes permit compact, rugged detectors to be constructed that operate at voltages less than 50 V, and are fabricated from planar wafers, typically 10 cm in diameter and between 150 μm and 300 μm thick. Passivation of these devices is required in order to maintain low surface leakage current characteristics. Thermally grown SiO_2 is the commonest passivation used with silicon detectors, providing a mechanically, thermally and chemically stable insulator. Alternatively, SiO deposited via thermal evaporation followed by substrate heat treatment can be used, but is not ideal. Organic coatings such as Parylene-C, polyamide, and polyimide can also be used, and these polymer-based coatings have been found to offer superior protection against possible contamination of the device. Discrete devices, or arrays of many small diodes can be produced on a single wafer. In addition, devices can be fabricated which offer intrinsic position-sensitivity through various electrode arrangements.

The main disadvantage of photodiodes is their lack of internal charge gain, which allows the combination of internal and external noise sources to have a significant affect upon the characteristics of the detector at low energies. Three photodiode designs are currently commercially available:

Conventional PiN photodiodes directly convert incident scintillation photons into charge carriers which can subsequently be collected. These devices are generally characterised by a low leakage current and a relatively high capacitance.

Avalanche photodiodes exhibit charge gain of between 10^2 and 10^3 depending upon the magnitude of the applied electric potential, which is typically several hundred Volts. Primary charge carriers that are ionised within the diode are accelerated by the high electric potential, and have sufficient kinetic energy to cause charge multiplication through the secondary ionization of charge carriers which are subsequently collected. However, extra noise is introduced by this avalanche, and is a function of photodiode bias potential which results in a degraded energy spectrum (Carrier and LeComte [23], and Lawton [73]).

Drift diodes have a very high ratio between the collection area which is available to collect photons compared with that available to collect electrons. Because of this, drift diodes are characterised by low capacitance at full depletion, and the resulting intrinsic noise of the device is also very low. However, these devices are considerably slower than conventional photodiodes due to the extra time taken for charge carriers to move through the drift region of the device before being collected. In addition, drift diodes are not yet commercially available.

Large area avalanche and drift photodiodes can potentially improve the signal-to-noise ratio and hence reduce the low energy detection threshold. However, the production of high quality large area devices in commercial quantities remains unreliable.

In view of the demonstrated quality and widespread commercial availability of conventional PiN photodiodes, they remain the most suitable devices for viewing some scintillators. Materials commonly viewed by photodiodes include BGO (Groom [43], and Yamashita et al. [134]), and more recently $CdWO_4$. Scintillation counters using these materials have found widespread use in high energy nuclear medicine applications such as PET. However, these crystals exhibit poor light yield, resulting in low signal-to-noise ratio and poor energy resolution, which prevents their use at lower energies. By virtue of its high scintillation yield and peak emission wavelength, CsI(Tl) is by far, the most common scintillator viewed by silicon photodiodes (Bird et al. [15, 17, 18], Carter [25, 26], Kilgus [67], and Kotthaus [69]).

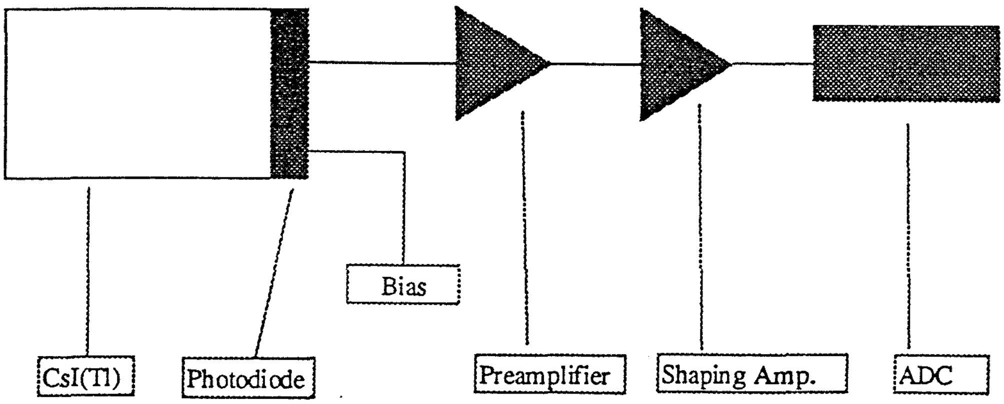

Figure 3.9: *Schematic arrangement for a scintillator -photodiode combination*

The energy resolution from a high quality CsI(Tl) - photodiode combination is expected to be approximately 4 % (FWHM) at 662 keV. In practice however, the electronic noise degrades this figure (Bird et al. [17]). The optimisation of both the light-collection efficiency through careful consideration of the optical coupling, and the electronic noise, yields energy resolutions as low as 5.5 % (FWHM) at 662 keV in practical systems. A typical arrangement is shown in Figure 3.9. Small CsI(Tl) - photodiode scintillation counters have recently been demonstrated to offer superior performance when compared with standard photomultiplier based systems for incident γ-ray energies above 300 keV. Below this energy, statistical fluctuations in the noise become more dominant, significantly affecting the energy resolution that can be achieved. However, low energy detection thresholds as low as 30 keV have recently been recorded.

The performance characteristics of a *standard* detector (1 cm^3 crystal mounted on a 1 cm^2 photodiode) and a *large volume* detector (43 cm^3 crystal mounted on a 4 cm^2 photodiode) are compared in Table 3.4.

Detector Type	Threshold (keV)	ENC (e^- rms)	Energy Resolution (% FWHM) 511 keV	662 keV	1275 keV
Standard	35	414	6.4	5.5	3.4
Large Volume	80	650	10.8	9.2	4.0

Table 3.4: *Performance characteristics of CsI(Tl) - photodiode detectors*

The success of PiN photodiodes used to view scintillators is principally due to the development of low-noise preamplifier readout electronics. Unlike photomultiplier tubes, photodiodes do not have any internal gain, and the electron-hole pairs generated within the depletion region constitute the total charge that can be collected. The charge carriers are collected as a pulse which develops over a period of several ns, and decays with a time which is characteristic of the scintillator. A low-noise charge-sensitive preamplifier is therefore required to integrate the charge and convert it into a voltage pulse. This signal is then passed to a shaping amplifier where the voltage pulse is shaped and amplified, and passed to an ADC. The amplitude of the voltage developed is proportional to the charge collected, but it fluctuates due to the stochastic nature of the electronic noise produced by the photodiode and the amplification system. A comprehensive analysis of this type of system has been performed by Radeka [92]. If the semi-gaussian pulse shape is approximated by a triangular pulse shape, the following expression can be derived:

$$ENC \approx \left[\frac{4kTC_{in}^2}{g_m \tau_p} + \left(2eI_d + \frac{4kT}{R_p}\right)\frac{\tau_p}{3} + A_{1/f}\right]^{1/2} \qquad 3.1$$

where

e is electronic charge (C)
k is Boltzmann's constant (J/K)
T is Temperature (K)
g_m is the transconductance of the first stage FET (S)
R_p is the parallel equivalent noise resistance (Ω)
I_d is the photodiode leakage current (A)
C_{in} is the total input capacitance = $C_{PD} + C_{FET}$ (F)
τ_p is the peaking time of the output pulse (s)
$A_{1/f}$ is the coefficient determining the magnitude of the 1/f noise

Since the signal has been converted from a charge pulse to a voltage pulse in the first stage FET of the preamplifier, the addition of subsequent stages of amplification will have no significant effect on the signal-to-noise ratio. In addition, the 1/f factor is usually several orders of magnitude smaller than the other terms and thus may be ignored. The terms R_p and g_m are characteristic of the preamplifier feedback resistor and the FET respectively. Good quality preamplifiers are now constructed with feedback resistors approaching 500 MΩ, and FET's with high transconductance in order to minimise the noise. However, low noise performance, particularly the transconductance component, is generally achieved at the cost of excess power consumption, typically 100's of mW.

The highest quality low-noise preamplifiers which are currently commercially available such as the eV Products eV-5093, have $R_p \sim 500$ MΩ, $g_m \sim 0.03$ mS, and a power consumption of 180 mW. This produces an ENC of less than 100 electrons rms with no detector attached. For comparison, a typical 1 cm^2 photodiode read out by the low noise preamplifier with a shaping time of 5 μs will have an ENC of about 450 electrons rms. Therefore the main variables are the detector capacitance, the leakage current and the shaping time. Generally, the optimum shaping time of the following amplifier network for these devices viewing CsI(Tl) is approximately 5 μs, whilst the contribution to the noise from the preamplifier is negligible for large area photodiodes since the noise due to the leakage current of the diode is dominant. The choice of preamplifier becomes increasingly important as the sensitive area of the photodiode decreases, and for photodiodes whose sensitive area is below 100 mm^2 the choice of preamplifier will be critical in determining the characteristics of the detector.

The reason for this relationship between preamplifier noise and diode area can be better understood by considering the capacitance of the photodiode which is related to the area of the diode and the depletion depth by the following expression:

$$C = \frac{\varepsilon_o \varepsilon_r A}{d} \qquad 3.2$$

where ε is the dielectric constant for silicon and d is the depletion depth of the silicon. The leakage current arises from a combination of bulk volume and surface effects in the silicon and so is also proportional to the detector surface area and volume. Several techniques are used by photodiode manufacturers to minimise the leakage current such as the use of high resistivity silicon and guard anodes. Therefore the noise of a photodiode is proportional to its sensitive area. However, this sensitive area is also the readout area for the scintillator and so the ability of the diode to collect and convert scintillation photons from larger crystals may be impaired. This compromise between sensitive area and light collection has been the subject of considerable research at Southampton (Bird et al. [15, 18], and Carter et al. [25]).

Because of the compactness of discrete CsI(Tl) - photodiode detectors, they are well suited for use in large scale detector arrays. The pixel size of these arrays will be critical in determining the suitability for the required application. A recent example of such an array is the prototype 37 element imager developed at Southampton for the INTEGRAL γ-ray astronomy mission [26, 58], whilst previous work by Dean et al. [33] has investigated the potential of constructing 13 mm x 13 mm x 150 mm position-sensitive bar detectors using CsI(Tl) coupled to two photodiodes. In addition, previous work by Mullerworth et al. [85], has investigated the possibility of developing a compact imaging system based upon a CsI(Tl) - photodiode detector array constructed on a single wafer of silicon.

3.4.5 The Hybrid Photodiode Tube (HPD)

A literature review reveals that the concept of the Hybrid Photodiode Tube (HPD) as an electron multiplier device is far from new, but has existed in principle since the late 1950s (Sclar [111]). Recent commercially available HPD devices have been constructed using many existing components from the large volume manufacture of night-vision gun sights. Two basic configurations may now be purchased from DEP Instruments of Roden in the Netherlands; these are either electrostatically or proximity focused devices [35].

Both electrostatically and proximity focused devices, if used to image x-rays and γ-rays, require a two-step conversion process. Incident energetic γ-ray photons are converted into optical photons through photoelectric absorption within a scintillation crystal which is optically coupled to the entrance window of the tube using an optical couplant of intermediate refractive index.

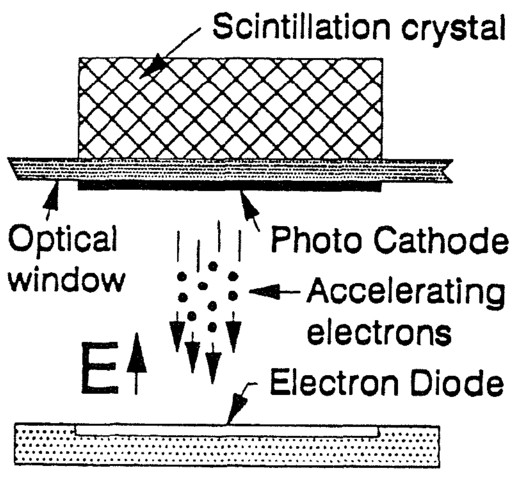

Figure 3.10: *Principle of a proximity focused HPD*

Photoelectrons liberated from the photocathode are accelerated by a strong electric field of between 10kV and 15kV towards the silicon anode structure (see Figure 3.10). These electrons bombard the silicon anode and penetrate up to 2.1 μm (at 15kV) into the material, with most of the kinetic energy being deposited within the first 1 μm (Arnaudon et al. [6]). Charge gain occurs linearly within the bulk silicon material as a function of the kinetic energy of the incident electrons, and the number of photoelectrons produced from a scintillation event. Typically, gains of the order of 3500 can be achieved by applying a potential of -15 kV between the photocathode and the surface of the diode. When this photodetector is used to view CsI(Tl) detector crystals for γ-ray scintillation counting applications, a low energy detection threshold of approximately 2 keV has been estimated to be achievable with 5 σ significance.

Clearly, these tubes can offer certain advantages over conventional photodiodes due to this modest intrinsic charge gain within the silicon. A camera based upon the HPD for γ-ray scintigraphy, and two *proof of principle* developments which exploit this technology will be presented in later chapters.

3.5 Conclusions

In this chapter we have reviewed some of the techniques available for the construction of position-sensitive γ-ray detectors suitable for applications in nuclear medicine and auroral imaging. The conclusions are briefly summarised as follows:

Photomultiplier tubes are suitable for existing scintigraphic applications, and are widely used in the Anger Camera. It could possibly be envisaged that the recently developed devices which employ compact T08 enclosures might be used to provide a scaled down version of the Anger Camera providing a modest field-of-view of ~200 cm^2 for proposed applications in scintimammography. However, since the packing fraction also reduces as the photomultiplier tube dimensions are reduced, the spatial resolution of a gamma camera will not scale directly with tube sensitive area. In addition, the Anger principle requires tubes to be located outside of the field-of-view of the camera, causing the sensitive area to be reduced in relation to the total area of the camera. This effect would be worse for smaller cameras than for larger cameras employing the same tubes, and would not be a desirable feature of a compact detector such as that which is being proposed. In addition, the application of a relatively thick lightguide to share the available light between a group of tubes is an integral part of the Anger Camera principle. Whilst the centroid of the light-spread function may be found using this technique, the number of photons collected by each photodetector will be reduced by increasing the thickness of this lightguide. For some applications such as auroral imaging, where the number of optical photons generated is relatively low at the low end of the spectral range required, the application of any form of lightguide would reduce the signal-to-noise ratio (SNR) by moving many of the optical photons away from the site of the interaction.

The position-sensitive photomultiplier (PSPMT) on the other hand offers the benefit of intrinsic position-sensitivity in a compact and rugged enclosure. A range of scintillation materials are compatible with the spectral response of the photocathode, and crystals can be coupled directly onto the entrance window of the tube. The sensitive area provided by the R2487-02 tube (64 mm x 64 mm) is compatible with small organ studies such as the thyroid gland, whilst the sensitive area of the smallest, and most recently available R5900-00-C8 tube (21 mm x 23 mm) within an enclosure of 28 mm x 28 mm x 20 mm offers the possibility of developing an extremely compact gamma camera probe for intraoperative nuclear medicine. It would therefore appear that the PSPMT offers excellent potential for inclusion within a compact gamma camera.

Photodiodes offer the possibility of constructing mechanically robust position-sensitive scintillation counters on a variety of scales based upon discrete photodiode-scintillator arrays. This modular approach to the design of a compact camera appears on the surface at least to be a very attractive alternative to the Anger Camera, since the problems associated with light sharing and the necessity for a *dead-area* enclosing the field-of-view are overcome with this technique. However, these benefits are at the expense of a significant increase in the number of channels of readout electronics which are required to process the image. In addition, the low energy detection threshold of most practical systems remains as high as 50 keV, and would not be suitable for an application such as auroral imaging, where the majority of γ-rays incident upon the detector are expected to be significantly less than this threshold. However, it is possible that a position-sensitive scintillation counter based upon this technology could be applied to a number of clinical nuclear medicine studies, since the radiopharmaceuticals would be easily detectable. Recently, a miniature device employing an array of CsI(Tl) - photodiode detectors has been proposed by Milliare et al. [82], for the monitoring of the ejection fractions from the left ventricle in ambulatory heart monitoring studies. Clearly, a small imager weighing less than 2 kg, which could easily be worn by the patient during periods of excercise and rest would be of interest for a number of clinical studies involving cardiac function. Such an imaging system has recently been proposed as a possible future research project at Southampton to investigate the potential and proof of principle of such an imager. It is expected that an array of 64 discrete CsI(Tl) - photodiode detectors employing the HX-2 hybrid multi-channel readout electronics will form the basis of this camera.

Hybrid Photodiodes might be of value to overcome some of the limitations associated with the electronic noise of conventional photodiodes through the principle of electron bombarded silicon to achieve some modest charge gain within the diode. It is potentially feasible that a compact position-sensitive scintillation counter could be constructed which uses the HPD as the position-sensitive photodetector. Such a camera would be capable of imaging a very broad range of incident energies with excellent resolution. However, HPDs which employ position-sensitive silicon anodes with sensitive areas suitable for the applications that we have described have yet to be developed, and considerable work and further study remains to be carried out in order that their capability and potential for scintillation counting applications can be fully realised.

Chapter 4

Design of a PSPMT Based Compact Gamma Camera

4.1 Introduction

The value of the PSPMT as a photodetector for use in modular scintillation detectors for γ-ray imaging applications where excellent spatial and energy resolution are required has been well established (Poulsen et al. [91], He et al. [51]). Several clinical applications have already been proposed in nuclear medicine (Yasillo et al. [136, 137, 138]), nuclear mammography (Pani et al. [86, 87]), positron emission tomography (Singh et al. [116]), and positron emission mammography (Thompson et al. [122]).

Apart from the physical characteristics exhibited by the scintillator crystal discussed in the previous chapter, when designing a position-sensitive detector system one must consider the geometric shape of the material, and its suitability for use with a particular type of photodetector. With thought, this reduces to a choice between either a thin continuous detector crystal, similar to that employed by the Anger Camera, or some form of segmented detector crystal array comprising many separate scintillation crystals optically isolated in some way, similar to that which is used in PET. The choice between these two alternatives for a compact camera based upon the PSPMT, depends upon the effect that each would have upon the reconstructed point-spread function, and hence the spatial resolution of the camera. Whilst a simple reduction in the depth of a continuous crystal could potentially localize the spread of light within the crystal sufficiently to yield millimetric spatial resolution, further improved localization of the light spread provided by discrete detector crystals could potentially offer still finer spatial resolution without the disadvantage of having to sacrifice detection efficiency.

The emphasis for this chapter will therefore be the development of a PSPMT based compact gamma camera, having a sensitive area of between 36 cm^2 and 75 cm^2 depending upon the PSPMT chosen, which will enable the distance between camera and patient to be reduced when imaging small organs such as the thyroid gland. When a parallel hole collimator is used to localize the incident flux, it can be seen from equations 2.2 and 2.3 that this reduction in distance from the source will directly translate into improved collimator resolution, and hence better spatial resolution in the resulting image. At the same time, it is expected that a reduction in the distance between the camera and the patient will enable either a higher count rate at the detector, shorter exposure time, or lower injected activity for the patient, which are all desirable. The characteristics which are important from a compact clinical gamma camera may be briefly summarised as:

- a high sensitivity $\geq$ 60% at 140 keV, and $\geq$ 50% at 160 keV with adequate sensitivity at other radioisotope energies up to 511 keV. This is the product of the stopping power of the scintillation crystal, determined by the density and depth of the detector crystal, together with the fractional sensitive area of the scintillation crystal. For a continuous crystal the fractional sensitive area will be 100%, but segmented crystal arrays will be affected by the packing density of the individual elements within the array, and the fractional sensitive area is typically no better than 75%.

- comparable energy resolution to clinical gamma cameras (~ 12% at 140 keV).

- spatial resolution of between 1 mm and 2 mm for incident γ-ray energies ranging from 140 keV up to 511 keV.

- high contrast enabling the accurate delineation of physiological features within the resulting image.

The first half of this chapter discusses the problems associated with designing a compact gamma camera which will be capable of meeting each of the above criteria. Several problems associated with the Anger Camera have been identified and are discussed in the context of the design of a more compact camera based upon the PSPMT. We advance the argument that many of these problems could potentially be overcome with more careful design of the scintillation crystal. In addition, the method used to generate the position information and hence to reconstruct the image will also contribute to the width of the reconstructed point-spread function, and hence the level of detail preserved as a function of the incident gamma-ray energy. Both conventional resistive charge-division and the newly developed multiwire readout techniques for the PSPMT are discussed.

The second half of this chapter considers measurements that have been made of the optimisation of the scintillation crystal design as a function of energy for the two cases where the detector crystal is viewed in turn by the 3 inch square (R2487), and the 5 inch diameter circular (R3292) PSPMT from Hamamatsu. We demonstrate that photoelectron statistics are affected by the size and shape of the detector crystal, leading to improved spatial resolution and low energy detection threshold for segmented detector crystal arrays. These measurements show good performance using small segmented crystals, having centre-to-centre dimensions ranging from 1.5 mm to 3.5 mm, which minimize the width of the PSF whilst increasing the light collection efficiency by using diffuse reflecting white titanium dioxide loaded epoxy to optically isolate adjacent crystals. Further measurements are presented which demonstrate the effect that the window thickness of the photomultiplier tube has in limiting the ability to resolve small crystal arrays.

Complementary to optimising the design of the detector is the choice of event reconstruction technique used in the imaging system. We will demonstrate that the method used to sample the charge emerging from the photodetector, together with the algorithm used to determine the position of interaction are also potentially important factors in the determination of both spatial and energy resolution, and position linearity. Measurements have been made which contrast two readout techniques for resolving the signals from adjacent small crystals when illuminated by 122 keV gamma-rays.

4.2 Continuous Detector Crystals

The Anger Camera described earlier uses a continuous scintillation crystal to detect incident γ-ray radiation. Scintillations within the crystal generate weak flashes of light which propagate isotropically, and will be incident upon a lightguide in intimate optical contact with the crystal. Photons within a cone of acceptance determined by Snell's law, will be transmitted and will propagate through the lightguide. Light spread occurs in the lightguide before subsequently falling upon a group of photomultiplier tubes. This light spread prior to its detection enables the centroid of the light pool to be found, and the position of interaction located. However, it is clear from this description of photon transport that a significant fraction of the photons generated by the scintillation process subsequently undergo multiple diffuse reflections, many being transported a significant distance from the site of the interaction before the criteria for transmission is met, and this *diffuse background* from the detector crystal is eventually transmitted into the lightguide (see Figure 4.1).

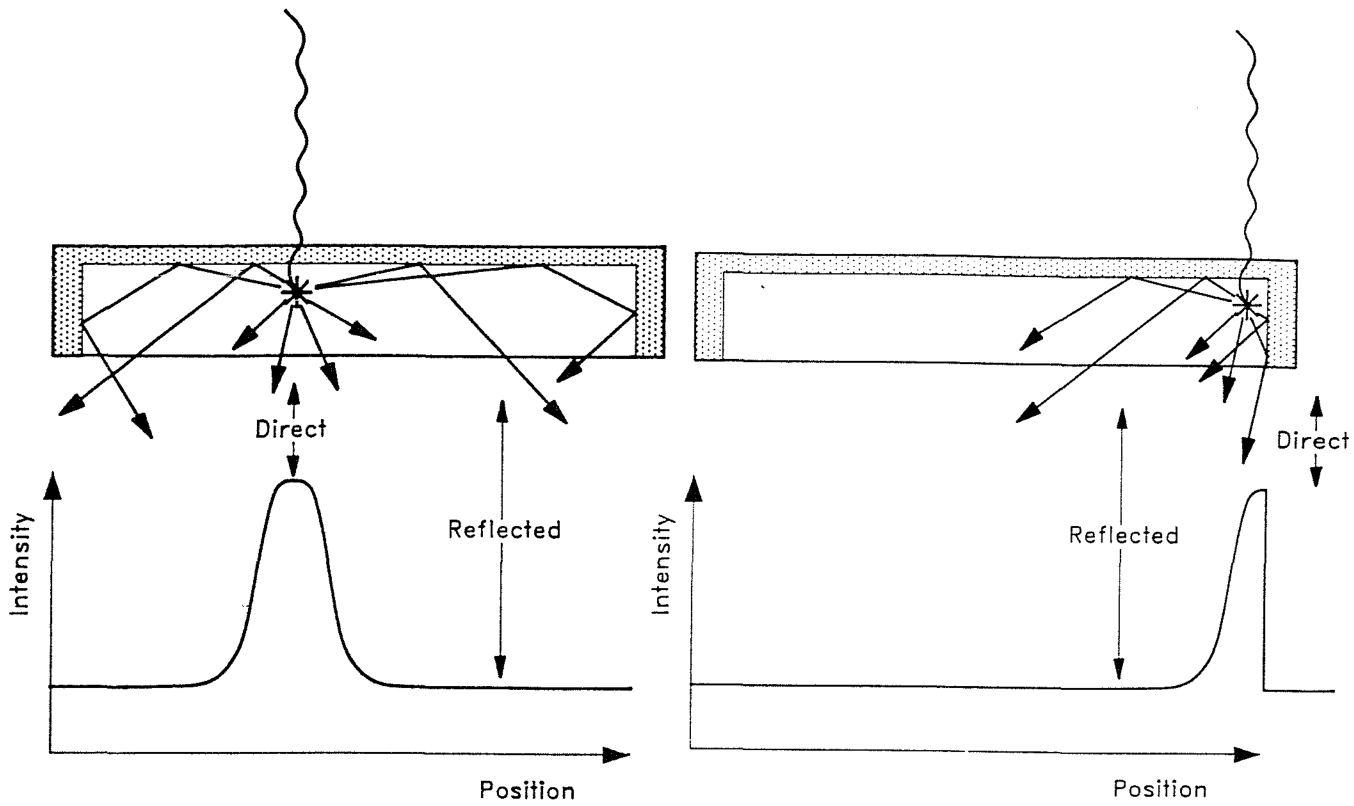

Figure 4.1: *Light transport in a continuous crystal*

Indeed, many photons never meet the criteria for transmission from the detector crystal, and as a consequence are effectively prevented from contributing to the spatial and energy resolution of the camera. The statistical fluctuations in this diffuse background will be distributed over the entire camera area and will combine with gain variations in the photomultiplier tubes, giving rise to significant centroid reconstruction errors. The weighting effect due to this background increases with detector area, and reconstruction errors will increase as a function of the radial distance of the interaction from the geometric centre of the crystal. To minimise this effect, modern cameras use arrays of pulsed LED's which periodically illuminate the photomultiplier tubes so that variations in the gain across the sensitive area of the camera can be recalibrated through electronic self-adjustment of the preamplifier gain to each tube.

However, the effects due to the intrinsic diffuse background in the crystal has so far not been overcome, most manufacturers simply choosing to absorb those photons reaching the edge of the detector crystal by making the edge of the crystal black. Potentially, if all of the photons generated within the crystal could be collected by the photodetectors, both the energy resolution and image quality could potentially be improved. Because of these well understood problems, commercial gamma camera manufacturers employ different readout techniques in order to overcome the intrinsic limitations of the detector crystal, and achieve the optimum spatial and energy resolution possible from a clinical gamma camera. Since the diffuse background will detrimentally effect both the position resolution, and the position linearity of the camera, pulse height discrimination techniques are applied to the output stage of each photomultiplier tube. Only the signals close to the point of interaction within the detector crystal that are above a predetermined level set by these thresholding preamplifiers can contribute to the position signal, and the result is improved position resolution and linearity. The spatial linearity of the Anger Camera has been found to be further improved by the addition of a radially concentric array of small black absorbing spots on the rear surface of the lightguide which is viewed by the cluster of photomultiplier tubes. These spots range from 3 mm at the centre of the camera to 5 mm at the edge of the sensitive area (source - Siemens Medical).

However, the readout previously described would have the unfortunate effect of rejecting many photons which could usefully contribute to the energy signal. For this reason, the output stage of each photomultiplier tube has an additional non-thresholded output which enables all of the photoelectron charge produced to contribute to the energy resolution of the camera. In this way, despite the intrinsic limitations of the detector crystal design resulting in diffuse background, the gamma camera can achieve good spatial and energy resolution characteristics which have over a period of several years proven difficult to improve upon. The classic Anger Camera that has been described is clearly well optimised, and relies upon the principle of sharing the available scintillation light between a group of several photodetectors in order to determine the centroid of the light-spread function. However, this principle cannot be directly scaled down and applied for the construction of a more compact gamma camera based upon the PSPMT.

The PSPMT described earlier offers intrinsic position-sensitivity, and lightguides such as those commonly used in the Anger Camera are unnecessary. Light spreading prior to reaching the photocathode of the PSPMT is in fact undesirable, and will lead to centroid reconstruction errors of the type previously discussed. The variance in the gain over the sensitive area of the PSPMT is significant, and cannot be corrected without lengthy calibration and the application of a look-up table. However, despite careful tube calibration, the spatial resolution and position linearity will remain a function of the detector area for the reasons previously described. It is therefore anticipated that improved spatial resolution and position linearity will be achieved by reducing the crystal thickness, individually sampling the signals from each anode wire of the PSPMT, and reconstructing each event using either a peak-fitting, digital centroiding, or thresholded centroiding algorithm.

4.3 Segmented Detector Crystal Arrays

When used to view continuous detector crystals, both the PSPMT and the conventional Anger Camera exhibit spatial resolution and position linearity which is a function of the detector area, and the radial distance of each interaction within the detector crystal from the geometric centre of the camera. This is principally due to the diffuse background and its weighting effect which was described earlier. It is therefore proposed that improvements in the spatial resolution and position linearity of a PSPMT based compact gamma camera might be achieved by segmenting the detector crystal to completely eliminate the diffuse background.

Those photons which in the continuous detector crystal are transported away from the site of the interaction, and subsequently removed from contributing to the charge signal from the camera, if localised and guided towards the photodetectors would increase the photon flux density. The scintillation photons undergo multiple diffuse reflections, constrained by the physical dimensions of each detector element. The intensity of the light output for such a detector element will vary as a function of aspect ratio, and also the angle at which the photons emerge from the detector crystal according to Lambert's law which can be expressed as:

$$dI/d\theta \propto \cos\theta \qquad 4.1$$

where I is the intensity of the reflected light, and θ is the angle of reflection with respect to the normal.

A modest improvement in the energy resolution of the scintillation counter might therefore be achieved. This improvement in energy resolution it is hoped will compensate for the broadening of the energy spectrum caused by Compton scatter within the patient, and permit better determination of the photopeak in subjects where this currently proves difficult. In addition, the absence of diffuse background it is felt will yield some improvement in the reconstructed position linearity. It should also be possible to eliminate reconstruction errors which are due to Compton scatter within the crystal. Providing the reconstruction error is less than the size of each detector element, photons which are photoelectrically absorbed within a single detector element will produce a light-spread function with a single vertex. The centroid of this light-spread function will correspond exactly with the centre of the crystal in which the interaction occurred.

However, a photon which Compton scatters from one detector element, and is subsequently photoelectrically absorbed in an adjacent detector element will provide a light-spread function having two distinct vertices. The relative amplitudes of these vertices is a function of the fractional energy deposited in each crystal, whilst their separation is dependant upon the pitch of the detector crystal array. The centroid of these false events will instead be reconstructed to a point somewhere between the two detector elements, the exact interpolation being dependent upon the ratio between the magnitude of each energy deposit. The inclusion of these scattered events within the image would clearly be undesirable, and would reduce the delineation of features within the region of interest leading to blurring. Previously reported work has considered the possibility of rejecting these false events for bar cross-sections of 1 cm^2 if the location of the centre of each bar is accurately known (He [53]). It remains to be proved from further investigation if this same technique can be applied successfully to segmented detector arrays with elemental cross-sections of only 2 mm^2. The successful application of this technique would require the FWHM of the reconstructed point-spread function from each crystal to be considerably less than the width of the crystals themselves.

A camera which employs a close-packed array of 2 mm x 2 mm x 4 mm CsI(Tl) crystals, separated by a thin diffusely reflective layer to optically isolate each detector element, would enable an aspect ratio of approximately 2:1 to be employed offering adequate light collection for applications in auroral imaging, whilst preserving the sensitivity for applications in nuclear medicine. In addition to their standard range of 1-dimensional segmented CsI(Tl) arrays developed specifically for use in airport baggage scanning systems, Hilger Analytical have developed for us a 2-dimensional segmented CsI(Tl) detector array which is suitable for testing in each of these imaging applications. Following this success, there has been increasing interest from the major scintillation crystal manufacturers to offer segmented NaI(Tl) and CsI(Na) detector arrays for many applications. However, due to the hygroscopic nature of these materials, considerable development effort has been required. Segmented NaI(Tl) and CsI(Na) detector arrays suitable for applications in nuclear medicine are expected shortly from Bicron and Hilger.

4.4 Choice of Scintillator for a PSPMT Based Gamma Camera

One application envisaged for our compact γ-camera is for example to image the physiology and anatomy of the thyroid gland, although its very modest dimensions will make it extremely suitable for many other studies, and a range of alternative applications in nuclear medicine have been proposed for such a camera. Knowing the performance characteristics of both the photodetector, and a range of suitable scintillator materials, the performance of the camera can be optimised to match this specific application.

Since the detected count rate in γ-ray scintigraphy is generally limited by the collimator to less than 25,000 cs^{-1} within the sensitive area of a clinical Anger Camera, a scintillator which offers a modest decay time is adequate. Only a few millimetres of moderately dense material will offer sufficiently high interaction probability at 140 keV. Generally, bright scintillators are chosen since they yield superior energy and spatial resolution through improved Poisson statistics.

There are a number of alternatives to be considered when choosing a scintillator for this imaging system. The choice of a higher density material would enable a continuous detector crystal of reduced depth to be used whilst preserving detection efficiency. This reduction in the depth might contribute to an improved localization of the light spread in the crystal, and potentially a corresponding improvement in the spatial resolution. Earlier suggestions, where the detector crystal is segmented and each element optically isolated, also have the potential to significantly improve the localization of the scintillation light, the position linearity of the photodetector response, and the spatial resolution.

The performance characteristics of several recently developed dense scintillation materials presented in Table 3.2 might enable the thickness of the detector crystal to be significantly reduced. However, the light ouput of almost all of these materials is substantially lower than NaI(Tl), yielding poorer Poisson ststistics and energy resolution. Whilst these new materials might be of interest for future developments, it is considered that many of the materials presented in Table 3.1 offer superior light conversion efficiency when viewed by a PMT with a bialkali photocathode, modest decay time, and moderate density. The three materials which appear to be most appropriate for this application are NaI(Tl), CsI(Na), and CsI(Tl), due to the very high photon yield of each. From the previous discussion, the most desirable configuration is to develop NaI(Tl) crystal arrays conformally coated using Parylene-C, coupled directly to the entrance window of the PSPMT. However such a development has only recently received the attention of the major scintillator manufacturers, and it will be several months before the first crystal arrays become commercially available. Having almost the same light yield as NaI(Tl), segmented arrays of CsI(Na) are already commercially available, although variations in their crystal-to-crystal response function is inexplicably non-uniform. More uniform results have been achieved using arrays of CsI(Tl), although the light yield of this material is less than half of that from NaI(Tl). Since CsI is a more dense material than NaI, the crystal depth can be reduced whilst preserving a high interaction probability. This reduction in crystal depth would improve the light output due to a reduced aspect ratio for segmented detector crystal designs, and would also enable a continuous crystal to be used effectively by limiting the spread of the scintillation light.

Clearly there are many uncertainties when we consider the optimisation for such an imaging system. To help to overcome some of this uncertainty, Monte Carlo modelling techniques have been used to determine both the complex interactions of incident γ-rays within the detector using GEANT 3, and the optical photon transport characteristics of the detector using GUERAP V. These techniques and a number of detector models will be described in more detail in chapter five.

4.5 Readout Method

In this section, two readout methods have been evaluated in order to determine the most suitable option for a practical imaging system based upon the PSPMT. The readout system chosen should be suitable for both low energy applications such as that required for auroral x-ray imaging, and for nuclear medicine where the count rate is likely to be significantly higher.

4.5.1 Resistive Charge-Division Readout

This readout technique uses a standard charge division network connected between each of the adjacent anode wires, 18 in the X axis and 17 in the Y axis for the R2487 PSPMT, and 28 in the X axis and 28 in the Y axis for the R3292 PSPMT. The electron charge cloud is sampled by typically more than 3 individual anode wires in each axis, in a ratio which is a function of the position of interaction in the detector. Only 4 charge amplifiers are therefore needed in order to provide the data from which one can derive the position of interaction and energy deposited (He et al. [51]). The strength of this technique lies in its simplicity, especially the relatively few channels of electronics needed. However, this resistor network contributes significantly to the time needed to read out a single event. In addition, the dark current from the peripheral regions of the photocathode contribute disproportionately to the uncertainty in the position and energy of the reconstructed event. Using 4 OPA 404KP operational amplifiers a low energy detection threshold of about 20 keV has been achieved when viewing CsI(Tl). Previous authors have shown that this simple technique generates non-linearities in the position response near the edges of the sensitive area (He et al. [51]), whilst others have made changes to reduce this effect (Fessler et al. [39]). The outputs X_A, X_B, Y_C, and Y_D from the resistor divider circuit, were passed to the inputs of four charge-integrating amplifiers. The integration time was set between 1 μs and 3 μs depending upon the decay time of the scintillator being used, and the last dynode of the PSPMT was used to gate the readout of charge from the amplifier into the ADC. Once digitised, the data was passed to an IBM PC where the event reconstruction was performed. The system is shown schematically in Figure 4.2.

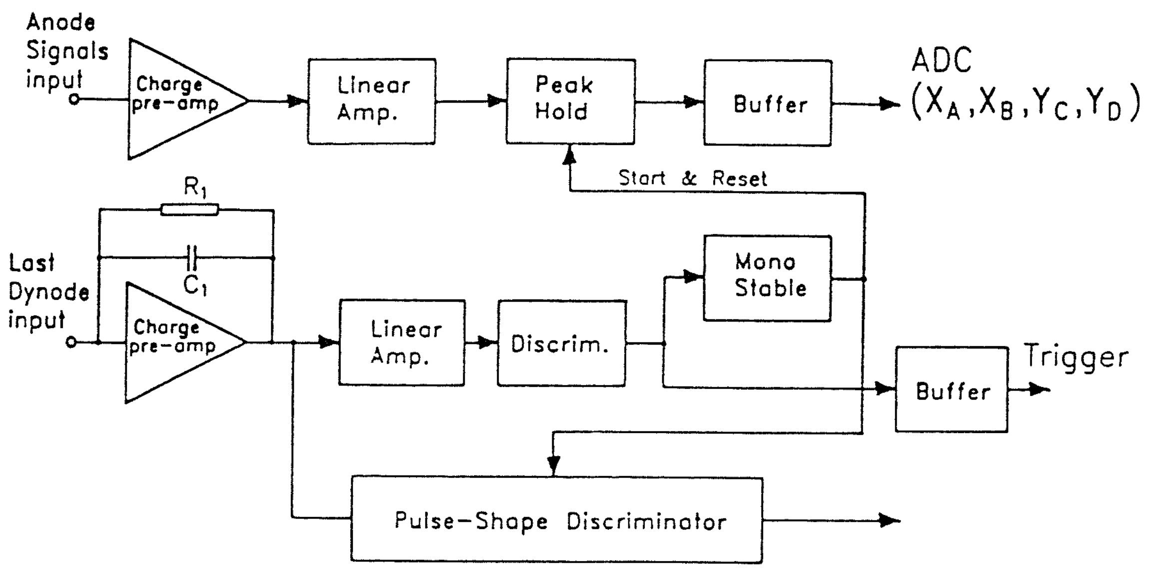

Figure 4.2: *Data collection system used*

4.5.2 Centroiding Method of Image Reconstruction

The conventional Anger Camera uses a network of either resistors or capacitors together with a centroiding interpolating algorithm to determine the position of each event within the detector crystal. This method of position-finding has also proved to be successful for PSPMT based cameras, and tubes are usually supplied from the manufacturer with a linear resistor divider board already provided. The signals emerging from each end of the resistor chain are weighted in a ratio which is directly proportional to the position along the chain at which the charge was injected. The relative amplitudes of these signals can therefore be used to determine both the centre of gravity, and energy deposited for each event within the detector crystal in each axis using the following algorithms:

$$\Delta X = \frac{X_A - X_B}{X_A + X_B} \tag{4.2}$$

$$\Delta Y = \frac{Y_C - Y_D}{Y_C + Y_D} \tag{4.3}$$

$$E = X_A + X_B + Y_C + Y_D \tag{4.4}$$

Clearly however, if an event occurs close to the edge of the detector crystal, the shape of the light-spread function will be non-symmetrical such as that illustrated in Figure 4.1.

These events are therefore incorrectly reconstructed, since the centroid of the light-spread function will be weighted towards the centre of the tube, giving rise to a non-linear position response when the PSPMT is used to view continuous detector crystals.

4.5.3 Multiwire Readout

In the second readout method, each of the 35 anode wires of the R2487 PSPMT are connected directly to a series of low noise charge integrators. The drawback with this is that reading out the charge distribution in this way requires many channels of electronics to fully sample the sensitive area of the PSPMT. This has been overcome by using the newly developed MXRP and HX-2 multi-channel charge integrating amplifiers and analogue shift registers designed by the Daresbury Rutherford Appleton Laboratory and previously reported (Bird et al. [16], and Truman et al. [124]). These VLSI chips each have 16 channels of charge sensitive preamplifiers, storing the charge collected over an integration period, and may be read out sequentially with the final output being a differential analogue signal. The event is then reconstructed using a gaussian-fitting algorithm followed by either a centroiding or a peak-fitting algorithm. Since one is sampling only the small region of the electron charge cloud, dark current from other regions of the tube are excluded from contributing to the event signal. Previous work suggests that when combined with the modest noise per channel of the VLSI chips themselves, an improved low energy detection threshold of below 5.9 keV (^{55}Fe) could potentially be realised (Bird et al. [16]).

The MXRP chip was mounted upon a prototype test board which operated the chip continuously with a readout cycle of 1 ms, during which the charge integration time was set to 15 μs. For the purposes of a practical application, the signal from the last dynode of the PSPMT could be used as a convenient trigger for the readout of the MXRP chip, and two of the boards that we have described, operated synchronously, could be used if imaging capability is required.

The analogue data stream from the MXRP board was then passed to the input of a digitising oscilloscope which was triggered from the clock pulse initiating readout from the test card to capture the distribution of the charge deposited upon the anode wires of the PSPMT. The waveform was subsequently passed to an IBM PC for pre-processing before being transferred to a SUN IPX workstation where the event reconstruction was performed using either a peak-finding, digital centroiding, or thresholded centroiding algorithm. This system is illustrated schematically in Figure 4.3.

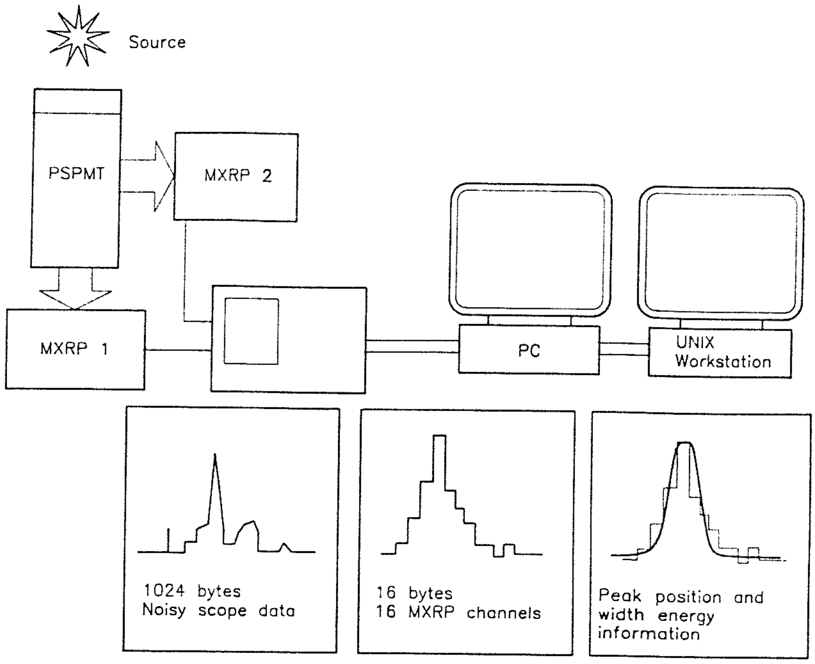

Figure 4.3: *Schematic diagram showing the original data acquisition system*

The data stream from the oscilloscope for each event consisted of 1024 binary characters. It was necessary to reduce this to the 16 analogue levels representing the charge distribution at the anode wires of the PSPMT. This was achieved by locating the start of the readout cycle at a fixed distance from the trigger point, and then averaging the values in each of 16 bins corresponding to the readout of the 16 amplifier channels.

4.5.4 Peak Fitting Method of Image Reconstruction

This alternative method of reading out the PSPMT has enabled the possibility for more sophisticated event reconstruction algorithms to be evaluated which could potentially offer enhanced image quality. The principal reason for considering this method of event reconstruction was to try to reduce the spatial non-linearity introduced by the centroiding method described previously. The charge distribution has been assumed to approximate to a Gaussian of the form:

$$x_i = e^{-(x-X_0)^2/2\sigma^2} \qquad 4.5$$

and a least-squares fit performed to the values x_i. Since the position of the original interaction is derived entirely in software, it is also possible to apply a range of alternative algorithms in an attempt to improve the response characteristics of the PSPMT. For example it would be possible to simulate the effect of the resistor-divider readout by performing a software centroid upon the charge distribution at the anode of the PSPMT.

4.6 Results

We have investigated the spatial resolution and the energy resolution performance of the PSPMT when used to view continuous detector crystals. Both the 3 inch square (R2487), and the 5 inch diameter circular (R3292) PSPMT were used to view a continuous NaI(Tl) scintillation crystal centrally illuminated by a collimated 122 keV (^{57}Co) point source. Both detector crystals measured 5 mm thick, and each was carefully designed to perfectly match the sensitive area of the appropriate tube. The scintillation crystals were mechanically encapsulated to preserve the chemical integrity of the material, and glass windows of 2 mm and 3.5 mm respectively were employed. Measurements have been obtained of the spatial resolution for the R2487 PSPMT with an applied bias potential of 1000 Volts, and was determined to be 2.7 mm FWHM. Similar measurements obtained from the R3292 PSPMT with an applied bias potential of 1250 Volts was determined to be 3.2 mm FWHM. Measurements of the energy resolution yielded a result of 20.2% FWHM for the R2487 PSPMT, and 14.2% FWHM for the R3292 PSPMT. The result for the R3292 tube appears to have been adversely affected by the additional thickness of the glass entrance window of the tube itself (6 mm compared with 3.2 mm for the R2487), combined with the additional 1.5 mm of glass window due to differences in the mechanical encapsulation of the two crystals.

In order to consider practically the effect that a reduction in the depth of the crystal directly optically coupled to the entrance window of the PSPMT would make upon the spatial resolution, a CsI(Na) image plate was procured from Hilger Analytical. This material was chosen for its relative chemical stability when compared with NaI(Tl), and because of its higher density (4.51 g cm^{-3} compared with 3.67 g cm^{-3}), which would enable such a reduction in the crystal depth. The crystal measured 5 inches in diameter, and was 3 mm thick. Measurements have been obtained of the spatial resolution when viewed by the R3292 PSPMT with an applied bias potential of 1250 Volts, and was determined to be 2.9 mm FWHM. We believe that this result is still being adversely affected by the thickness of the glass entrance window of the tube. These results will be presented as part of the preliminary trials of a compact gamma camera in Chapter 6.

Further measurements have been made of the performance of various 1-dimensional segmented CsI(Tl) scintillation detectors of the type used in conventional airport baggage scanners, illuminated using a variety of collimated radioactive sources with energies ranging from 22.1 keV to 122 keV. Two of these detector crystal arrays, have crystal sizes of 3 mm and 2 mm respectively, with a crystal separation of 0.5 mm, and one detector crystal array has 1.25 mm crystals with a crystal separation of 0.25 mm. These arrays were viewed in turn by both the 3 inch square R2487 PSPMT, and the 5 inch diameter circular R3292 PSPMT from Hamamatsu, and their position and energy resolution characteristics measured as a function of incident photon energy. A conventional resistive charge-division readout technique was initially used to read out the tubes, together with a simple centroiding algorithm to reconstruct the position of interaction. When all three detectors were viewed together, and uniformly illuminated by a ^{57}Co gamma-ray source, the detector performance as a function of crystal size can be clearly identified (see Figure 4.4).

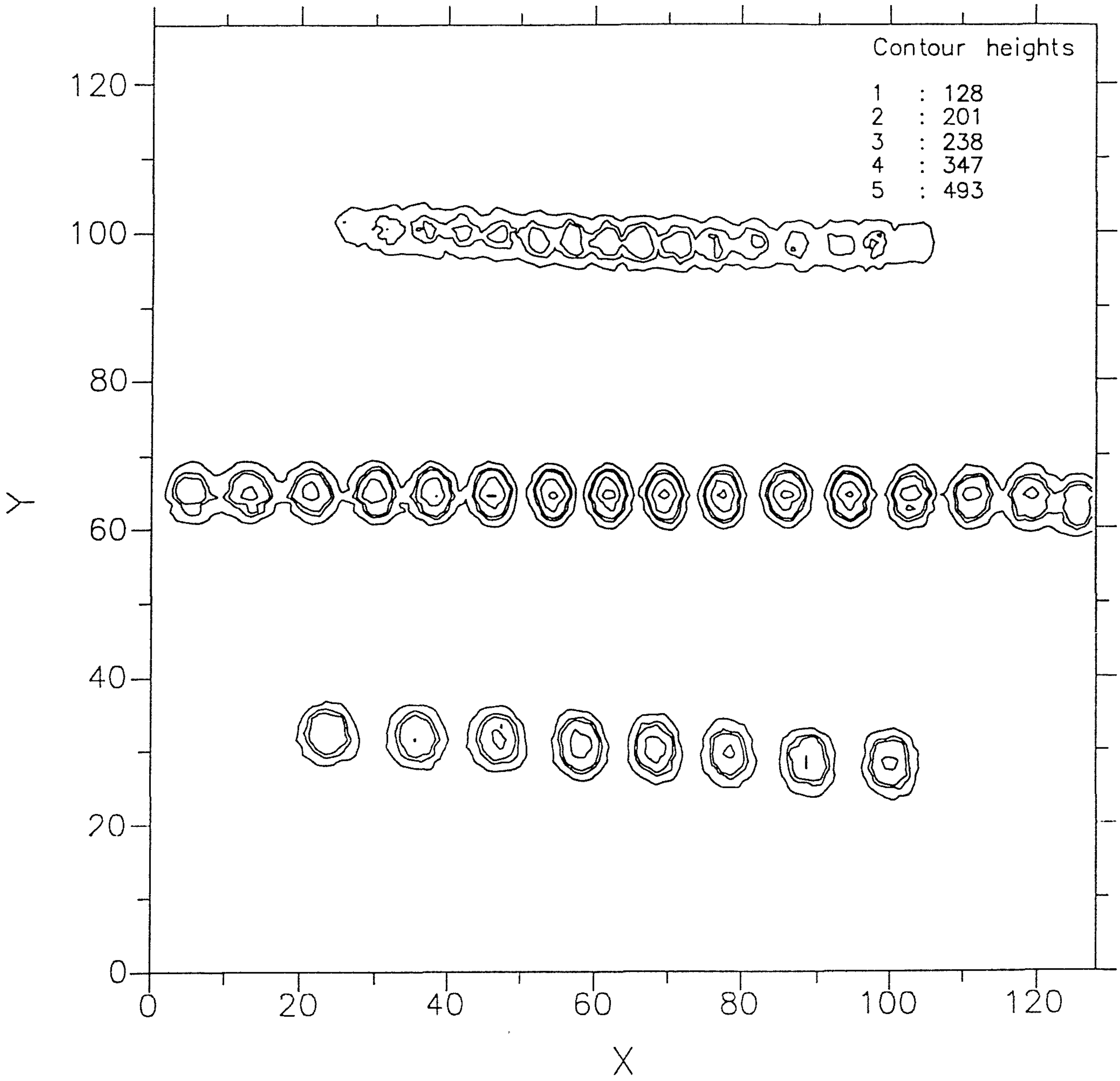

Figure 4.4: *Contour plot of all detectors viewed together by the R2487 3 in. PSPMT, illuminated with 122 keV (57Co). Crystal sizes from top to bottom are 1.25 mm, 2 mm, and 3 mm.*

4.6.1 Spatial Resolution

The detector spatial characteristics as a function of energy and crystal size, for both the R2487 and R3292 PSPMT have been investigated and are illustrated in Table 4.1.

Energy (keV)	1.25 mm Crystal	2 mm Crystal	3 mm Crystal
22.1	4.5 (5.2)	3.5 (10.7)	3.7 (15.2)
32.1	3.5 (4.8)	2.7 (5.2)	2.4 (9.9)
59.5	1.9 (3.8)	2.0 (3.7)	2.1 (5.8)
122	1.3 (3.3)	1.5 (2.6)	2.1 (4.3)

Table 4.1: *Mean PSF characteristics as a function of energy and crystal size for the R2487 PSPMT. Numbers in brackets indicate the performance of the larger R3292 tube type. All measurements are in mm.*

Collimation was provided by placing a lead block with a hole drilled through the centre measuring 0.5 mm in diameter, between the point source and the detector crystal element. Considerable care had to be taken to ensure that the hole was located as close to the centre of each detector element as possible. Measurements were repeated for three adjacent detector elements, and the mean value of position resolution noted for each segmented array.

These data once again imply that the 3 inch square R2487 PSPMT is capable of much finer spatial resolution than the R3292 PSPMT with its larger sensitive area. Since all of these measurements were made using the same conventional readout technique, and the only difference between the two tubes is the thickness of the glass window, we conclude that the spreading of light in the entrance window before reaching the photocathode is a singularly dominant effect involved in reducing the spatial resolution in the PSPMT. This was so marked in the case of the R3292 PSPMT with its 6 mm thick glass window, that adjacent crystals could not be resolved from even the largest of the one-dimensional arrays when all of the crystals were flood illuminated with 122 keV (^{57}Co).

At low energies, poor photon counting statistics caused by a reduction in light output from the 1.25 mm and 2 mm crystals compared with that of the 3 mm crystals has led to the PSF for these small crystals at low energies being broader than for larger crystals. This shows that at low energies, it is photoelectron statistics and not the crystal size which dominates the position resolution. In addition, it is clear that the light output from adjacent crystals must be as uniform as possible, and manufacturers suggest that a variance between crystals of ± 10% can be consistently achieved (Day et al. [34]).

Complementary to optimising the design of the detector is the choice of event reconstruction technique used in the imaging system. Measurements have been made which contrast two readout techniques for resolving the signals from adjacent small crystals at 122 keV. Further measurements are presented which demonstrate the effect that the window thickness of the photomultiplier tube has in limiting the ability to resolve small crystal arrays. Improvements in the spatial resolution of either tube may be achieved by using the multiwire readout technique, and event reconstruction using a gaussian-fitting and centroiding algorithm.

Crystal Size (mm)	FWHM (mm)	Peak/Valley Ratio
1.25	0.9 (1.3)	5.38:1 (1.22:1)
2	1.2 (1.5)	7.58:1 (3.1:1)
3	1.5 (2.1)	8.39:1 (6.36:1)

Table 4.2: *Mean PSF characteristics and peak-to valley ratio as a function of crystal size for the R2487 PSPMT with multiwire readout. Numbers in brackets indicate the performance for conventional readout.*

Results are presented in Table 4.2 which compare the measured values of position resolution and peak-to-valley ratios obtained experimentally in the laboratory using both readout techniques, when each detector crystal is viewed in turn by the 3 inch square PSPMT. In order that these results can be considered relevant for applications in nuclear medicine, a 122 keV (^{57}Co) collimated point source was chosen for these measurements.

The results from the smallest of the one-dimensional arrays, sixteen 1.25 mm crystals each separated by 0.25 mm of white titanium dioxide loaded epoxy, are illustrated in Figures 4.5 and 4.6. The first spectrum (Figure 4.5) was taken using the conventional readout technique. The limitations associated with this method of event reconstruction, as previously discussed become apparent when viewing such small crystals, where adjacent crystals are barely resolved. In marked contrast, the spectrum taken using the multiwire readout (Figure 4.6), shows adjacent elements well spatially resolved with excellent peak-to-valley ratio. Results from the sixteen slightly larger, 2 mm crystals each separated by 0.5 mm of epoxy demonstrate good spatial resolution for both conventional readout, and multiwire readout. Once again however, superior position resolution and higher peak-to-valley ratio have been exhibited by the latter technique.

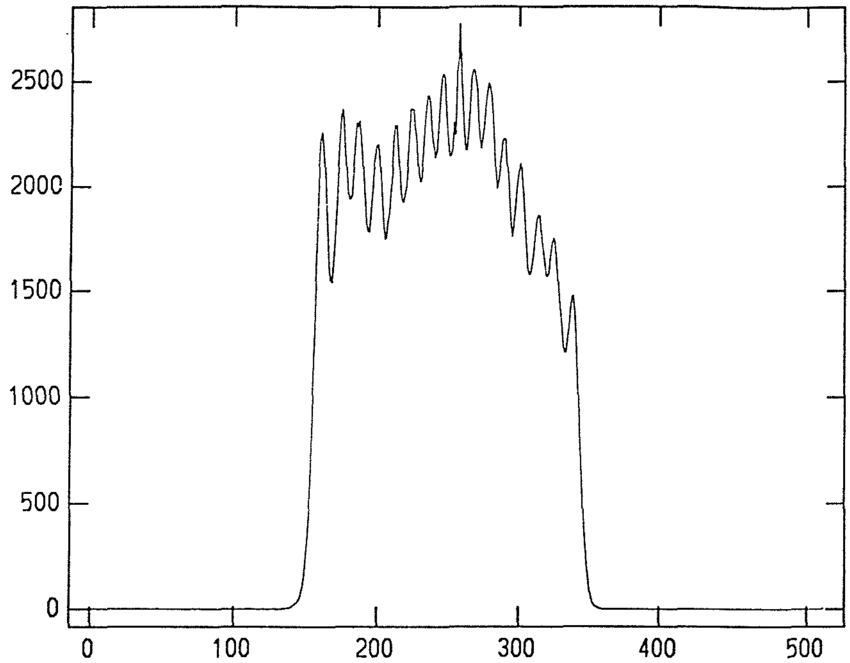

Figure 4.5: *16 crystal elements each 1.25 mm, illuminated with 122 keV (^{57}Co) with conventional readout. Mean position resolution = 1.3 mm FWHM.*

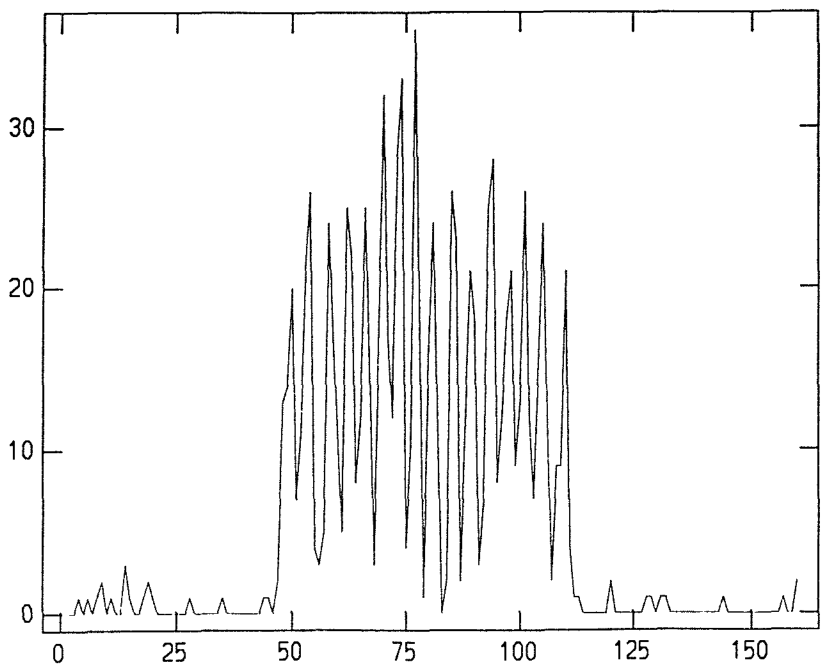

Figure 4.6: *16 crystal elements each 1.25 mm, illuminated with 122 keV (^{57}Co) with multiwire readout. Mean position resolution = 0.9 mm FWHM.*

Finally, results from the largest array of eight 3 mm crystals each separated by 0.5 mm of white epoxy, as expected show adjacent crystals to be well spatially resolved by both readout techniques with the best position resolution exhibited by the multiwire technique. For these large crystals, however, where the FWHM light spread is less than the dimensions of the crystals themselves, the peak-to-valley ratio is comparable for both readout techniques.

For this study, the prototype MXRP test boards interfaced directly with a PC which in turn interfaced with a Sun workstation where the peak-fitting is performed. This was far from ideal and is consequently slow, limiting the rate of data collection. It should then be said that the results for multiwire readout would be further improved by better statistics. Differences in software binning for the two readout systems mean that the scaling displayed is not always consistent.

4.6.2 Position Linearity

It has also been demonstrated by Bird et al. [16], that this technique provides superior position linearity across an extended sensitive area of the tube (see Figure 4.7).

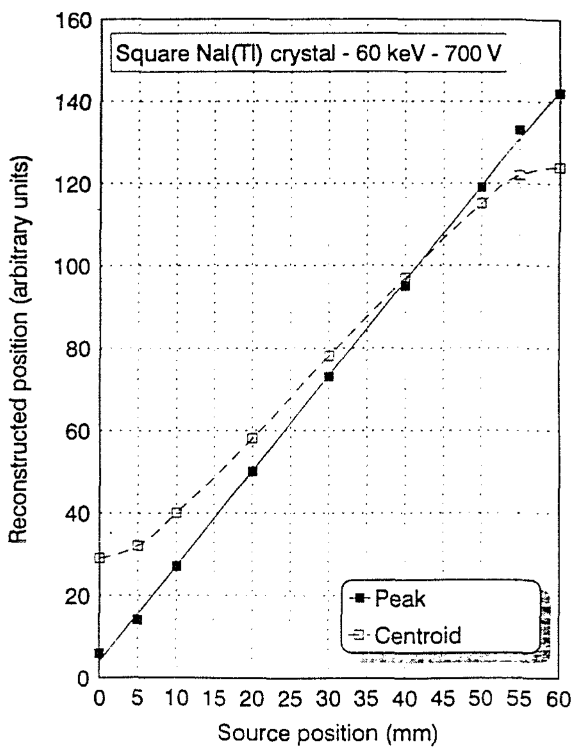

Figure 4.7: *Plot of spatial linearity of the R2487 PSPMT*

4.6.3 Energy Resolution

Measurements have been made of the uncorrected energy resolution as a function of energy, obtained by flood illuminating the whole of the tube sensitive area, for both CsI(Tl) and NaI(Tl) viewed by the 3 inch square PSPMT configured for resistive charge division readout. Previously reported measurements using the multiwire readout technique show superior energy resolution for more localised regions of the photocathode (Bird et al. [16]).

Energy (keV)	CsI(Tl) (% FWHM)	NaI(Tl) (% FWHM)
22.1	57	47
32.1	50	40
59.5	44	30
122	28	25

Table 4.3: *Energy resolution measurements with the 3 in. square R2487 PSPMT*

The results presented in Table 4.3 illustrate that modest energy resolution can be achieved using this tube to view CsI(Tl), whilst quite good energy resolution is demonstrated when viewing NaI(Tl) for a broad range of energies. Although these results are worse than can presently be achieved with the Anger camera, it is expected that comparable energy resolution could be achieved if the very much larger charge signal from the last dynode combined with some form of lookup energy correction is used to read out the energy deposited for each event.

4.7 Low Energy Detection Threshold

Results presented in the previous sections suggest that by directly sampling the charge collected upon individual anode wires, the charge contribution due to dark current would approximate to the line integral of the dark current from a smaller region of the photocathode which corresponds to the wire being sampled. The amount of charge deposited upon each anode wire N_e for a typical event can be estimated using the following expression:

$$N_e = \frac{0.5 E_\gamma \eta_s \eta_c \eta_q G}{W/3.7} \qquad 4.6$$

where W is the width of the electron cloud at the anode (expressed in mm), E_γ is the energy deposited in the scintillator (in units of keV), η_s is the scintillation efficiency (expressed in photons/keV), η_c is the light collection efficiency from the scintillator, η_q is the photocathode quantum efficiency, and G is the gain of the photomultiplier tube. For an imaging system which employs a small CsI(Tl) detector crystal, $W \sim 9$, $\eta_s \sim 52$, $\eta_c \sim 0.75$, $\eta_q \sim 0.1$, and G at 1100 V is $\sim 4 \times 10^4$. Applying these somewhat pessimistic values for these parameters, an energy deposit of 6 keV gives a resulting charge of $> 10^5$ electrons on each anode wire. It is clear from this analysis that provided adequate SNR is maintained, operating the PSPMT at higher voltages enables the detection of much lower energies.

The detection threshold for low energy x-rays, E_t, can be estimated by setting N_e to some multiple n of the total electronic noise of the readout system. This will be the sum of two contributions: (a) the electronic noise per channel from either the MXRP or HX-2 chip which is approximately 2000 e$^-$ (rms), and (b) the charge which will be collected due to photocathode dark current during the integration period. For the MXRP chip, having an integration time of some 15 μs, operated at a bias voltage of 1100 V, this contribution can be determined to be ~ 15000 e$^-$ per anode wire. Taking the typical values used previously, the low energy detection threshold can be easily estimated from the following expression:

$$E_t = \frac{15000nW/3.7}{\eta_s \eta_c \eta_q G} \qquad 4.7$$

This gives a theoretical low energy detection threshold of 2.4 keV.

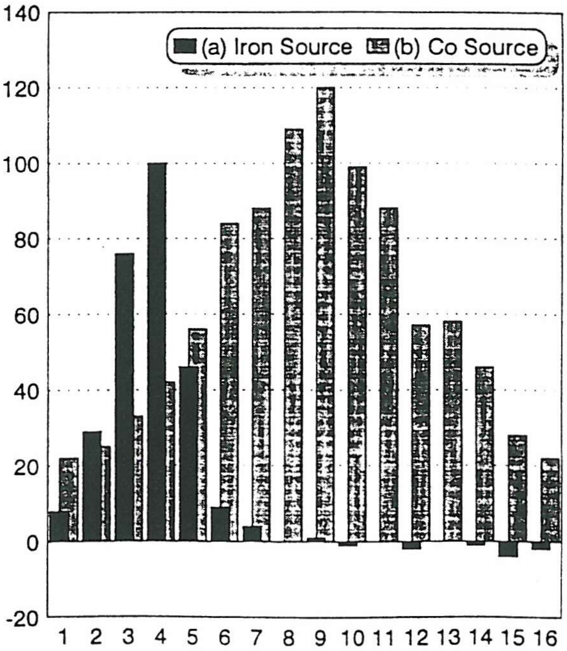

Figure 4.8: *Electron distribution profiles*

Preliminary measurements have been made using the PSPMT in combination with this readout system to view a small 2 mm x 2 mm x 5 mm CsI(Tl) detector crystal, illuminated by a source emitting 5.9 keV (^{55}Fe) x-rays.

This technique has enabled the measurement of both spatial and energy information without difficulty, and Figure 4.8 shows typical electron distributions for each of the 16 channels with (a) a 2 mm x 2 mm x 5 mm CsI(Tl) crystal located towards the edge of the sensitive area of the PSPMT illuminated by a 5.9 keV (^{55}Fe) source, and (b) a collimated 122 keV (^{57}Co) source illuminating the centre of a continuous 80 mm x 80 mm x 3 mm NaI(Tl) crystal (Bird et al. [16]).

4.8 The HX-2 Readout

Initial measurements reported in the previous section employed a prototype signal processing board containing a single MXRP 16 channel VLSI charge-integrating amplifier. For the purposes of the measurements described in the previous section, the charge distribution at the anode of the PSPMT could only be partially sampled in one axis only. Two such boards operating synchronously would obviously facilitate the possibility of obtaining two-dimensional images. Whilst desirable, this was not necessary in order to prove the principle of a readout system capable of processing each signal from the PSPMT individually. Indeed, the chips themselves were only specified to provide an integration time of 15 μs, which is a little slow for most applications in nuclear medicine.

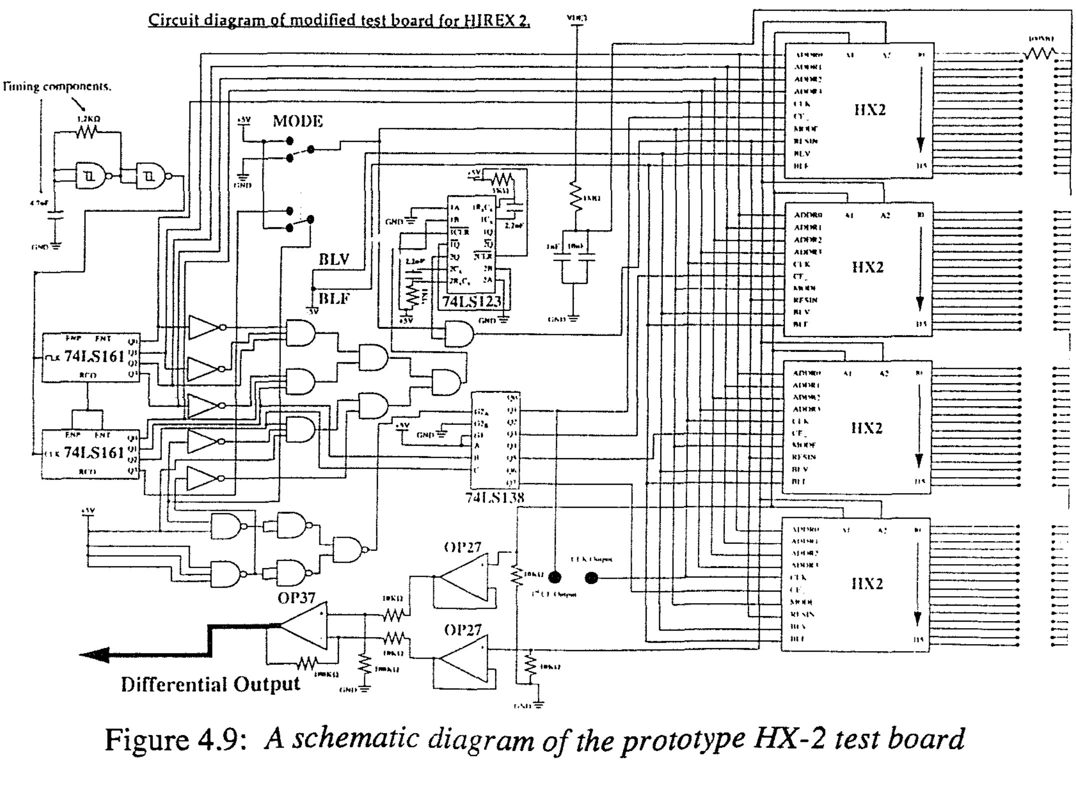

Figure 4.9: *A schematic diagram of the prototype HX-2 test board*

Whilst this initial study had been in progress, a second generation of 16 channel amplifier chips had been designed and developed at DRAL, and were ready for testing. Our work was sufficiently advanced that we were able to take full advantage of this development, and an early evaluation of these HX-2 devices as they are called was proposed. We considered a simple system comprising four HX-2 chips, together with the timing circuitry and decoding logic, mounted on a prototype test board (see Figure 4.9). The integration period on each of these test boards is determined by a presetable counter generating a number of clock cycles between two 1 μs pulses which simultaneously reset the inputs of all 64 channels. Thus the synchronous integration of the deposited charge is assured, with the integrated charge being read out from each chip sequentially. A timing diagram for this circuit is illustrated in Figure 4.10.

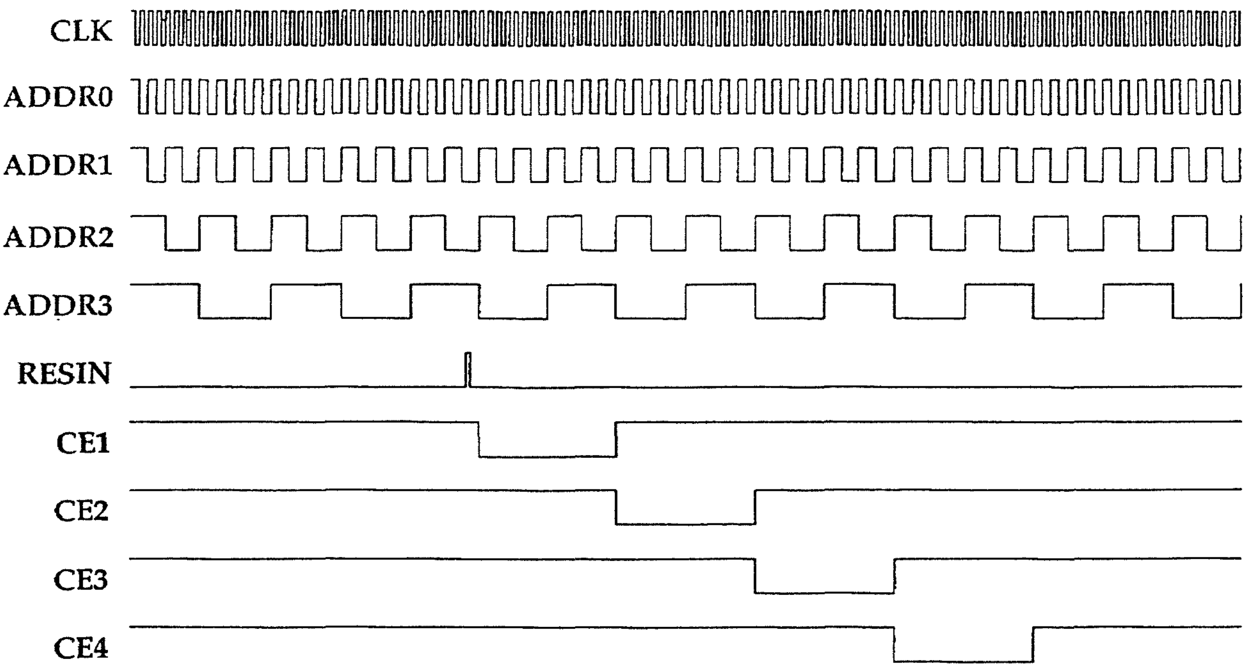

Figure 4.10: *Waveform diagram for the prototype HX-2 test board*

Whilst the theoretical range of integration times possible with these second generation chips extends from 5 μs to 100 ms, the minimum integration time of this proof of principle data acquisition system was effectively limited to only 40 μs. This was principally due to the modest data acquisition speed of the ADC card resident inside the PC that was used to sample the waveform from the HX-2 card. In order that this waveform could be accurately captured for subsequent event reconstruction, it was necessary to oversample the data by up to 10 times. The 250 kHz acquisition rate imposed by the ADC, combined with this requirement to oversample the data therefore placed an effective count rate limitation of 25,000 cs^{-1}. Ironically, this in fact represents an improvement in the data acquisition process from that described earlier.

For the measurements using the MXRP test boards we had relied upon downloading the data between the digital oscilloscope and the PC using the serial data port. This had previously limited the rate at which we could acquire our data to one event every five seconds or so, and the poor counting statistics are evident by looking at the data presented in the previous section. In addition, the new HX-2 test boards enabled the acquisition of images for the first time employing the multiwire readout technique. Further, the necessity to download the data onto the SUN IPX no longer existed, since all of the digitisation, and image processing was now performed directly upon the PC in real time. However, the obvious drawback is that the much longer integration time required by our prototype imaging system prevented the detection of the 5.9 keV (^{55}Fe) line which had previously been observed, and has naturally led to an increased low energy threshold of approximately 15 keV in these tests. This prototype readout system was by no means ideal, but provided a convenient platform for the evaluation and further development of these new multiwire readout techniques. In particular, the test boards used exhibited *dead-time* which increased significantly with decreasing integration times, and is demonstrated by the timing diagram illustrated in Figure 4.10. Whilst this is acceptable in an experimental system, it would present an unnecessary performance limitation for a practical imaging system. The dead-time exhibited by the prototype boards was greater than necessary because more chips than were actually required to read out the PSPMT were used. However, despite these obvious limitations, the boards performed well, and images were acquired using the data acquisition system we have described. These results will be presented as an integral part of the development of an auroral imager in Chapter 7.

4.9 A Dedicated HX-2 Readout Board for the 3 inch Square PSPMT

In order to address some of the performance limitations which were identified through the operation of the prototype test system, two dedicated readout boards have been developed based upon the HX-2 chips.

These signal processing boards were reduced in size using surface mounted components enabling the boards to exactly match the cross-sectional dimensions of the 3 inch square tube. The first of these boards uses a modified configuration of the prototype with similar decoding logic as illustrated schematically in Figure 4.11.

An amplified last dynode signal from the PSPMT is sampled, and a comparator circuit used to discriminate between dark current noise and a real event. Once a signal is detected above a given threshold which is adjusted with a variable resistor, an S-R flip-flop is used to generate a series of 48 timing pulses which could be applied to the strobe input of the ADC. The purpose of this trigger is to try to ensure the accurate gating of the data arriving at the input of the ADC. An order of magnitude reduction in integration time could potentially be achieved by making this change alone, because the requirement to oversample the data as it arrives at the ADC was no longer necessary.

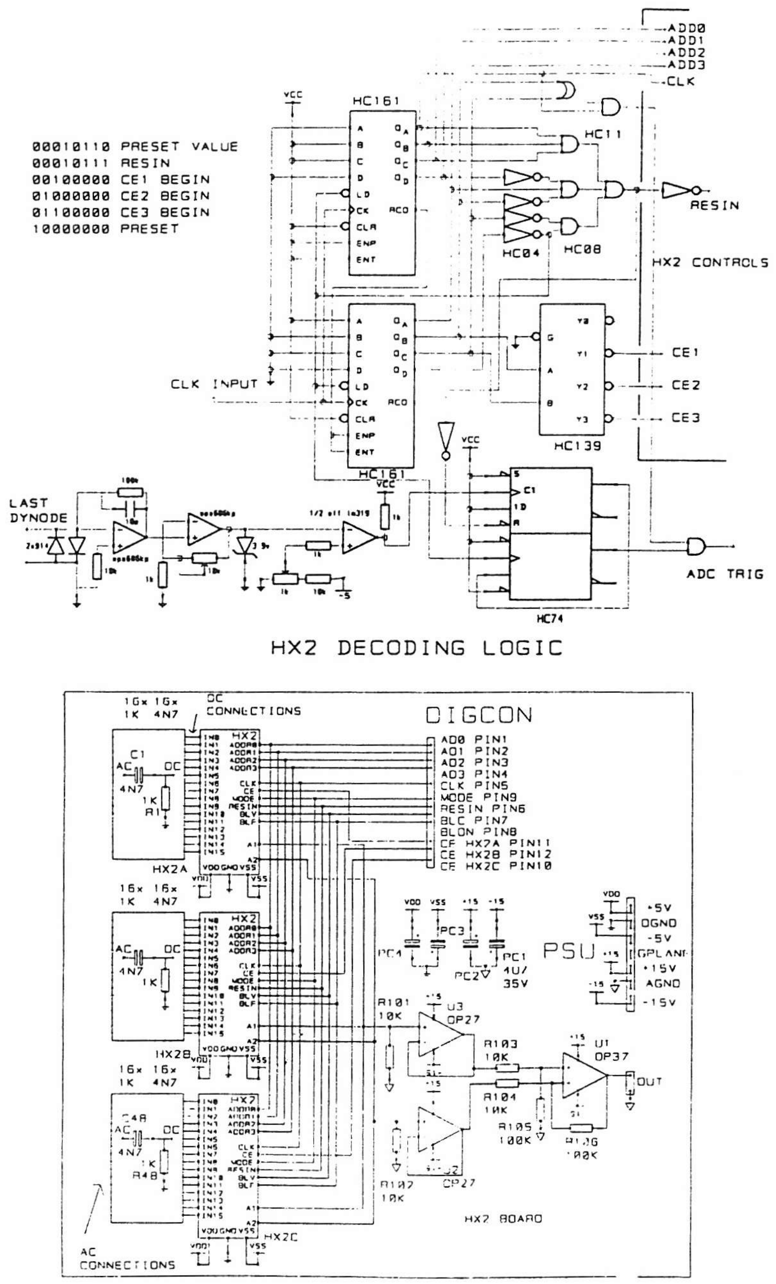

Figure 4.11: *A schematic diagram of the modified HX-2 board*

In addition, changes were made to the timing pulses used to instruct the HX-2 chips, enabling the dead-time to be reduced significantly. Since the board is required to sample only 35 anode wires, only three HX-2 chips were required. In addition, the timing was modified such that the readout cycle matched the integration time exactly, enabling the development of a board which exhibits complete overlap between integration and read cycles, with few wasted channels, and very little associated dead-time (see Figure 4.12).

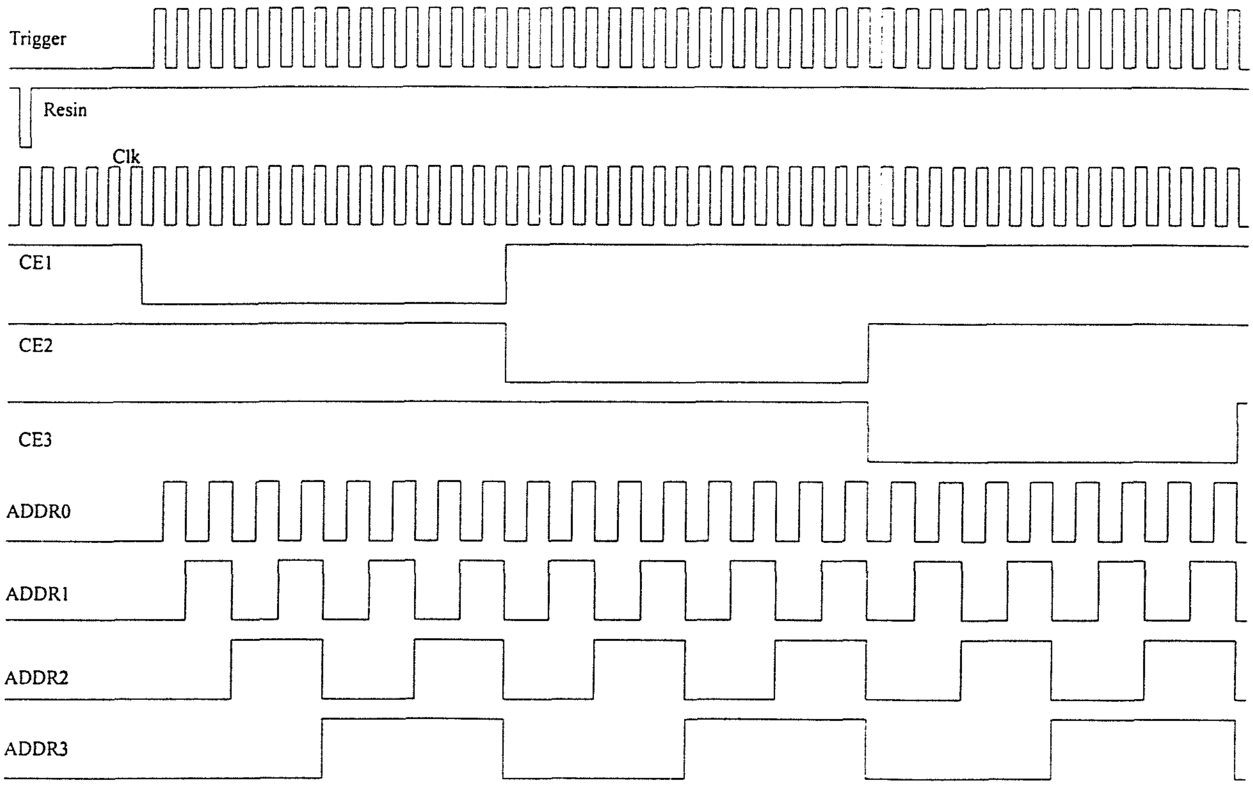

Figure 4.12: *Waveform diagram of modified board*

In addition to these changes, it was identified that the ability to adjust the integration time to suit the type of scintillator being viewed was also desirable. Since all onboard timing for these boards was a fixed multiple of the clock determined using combinational decoding logic, it was felt that the simplest way to achieve this in practice would be to vary the frequency of the clock itself. This would be difficult to engineer in hardware, but might be possible in software. If the divide-by-n counter from the ADC inside the PC could be used to generate the clock remotely, the clock frequency could be varied in software by simply choosing n to be a different value. This modification has also been made to the circuit, and has been demonstrated to work well.

The completed readout system occupies three surface mounted boards which interface together. The first board simply interfaces directly with the plug at the back of the PSPMT. The centre board is populated with three HX-2 chips, and the analogue differential amplifiers which convert the output of the three chips into a serial stream of analogue data. This centre board is also ac coupled through the application of a high-pass R-C filter to each channel. Therefore, only fast signals from the PSPMT can contribute to the signal, and ensures that any long-lived dc afterglow from the scintillator due to ultra-violet phosphorescence is effectively isolated. The third board is populated with the combinational decoding logic for the timing pulses, the amplifier for the last dynode signal, comparator, and S-R flip-flop. This circuit is illustrated in Figure 4.13.

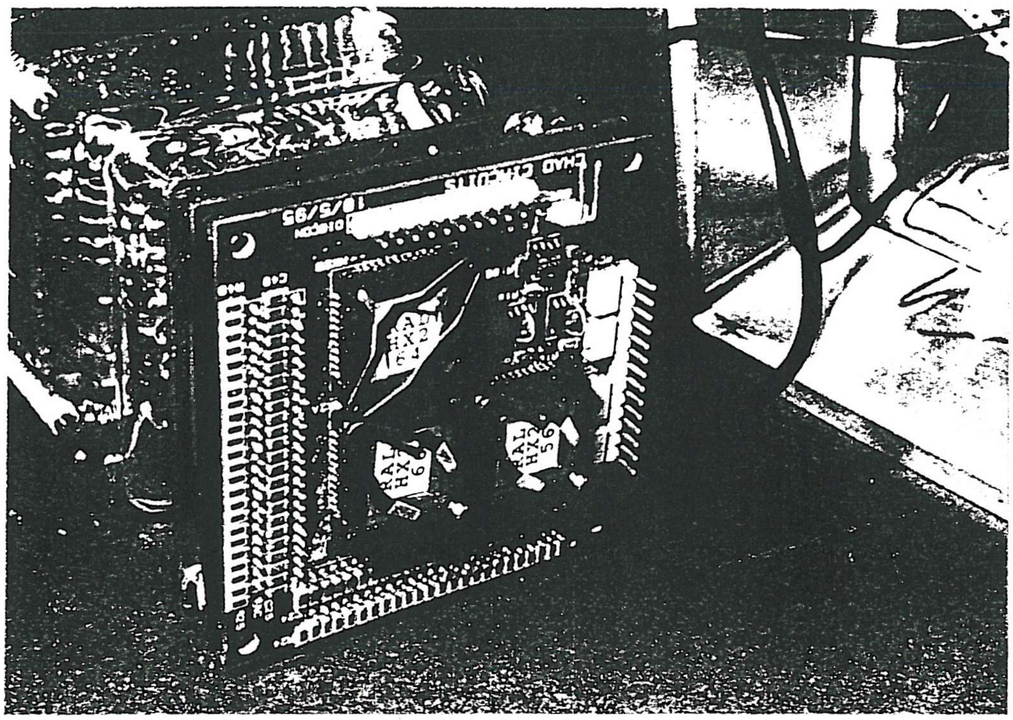

Figure 4.13: *A photograph detailing the modified HX-2 board*

In the original prototype boards, we had observed that each output requires approximately half of one clock cycle before each output settles to a predictable level. This instability was partially responsible for the difficulties experienced in sampling the data at the correct time, which necessitated such considerable oversampling. The manufacturer suggested that this problem could be overcome by gating the clock high during the readout period when each chip is enabled (Thomas [121]).

This modification was incorporated into the design of the modified HX-2 board with the expectation that the output from each channel of the new board would be stable for the whole readout cycle. However, this modification was not successful, and upon further investigation we subsequently learned that the HX-2 chips require a single clock pulse after each chip enable goes low to ensure that the output remains stable.

It was therefore decided that a third generation readout board should be developed. However, the necessary timing pulses would be difficult to generate using combinational logic, and so it was decided that an EPROM should be used. This development enables the component count to be reduced by 45 chips, and will provide a new flexible design where the integration time can be set by simply varying the length of the resin pulse in either hardware or software. A schematic diagram and timing diagram of the test board currently under development are illustrated in figures 4.14 and 4.15.

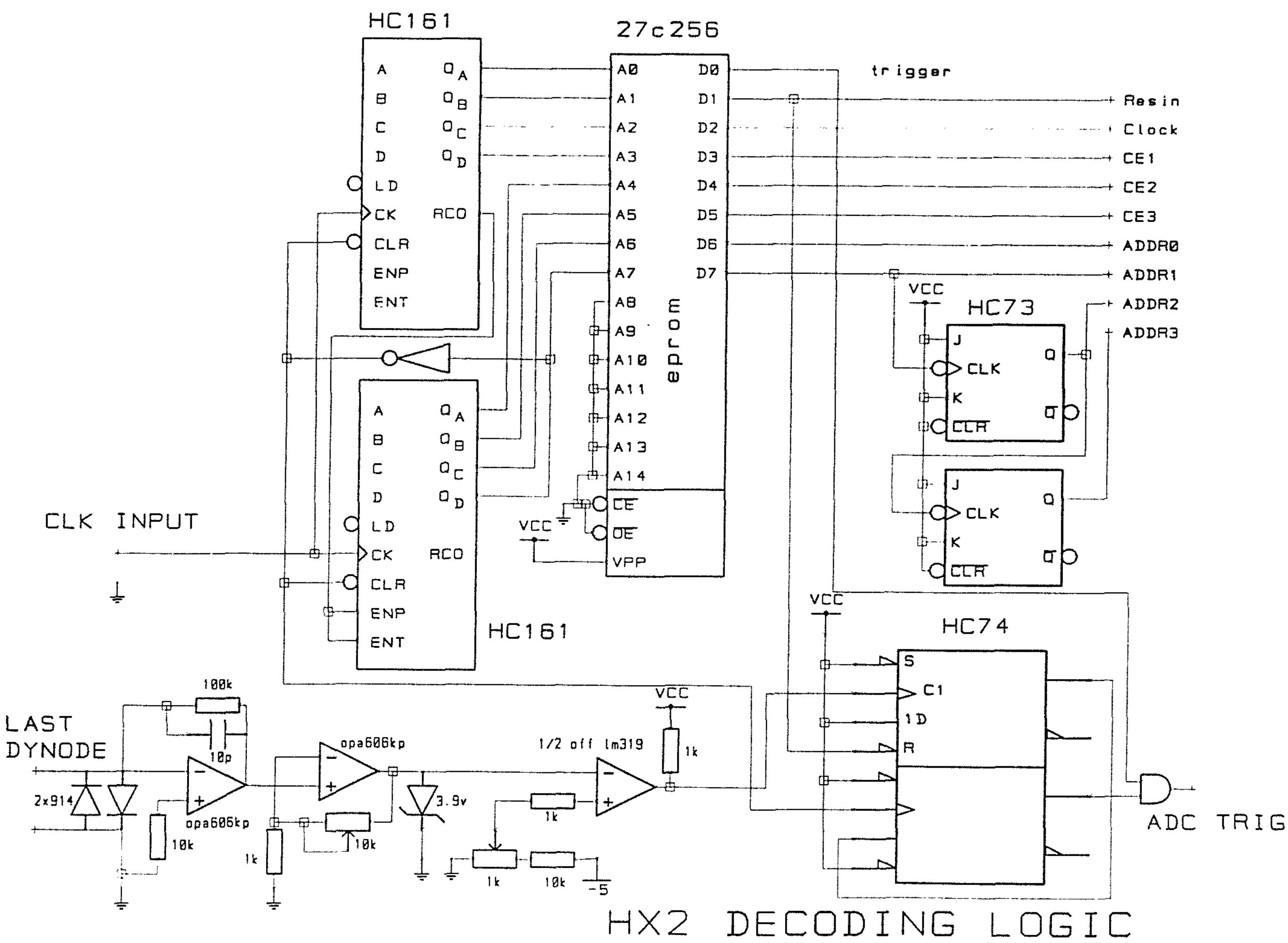

Figure 4.14: *Schematic diagram of EPROM based HX-2 board*

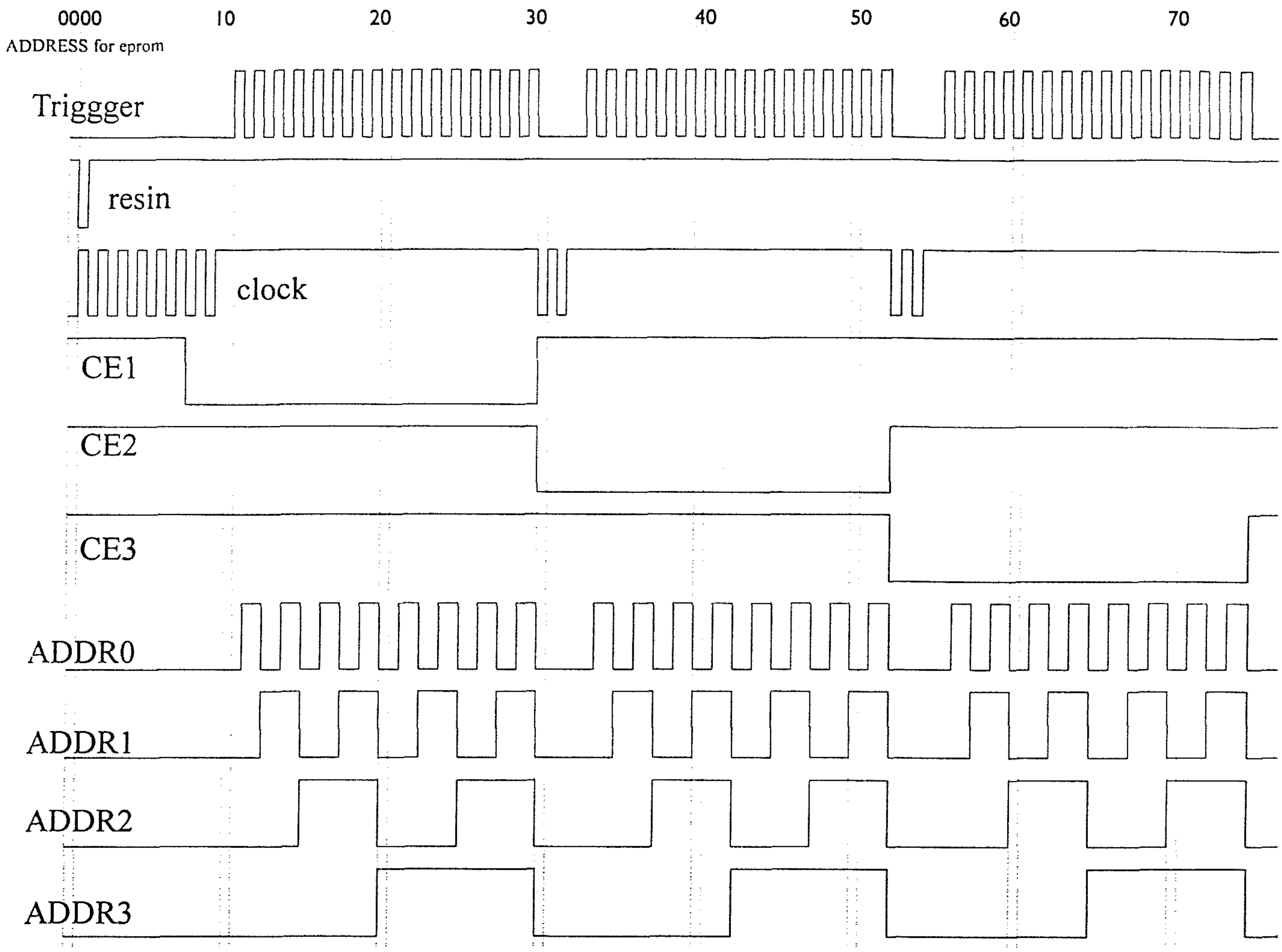

Figure 4.15: *Waveform diagram of EPROM based HX-2 board*

This circuit has recently been manufactured, and initial results look very promising. The problem of the chips requiring half of each readout cycle per channel before settling to a predictable level has been successfully engineered out of this final iteration. This represents a considerable improvement over previous designs, and should facilitate more accurate sampling of the analogue data stream by the ADC. Finally, since tha largest contribution to the dead-time of this signal processing board is caused by reading out the charge that has been integrated by unused channels, it is believed that this dead-time could also be eliminated by carefully programming the eprom to address only those channels that are connected to the PSPMT. This modification remains to be proved, but would represent an even more significant improvement in the performance of this data acquisition system.

4.10 Conclusions and Future Work

We have demonstrated that the spatial and energy resolution performance of compact gamma cameras based upon the PSPMT for applications in γ-ray scintigraphy can be optimised by considering the geometrical design of the scintillation crystal. Guidelines for this optimisation can be summarized as follows:

- Reduce the contribution of diffuse background due to scintillation photons being transported away from the site of the interaction. This can be achieved by segmenting the detector crystal to localize the light spread. The effect of this is to increase the number of photons collected at the site of the interaction. The results of optical Monte Carlo simulations suggest that by selecting a modest aspect ratio of for example 1:1, more photons will be collected by the photodetector causing a corresponding improvement in the energy resolution.

- Errors in the reconstructed point-spread function can be reduced by decreasing the diameter of the light pool emerging from the crystal. This can be achieved either by reducing the thickness of a continuous detector crystal, or more effectively by segmenting the detector crystal.

Recent work by Pani et al. [87] has proposed that individual detector crystal elements based upon an array of YAP:Ce could be reduced to only 600 μm x 600 μm x 7 mm. The claimed intrinsic spatial resolution of this camera is 0.7 mm FWHM at 140 keV. However it is clear that unless the hole size used in the collimator is of comparable dimensions to the elemental cross-section of the detector crystal, the maximum resolution that can be achieved will be determined by the collimator. If very small holes were defined by the collimator, the sensitivity of the camera would be decreased considerably, whilst having so many holes in close proximity would undoubtedly lead to increased septal penetration which would lead to blurring in the image.

In addition, the light output of YAP:Ce is relatively modest at only 40% of NaI(Tl). The aspect ratio of each detector element is approximately 12:1, and this combination will severely degrade photon counting statistics, and the energy resolution of this camera. In order that Compton scattered photons from within the patient can be rejected, we consider that the preservation of energy resolution is a very important design criteria for a compact clinical γ-camera. When specifying the geometry of the detector crystal for such an application, one must therefore determine the most appropriate compromise between the sensitivity of the camera, the spatial resolution that can be achieved, and the preservation of energy resolution for background rejection.

Measurements have been obtained which suggest an optimum elemental detector crystal cross-section lying somewhere between 1 mm^2 and 4 mm^2, and aspect ratios as small as can be achieved whilst preserving the sensitivity of the camera over a range of energies characteristic of commonly used radiopharmaceuticals. We have concluded from these data that a detector crystal having elemental dimensions of 2 mm x 2 mm x 4 mm, with a dead-space between elements of less than 250 μm would provide an acceptable compromise between energy resolution, spatial resolution, and sensitivity.

A variety of segmented CsI(Tl) detector crystals have been successfully viewed by both the 3 inch square, and the 5 inch diameter PSPMT for applications requiring the detection of a range of γ-ray energies up to 122 keV using both conventional and multiwire readout techniques. The effect of increasing the segmentation of the detector crystal is a reduction in the width of the PSF whilst the light collection efficiency can be increased by using diffuse reflecting white titanium dioxide loaded epoxy to optically isolate adjacent crystals. It has been shown that for viewing small crystal arrays over a broad range of energies, the multiwire technique with its peak-fitting algorithm provides superior spatial resolution together with higher peak-to-valley characteristics. Clearly, the choice of readout technique forms a vital part of the overall detector design process. For example, in nuclear medicine applications where very fine spatial resolution is usually not required, where the incident gamma-ray flux is high relative to the background, and the energy above 60 keV, the results suggest that the conventional readout would be adequate. For applications in auroral imaging, where the detection of lower energies than this are required, or where better spatial resolution is desired, we conclude that the multiwire technique is more suitable. However, the previously reported improvements in position linearity when using the multiwire technique (Bird et al. [16]), showing detailed calibration of the tube to be unnecessary, could make this type of readout popular for many applications.

The results of the measurements of spatial resolution of both the 3 inch and the 5 inch PSPMT indicate that the larger tube is less suitable for resolving close-packed arrays of small crystals such as would be desirable in some imaging systems. This is due in large part to the light spread in the glass window of the tube, and it is possible that if this dimension could be reduced comparable performance could be obtained. However, as will be discussed in Chapter 6, this inability to resolve individual detector crystal elements could be advantageous in a compact clinical gamma camera where a segmented image would not be desirable. We have additionally demonstrated that it is possible to develop compact multiwire readout solutions that are suitable for using with both versions of the PSPMT that have been discussed in this chapter.

In future, one possible development upon these boards would be to enable self-triggering using a sample and hold circuit on each of the input channels to the HX-2 chips. These results provide a baseline study from which it will be possible to develop scintillation counters based upon the PSPMT that are optimised for a particular application and energy range, within which excellent spatial resolution will be maintained, whilst continuing to provide good energy resolution.

Chapter 5

Modelling the Detector Crystal Design

5.1 Introduction

This chapter provides a detailed justification of the design of the scintillation crystal detectors for the applications outlined in Chapter 1, whilst bearing in mind the performance characteristics of the two types of PSPMT described in the previous chapter.

Modern gamma camera development relies upon a careful design process in which the performance of every component will have been predicted and optimised through a series of computer simulations prior to manufacture. This is also true for small prototype camera systems such as that which is proposed in Chapter 4, and ideally each stage in the conversion process should be simulated so that the complex interactions and inevitable compromises can be comprehensively studied. Existing code can be utilized to consider both the interaction of γ-rays within the detector crystal, and the subsequent optical photon transport prior to the photodetector. Unfortunately, estimates of the electrostatic performance of the PSPMT from Hamamatsu could only be derived from measurements of the photoelectron distribution at the anode for a known light spread function at the photocathode. Since the light-spread function varies as a function of the crystal geometry, a general simulation including the electrostatic performance of the PSPMT used to view various configurations of scintillation crystals is non-trivial, and has not been attempted. Monte Carlo code has recently been specifically developed for the PSPMT at The UCL Middlesex Hospital. This is based upon the EGS simulation software, and has successfully integrated both the γ-ray interactions and optical photon transport into a single model. However, this code has similarly not attempted to include a general model which reflects the tube's electrostatic characteristics. Therefore, for the purposes of the work presented in this chapter, the PSPMT has been assumed to be a black box which simply converts an optical signal into an electronic signal. Whilst both the distribution of charge at the anode wires, and to the reconstructed point-spread function of the compact gamma camera are related to the predicted light-spread function of the detector crystal, they cannot be reconciled without a model that includes the electrostatic performance of the PSPMT. Consequently, at the present time, each remains unavoidably decoupled from the other in our simulations.

The dependence of both energy and spatial resolution upon photon counting statistics has been identified in previous chapters, and therefore the principal components affecting the performance of a PSPMT based gamma camera are the collimator and the detector crystal. Whilst it is clear that the collimator will have a dominant effect upon the overall resolution of the camera, this chapter focuses upon the optimisation of the intrinsic camera resolution due to the detector crystal using Monte Carlo modelling techniques.

Two types of simulation can be performed for a particular detector geometry. The first type simulates the complex interaction processes within the detector crystal for γ-ray photons normally incident upon the detector plane, whilst the second type simulates the transport of the optical photons generated within the detector crystal. The following sections consider each of these types of simulation in turn for a gamma camera which is expected to demonstrate millimetric spatial resolution, and improved energy resolution.

5.2 The GEANT 3 Monte Carlo

The first version of GEANT was written at CERN in 1974 as a bare framework which initially emphasised tracking of a few particles through relatively simple detectors used in particle accelerators. The software has since evolved with some continuity, and in 1982 work began to develop the latest version from the existing code. The result of this development is GEANT 3, an elaborate and fully comprehensive suite of Monte Carlo simulation libraries. Developed and maintained at CERN, GEANT 3 offers its users a range of detector description and simulation tools for studying the design and optimisation of detectors for high energy physics applications.

The GEANT program simulates the passage of elementary particles or photons through matter, and tracks the γ-ray photons and particles that are produced as a result of interactions within the material. Originally designed for use in high energy physics experiments, it has also been used in nuclear medicine, radiotherapy, biological sciences, radiation protection, and astronomy, where it is used to study the interaction of γ-ray photons or electrons with matter. Other code is also available to perform simulations in medical physics. The EGS simulation software mentioned in the introduction was incorporated into GEANT for the simulation of electrons and γ-rays, and as a simulation tool in its own right EGS has found widespread application in nuclear medicine and radiotherapy.

5.3 GEANT 3 Monte Carlo Models of Detector Crystal Geometry

GEANT 3 has been used to determine the relative depth of interaction profiles for CsI(Tl) and NaI(Tl) respectively for incident energies of 140 keV. Being more dense than NaI(Tl), CsI(Tl) absorbs a greater proportion of the incident energy within a depth of a few millimetres compared to the NaI(Tl) used in conventional clinical gamma-cameras (see Figure 5.1). Clearly the improved detection efficiency offered by CsI(Tl) makes this an interesting material for some applications in nuclear medicine where high stopping powers combined with good energy resolution are desired.

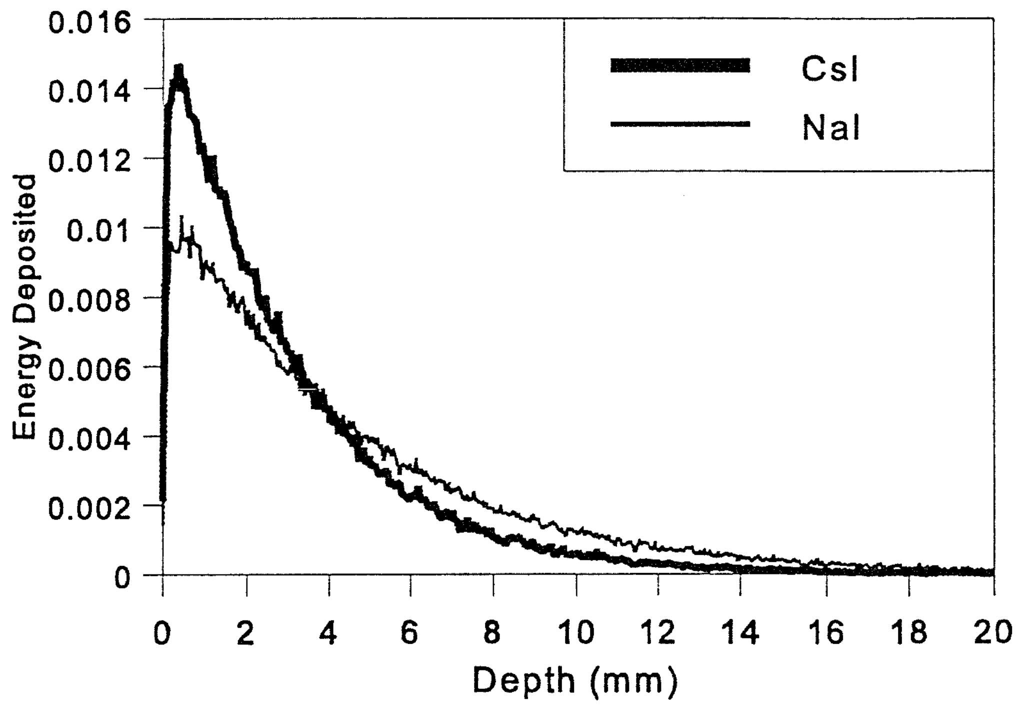

Figure 5.1: *Energy deposited as a function of depth for NaI(Tl) and CsI(Tl) at 140 keV*

Monte Carlo simulations have also been performed to determine the trade-off between detection efficiency and light output as a function of incident energy and crystal thickness for CsI(Tl). GEANT and GUERAP V simulations have been combined in the chart illustrated by Figure 5.2 to provide a guide to which segmented detector configuration is most suitable for nuclear medicine studies over a range of energies. A segmented CsI(Tl) detector crystal comprising elements which each have a cross-section of 2 mm x 2 mm has been modelled for incident photon energies of 140, 160, 200, 250, 350, and 511 keV, and a series of efficiency curves obtained. Overlaid upon this data is a further efficiency curve which represents the light output as a function of aspect ratio for a single CsI(Tl) detector crystal having a cross-section of 2 mm x 2 mm, optically coupled to the entrance window of a PSPMT.

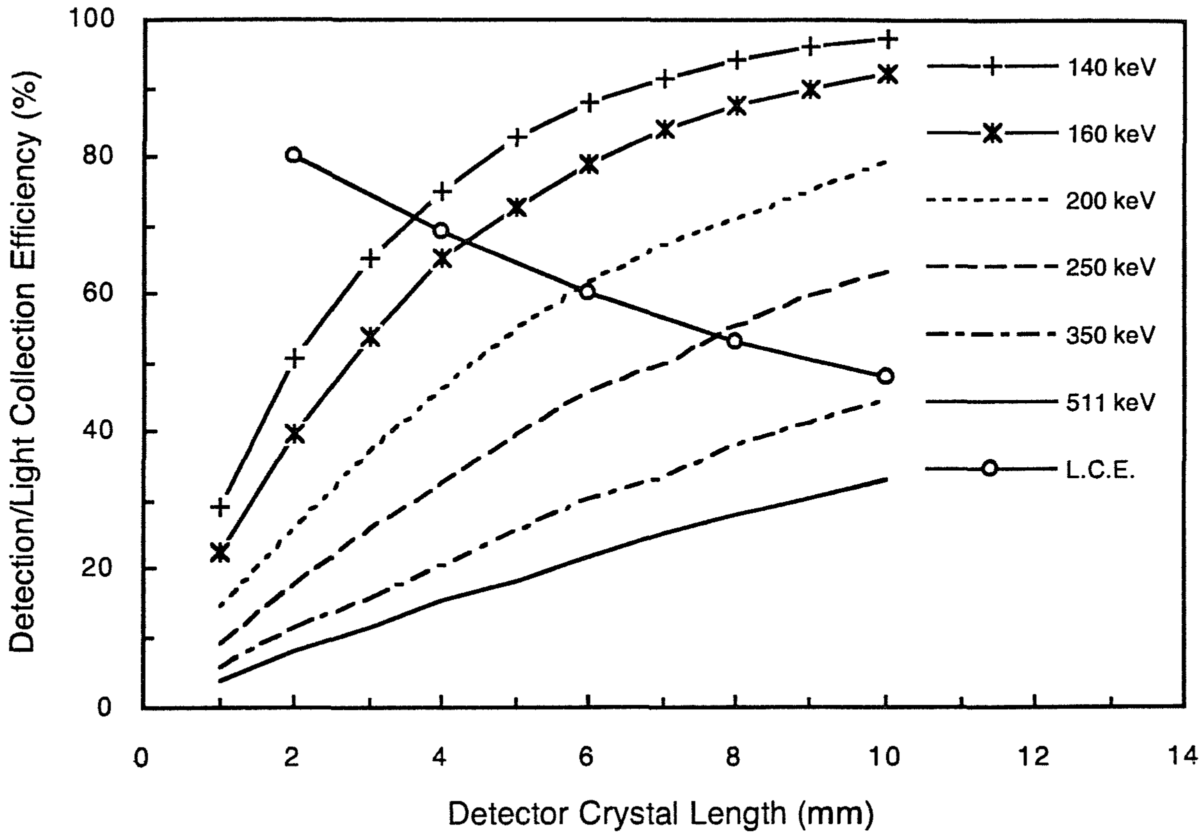

Figure 5.2: *Trade-off between detection efficiency and light output for CsI(Tl)*

For incident photon energies of 140 keV, it can be seen that a crystal depth of 4 mm provides a good compromise offering both excellent light output, and high detection efficiency. Whilst reducing the detector crystal thickness to 2 mm (an aspect ratio of 1:1) offers an improvement in light output of ~5%, it is at the expense of a reduction in detection efficiency of ~20% which would be undesirable.

Compton scattering of γ-ray photons in nuclear medicine studies is a major cause of image blurring in nuclear medicine, and can be attributed to either internal scattering within the patient, or scattering within the detector crystal of the gamma camera. Pulse height discrimination techniques are commonly used in order to reject those γ-ray photons which have Compton scattered within the body, ensuring that only events lying within the photopeak are accepted. However, because of the non-uniform energy response characteristics of a PSPMT based clinical gamma camera, an energy correction using a look-up table is also necessary to ensure that only those photons which have Compton scattered prior to detection are excluded from the image.

Incident γ-ray photons which have not scattered within the body, but which subsequently scatter within the detector crystal present another problem. Multiple energy deposits within the detector plane are caused by energy being transported and deposited at some distance from the original site of interaction. This situation arises either as a result of incident γ-ray photons which Compton scatter and are subsequently absorbed within the detector crystal, by photoelectric absorption accompanied by K_α emission which is subsequently absorbed, or by the recoil electrons of each of these two mechanisms losing their kinetic energy to the surrounding material. If the sum of the energy deposited within the detector crystal is equal to the energy of the incident unscattered photon, the scattered photons will be accepted as a valid single event. Hence the correct energy is accepted, but the wrong position is reconstructed for the event.

Alternatively, Compton scatter may similarly occur within the detector crystal, and the scattered γ-ray photon may exit the crystal without being absorbed. Here the event will be rejected as being invalid because a significant fraction of the incident photon energy will be carried away by the escaping photon as it leaves the crystal. Clearly we have no way of distinguishing between γ-ray photons which Compton scattered prior to entering the detector, and those that scattered out of the detector in this way. Hence although the site of interaction can be correctly determined, the event will be rejected.

Clearly, the geometry of the detector crystal cannot influence those γ-ray photons which Compton scatter internally within the patient. However, it is possible that a carefully designed scintillator might influence those γ-ray photons which Compton scatter within the detector crystal. Since the light-spread function at a particular energy is determined both by the size of the detector crystal, and by the probability of an interaction involving more than one detector crystal, it is obviously important to identify the exact relationship between these two quantities. If the detector crystal array can be designed such that Compton scattered photons, K_α emission, and energetic electrons, will have a high probability of being subsequently absorbed within the crystal in which the incident γ-ray photon interacted, the photodetector will see a single bar event resulting in the correct reconstruction of the original position of interaction. However, we realise that it might be necessary to increase the size of the detector crystal in order that this should happen.

Inevitably this will lead to a slightly coarser image, but the increased probability of correctly reconstructing these events should improve both the contrast and the image definition.

GEANT 3 has therefore been used to investigate the significance of scattered photons, K_α emission, and recoil electrons which give rise to multiple site interactions within adjacent detector elements of various cross-sections. Incident γ-ray photons at energies of interest in nuclear medicine studies, interacting within detector crystals of various dimensions have been simulated, and it has been possible to predict the effect that crystal geometry has upon Compton scatter between adjacent detector crystals at certain monochromatic energies. Monte Carlo models have been performed using GEANT 3 for incident γ-ray photon energies of 140, 160, 200, 250, 275, 350, and 511 keV, interacting within 4 mm thick segmented CsI(Tl) detector arrays of various crystal dimensions. The initial simulation used a continuous detector crystal for the simulation during which the γ-ray photons and electrons were tracked, and a series of virtual cuts were then used to bin the data into the required detector cross-section for analysis.

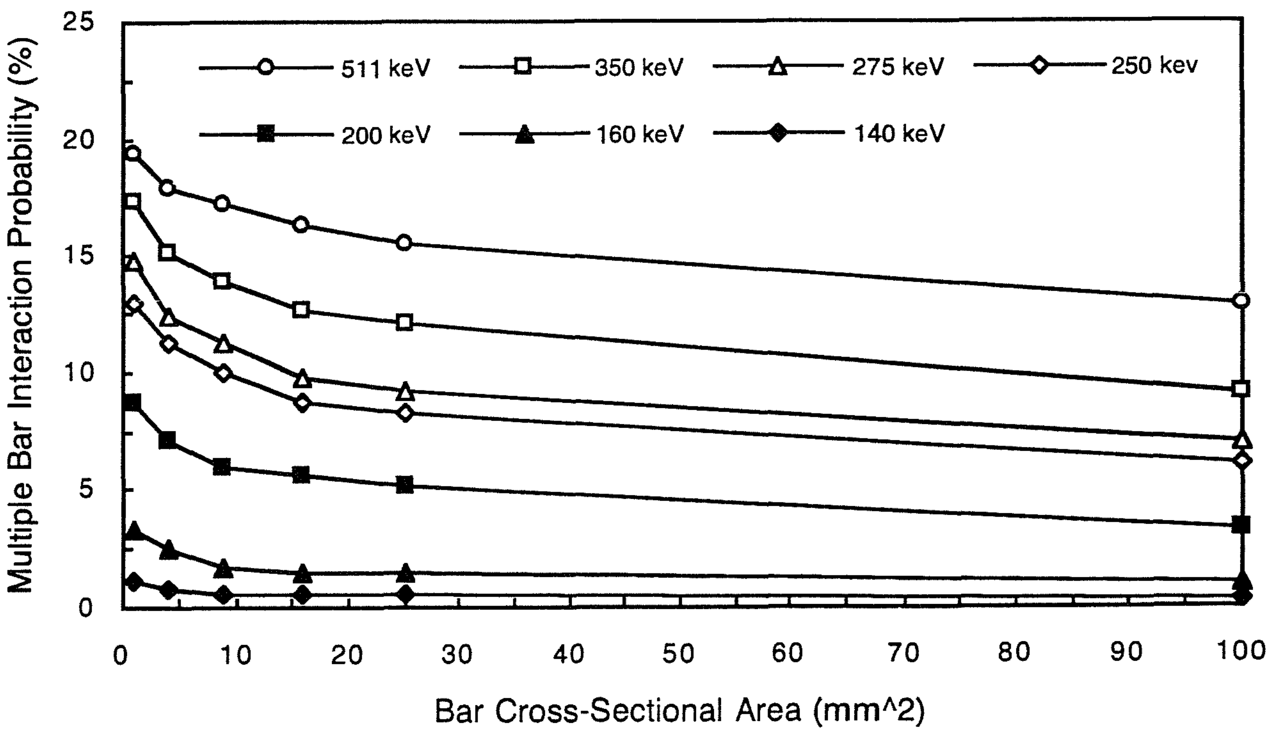

Figure 5.3: *Multiple bar interaction probability as a function of cross-section of CsI detector crystal elements with virtual cuts, 40 keV threshold*

A 40 keV threshold was used in the simulation to discriminate between multiple bar interactions caused by Compton scattered photons, and to reject the 35 keV K_α photons induced by photoelectric absorption. The probability of multiple bar interactions due to Compton scatter alone, involving usually two, but occasionally three detector elements is presented for each detector crystal cross-section as a function of energy in Figure 5.3. For incident photon energies of both 140 keV and 160 keV, it can be seen that the probability of an interaction involving more than one detector crystal element due to Compton scattered photons, and photoelectrons alone is low, enabling the preservation of spatial resolution by reducing the crystal size to perhaps as little as 1 mm. However, as one would expect this probability increases markedly at higher incident energies due to the more penetrating nature of the scattered photons and energetic electrons. However, the situation changes somewhat when the detector model is modified to reflect the more realistic case where photons and electrons having energies as low as 1 keV are tracked by the simulation software. In addition, a modification to the code was made to enable the addition of "dead-space" of variable thickness between adjacent detector elements in order to simulate the effect that white TiO_2 loaded epoxy has in attenuating the scattered γ-ray photons, and particularly electrons of a range of energies. This simulation demonstrates the effect that the combination of both photoelectric absorption and Compton scatter has upon the probability of multiple bar interactions.

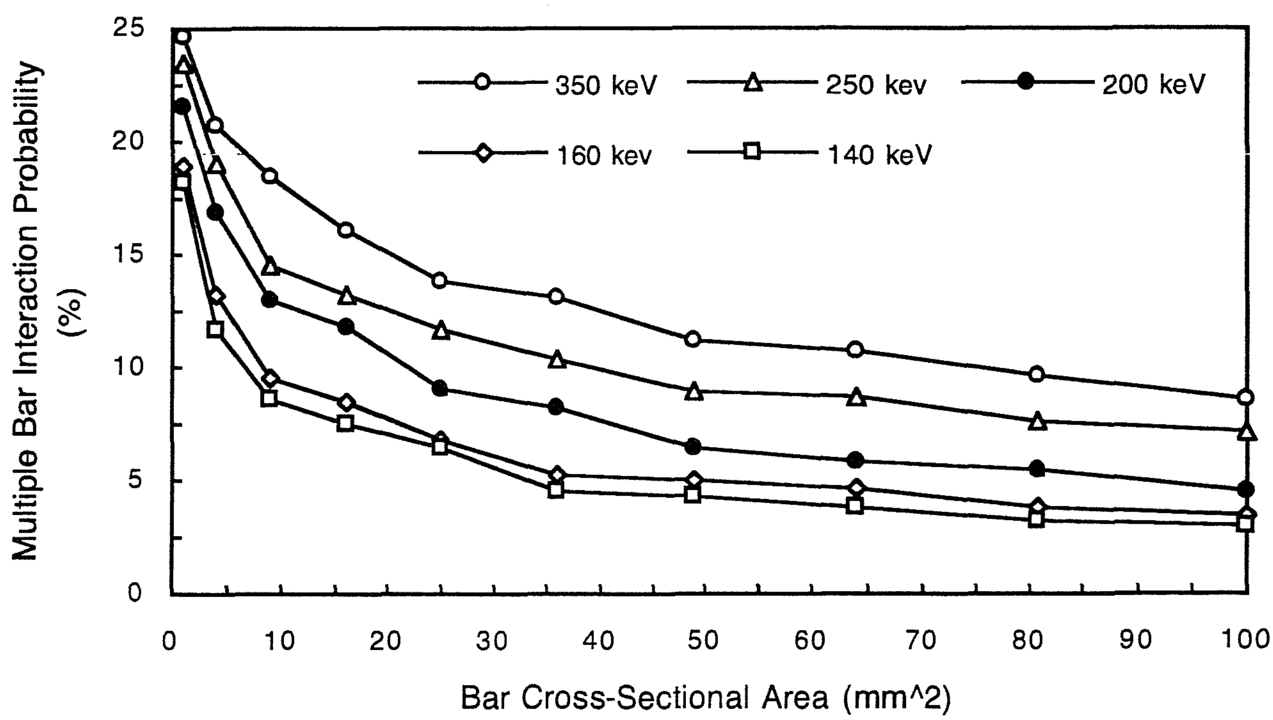

Figure 5.4: *Multiple bar interaction probability as a function of cross-section of CsI detector crystal elements separated by 500 μm of epoxy, 1 keV threshold*

The difference between this and the previous model is principally due to the emission of 35 keV K_α photons, and photoelectrons accompanying the full-energy deposit within the detector crystal. Illustrated by Figure 5.4, it can clearly be seen that the probability of multiple bar interactions for a 4 mm thick CsI(Tl) detector crystal, uniformly illuminated by 140 keV incident photons has increased considerably for detector crystals having very small cross-section. However, these data should be interpreted with caution, since the effect that these low energy deposits will have in skewing the light spread function will be slight.

This marked increase in the number of events occurring in adjacent detector elements will also be affected by the much higher probability of photoelectric absorption accompanied by K_α emission (75%), than Compton scattering (25%), for 140 keV incident photons in CsI(Tl). Although the path length of these 35 keV photons and photoelectrons in CsI(Tl) is very short for 100% absorption (the mean path length of 35 keV photons $\leq 700\ \mu$m, and of photoelectrons $\leq 80\ \mu$m), some proportion of those generated close to the perimeter of the crystal will deposit energy in adjacent crystals through photoelectric absorption. It would therefore be true to say that this increase in probability is partially geometrically dependent, and will scale in proportion to the ratio between perimeter length and detector cross-section. Because of the high ratio of perimeter to cross-sectional area for small crystals, this effect will be considerably greater for crystals less than 3 mm x 3 mm. Despite their low energy, these photons cannot be rejected by pulse height discrimination techniques, and so must be taken into account in any segmented detector crystal design. However, compared with Compton scatter their weighting effect giving rise to reconstruction errors is small, and can effectively be neglected.

5.4 The GUERAP V Optical Monte Carlo

The optical Monte Carlo simulation package known as GUERAP V is an optical ray tracing computer program for simulating the transfer of electromagnetic radiation between the surfaces of a physical structure. The principal application of this being to determine through simulation, the sensitivity of a radiation detector to external radiation sources. Designed specifically for use with the present generation of fast personal computers, GUERAP V is an upgrade from the GUERAP User-Friendly Data Input Program Package known as GUFDIPP which was developed at the Daresbury Rutherford Appleton Laboratory (DRAL). The new package offers much greater flexibility than did its predecessor, and has enabled the simulation and comparison of continuous and segmented detector crystals with relative ease.

Because the optical Monte Carlo is only capable of predicting the distribution of optical photons incident upon the photocathode, and the electrostatic performance of the PSPMT remains unknown, results of these simulations cannot be extrapolated to determine the charge distribution which would be observed at the anode wires of the PSPMT. Furthermore, because the techniques used to reconstruct the position of interaction of the incident γ-ray photons finds either the centre of gravity, or the point of maximum intensity of the charge distribution at the anode wires, the range of uncertainty in the reconstructed position will tend to be considerably less than either the FWHM of the light pool at the photocathode, or the FWHM of the photoelectron distribution at the anode.

In addition, at the time these simulations were performed, no available data existed relating to the reflectivity of the DWO131 white TiO_2 loaded epoxy from Ciba Geigy, which is used to optically isolate segmented detector crystal arrays. Therefore when modelling these detector crystals, the choice of surface properties has had be estimated based upon experimental results previously obtained (Bird et al. [15], and Carter et al. [25]). Samples of this material of various thickness have recently been obtained from the manufacturer, and when these results are reported it is expected that more accurate modelling of segmented detector crystal arrays will be performed.

In order that good statistics could be obtained, the GUERAP V optical Monte Carlo simulations described in these sections considered a million rays interacting within the detector crystal. This compares with the actual light yield from a 122 keV γ-ray deposit within a CsI(Tl) detector crystal of a few thousand photons. However, since the light pool from a 1,000,000 photon event will have the same light pool shape at the photocathode as a 1,000 photon event, the simulated spatial distribution of photons within an individual crystal will be similar to that observed by experiment.

5.5 Optical Monte Carlo Models of Detector Crystal Geometry

Monte-Carlo simulations of the optical characteristics of thin, continuous and segmented detector crystal designs have been made using GUERAP V. By performing simulations which consider the detector crystal, its surface finish, the optical coupling layer, and the glass window thickness of the PSPMT, it has been possible to directly compare the performance of a range of detectors viewed by the 3 inch square (R2487), and the 5 inch diameter circular (R3292) tubes from the Hamamatsu family of position-sensitive photomultipliers. These Monte Carlo simulations have, as expected, confirmed that the spread in the spatial distribution of scintillation photons incident upon the photocathode, and hence the size of the emerging photoelectron cloud is a function of crystal design.

A simulation was used to directly compare the optical performance of the R2487 and the R3292 tubes used to view thin continuous, and small segmented detector crystals. The simulation assumed the detector crystal to have a refractive index of 1.79, the optical couplant to have a refractive index of 1.5, and the glass entrance window to have a refractive index of 1.5. Recent measurements have enabled an estimation of the reflectivity of the Millipore paper used to wrap small crystals to be approximately 97% reflecting. Advice from gamma camera manufacturers (Siemens Medical), suggest that optimum light collection from continuous crystal is achieved by roughening the rear, and side surfaces of the crystal, whilst the front surface is highly polished. Previous measurements investigating the surface finish of small segmented crystals suggested that optimum light collection is achieved when the rear surface, and sides are polished, and the top of the crystal is roughened (see Table 5.1). In our simulations, the rear and sides of continuous crystals were therefore assumed to be 97% diffuse reflecting, and 3% absorbing. For segmented crystals, the sides of the crystal were assumed to be 97% specular reflecting, and 3% absorbing, whilst the top of the crystal was assumed to be 97% diffuse reflecting, and 3% absorbing. The interface between the crystal, optical couplant, and the glass entrance window was chosen to be 80% specular transmitting, and 20% specular reflecting in both cases.

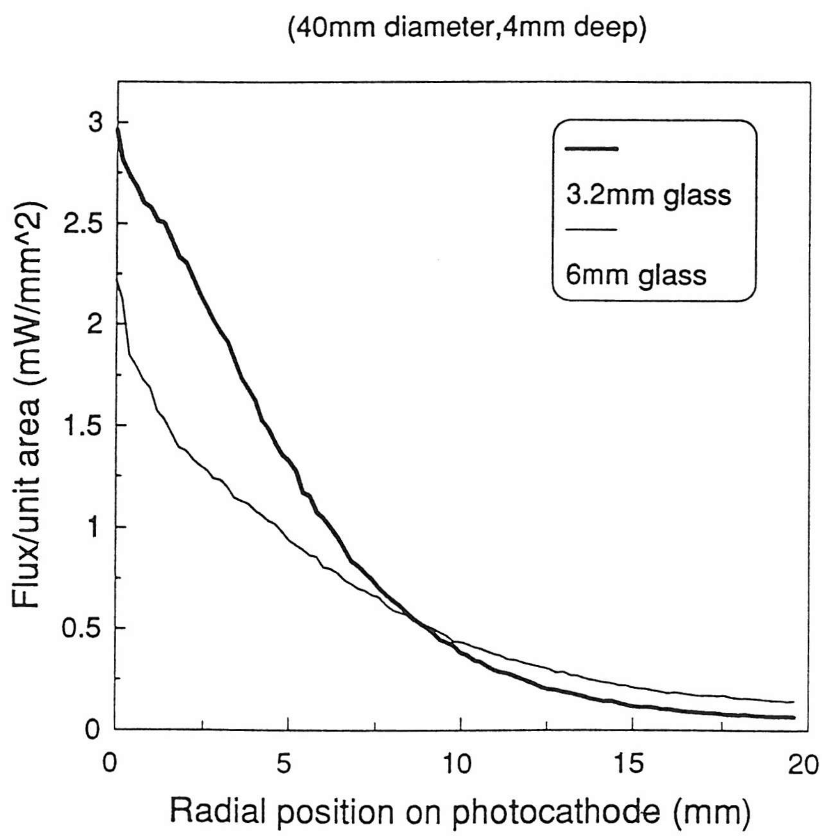

Figure 5.5: *Optical Monte Carlo simulation illustrating the effect of glass window thickness upon light spread when viewing continuous detector crystals*

The results presented in Figure 5.5 suggests that the effect of the entance window upon light spread, when viewing continuous crystals, is quite modest. However, results of simulations presented in Figure 5.8 suggest that the diffuse light spread in the 6.0 mm thick glass window of the R3292 tube accounts for an increase in the FWHM value of the radial photon distribution of approaching 100% and a reduction in the peak photon flux of 64% compared with the thinner 3.2 mm entrance window of the R2487 tube when used to view small segmented detector crystals. We have also compared both continuous and segmented crystals, and demonstrated the effect of crystal dimensions upon light spread. From these simulations it is evident that small, segmented crystals exhibit markedly superior spatial performance when compared with continuous crystals of equal and smaller thickness. In each case, the FWHM of the light pool reaching the photocathode has been estimated (see Figure 5.6).

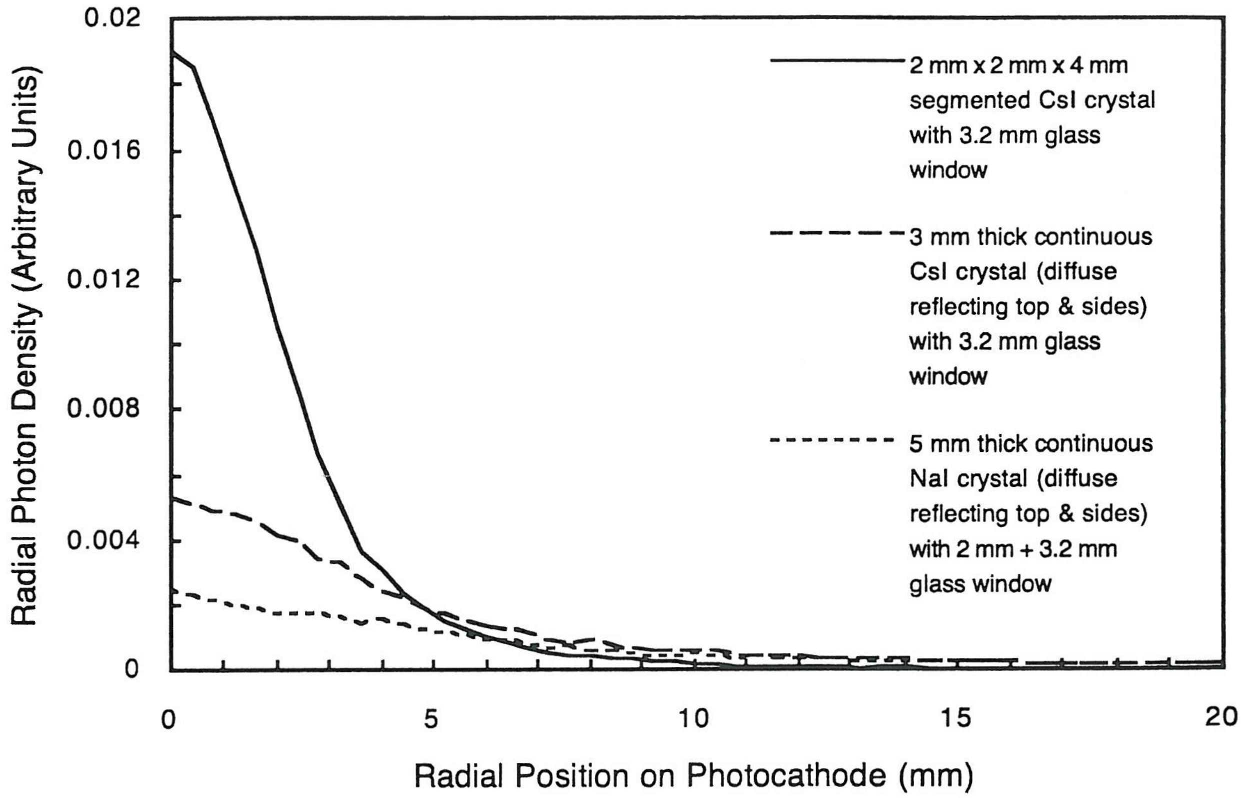

Figure 5.6: *Optical Monte Carlo simulations illustrating the effect of crystal dimensions upon light spread*

Usually, an optical coupling compound with a refractive index between that of the detector crystal and the glass entrance window is chosen in order to maximise the light collection by the photodetector (see Figure 5.7). Here the refractive index of the detector crystal is 1.8, and the refractive index of the glass entrance window is 1.5.

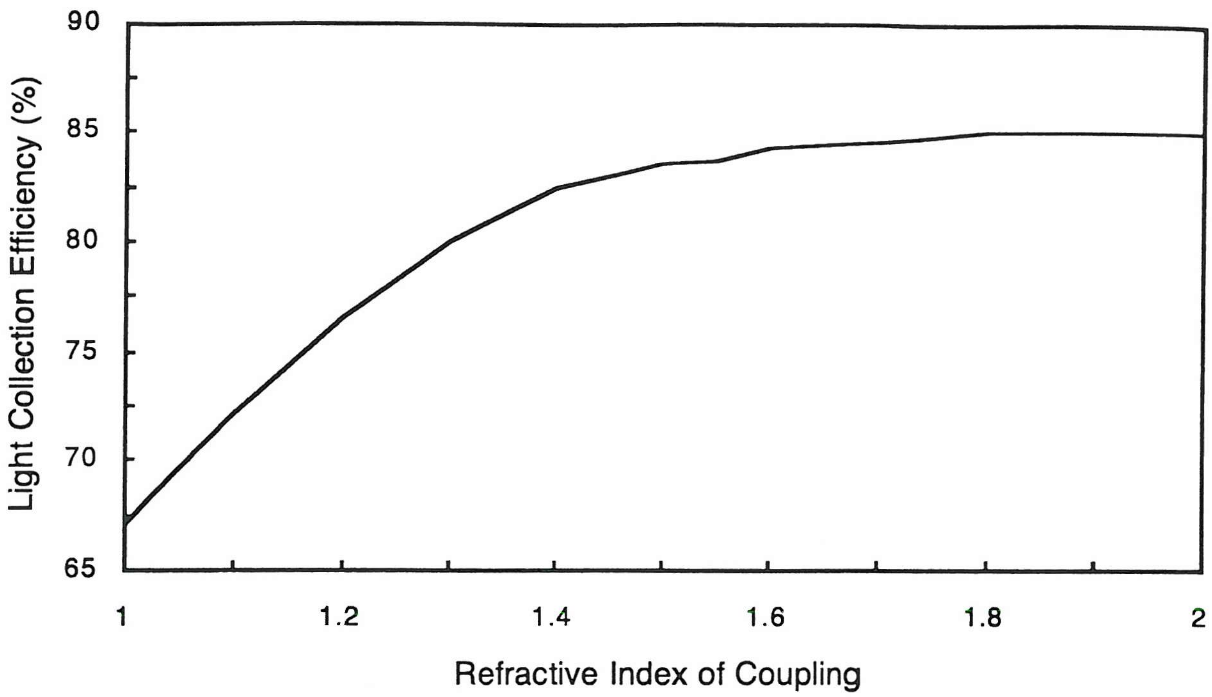

Figure 5.7: *Optimisation of optical coupling compound*

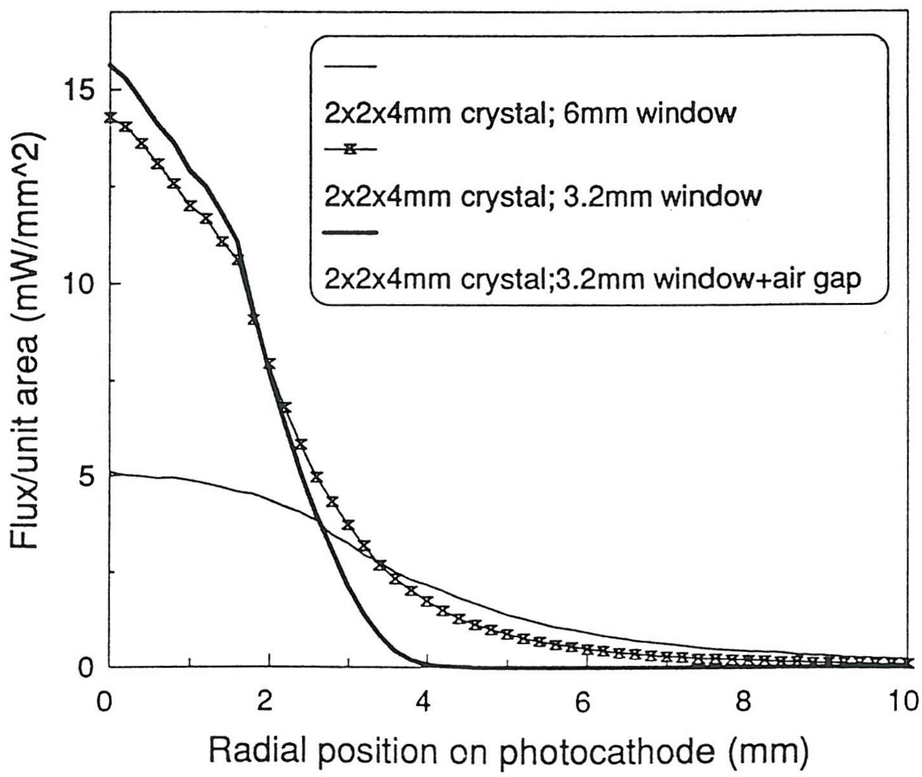

Figure 5.8: *Optical Monte Carlo simulation illustrating the effect of a small air gap upon light spread*

However, a recent development to the Anger Camera has been suggested by Roche et al. [97], which enables improved spatial resolution to be achieved by replacing the optical coupling compound with a small air gap. The effect of introducing a 50 μm air gap between crystal and glass entrance window of the PSPMT is illustrated by Figure 5.8.

The provision of a small air gap between the detector crystal and the entrance window causes the cone of acceptance between the scintillator crystal and the air gap to be greatly reduced, constraining the light spread. The density of the photon flux emerging from the centre of the crystal increases slightly, and the long tail of the light spread function is abruptly cut off when compared with the coupled model described previously. Thus very accurate event location is potentially possible with this method of coupling in a PSPMT. However, despite this increase in flux density, the total emergent flux at the exit aperture is reduced. This is principally due to the smaller solid angle defined by the angle of acceptance between the detector crystal and the air gap, causing the number of photons which become trapped within the crystal to increase. The photon density increases by only a small amount, and any noticeable improvement in position resolution will be correspondingly small, compensating only slightly for the adverse affects caused by the reduction in the light collection efficiency. Subsequent experimental measurement of the reconstructed point spread function yielded by each configuration to incident γ-ray photons of 122 keV proved this to be true, with virtually identical values of FWHM in each case.

We have already discussed in this chapter how in nuclear medicine, the energy resolution is important to enable the rejection of Compton scattered photons from within the patient. Since the light collection efficiency is poorer with this technique, it would offer inferior energy resolution and consequently inferior discrimination of Compton scatter, and is therefore not considered suitable for optically coupling the detector crystal to the PSPMT in a compact gamma camera such as that proposed, or for Anger Cameras for general clinical use in nuclear medicine.

Simulations of a range of segmented crystals were performed to compare the relative optical performance between optically coupled crystals and those where an air gap was maintained between the crystal and the entrance window. The effect of aspect ratio upon total flux at the exit aperture for both cases is presented in Figure 5.9.

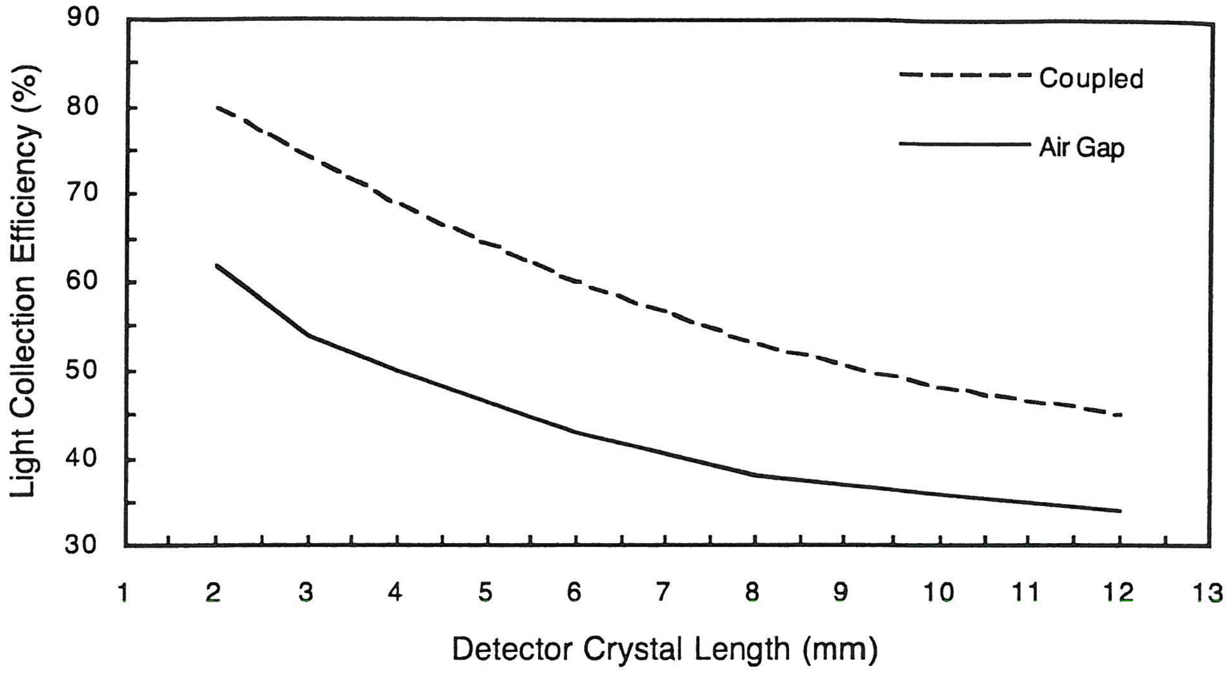

Figure 5.9: *Effect of aspect ratio upon light collection for 2 mm x 2 mm CsI(Tl) crystal*

The decrease in light collection with increasing aspect ratio is principally due to increased absorption at the surfaces of the crystal due to the increased number of reflections before a photon leaves the crystal. However, there will also be increased linear attenuation of reflected photons due to the increase in their mean path within the crystal, and some increase in the trapping of photons at the edges and corners of the crystal.

The effect of surface finish upon the total number of photons collected at the exit aperture has also been investigated both by simulation, and through experiment. For the purpose of this simulation, values of light output for various surface treatments were obtained for small segmented detector crystals having refractive index of 1.8, coupled to a glass entrance window having refractive index of 1.5, using an optical couplant of refractive index 1.48 (see Table 4.4). Experimental values of light output were obtained by optically coupling small CsI(Tl) crystals to silicon PiN photodiodes having sensitive areas of 36 mm^2 (Hamamatsu S2620), and 100 mm^2 (Hamamatsu S3590-01) using BDH DCQ2-3067 optical coupling grease. The output of the photodiode was DC coupled to an Amptek A250 charge-sensitive preamplifier, which in turn was coupled to an EG&G Ortec 570 spectroscopy amplifier with a shaping time of 3 μs. Minor variations between the predicted and measured values of light output is caused by the additional intervening glass entrance window associated with the PSPMT model compared with the combination of scintillator and photodiode used to obtain the measurements presented in Table 5.1. Values presented here have been normalised.

Surface Finish	Light Output By Simulation	Light Output By Experiment
top roughened, sides polished	1.00	1.00 ± 0.01
top and sides roughened	0.90	0.99 ± 0.01
top polished, sides roughened	0.89	0.98 ± 0.01
top and sides polished	0.94	0.95 ± 0.01

Table 5.1: *Effect of surface finish upon light output*

The results of this simulation indicate that the optimum surface finish for detector crystal is when both the sides and the exit face are polished, with the top surfaced roughened. This is confirmed by recent measurements made using photodiodes (Bird et al. [15], and Carter et al. [25]). The method by which segmented detector arrays are fabricated does not usually permit the side surfaces to be polished, and generally in practice it will prove difficult to match the results obtained in the simulation. However, both predicted and measured values of light output for crystals roughened on all sides were higher than expected. It is therefore expected that small segmented CsI(Tl) detector arrays will exhibit high light output.

In addition to the surface finish of the detector crystals themselves, simulations have been performed using GUERAP V to investigate the effect that thin layers of various refractive index materials used to clad individual segments of the detector will have upon the light output. This was necessary in order to determine the effect that both TiO_2 loaded epoxy, having a refractive index of approximately 1.5, and conformal coating materials such as Parylene-C, having a refractive index of approximately 1.64, would have upon the light output of the crystal.

Figure 5.10 illustrates how light output changes as a function of the refractive index of the cladding material. From this it can be seen that the optimum light output is achieved for cladding which has a refractive index of between 1.5 and 1.6 for CsI(Tl). Since the refractive index of the TiO_2 loaded epoxy used to optically isolate individual segments of the detector array is approximately 1.5, the value obtained in this simulation confirms this isolation compound to be very well matched to the scintillation material being used.

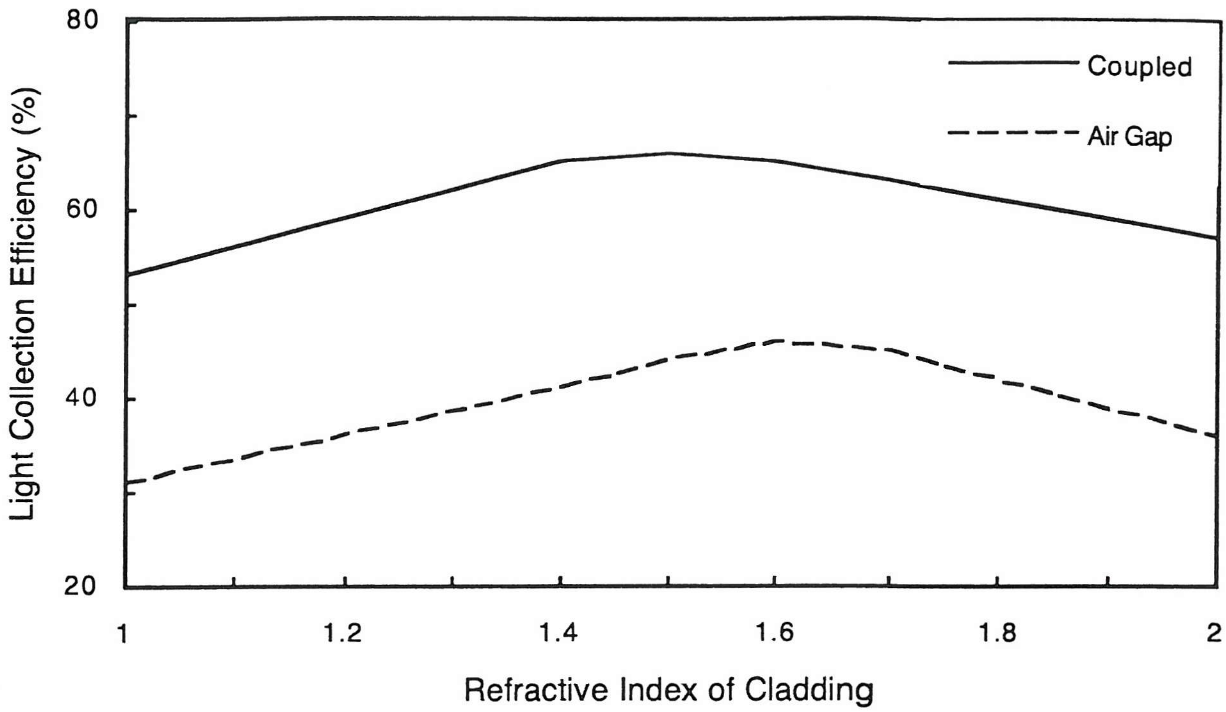

Figure 5.10: *Effect of cladding upon light output for a 2 mm x 2 mm CsI(Tl) crystal*

Subsequent measurements of a range of segmented detector crystals have generally demonstrated good agreement with the predictions of these simulated data, with detectors which yielded increased light spread in the simulations also exhibiting poorer spatial resolution experimentally. It was found that when viewing segmented detector arrays having a pitch as large as 3.5 mm, adjacent crystals could not be spatially resolved with the R3292 PSPMT.

5.6 Conclusions & Future Work

Gamma-ray Monte Carlo simulations were performed using GEANT 3 to determine the optimum crystal size for this application. Figure 5.2 illustrates that a 4 mm thick CsI(Tl) detector crystal yields adequate detection efficiency (75%) for 140 keV incident photons, whilst crystals with aspect ratios less than 2:1 have been shown to yield excellent light output. The results presented in Figure 5.3 illustrate that segmented detector arrays which have scintillation crystal dimensions of approximately 2 mm x 2 mm x 4 mm, exhibits a low multiple bar interaction probability due to Compton scatter at 140 keV. These simulations confirm the results obtained from previous measurements discussed in Chapter 4, that a detector crystal geometry of 2 mm x 2 mm x 4 mm represents an excellent compromise for nuclear medicine applications at energies less than 160 keV.

Previous results presented by Bird et al. [16], have demonstrated that the charge distribution at the anode of the PSPMT can be localised by reducing the radial distribution of photons incident upon the photocathode. This work also demonstrates that the anode signal can be locally increased by a corresponding increase in the radial photon flux density emerging from the scintillator. Therefore, if the optical performance of the detector crystal bonded to the entrance window of the PSPMT can be simulated, it will be possible to determine an optimised configuration for applications in nuclear medicine.

Optical Monte Carlo simulations have therefore been performed in order that the spatial and energy resolution can be optimised by reducing the width of the light-spread function emerging from the detector crystal. Since the electrostatic performance of the PSPMT cannot be easily described, the effect of modifications to the light spread function upon spatial resolution cannot be predicted by Monte Carlo simulations such as GUERAP V. Therefore, the spatial resolution for each scintillation crystal configuration must be quantitatively determined by conducting experimental measurements. The outcome of each simulation can therefore only be considered to provide information from which the relative performance of each detector configuration can be compared.

The simulated results presented in this chapter have provided comparative information of a number of detector crystal designs from which it is possible to predict the radial flux density at the photocathode. These simulations confirm our observations that the radial photon flux density, and the localisation of the photon flux emerging from the detector crystal, are both improved by the application of segmented detector crystal arrays. In addition, we have demonstrated that the glass windows used to encapsulate hygroscopic continuous crystals, together with the thickness of the glass entrance window can contribute to significantly broaden the light-spread function at the photocathode.

These simulated data can be compared with the measured point spread functions for various detectors described in Chapter 4. These simulations, combined with the results presented in Chapter 4, as expected confirm that detectors which yield a more confined light-spread function also yield improved spatial resolution. However, further work to calibrate the simulated data against values of the point spread function of various detector crystal geometries measured through experiment remains to be performed, which would enable GUERAP V to become a considerably more effective tool for the design of detectors for γ-ray imaging.

Chapter 6

Preliminary Trials of a Compact Gamma Camera

6.1 Introduction

This chapter considers the development and trials of a new range of compact γ-cameras based upon the PSPMT for both new and existing applications in clinical nuclear medicine. Preliminary trials have been performed using three basic configurations of camera, and measurements have been made of the performance characteristics of each.

6.2 Clinical Applications of a Compact Gamma Camera

The development of the three gamma cameras presented in this chapter was stimulated by recently proposed new applications for nuclear mammography, intraoperative nuclear medicine, and for imaging the thyroid gland.

Following lung cancer, breast cancer is the leading cause of cancer related death with approximately one in nine women developing the disease. Screening for primary breast cancer is currently performed by methods which include breast self-examination and breast-compression mammography. There are now data to support the opinion that the detection and diagnosis of breast cancer at an early stage will improve mortality and disease free interval. Currently, the most effective method of detecting the early stages of breast cancer is using mammography. However, whilst mammography is a sensitive imaging modality for detecting occult breast cancer, it has low specificity, and confirmation of an abnormality is usually achieved either through biopsy, or by fine needle aspiration (Parker et al. [88], and Sickle [113]). Recently, data published by

Anderson et al., has suggested that the routine use of mammography only results in a 30% reduction in breast cancer mortality in women over 50 years of age [2].

This disturbingly low figure is principally dependent upon factors which affect the image. The range of reported sensitivity for mammography varies between 55% and 94%, whilst the range of reported specificity varies between 88% and 99%, with the positive predictive value varying between 10% and 35%. The false negative rate varies between 25% and 50%, being lower in patients aged 50 or over (Schmidt [105]). Therefore, whilst mammography is currently the gold standard in the early detection of breast cancer it does have limitations, and nuclear medicine imaging techniques are currently being evaluated to assess if they can contribute to improvements in the early detection of breast cancer (Thompson et al. [122]).

Thallium (^{201}Tl) was first reported as a potential cancer imaging agent in 1976 (Cox et al. [30]), where uptake in a bronchial carcinoma was reported. In 1978, two patients with breast cancer were shown to have uptake of Thallium in the primary tumours (Hisada et al. [56]). The largest evaluation of this technique in the evaluation of patients with breast cancer was by Waxman et al. [130], who evaluated 81 patients with palpable breast masses, using Thallium γ-ray scintigraphy. This population was compared with 30 volunteers who had no palpable breast abnormalities. Ninety-six percent of 44 patients with palpable breast cancers were shown to have abnormal Thallium uptake at the site of the tumour. By contrast, no benign breast abnormalities showed Thallium uptake. However, ^{201}Tl is not an ideal imaging agent, with considerable attenuation of activity, and loss of resolution.

Technetium (^{99m}Tc) Sestamibi was originally introduced as a myocardial perfusion imaging agent. Because of similarities to Thallium it also has been evaluated as a tumour imaging agent. Recently, Khalkhali et al. [66], have reported a study in which 59 patients with either abnormal mammograms or palpable masses, were imaged prior to breast biopsy or fine needle aspiration biopsy. In 39 benign breast lesions in this population, no increased uptake of Sestamibi was noted. In 23 patients with subsequently confirmed breast cancer, the scintigrams were positive. Five false positive scans were obtained in patients with benign breast lesions. In this preliminary study the sensitivity of the technique was 96% and the specificity 87%. Importantly, the positive predictive value was 82% and the negative predictive value 97%. This study clearly demonstrates the feasibility of using radiopharmaceuticals to image patients with breast cancer.

The limitation of diagnosis as presently performed using planar imaging is the relatively modest spatial resolution that can be achieved, with sensitivity for the detection of malignant masses increasing significantly for lesions over 1.5 cm in diameter. Unfortunately, the limited spatial resolution offered by the conventional camera of approximately 5 mm FWHM contributes significantly to this very poor resolution.

Therefore, a camera is required which has a field-of-view between 40 cm^2 and 200 cm^2, which could be easily integrated within a standard breast-compression mammography unit. It is envisaged that these cameras might be used in pairs, either with or without coincidence, and possibly with a degree of compression, as a nuclear mammography device which is capable of offering millimetric spatial resolution. The technical feasibility of this concept has been facilitated by the invention in the last decade of the PSPMT from Hamamatsu. Several prototype systems based upon these tubes are already in the process of being developed by various groups around the world. This new imaging technology has potential advantages for imaging the breast over conventional scintigraphic methods in both spatial resolution, and more importantly, in the ability to isolate volumes of high activity within a region of interest from background interference. This will improve both the sensitivity and quantitative nature of this imaging modality for this particular application.

Results have been published by various authors demonstrating the 3 inch diameter circular PSPMT to offer sub-millimetric intrinsic spatial resolution for scintigraphy (Barone et al. [10], and Pani et al. [86, 87]). However, a sub-millimetric collimator would clearly also be required in order to achieve this level of spatial resolution in a clinical camera. Results of more recent work with the Hamamatsu 3 inch square PSPMT has suggested that both the energy resolution, and the sensitivity of a clinical gamma camera can be better preserved by accepting a more modest spatial resolution (Bird et al. [16], and Truman et al. [125]).

Clinical applications have recently been identified where an extremely compact, high resolution camera might be of value for performing intraoperative nuclear medicine studies. Since the region of interest is typically less than 1 cm^2 in area, a camera which offers a small field-of-view combined with high spatial resolution might facilitate the identification of multiple lesions. The completeness of the surgical excision could be confirmed *in vivo* to ensure the maximum volume of healthy tissue is preserved. Small gamma cameras based upon the PSPMT have been proposed by several authors (Chen et al. [27], Redus et al. [95], and Yasillo et al. [137, 138]), whilst other authors have proposed beta cameras based upon the same technology for performing similar studies (Carswell [24], Daghighian [31], and Tornai et al. [123]). Further applications for this technology have been proposed for small animal PET studies in veterinary nuclear medicine (Siegel et al. [114]).

It is envisaged that preliminary trials of first-generation compact gamma cameras based upon the PSPMT might enable the imaging the thyroid gland with improved spatial resolution over the conventional Anger Camera and pin-hole collimator. By moving the camera closer to the patient, reducing the distance between the source and the detector, an improvement in the overall resolution can be realised whilst at the same time increasing the count rate at the detector. A number of thyroid phantom sources were available in the laboratory, and have been used to examine the performance of three prototype compact gamma cameras based upon the PSPMT.

6.3 Images Obtained with a Segmented Detector

A small gamma camera based upon a Hamamatsu 3 inch square R2487 position-sensitive photomultiplier tube (PSPMT) with conventional readout has been developed for a range of possible clinical applications. This camera exhibits a field-of-view of approximately 40 cm^2 and complements the conventional Anger Camera. Measurements of segmented detector arrays viewed by this photodetector were presented in Chapter 4, and were shown to offer both improved spatial resolution and improved position linearity, due to the localisation of the light-spread function, and an increase in the radial photon flux density. We have advanced the argument that a reduction in the spatial resolution to approximately 2 mm can offer considerable advantages for nuclear medicine applications. Therefore, a two-dimensional segmented scintillation crystal array comprising 676 detector elements, each measuring 2 mm x 2 mm x 4 mm, was chosen. This configuration enabled excellent spatial resolution to be achieved, whilst preserving adequate the energy resolution. In addition, this choice of crystal thickness provided an acceptable compromise between light collection efficiency and the sensitivity of the camera for the detection of some of the most commonly used radionuclides in nuclear medicine. Localisation of the incident γ-rays was provided by modifying a low energy general purpose (LEGP) parallel multi-hole collimator such as that used in a conventional clinical Anger Camera with each hole measuring less than 2 mm in diameter, to match the dimensions of the camera housing (see Figure 6.1).

Clearly, for sources located close to the camera, the combined spatial resolution due to the intrinsic geometrical effects of both the detector crystal and the collimator will be limited to approximately 2 mm at the photodetector. Whilst the position resolution of the reconstructed image cannot be improved beyond this value, it has been shown in earlier chapters that the statistical uncertainty in reconstructing an event within an element will also be affected by the Poisson statistics of the photoelectrons as they emerge from the photocathode.

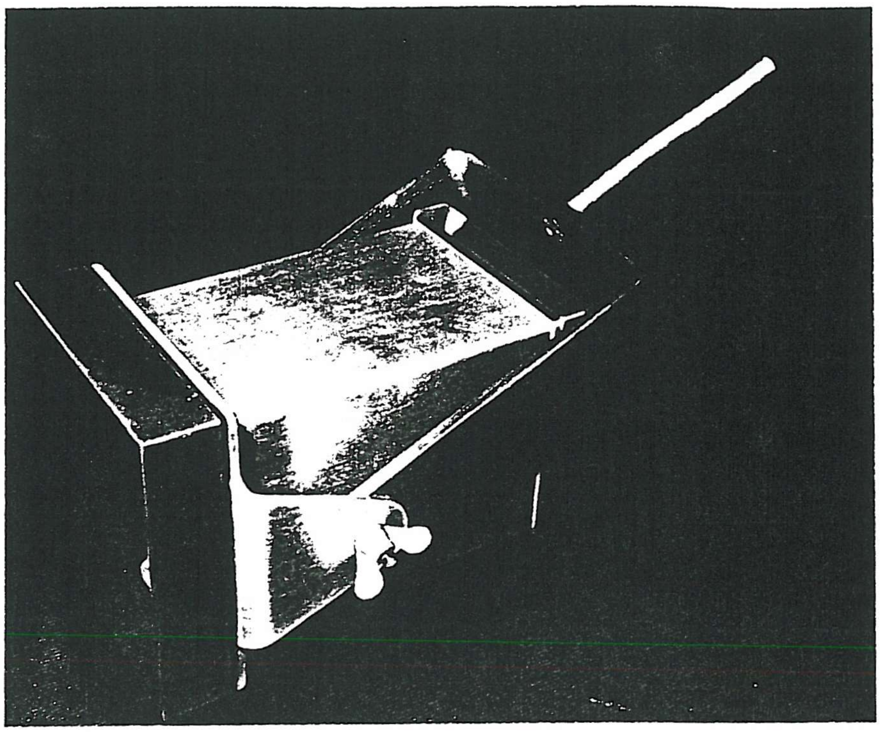

Figure 6.1: *The compact gamma camera*

Previous measurements have demonstrated this dependence upon incident energy, and for arrays of 2 mm x 2 mm x 4 mm detectors has been shown to be better than 1.5 mm FWHM at 122 keV. The intrinsic spatial resolution of the R2487 PSPMT measured with a 1 mm diameter laser spot is specified by the manufacturer to be 0.3 mm FWHM. Initial test images similar in morphology to those expected in clinical studies have been obtained by using the camera to view a 122 keV (^{57}Co) thyroid phantom source.

The raw image of the thyroid contrast phantom source presented in Figure 6.2 has a considerably pixellated appearance due to the segmentation of the detector crystal, which causes the response function of the camera to vary as a function of position. In effect, we are able to resolve the gaps between the reconstructed point-spread functions from adjacent individual elements from which the detector array is comprised. From this result, have identified that the potential spatial resolution of this camera configuration is excellent, with the reconstructed point-spread functions lying well within the elemental crystal dimensions. In addition, we can clearly delineate regions of high and low activity in the phantom, with very few background counts being reconstructed in the image, and the image appears relatively uniform, despite the source having filled the field-of-view. However, in practice the clinical community would undoubtedly prefer a smoother appearance to the images presented by this camera configuration.

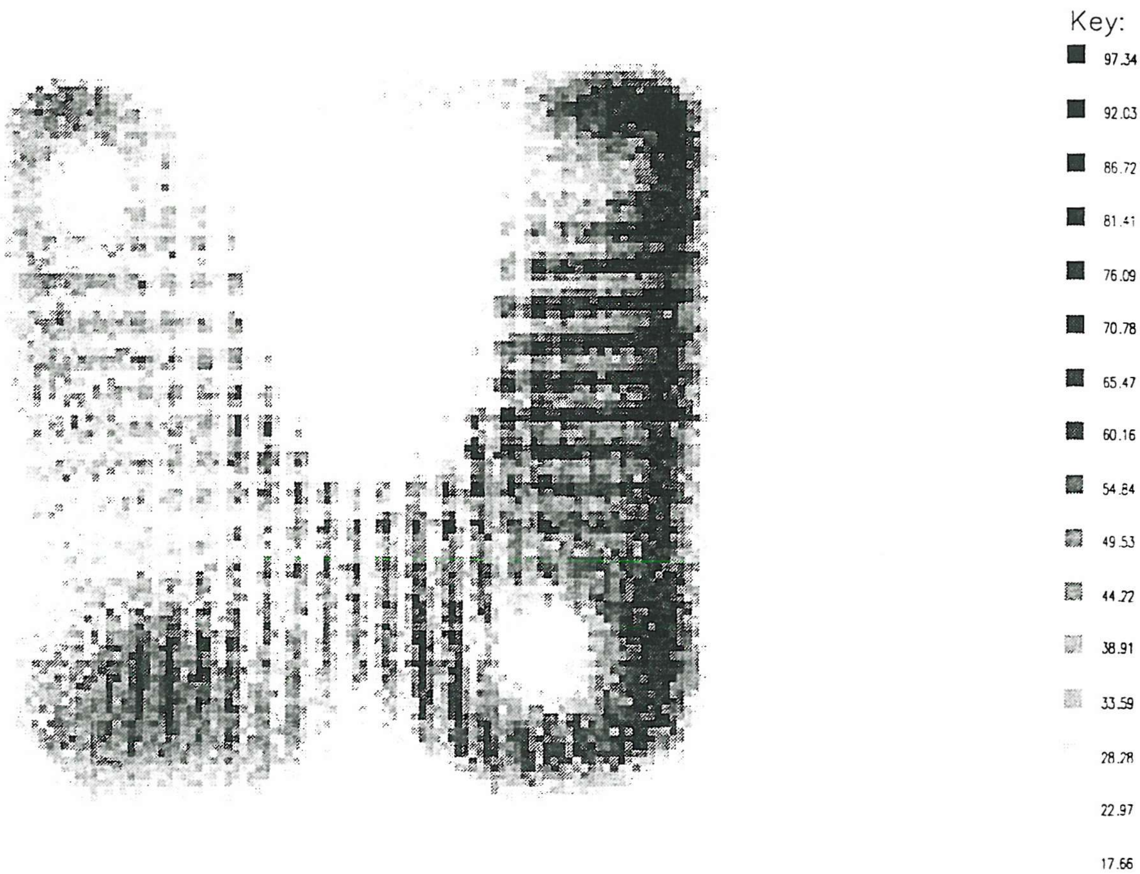

Figure 6.2: *Segmented CsI(Tl) detector used to view a thyroid phantom source*

In order to achieve a smoother image, the image could of course be rebinned such that there is a direct correlation between each image pixel, and the crystal pixel that it represents. Alternatively, both the size of each element, and the gaps between adjacent elements could be reduced until the reconstructed point-spread function from each element overlaps with that of its neighbour. Inevitably this would result in a compromise between the sensitivity, energy resolution, and spatial resolution of the camera. Another solution would be to computationally convolve each reconstructed point-spread function with a gaussian which is broader than the crystal pitch. This has been performed, and is presented for a simulated auroral image in the following chapter. It is hoped that it will be possible to complete clinical trials of the camera in the Department of Nuclear Medicine at the UCL Middlesex Hospital, to enable a more complete assessment of the benefit that this camera can offer as a diagnostic instrument.

6.4 Images Obtained with a Continuous Detector

The gamma camera discussed in section 6.3 was modified slightly in order to compare the performance of the 3 inch square PSPMT used to view a continuous NaI(Tl) detector crystal. Here, the segmented scintillation crystal array used previously has been replaced with a continuous 5 mm thick NaI(Tl) detector crystal that has been mechanically encapsulated in an aluminium housing, painted on the inside using diffuse reflecting white paint, with a 2 mm thick glass window. The collimator and readout technique employed previously have once again been used.

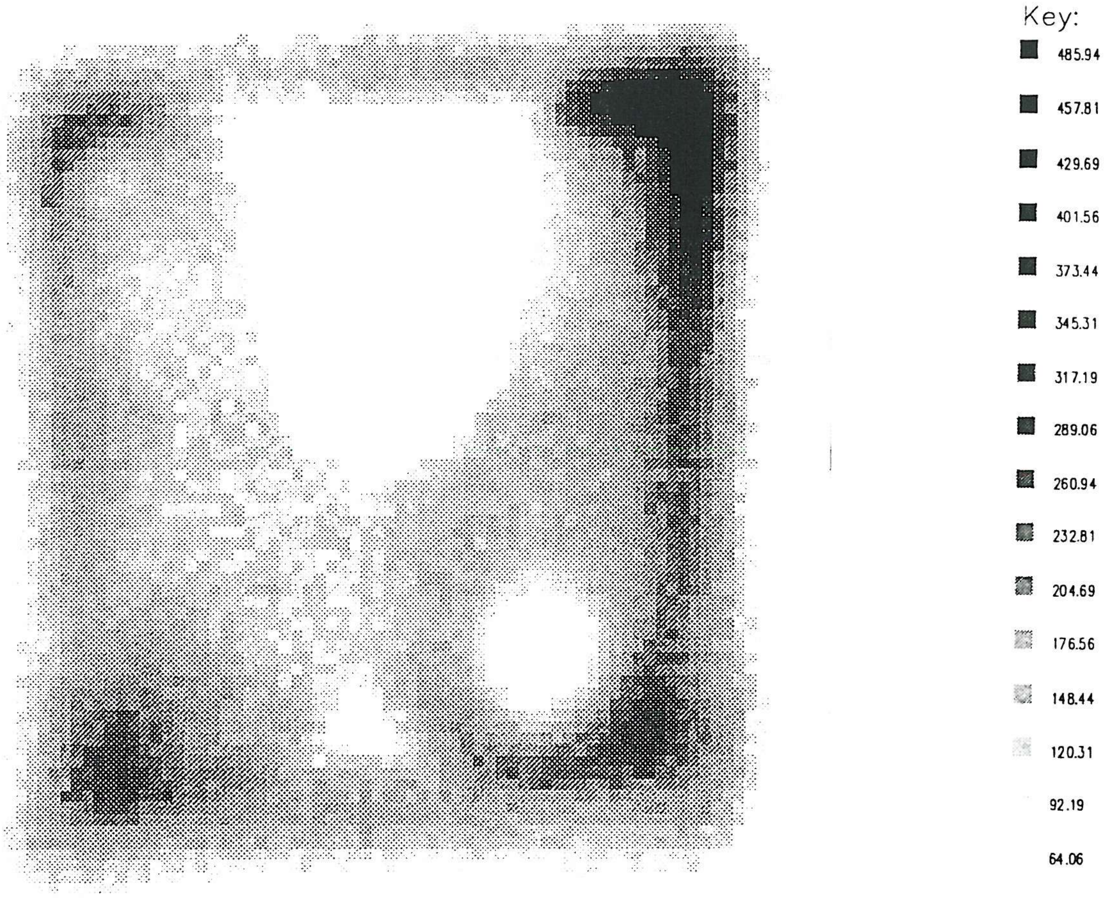

Figure 6.3: *Continuous NaI(Tl) detector used to view a thyroid phantom source*

Measurements have been made that demonstrate the imaging performance of this camera configuration used to view a 122 keV (^{57}Co) thyroid phantom source (see Figure 6.3). Whilst the raw image obtained using this detector crystal is considerably smoother than that achieved in the previous section, this is at the expense of poorer spatial resolution of only 2.7 mm FWHM, and considerable light spread within the crystal.

Unfortunately, this increased light spread has caused unwanted artifacts to be present towards the edge of the field-of-view, and despite more counts having been detected during the 10 minute exposure, the delineation of features present within the region of interest was qualitatively observed to have decreased significantly from the image acquired with the segmented detector crystal array. Although the fractional sensitivity has increased, the image quality has been degraded by edge effects in the crystal.

6.5 Trials of a 5 in. Diameter PSPMT and Continuous Detector

The two cameras discussed previously had a sensitive area of 65 mm x 65 mm which was determined by the linear region of the 3 inch square PSPMT. Whilst for some clinical applications this is adequate, the images presented in the preceding sections clearly demonstrate evidence of distortion towards the edge of the field-of-view. This has occurred because the region of interest exceeds the field-of-view, with the resultant *cropping* leading to a squaring of the thyroid phantom image. In order to overcome this problem for applications such as imaging the thyroid gland, either a diverging collimator could be used, or alternatively a larger PSPMT could be used. In order to determine the imaging performance of a compact camera having a position-sensitive field-of-view of almost 80 cm^2, the performance of the larger 5 inch diameter circular R3292 PSPMT from Hamamatsu has been investigated.

Because of its high light yield, a continuous CsI(Na) detector crystal of equal diameter to the PSPMT was chosen for this camera. The relatively high density of this material compared with that of NaI(Tl), has led to a reduction in the light-spread function by using a crystal measuring only 3 mm thick (see Figure 6.6). By employing a continuous detector crystal, both the fractional sensitivity, and useful area can be increased compared with the segmented camera configuration presented in the previous section. The light collection efficiency of the camera was optimised by polishing the front surface, whilst roughening both the rear surface and edges of the crystal. A thick fibrous white paper known as Tyvek was used to provide a reflective backing for the crystal, whilst black tape was used at the edges of the crystal in order to reduce unwanted edge effects. After this preparation, the detector crystal was directly coupled to the glass entrance window of the tube using an optical coupling compound of intermediate refractive index. Finally, the combination of scintillator and PSPMT was placed inside a camera housing constructed from 4 mm thick lead sheet, and the collimator positioned in front of the detector crystal. Both the camera and all associated signal processing electronics were then mounted on an arm which allowed six degrees of freedom. The arm was itself mounted on a trolley carrying all the necessary electronics.

Tests were carried out in order to determine the count-rate response of the camera as a function of source activity. Different volumes of ^{99m}Tc were placed in nine separate vials, and the activity of each source normalized using a standard sample against which the decay of each was calculated as a function of time. Each vial was subsequently placed in turn at the same position in the centre of the camera, and an energy window was used to select the full-energy peak of the sample from the pulse-height spectra obtained.

As the source activity increases, the acquisition time will decrease considerably, and the systematic errors due to inaccurate measurements will increase. In order that these could be reduced to within ± 0.5% for all sources, a large sample size of 30,000 counts was acquired under the photopeak for each measurement, and the time taken to acquire the data was measured using a stop-watch. The time was then recorded for each sample, and from the normalized value of activity that we had calculated, and the time taken to acquire the data, the normalized count-rate response could be determined. It can be seen from Figure 6.4 that the maximum effective count-rate that can be achieved with this system in practice is approximately 175 counts per second, and it is evident that certain count-rate losses exist which are adversely affecting the performance of this camera.

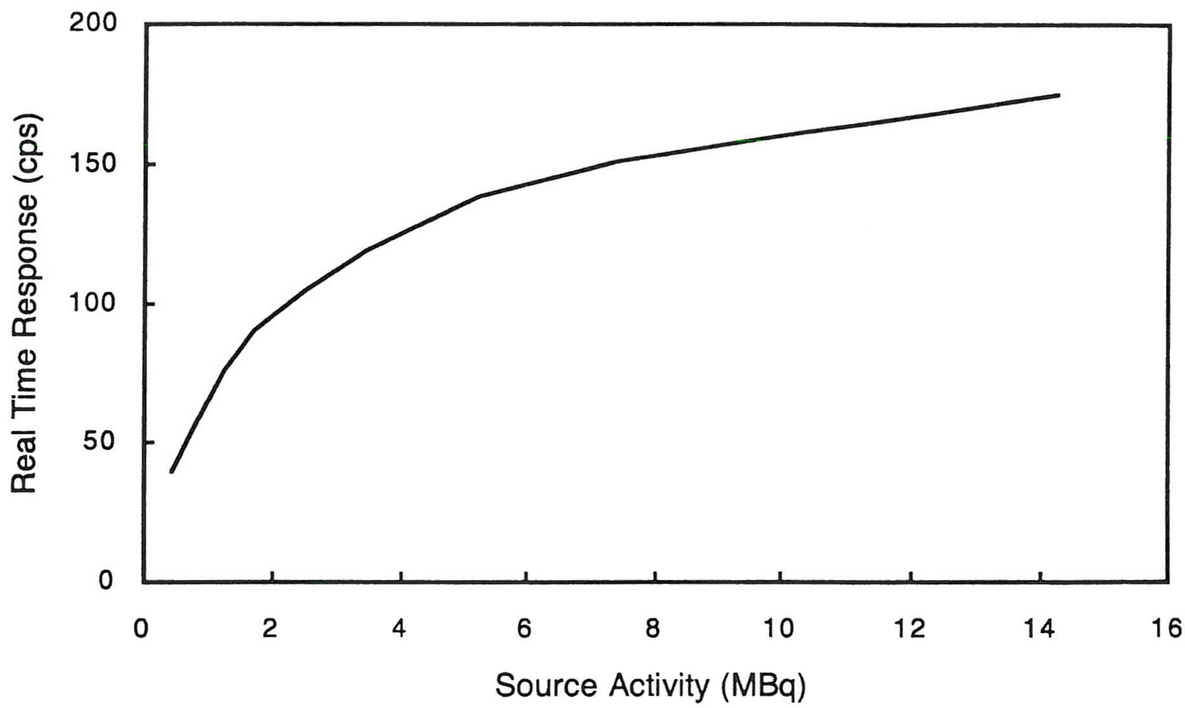

Figure 6.4: *Count-rate response of camera in real time*

These count-rate losses could be due to *pulse pile-up* occurring when two incident γ-rays deposit their energy within the detector crystal, and the scintillation light produced is temporally unresolvable. Their combined energy therefore exceeds that defined by the energy window, and so both events are rejected. If pulse pile-up is occurring, it will obviously take considerably longer to acquire the 30,000 counts, and so the real time count-rate will decrease accordingly leading to increased dead-time. For pulse pile-up to occur, two γ-rays must be detected within the 630 ns decay time of the scintillator, and will increase significantly for source activities greater than 1.6 MBq.

Since the point at which the count-rate response of the camera becomes non-linear begins at approximately 1.6 MBq, we needed further confirmation that pulse pile-up was the cause of the non-linear performance of our gamma camera. We obtained an energy spectrum with the energy window removed, and found evidence of pulse pile-up to the right of the photopeak which increased as a function of source activity. However, we have observed additional count-rate losses which are associated with the time taken to write the data to the hard-disk of the computer. The higher the activity of the source, the more events are recorded within a unit of time which in turn increases the frequency with which data is written to the hard-disk. As the time spent writing data to the hard-disk increases, the time spent acquiring the data reduces, with the result that dead-time increases. The time to write the data to the hard-disk has been estimated to be approximately 30 μs, and it is envisaged that this problem could be at least partially resolved if not completely eliminated by employing a more efficient data storage subroutine that buffers the acquired data in memory before writing to the hard-disk on a less frequent basis.

Variations in the sensitivity of the photocathode as a function of position produces an energy response function that is non-uniform. This problem is endemic in the Hamamatsu PSPMT, and in order to predict the potential imaging performance of the camera, the pulse-height response of the camera was investigated as a function of source position.

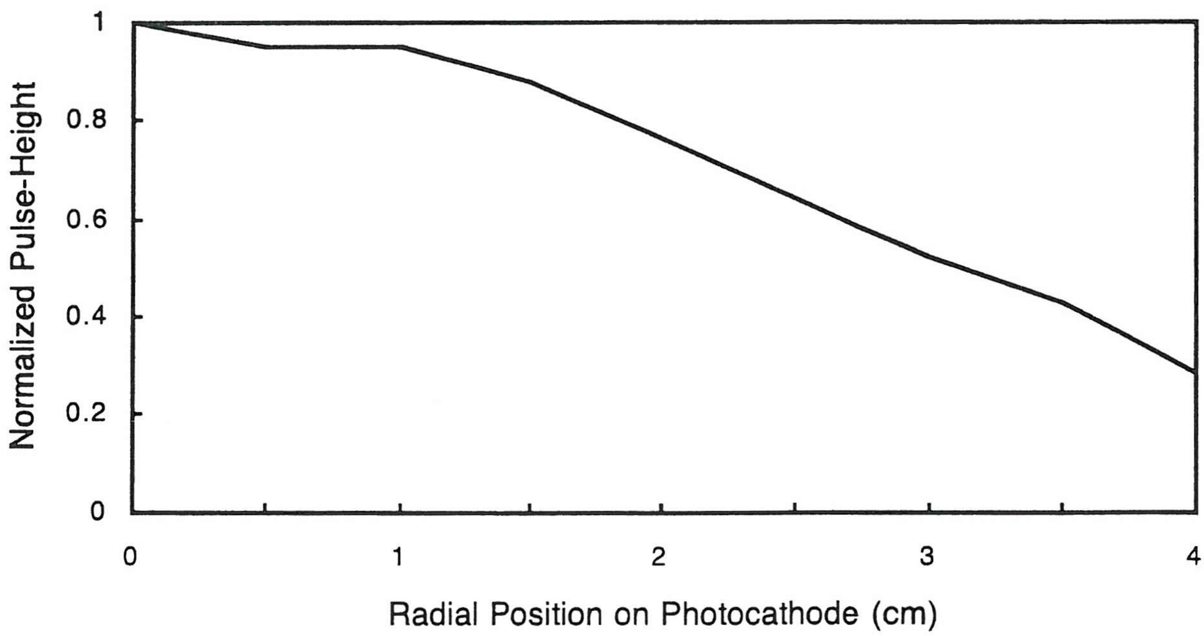

Figure 6.5: *Energy response as a function of radial position*

The energy response of the camera has been investigated by moving a 1 MBq ^{99m}Tc point source in steps of 5 mm between the centre and the edge of the effective field-of-view. Measurements of the pulse-height, and energy resolution were recorded at each position, and the pulse-height of each energy spectrum was then normalized against the maximum value which was obtained (see Figure 6.5). This variation in energy response would have the effect of grossly broadening the energy spectrum obtained from extended sources within the field-of-view, preventing the effective use pulse-height discrimination to reject γ-rays that have undergone internal Compton scatter within the patient. Photons which have Compton scattered would therefore be accepted as valid events, increasing the number of background counts present in the image. However, accurate mapping of the energy response at every position within the field-of-view of the camera would enable a correction factor to be applied to each photon stopped by the detector, and the electronic signal derived from that location normalized. A thorough treatment of this technique has been previously presented by various authors (He [53], Yasillo et al. [136]). In order to further examine the response characteristics of the gamma camera, a ^{57}Co (122 keV) point source was located at the centre of the field-of-view, and both position and energy spectra were acquired (see Figure 6.6).

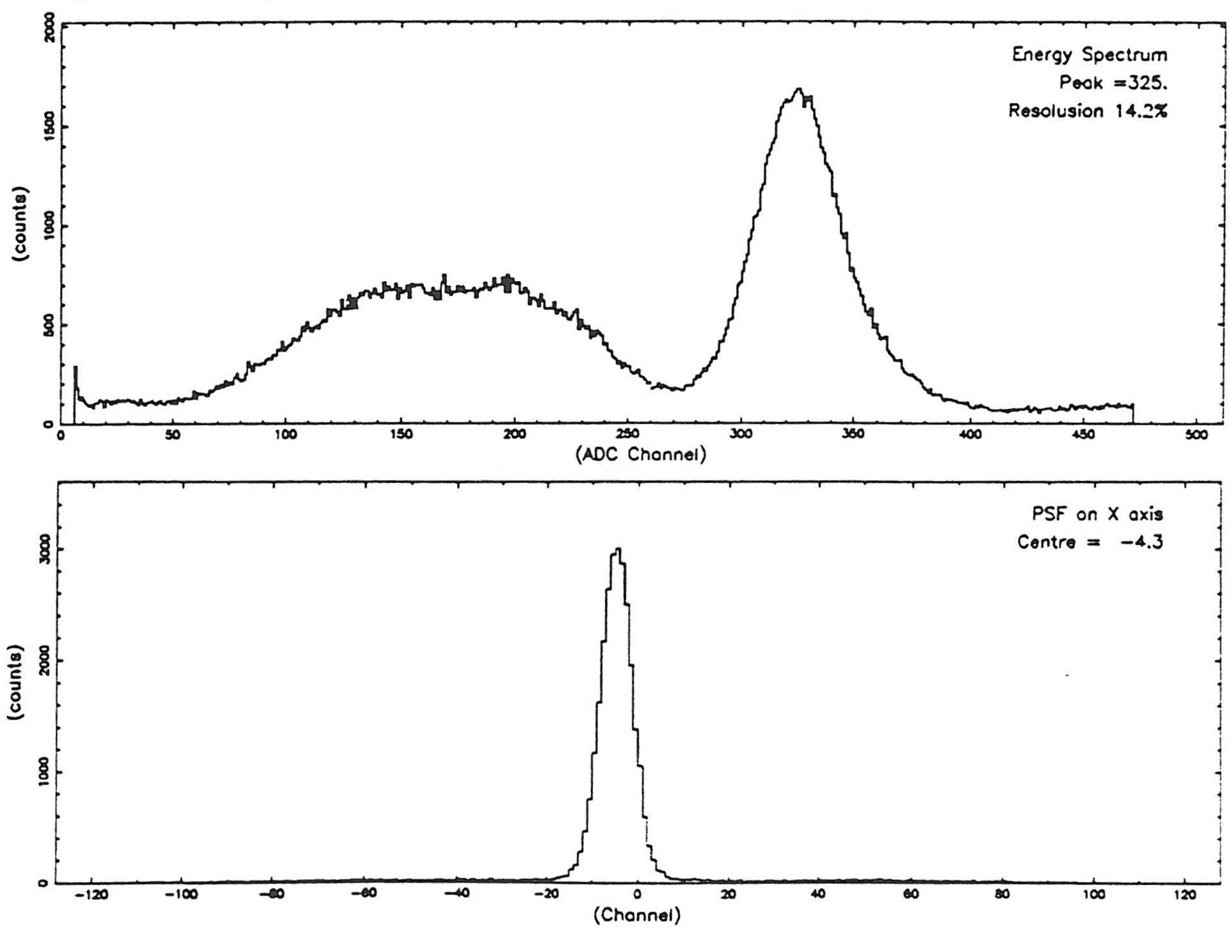

Figure 6.6: *Position and energy spectra of R3292 PSPMT viewing a 3 mm thick CsI(Na) image plate illuminated by 122 keV (^{57}Co)*

The spatial resolution of our camera was found to be 2.9 mm FWHM, and the energy resolution was 14.2% FWHM. These measurements demonstrate that a modest improvement in the spatial resolution has been achieved by reducing the depth of the detector crystal. However, further improvements in the spatial resolution would require some sensitivity to be sacrificed.

Of significance to the imaging performance of our camera system is the relationship between the severity of the spectral broadening of the photopeak due to the photocathode non-uniformity, and the position non-linearity of the PSPMT due to the centroiding algorithm. The cause of spatial non-linearity in the PSPMT was discussed in Chapter 4, and is the result of events towards the edge of the sensitive area of the tube being incorrectly reconstructed away from the point of interaction, and shifted slightly towards the centre of the tube, and occurs for two very different reasons. Firstly, the crossed wire anodes at the bottom of the tube do not extend as far as the edge of the glass envelope, thus limiting the ability to fully sample the charge at the periphery of the tube. This is the reason why the effective sensitive area of the 5 inch diameter PSPMT is quoted by the manufacturer as being only 100 mm in diameter. In addition to this, the constraining physical boundary of the scintillation crystal produces an asymetric distortion of the light-spread function from a γ-ray interaction at the edge of a continuous detector. Whilst the position of the γ-ray interaction in the crystal corresponds with the peak in the light-spread function, the reconstructed position of interaction will be different since the centroid of this non-symmetric light-spread function will not correspond with the peak.

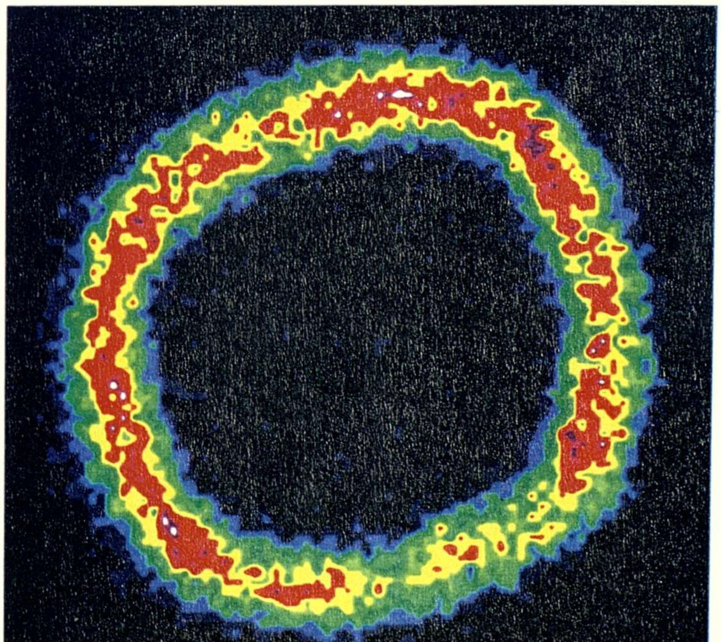

Figure 6.7: *Image of an extended ^{57}Co source without pulse-height discrimination*

The combination of position non-linearity together with the gain variation across the sensitive area of the tube presents considerable problems for imaging applications. If pulse-height discrimination cannot be used due to the severe broadening of the photopeak described earlier, events will be accepted from the whole of the tube's sensitive area. Events at the very edge of the tube will then be incorrectly centroided towards the centre of the tube where they will be binned together with genuine events from that position on the tube. The result for a uniform extended source is an annulus of activity at several times the level of events binned in the centre of the image (see Figure 6.7). This annulus of activity which was accepted by the data acquisition system clearly demonstrates the problem of the non-linear spatial response of the PSPMT for imaging applications where any detail present at the centre of the image is effectively lost. The application of an energy correction would offer the advantage of a uniform energy response as a function of radial position, but the position non-linearity causing the events to pile up would remain a problem. Whilst this may be solved by applying a position correction such as that proposed by Fessler et al. [39], an alternative and much simpler solution is to physically exclude the photons from reaching the non-linear region of the photodetector. A detector crystal might be chosen whose physical dimensions exactly match the 80 mm diameter central linear region of the tube. However, the edge effects due to the incorrect centroiding of the light-spread function would remain.

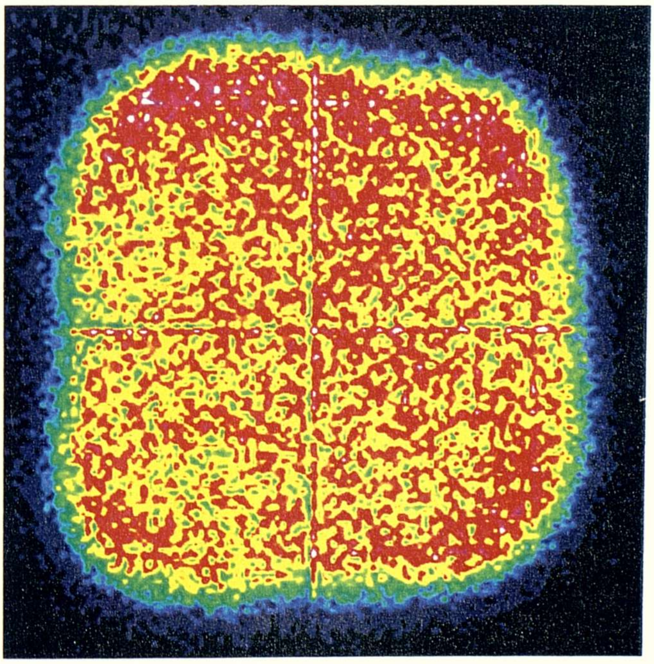

Figure 6.8: *Image of an extended ^{57}Co source without pulse-height discrimination*

It was therefore decided that an annular black acetate mask having an inner diameter of 80 mm, and an outer diameter of 130 mm should be placed between the detector crystal and the entrance window of the PSPMT. A second mask having the same dimensions was placed between the detector crystal and the collimator, and the edges of the crystal were once again masked using black tape. In order to reduce the number of γ-rays that interact in this region of the detector crystal, a 5 mm thick annular lead mask of the same dimensions was constructed and placed in front of the collimator. The previous test was once again repeated to qualitatively determine the degree of improvement provided by this modification (see Figure 6.8). This image confirms that the combination of masks described earlier is preventing photons from reaching the photocathode in the non-linear region of the tube offering improved position-linearity. However, whilst the imaging performance of the camera was improved by this modification, the pulse-height was also observed to have been reduced as a function of radial position. The energy response illustrated by Figure 6.5 was therefore degraded through a combination of poorer photon counting statistics, and the non-uniformity of the photocathode towards the edge of the tube. The light output was estimated to have been reduced by approximately 15% at the centre, and approximately 66% at the edge of the 80 mm diameter field-of-view, contributing significantly to the overall reduction in pulse-height observed.

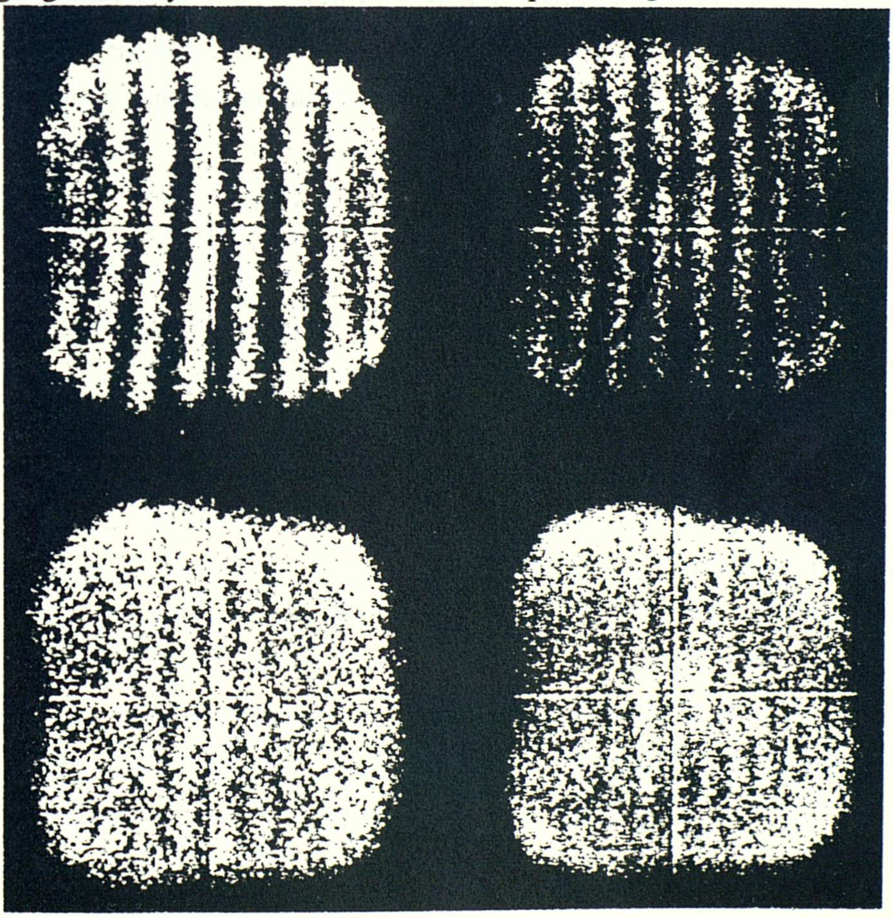

Figure 6.9: *Transmission phantom images of 4 mm, 3.5 mm, 3 mm, and 2.5 mm bars*

In order to evaluate the imaging performance of the modified camera, a number of tests were performed using sources of a variety of geometries. A transmission bar phantom has been used to make a qualitative assessment of both the spatial resolution, and the position linearity of the camera. The phantom has four segments, each containing a pattern of multiple lead bars of a certain width and bar separation encased within plastic. Each segment has bars and bar separations of 4 mm, 3.5 mm, 3 mm, and 2.5 mm respectively. The phantom was placed directly above the camera, and uniformly illuminated with an 18 MBq ^{99m}Tc flood source. The result of this test is illustrated in Figure 6.9 where it can be seen that each segment of the phantom can be clearly resolved. However, there is a considerable amount of blurring present in these images which is believed to be due to having positioned the extended source too close to the bar phantom. Since it was not possible to suspend the source above the camera, the source was placed in intimate contact with the transmission phantom as a matter of convenience. This was obviously not ideal, and is believed to have given rise to blurring in the image due to geometrical effects and some septal penetration. In addition, this result demonstrates that the problems relating to position non-linearity which were previously apparent have been almost completely eliminated, and the bars themselves appear very parallel in the image, confirming that the spatial linearity of the camera is within acceptable limits. However, there are some observable artifacts in these images which are believed to be due to the way in which the reconstructed position of each individual event is determined by the centroiding algorithm.

In addition to these measurements, another transmission phantom has been used to qualitatively estimate the imaging performance of the camera for the detection of small regions of activity within the field-of-view. A thick lead plate has been drilled with an array of holes having diameters of 4 mm, 3 mm, 2.5 mm, 2 mm, 1.5 mm, and 1 mm, with hole spacings between centres of 20 mm, 16 mm, 14 mm, 12 mm, 10 mm, and 8 mm respectively. Since the array of holes have been grouped together by size, each of the six segments have been viewed in turn by our camera. Since previous results demonstrated that the black annular mask alone was adequately preventing photons from reaching the photocathode and distorting the image, the lead annular mask was not considered to be necessary for these measurements. The phantom has been uniformly illuminated from behind using an 18 MBq extended ^{99m}Tc flood source placed in front of the camera in the same manner as before, and then exposed for between 18 and 45 minutes depending upon the hole size. This exposure time permitted between 30 and 50 counts per pixel to be acquired depending upon the size of the apertures being viewed. This series of images demonstrates the excellent resolution that has been achieved at each hole size and hole separation (see Figure 6.10).

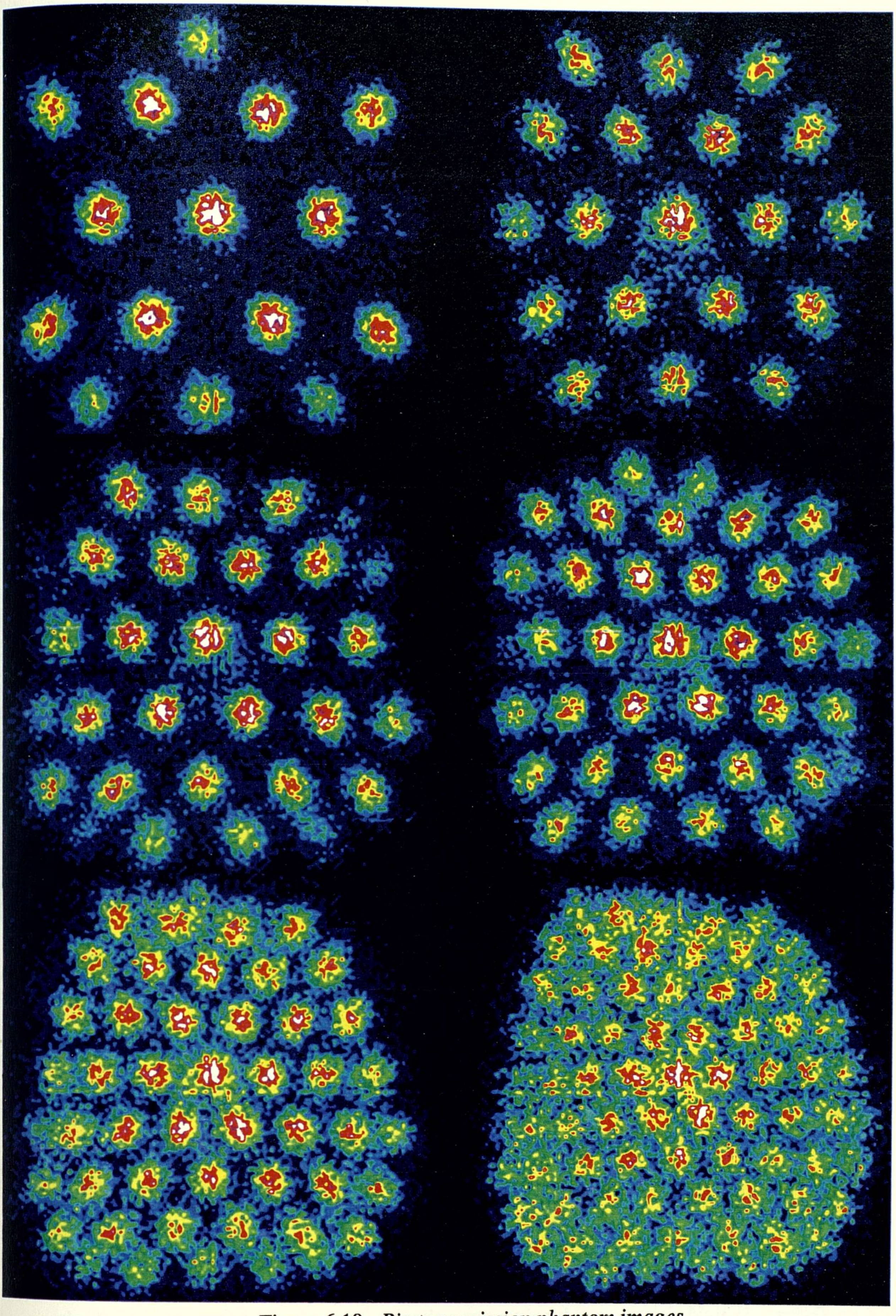

Figure 6.10: *Pie transmission phantom images*

Once again there is the problem of having located the source too close to the transmission phantom which has undoubtedly caused the number of background counts present in each of these images to have increased. The excellent position linearity demonstrated by this modified camera configuration is once again confirmed. In order to overcome the problem of unwanted background counts associated with both types of transmission phantom used previously, the response of the camera was further investigated by placing seven capillary line sources within the field-of-view. Each capillary was filled with ^{99m}Tc and placed in front of the camera at intervals of 10 mm. The resulting image obtained has enabled both a qualitative and a quantitative assessment of the imaging performance of the gamma camera, and its comparison with a conventional clinical gamma camera (see Figure 6.11).

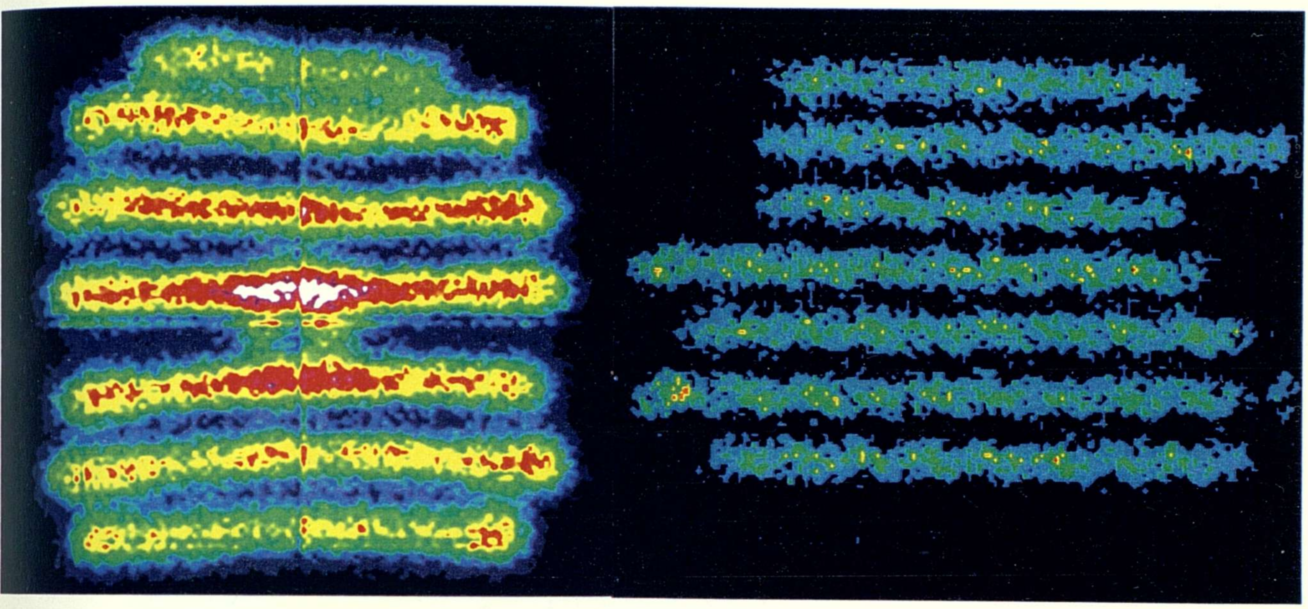

Figure 6.11: *Images obtained with the PSPMT based camera and an Anger Camera*

The most noticeable feature of this image is the reduction in background counts which tended to blur the image in the case of the transmission bar phantom. This increased signal-to-noise ratio has enabled a quantitative estimation of the spatial resolution. The width of the line-spread function has been calculated by considering the profile of both the 3rd and 4th line sources from the top of the image, and was determined to be approximately 5 mm FWHM. Clearly this figure has been influenced by the relatively broad line-width of the sources themselves, since the intrinsic position resolution of a similar camera employing a mechanically encapsulated 3 mm thick NaI(Tl) crystal with

3.5 mm thick glass window coupled to this PSPMT, illuminated with a ^{57}Co (122 keV) point source has previously been determined by He et al. to be 4.0 mm FWHM [51]. However, whilst relatively modest, this value of position resolution is consistent with that which is currently achievable from commercially available clinical gamma cameras.

Finally, tests have been performed using a source similar in morphology to the thyroid gland. The camera has been used to image a ^{57}Co (122 keV) thyroid contrast phantom of similar dimensions to that observed in clinical studies of the thyroid gland. The total activity of the phantom is approximately 3.6 MBq, and consists of two lobes each containing hot regions representing higher uptake, and cold regions representing lesions or tumours within the thyroid gland. The camera must be able to distinguish between these regions with adequate contrast to identify abnormality. Images have been acquired with our camera with excellent and encouraging results (see Figure 6.12).

Figure 6.12: *Image of a thyroid contrast phantom*

The quality of this raw and uncorrected image is really very good, with surprisingly little observable distortion due to either position non-linearity, or the non-uniformity of the energy response. Some of the events in the *hot* left-hand lobe have been shifted slightly towards the left of the image. The hot and cold regions in the image are very clear indeed which is obviously an important test for a clinical camera. The encouraging quality of these results should however be moderated by a cautionary note, since clearly in a clinical study the number of background counts present in the image will be considerably higher than was the case for the phantom image here. Obviously, if both the energy and position responses were to be mapped, this image could be further improved and corrected by rebinning the events to their correct positions. This has been the subject of work by previous authors (Fessler et al. [39], and He et al. [51]).

6.6 Conclusions and Future Work

Clearly, the results of the preliminary trials of the three gamma cameras described in this section are extremely encouraging. Images have been acquired which undoubtedly demonstrates the potential that these small cameras have for a range of nuclear medicine applications. More work remains to be done in improving the data acquisition system as we have identified in the text, and the application of both energy and position correction through the application of a lookup table would be extremely useful for a clinical version of these cameras. Some advantages are offered by the segmentation of the detector crystal, whilst more work needs to be performed to reduce the undesirable segmentation present in the image. This might be performed after the data has been acquired by rebinning the data, or through more careful selection of the detector crystal.

A recent development from Hamamatsu is the very small R5900-00-C8 PSPMT encased within a metal enclosure measuring only 28 mm x 28 mm x 20 mm, having a sensitive area of only 23 mm x 21 mm, and a glass window thickness of only 1.2 mm. This extremely small tube offers the possibility of constructing a camera having very modest dimensions for new applications in intraoperative nuclear medicine. However, possibly the most important implication of these results for future applications in clinical nuclear medicine will be the increasing pressure that is building to develop a compact gamma camera for scintimammography.

The excellent collaboration that has existed between the University of Southampton, Department of Physics, and the UCL Middlesex Hospital, School of Nuclear Medicine, would be the perfect vehicle to take this exciting work forward into a clinical trials phase, and then towards a compact gamma scintimammography, or intraoperative imaging system.

Chapter 7

A Prototype Auroral X-Ray Imager

7.1 Imaging Auroral X-Rays

This chapter considers a design for an auroral x-ray imager which will form part of the Auroral Imaging Observatory (AURIO), selected for inclusion within the payload complement of ENVISAT II. The imager will be located on a polar orbiting platform at an altitude of 800 km. Previous studies have shown that the auroral x-ray spectrum extends from a few keV to more than 200 keV, and the current proposal for AURIO envisages the use of two complementary instruments in order to provide efficient coverage for this wide range of energies [7, 8]. The first of these detectors, AURIX-L, is a position-sensitive multiwire gas-proportional counter that is designed to detect x-rays below 10 keV. The second detector, AURIX-H, comprises several position-sensitive scintillation counters based upon the position-sensitive photomultiplier tube (PSPMT) from Hamamatsu, whose imaging characteristics have been demonstrated in both earlier chapters, and by previous work (Bird et al. [13, 16] and He et al. [51]).

7.2 A PSPMT Based Auroral X-Ray Imager

We have investigated the possibility of reducing the low-energy detection threshold of AURIX-H through the careful design of the scintillator crystal and the application of a different readout electronics technique. Previous tests made using a single small crystal and multiwire readout suggested that the low energy threshold could be reduced to significantly below 6 keV (Bird et al. [16]). Such a development could potentially avoid the requirement for two separate AURIX instruments, and offer a corresponding increase in the sensitivity at all energies within the existing payload allocation for the combination of these two instruments.

7.3 Experimental Setup

A pinhole camera has been designed to operate in the range 2 keV to 200 keV, based upon the 3 inch square position-sensitive photomultiplier (PSPMT), and has been used to view a two-dimensional segmented CsI(Tl) scintillation crystal. This camera has been used to generate extended test images by rotating two radioactive sources of different energies in the field-of-view. The optical characteristics of the system have been simulated using a Monte-Carlo package in order to optimise the detector crystal geometry. The detector performance has also been investigated experimentally as a function of crystal dimensions, and measurements made using different readout techniques are presented.

Results have been obtained using an adjustable aperture pinhole collimator together with a 676-element two-dimensional segmented CsI(Tl) crystal array viewed by a Hamamatsu R2487, 3 inch square PSPMT. Test images are presented which illustrate the detector performance at 122 keV (^{57}Co), and at 60 keV (^{241}Am). The effectiveness of readout techniques based upon conventional resistive charge-division, and the multi-channel readout methods discussed in Chapter 4, which use gaussian-fitting and peak-finding algorithms to determine the event location will be compared. A suitably extended test source was generated by rotating two 5 mm diameter radioactive sources in the field-of-view of the pinhole camera (see Figure 7.1). This provided a test scene similar to that which might be expected from an auroral arc.

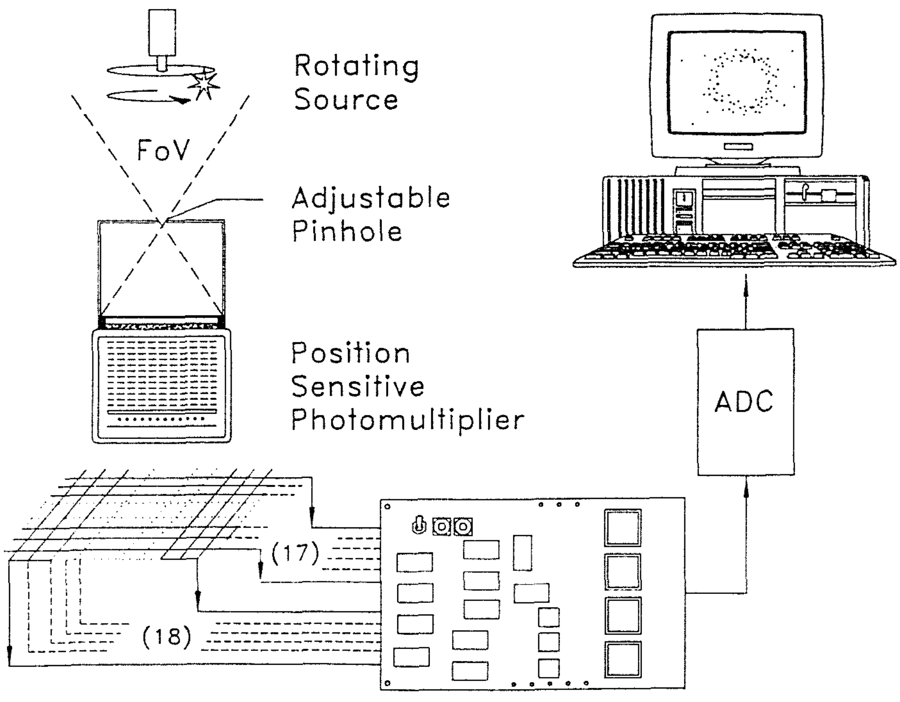

Figure 7.1: *Arrangement of rotating x-ray source and imager*

7.4 Detector Crystal Design

Since the auroral x-ray spectrum is very steep at low energies (see Figure 7.2), it is particularly important to arrive at an optimum detector crystal design in order to be able to use a scintillation counter for imaging at these unusually low energies.

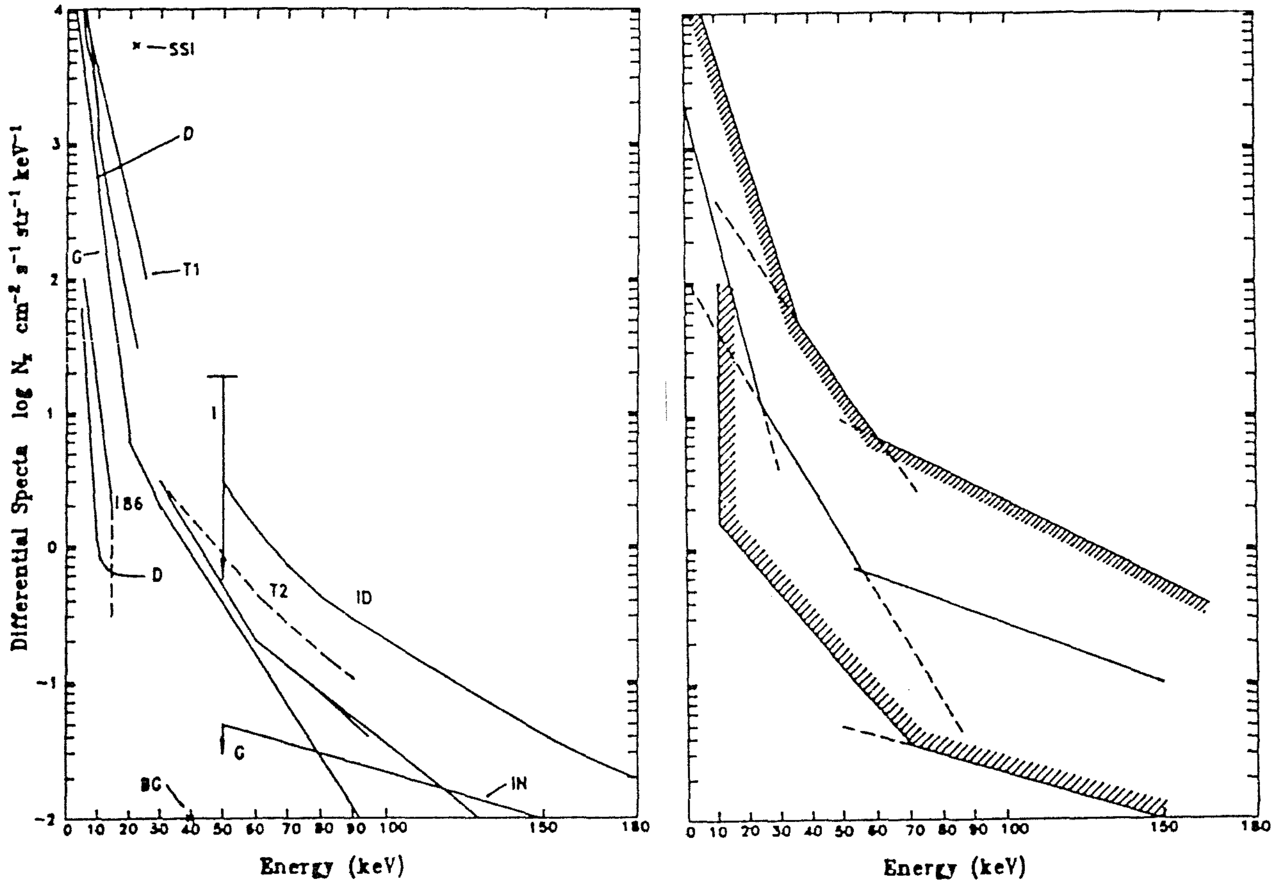

Figure 7.2: *A compilation of available auroral x-ray spectra*

This objective might be achieved if one could localize the spread of the scintillation photons within the detector crystal, thus reducing the width of the PSF, increasing the photon flux density, and consequently the SNR of the photodetector response. This subsequent increase in the photon flux density incident upon the photocathode is expected to yield improved Poisson statistics and correspondingly superior spatial resolution.

Previous measurements made using arrays of small CsI(Tl) scintillator crystals that are optically isolated using white TiO_2 loaded epoxy have shown significant advantages over the use of continuous crystals, especially when optimum light collection is required for low energy x-ray detection and a broad band of incident energies is envisaged (Bird et al. [16], and Truman et al. [124]).

7.5 Readout System

In Chapter 4, we have already identified that the method used to read out the charge from the crossed-wire anodes of the PSPMT is also important in optimising the performance of the PSPMT for use at low energies. In order to determine the most suitable readout for this particular application, we have compared the conventional resistive charge-division method, together with a VLSI multi-channel charge readout technique.

Conventional readout methods use a resistor chain to divide the charge collected by each anode wire and a simple interpolating algorithm is then used to reconstruct the position of the interaction in the detector (Bird et al. [13, 16], and He et al. [51]). One problem associated with this readout technique is that the crossed-wire anodes accept the dark current from the whole of the photocathode, reducing the signal-to-noise ratio from the tube. This causes the lowest energy deposit in the scintillator which can be detected by the photodetector to increase, and we believe causes a disproportionate weighting of uncertainty in the reconstructed position towards the edge of the tube's sensitive area.

Multiwire readout techniques rely upon the ability to directly sample the charge deposited upon individual anode wires. Earlier work has suggested that the charge contribution due to dark current with this technique would approximate to the line integral of the dark current from a smaller region of the photocathode which corresponds to the wire being sampled. Indeed, preliminary tests with such a readout system indicated the low energy threshold to be below 6 keV whilst at the same time providing better position linearity across an extended sensitive area of the tube (Bird et al. [16]).

The tests reported here were made using the HX-2 VLSI multi-channel charge-integrating amplifier designed by DRAL. In order to investigate the proof of principle of such a development, a simple system comprising four HX-2 16 channel amplifier chips, together with the timing circuitry and decoding logic, were mounted on a prototype test board. The synchronous integration of the deposited charge is assured through a presetable integration time extending from 5 μs to 100ms, with the integrated charge being read out from each chip sequentially. Due to the speed of our existing data acquisition system, for these tests the minimum integration time was restricted to 40 μs. In earlier work, a faster integration time of 15 μs enabled the detection of the 5.9 keV (^{55}Fe) line. Therefore, the low energy threshold that was achievable in these tests was restricted to about 15 keV. This readout system is clearly not ideal, and was used purely for convenience as a valid test of the principles involved.

7.6 The Optical Montecarlo

Monte-Carlo simulations were used to compare the optical characteristics of both thin continuous and segmented scintillator crystals using GUERAP V. These indicated that the spread in the spatial distribution of scintillation photons incident upon the photocathode, and hence the size of the emerging photoelectron cloud might be much better constrained with the use of optically isolated segmented detector crystals (see Figures 7.3(a) and 7.3(b)).

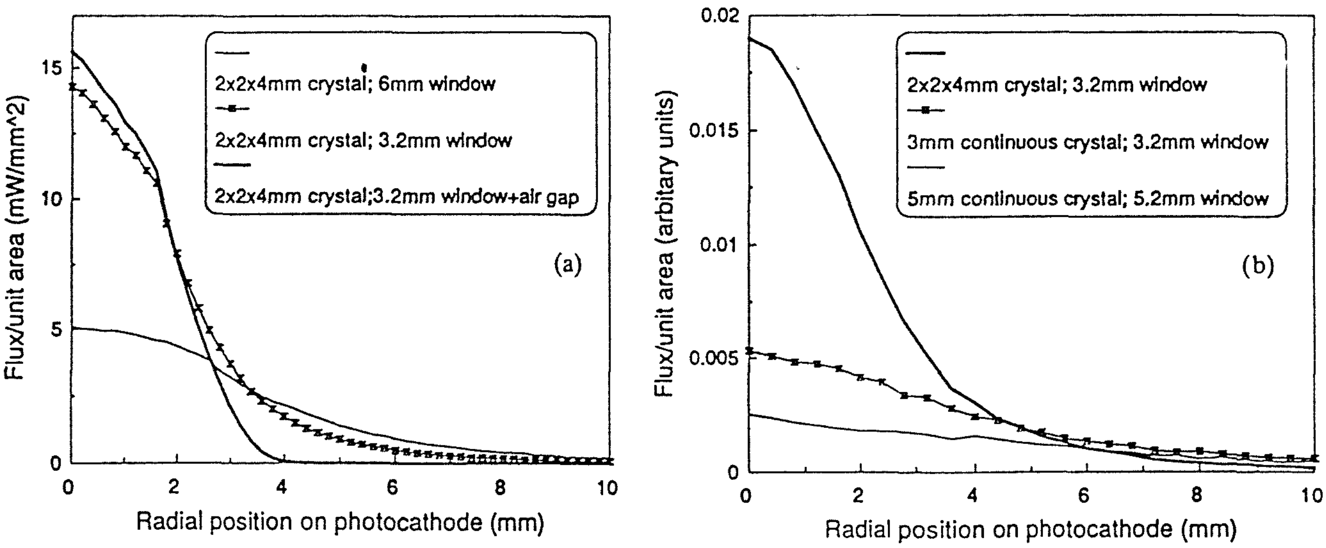

Figure 7.3: *(a) Optical montecarlo simulations illustrating the effect of glass window thickness on light spread. (b) Optical montecarlo simulations illustrating the effect of crystal dimensions on light spread.*

In each case, the FWHM of the light pool reaching the photocathode has been estimated. By running simulations which include the crystal, optical coupling layer, and the glass window of the PSPMT, we have been able to directly compare both the 3 inch square (R2487), and the 5 inch diameter circular (R3292) tubes from the Hamamatsu family of position-sensitive photomultipliers. These simulations suggest that the light spread in the 6.0 mm thick glass window of the R3292 tube accounts for an increase in the FWHM value of the radial photon distribution of approaching 100% and a reduction in the peak photon flux of 60% compared with the thinner 3.2 mm entrance window of the R2487 tube (see Figure 7.3(a)). Indeed, we found that when viewing even the largest segmented array having a pitch of 3.5 mm, adjacent crystals could not be spatially resolved with the R3292 PSPMT due to the effect of increased light spread in the much thicker glass entrance window causing degraded accuracy of the reconstructed point-spread function.

Demonstrated also is the effect of introducing a 50 μm air gap between crystal and glass window. This has the effect of cutting off the long tail of the **PSF** and slightly increases the density of the photon flux at the centre of the crystal, and was first proposed by Roche et al. in 1985 [97]. For imaging auroral x-rays, where accurate event location is desired for incident energies as low as a few keV, this technique could prove useful, but could equally well be applied to nuclear medicine or to the monitoring of contaminated areas within the nuclear industry (He et al. [52], and Redus et al. [96]). We have also compared continuous with segmented crystals, and the effect of crystal dimensions upon light spread. From these simulations it is evident that small, segmented crystals demonstrate superior spatial performance when compared with continuous crystals of equal and reduced thickness (see Figure 7.3(b)).

7.7 Detector Response

Recent measurements, together with earlier work, have used a variety of incident photon energies to illuminate one-dimensional detector arrays of crystals having different sizes and crystal pitches (Truman et al. [124]). These arrays, viewed in turn by the 3 inch square PSPMT, have been read out using both resistive-charge division, and multi-wire readout methods, comparing the response function for each detector at each energy. The results of these measurements for 2 mm and 3 mm crystals, having a crystal separation of 500 μm, when uniformly illuminated by 122 keV photons from a ^{57}Co point source placed several centimetres away, are presented in Figures 7.4 through to 7.7. It is clear from these results that for arrays of small crystals in particular, the peak-to-valley ratio is improved by individually sampling the charge from each anode wire. This in turn improves the accuracy of event location in the reconstructed image.

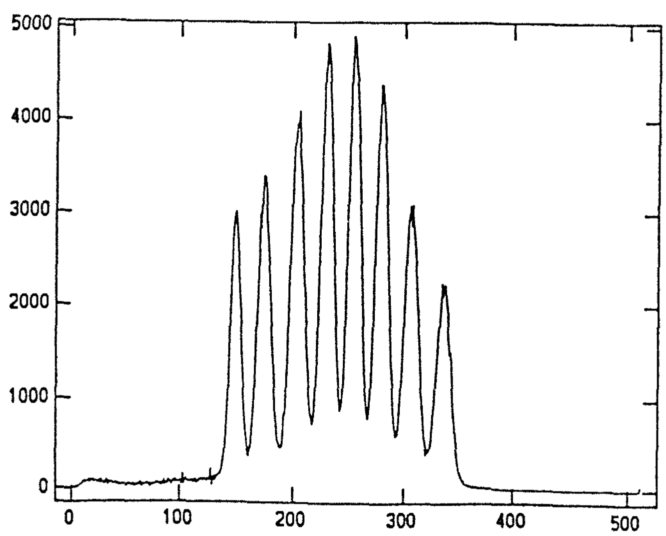

Figure 7.4: *3 mm crystals illuminated by 122 keV (^{57}Co) with conventional readout. Detector response is 2.1 mm FWHM.*

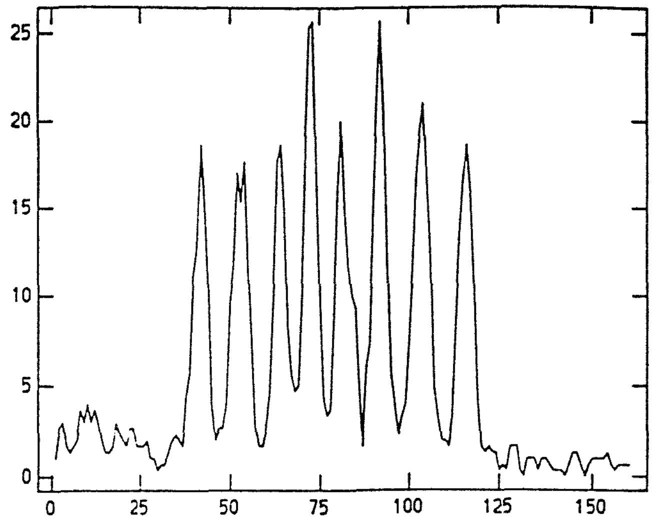

Figure 7.5: *3 mm crystals illuminated by 122 keV (^{57}Co) with multi-wire readout. Detector response is 1.5 mm FWHM.*

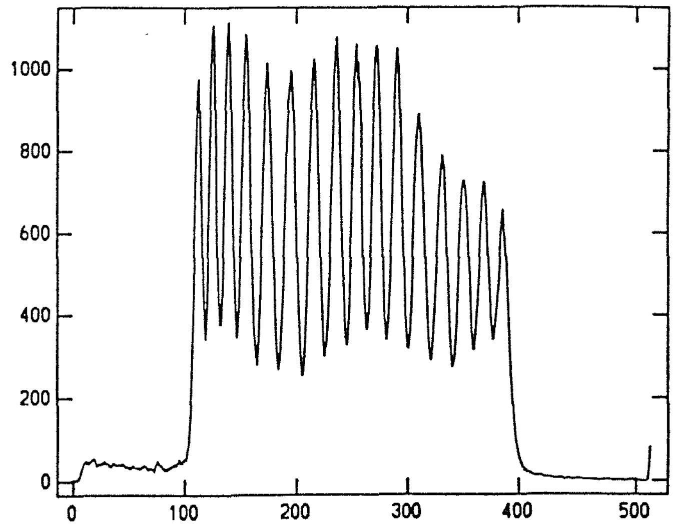

Figure 7.6: *2 mm crystals illuminated by 122 keV (^{57}Co) with conventional readout. Detector response is 1.5 mm FWHM.*

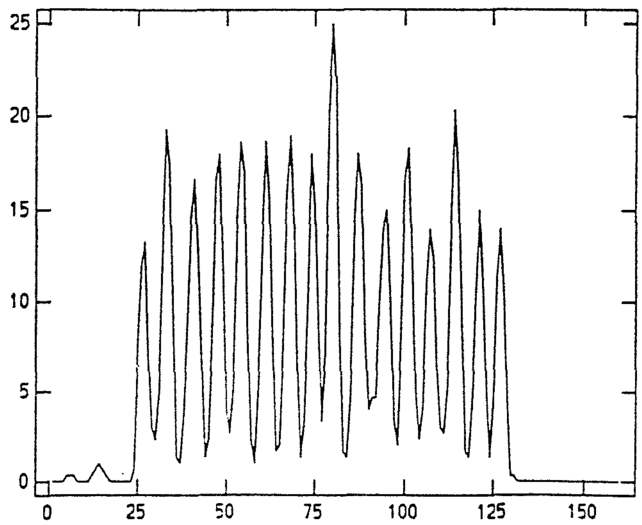

Figure 7.7: *2 mm crystals illuminated by 122 keV (^{57}Co) with multi-wire readout. Detector response is 1.2 mm FWHM.*

The problem associated with segmented detector crystals is all too apparent from these measurements. Because the response function of the detector is far from flat with uniform illumination even at low energies, it becomes necessary to rebin the image so that events located within each scintillator crystal are uniformly redistributed over the whole area of each crystal. Thus each scintillator crystal effectively becomes one image pixel, resulting in a contiguous image which represents the true resolution of the imager. Also, a smoother image can be achieved if the scintillator crystal geometry is chosen such that the photon PSF of each crystal overlaps sufficiently with that of its neighbours that the peak-to-valley ratio approaches zero for a uniformly illuminated crystal. This might occur if the crystal pitch and the crystals themselves were much smaller than the uncertainty of the reconstructed event. Alternatively this can be achieved after the image has been formed by simply convolving each data point in turn with a gaussian having the same FWHM as the pitch of the array.

7.8 Low Energy Detection Threshold

The low energy detection threshold of the detector in its current configuration was limited by the use of a much longer integration time than is desirable because of the limitations of our present data acquisition system. The level of charge due to the dark current is typically ~ 100 times more than expected with the new system electronics. Nevertheless, a 22 keV (Ag) X-ray fluorescence source has been used to illuminate a one-dimensional CsI(Tl) detector crystal array and the signal from the PSPMT subsequently read out using the HX-2 prototype test system. The response function of this detector for 22 keV incident photons is presented in Figure 7.8.

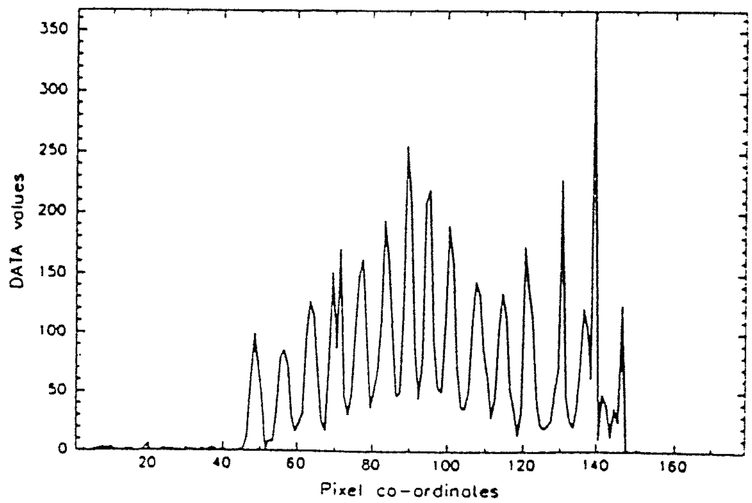

Figure 7.8: *Response function of CsI(Tl) ladder illuminated with 22 keV x-rays*

Although the theoretical 5σ threshold achievable with the present system is limited to approximately 15 keV, with the implementation of the faster data acquisition system, a 5σ threshold of 2.4 keV should be possible.

7.9 Imager Performance

Test images have been obtained by rotating 122 keV (^{57}Co) and 60 keV (^{241}Am) sources in the field-of-view of the detector where the outer ring represents 60 keV and the centre spot 122 keV. Using the peak-finding interpolating algorithm, the uncertainty in the reconstructed position of events within the image yields a profile of the PSF which resembles a delta function convolved with a gaussian. The PSF is sharper at higher energies due to Poisson statistics which subsequently leads to events being preferentially reconstructed towards the centre of each crystal in the array, with the consequence that the image takes on a very pixellated appearance (see Figure 7.9). This figure also shows some other artifacts in the image (gaps) which correlate well with previously observed dynode support structures within the PSPMT itself.

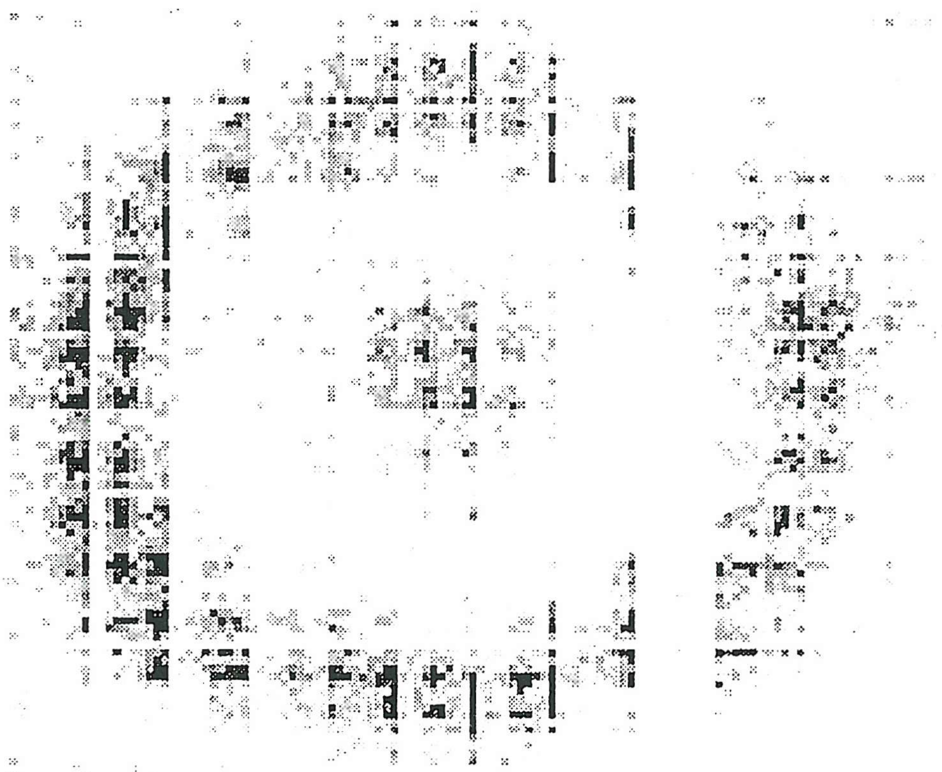

Figure 7.9: *Raw data of extended 60 keV and 122 keV x-ray source*

Clearly one could rebin the data in such a way that events within each crystal are uniformly redistributed within each pixel and corrected to give a contiguous appearance to the image. We have performed this simple convolution in Figure 7.10 using a subroutine called GAUSS.

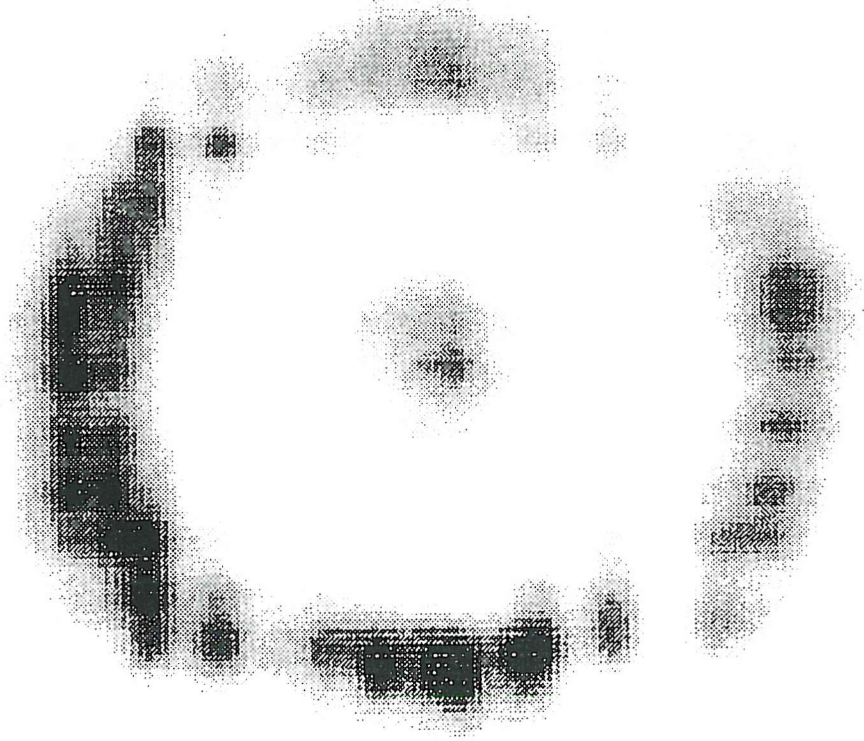

Figure 7.10: *Extended 60 keV and 122 keV x-ray source after smoothing*

7.10 A Proposed Auroral Imager

It has been proposed that several imaging detectors of the type we have discussed will be mounted beneath a platform placed in an 800 km polar orbit. Illustrated in Figure 7.11 is a line representation of the present proposal for such an arrangement comprising two AURIX-L and four AURIX-H detectors.

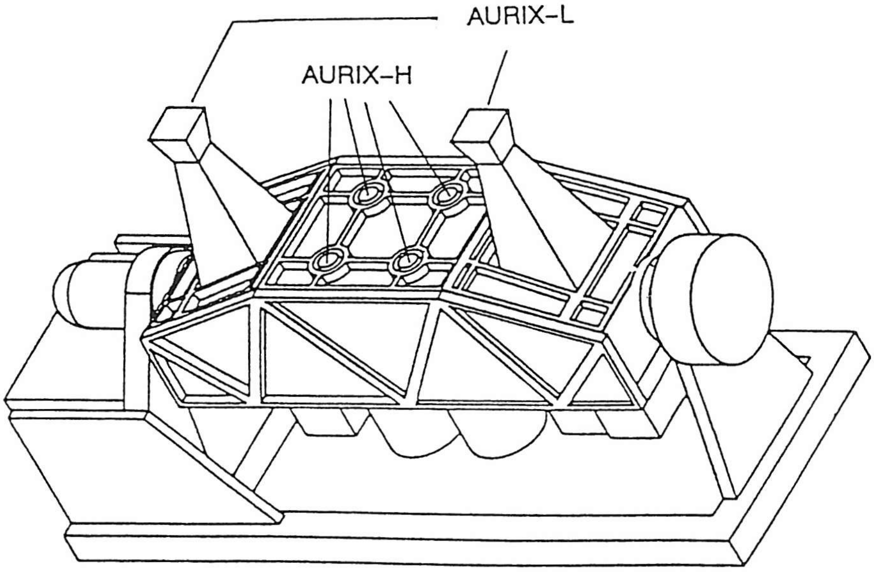

Figure 7.11: *A proposed imager for auroral x-rays*

The AURIX-H detectors have adjustable aperture pinhole collimators and the instruments themselves are mounted on a tilt-table which is all controllable via a telemetry link from the ground. Obviously the mass and space currently occupied by the AURIX-L detectors would accommodate several more of the detectors that we have described.

7.11 Conclusions and Future Work

Using Monte-Carlo simulations we have designed a scintillation counter which is suitable for imaging the aurora at low energies. These simulations suggest that event localization can be further improved through the use of segmented detector arrays and the possible addition of a small air gap between the detector crystal and the tube. Despite the limitations of the data acquisition system employed, we have shown that for imaging applications, where accurate event location of low energy x-ray sources is of critical importance, the HX-2 multi-wire readout offers significant performance advantages over the conventional resistive charge-division technique. Using this configuration we have successfully obtained images of similar morphology to an auroral arc, and have discussed the resulting uneven response function of this type of detector, suggesting that a smoother image can be achieved with some post-processing of the data. A more sophisticated, and dedicated HX-2 readout system has been developed specifically for reading out the 3 inch square PSPMT. This modified circuit exhibits very little dead time, and is capable of integrating at 5 μs which is the limit of the manufacturers operating specifications for the HX-2 chips. This development will be of interest for any application requiring dedicated signal processing electronics to read out individual wires of the PSPMT.

Chapter 8

The Potential of a Position-Sensitive Hybrid Photodiode

8.1 The Need For a New Approach

It is apparent that many applications requiring systems for detecting or imaging x-rays and γ-rays look for the same desirable features from the photodetectors which form the detection plane. These imaging systems require that adjacent photodetectors should tessellate well, with a minimum of non-sensitive *dead area* between adjacent elements of the photodetector array. In addition they are expected to demonstrate high spatial and energy resolution, whilst exhibiting a very uniform position response, and requiring as few channels of readout electronics as possible. Some future development is therefore expected to be concentrated upon a more compact and lightweight detector design that ultimately will necessitate the inclusion of the signal processing electronics within the packaging of the device itself. Developments are currently moving at such a pace that at some point in the future, a compact imaging system could emerge which integrates the signal processing, shaping, ADC, and display device within a single compact enclosure. The benefits that such a simple, light, compact, and potentially portable single organ imaging system might bring to an application such as nuclear medicine are intriguing.

Clinical applications have recently been proposed where the usefulness of a clinical gamma camera demonstrating a modest field-of-view has been identified (Hayashi [50], and Yasillo et al. [137]). The most widely reported photodetector for this application at the present time appears to be the PSPMT from Hamamatsu [45, 46, and 47]. However, a new device known as the Hybrid Photodiode (HPD) has emerged which deserves consideration for inclusion within such a camera (Johansen et al. [62], Suyama et al. [117], DEP [35], Hamamatsu [48]).

The HPD discussed in this chapter exhibits many desirable characteristics which would prove to be of great benefit to either auroral imaging, or nuclear medicine imaging. However, the potential of the HPD as a position-sensitive scintillation counter remains undemonstrated at the time of writing.

The first generation HPD tubes currently available exhibit certain performance limitations which make them less attractive than the PSPMT for many new applications in nuclear medicine. The principal disadvantage of the currently available HPD is the very small sensitive area of even the largest device (12 cm^2), when compared with the dimensions of the circular enclosure (49 cm^2), an active surface area of only 24%. Whilst the sensitive area of these devices is comparatively small, they offer the advantage of a very uniform photocathode response due to the very accurate transfer deposition process employed. This uniformity is a very desirable feature of these devices, and this characteristic is not intrinsically limited by the sensitive area emplyed. However, these early HPDs have not been developed with nuclear medicine imaging applications in mind, and they do not intrinsically exhibit continuous position-sensitivity. Indeed, the imaging capability of prototype scintillation counting devices based upon the multi-anode HPDs discussed in Chapter 9 remains to be proved through the application of a resistive divider and interpolating algorithm (Durrant et al. [38]). There is therefore a clear requirement for a second generation HPD for use as a position-sensitive scintillation counter, offering a sensitive area approaching 40 cm^2, demonstrating good tessellation efficiency, a low noise threshold, and an intrinsic spatial resolution of the order of 2 mm.

8.2 History of the HPD

As early as 1966 reference was made to a device employing a multiplier diode structure to provide the charge gain within a vacuum phototube (Kalibjian [64], and Wolfgang et al. [132]). However, a previous reference dating back to 1957 explored the potential of charge amplification in electron bombarded silicon (Sclar [111]). The recently developed hybrid photodiode (HPD) is therefore not a new idea, but merely an extension of this concept. In fact the essential technology required to develop the HPD already existed in the form of image intensifier tubes which were developed in the early sixties. These early tubes found many applications in nuclear experiments, and in observational astronomy, where low dark currents and high position resolution are required. Progress has been slow until recently, when very rapid progress in silicon PiN photodiode fabrication technology has facilitated the accurate ion implantation of extremely thin contact layers, and the controlled deposition of high quality silicon dioxide (SiO_2) and silicon nitride (Si_3N_4) layers from the vapour phase to passivate devices very effectively. These photodiodes have been combined in the HPD with recently developed transferable photocathode technology, where a photocathode may be deposited onto a glass or fibre window inside a vacuum chamber before being transferred to a device, enabling the production of high performance devices with stable characteristics. This method of vacuum photocathode deposition directly onto the entrance window of the device provides superior uniformity of response with no shadows of internal structures which will affect the image such as we have found in the case of the PSPMT.

8.3 Principle of Operation

The HPD was briefly introduced in Chapter 3, and its potential as an electron multiplier device was discussed for γ-ray scintillation counting applications in nuclear medicine or auroral imaging. These new devices essentially rely upon the same basic principles exploited by image intensifier tubes of the early 1960s, replacing the phosphor screen anode with a silicon anode structure of some kind. In 1981, Roziere et al. [103], proposed a version of the image intensifier which used a silicon anode (see Figure 8.1).

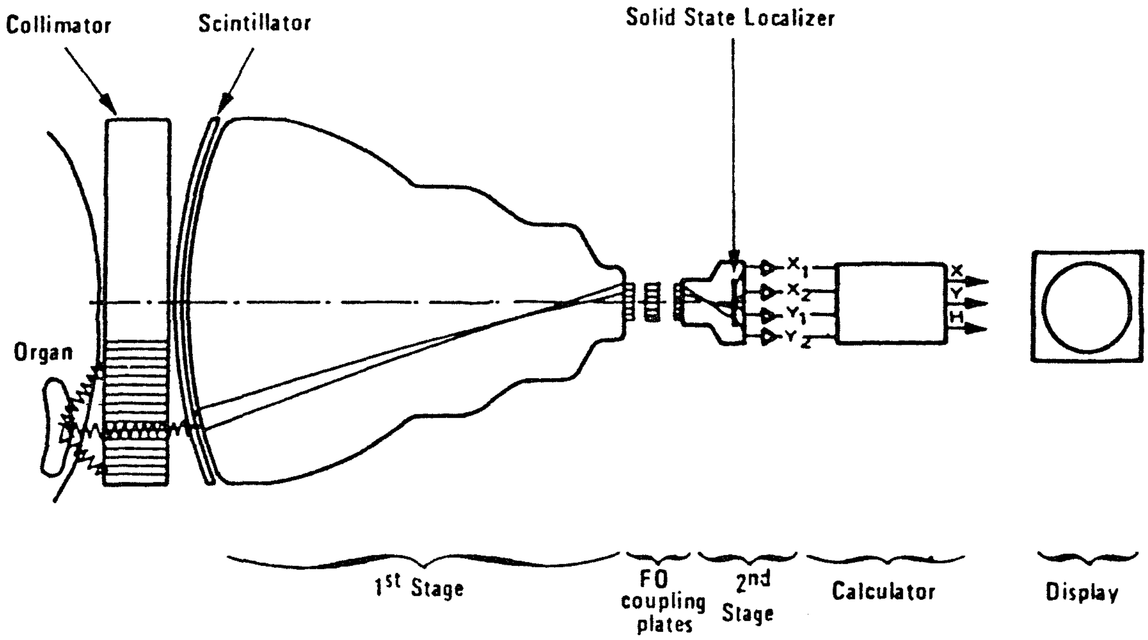

Figure 8.1: *An image intensifier tube with a silicon anode*

Photoelectrons that are generated by the photocathode are accelerated by a high electric potential towards this silicon anode structure, where they penetrate into the silicon. Each electron that is incident upon the silicon anode will generate several thousand electron-hole pairs within the bulk material, and hence the amplitude of the original signal is increased by a factor of several thousand. Typically, a voltage of -15 kV is applied between these two surfaces which provides a gain of approximately 3500 depending upon the quality and construction of the silicon material (Schmidt-Ott et al. [106]).

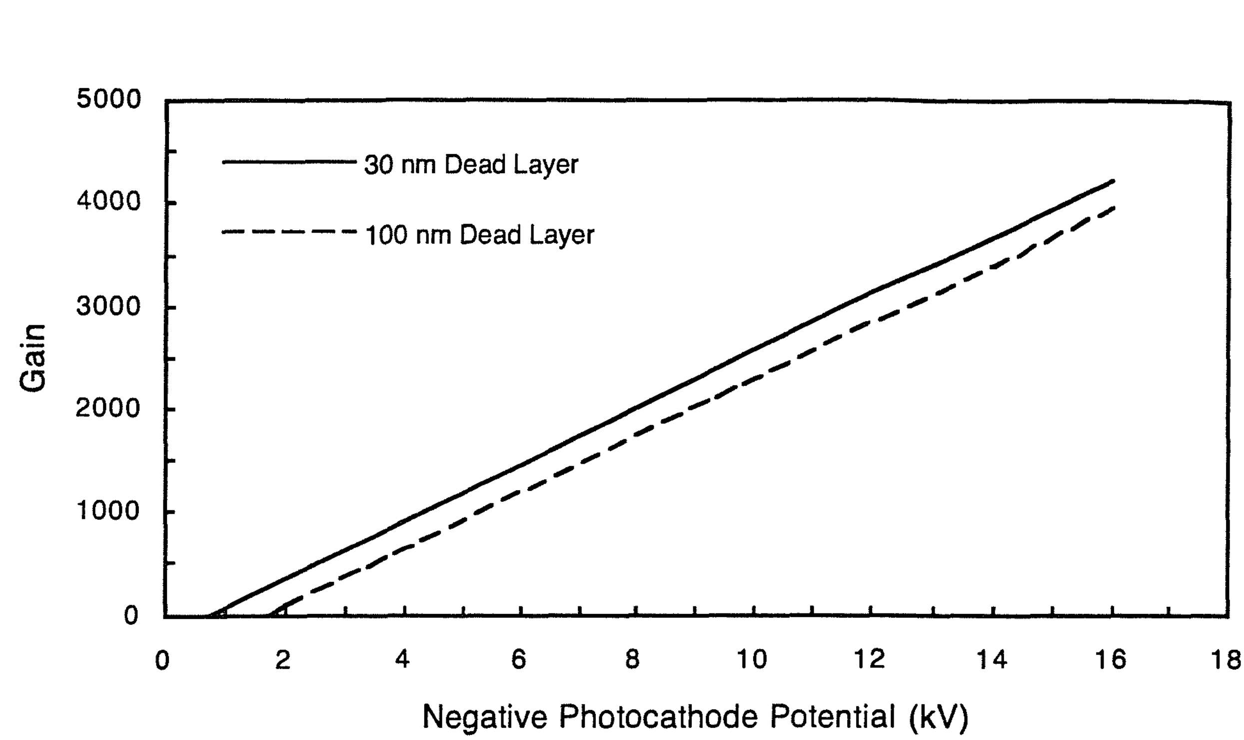

(a) Simulated HPD gain characteristic, B = 0

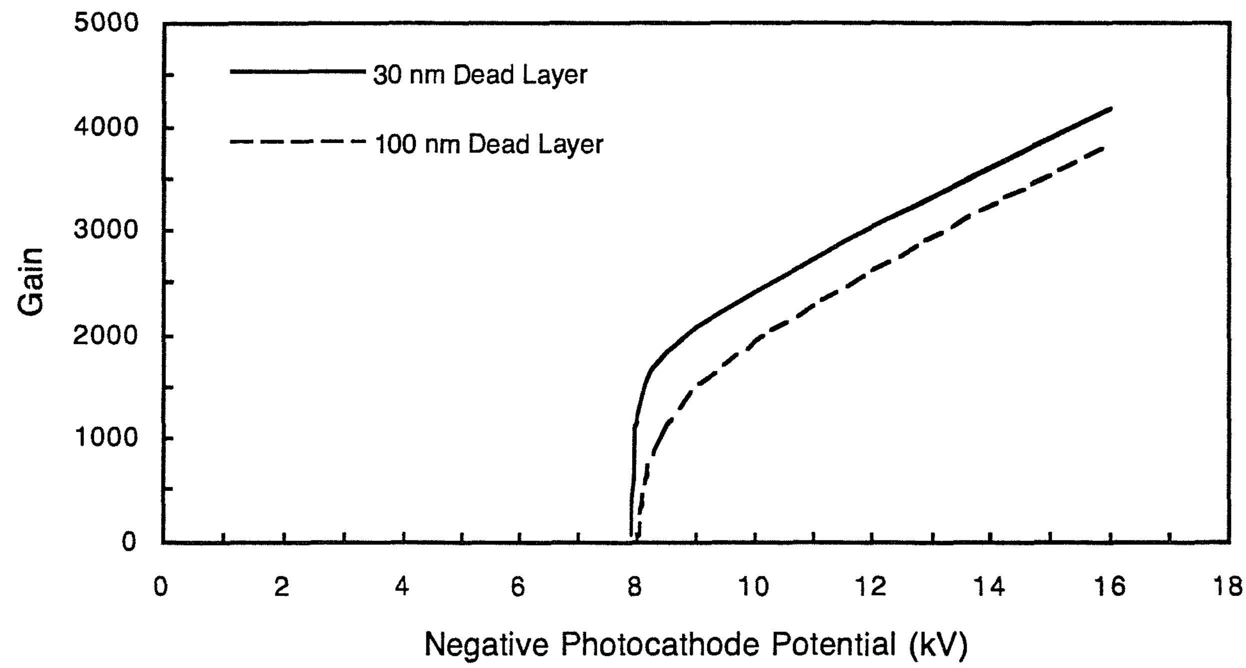

(b) Simulated HPD gain characteristic, B = 2 kGauss

Figure 8.2: *HPD gain characteristics as a function of contact layer thickness and transverse magnetic field*

If the accelerating potential is known the penetration depth may be calculated according to the following expression:

$$d_{tot} = 3\text{x}10^{-10}V^{1.4}[cm] \qquad 8.1$$

where V is the negative photocathode potential in volts. Charge gain will occur within the silicon once this threshold voltage has been exceeded. This threshold is a value of voltage which corresponds to the kinetic energy required to enable electrons to penetrate the contact layer, since gain occurs only in the bulk silicon material (see Figure 8.2).

Once the gain threshold voltage has been exceeded, gain occurs within the fully depleted bulk material, linearly for the B=0 case, approximating to the theoretically expected value of 1/3.62 (electron-ion pairs per eV). The multiplied charge is then quickly swept away and divided between the outputs where electronic readout and subsequent signal processing takes place. The gain threshold may be calculated using the above expression if the contact layer thickness is known accurately, or alternatively by experiment. The value of gain threshold is affected by two parameters. Firstly, the thickness of the contact surface or *dead layer* should be as thin as possible, and secondly the incident photoelectrons should ideally penetrate the silicon perpendicular to its surface (θ =0) for the lowest gain threshold and the highest gain due to geometrical effects. If $\theta \neq 0$ the following expression may be used to calculate the effective penetration depth (d_{ef}) of electrons in the bulk silicon material:

$$d_{ef} = d_{tot} - \frac{d_c}{\cos\theta} \qquad 8.2$$

Whilst the contact layer thickness is determined at the time of wafer fabrication, the angle θ, which the incident electrons make with the normal to the silicon wafer may increase either as a result of space charge effects, or more probably due to the presence of a strong transverse magnetic field causing the gain and signal to be reduced (see Figure 8.3). These effects may be compensated for by either increasing the accelerating potential applied to the photocathode, or alternatively by reducing the distance between the photocathode and the silicon diode. Clearly from the characteristics illustrated in both Figures 8.2 and 8.3, the HPD exhibits excellent immunity to very strong magnetic fields. This is principally due to the very high electric fields involved in its operation, and the very short distances over which the photoelectrons are accelerated. When this device is employed in a clinical imaging system, it will be insensitive to stray magnetic fields from the superconducting magnets used in modern MRI scanners. The potential of integrating these two imaging modalities for improved image registration can be envisaged.

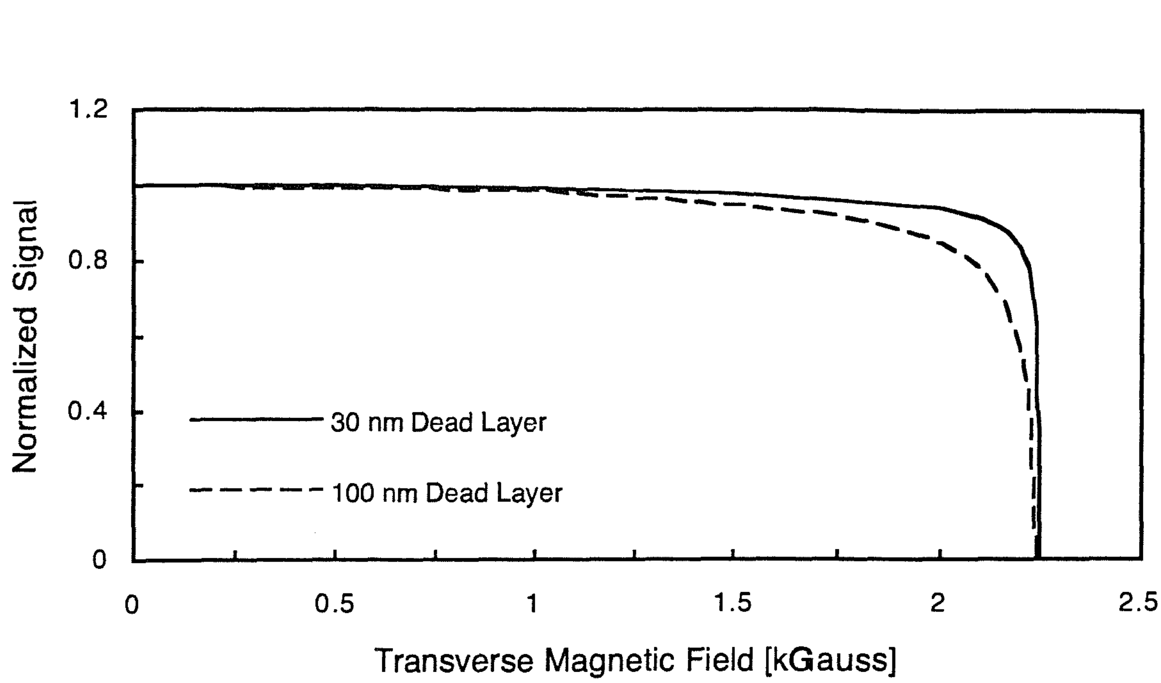

Figure 8.3: *Normalized HPD response as a function of transverse magnetic field*

However, the theoretical response characteristic of the HPD when operated in a magnetic field environment where the angle that the magnetic vector makes with the electric vector is less than 90°, is considerably less linear than that illustrated by Figure 8.3. This can be explained by considering changes in the electron trajectory due to increases in the magnetic field, giving rise to slight fluctuations in the gain produced in the silicon anode (see Figure 8.4).

Previous authors at the University of Bergen, Norway have been successful in demonstrating the feasibility and operation of early experimental devices for applications in auroral imaging (Johansen et al. [60, 61, 62]). In parallel with this work, a great deal has already been achieved by the longstanding collaboration between DEP, working together with the CERN-LAA group led by Dr. Riccardo DeSalvo, in successfully demonstrating the first available electrostatically and proximity focused hybrid tubes (Arnaudon et al. [6], Basa et al. [11], DeSalvo et al. [36], and van Geest et al. [127]). Tests carried out by both of these groups have shown good diode and photocathode survivability under normal operating conditions, and in the case of the proximity focused variant, an outstanding immunity to magnetic fields to the Tesla level (Arnaudon et al. [6]). Their early devices have demonstrated a very fast response of the order of a few ns rise and fall time and a very linear response over 8 decades of signal intensity. Recently published results from DEP have revealed the ability to clearly resolve many single photoelectron events illustrating the sensitivity and low noise characteristics so desirable of modern scintillation counting detectors.

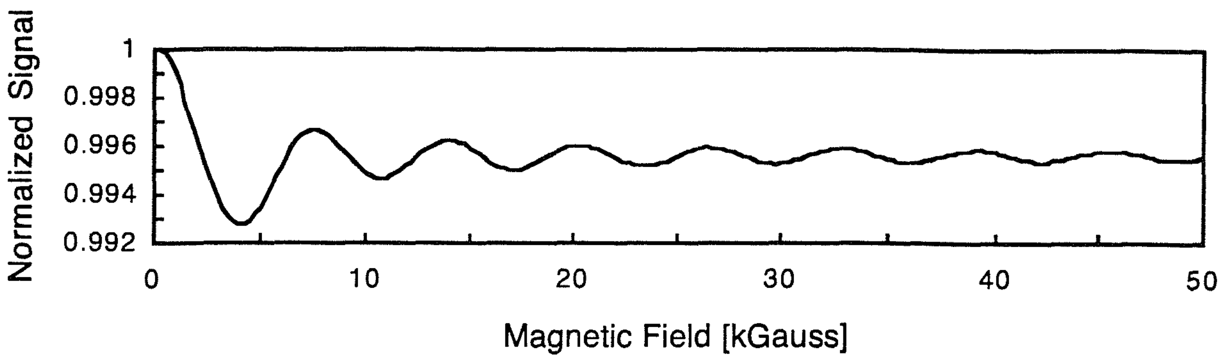

(a) Magnetic field angle = 15 degrees

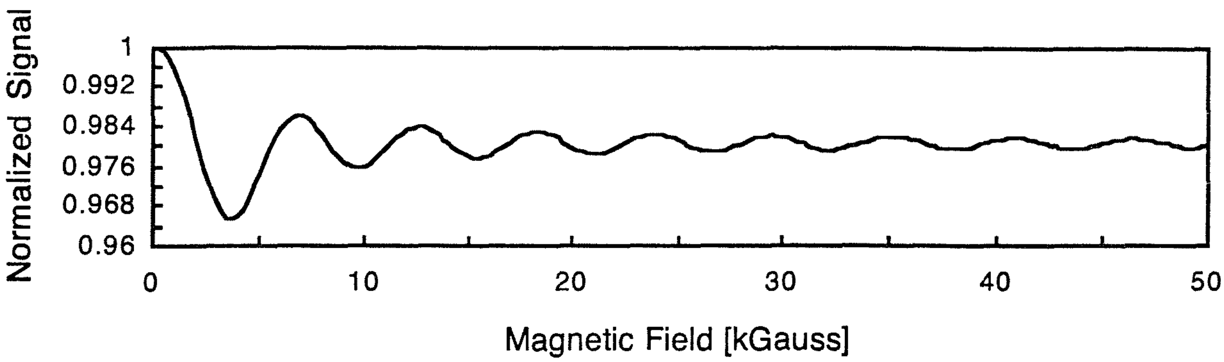

(b) Magnetic field angle = 30 degrees

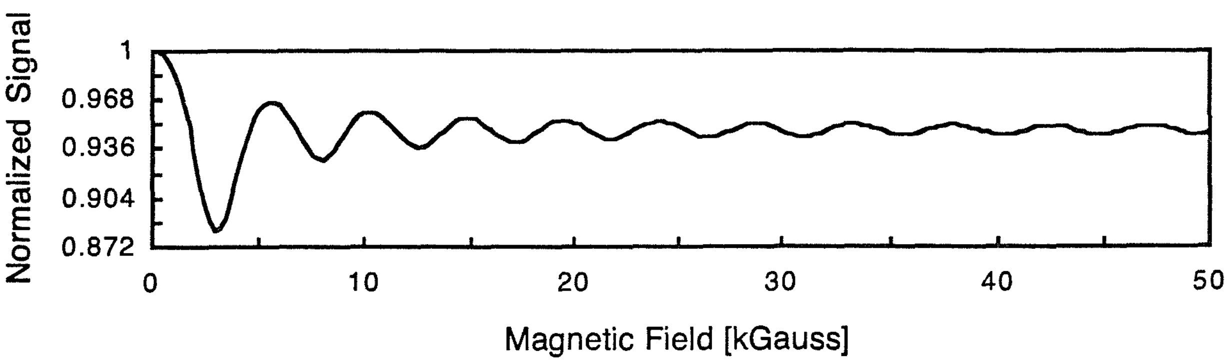

(c) Magnetic field angle = 45 degrees

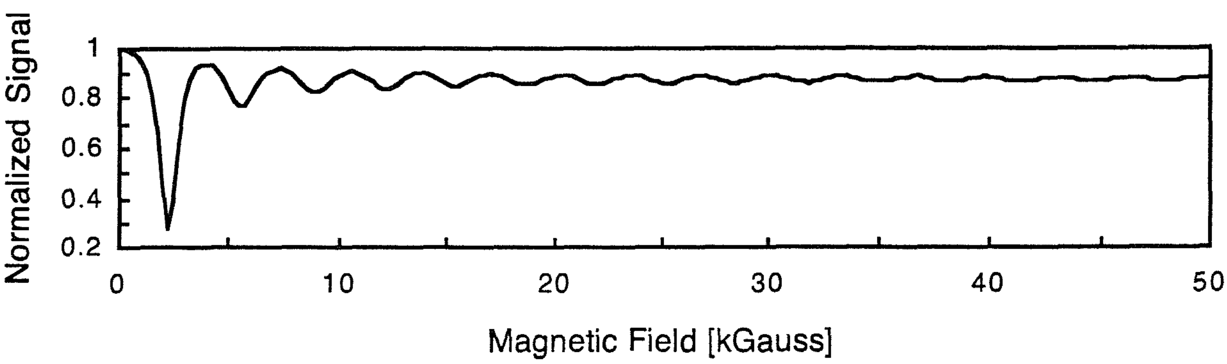

(d) Magnetic field angle = 60 degrees

Figure 8.4: *Effect of magnetic field angle upon HPD response*

8.4 A New Detector Based Upon The HPD Principle

The feasibility of the HPD for scintillation counting applications will be demonstrated in Chapter 9, by the excellent performance of single-anode electrostatically focused devices supplied through a collaboration with DEP. However, these devices could not be used as they stand at present to provide a readout system for a position-sensitive scintillation counter such as is needed for many applications requiring a detector of modest dimensions. If an array of these devices could be made to tessellate together more efficiently, with little *dead-space* between adjacent tubes, these simple tubes could offer a low noise, if slightly expensive, alternative to the PMT for inclusion within a clinical gamma camera. However, existing single-anode HPDs have relatively small, circular sensitive areas of up to 25 millimetres in diameter which occupy only a small fraction of the total area of the package which is itself circular. It would therefore be extremely difficult to construct a useful camera based upon such an array. Recently however, prototype multi-anode HPD tubes have become available from DEP, and whilst these devices were not specifically developed for scintillation counting, they do offer some limited position-sensitivity. Despite these advances, by far the most preferable option is to consider the development of a new device conceived with nuclear medicine imaging applications in mind. Such a device would have a sensitive area of between 25 cm^2 and 50 cm^2, and would have a high ratio between sensitive and total area of perhaps 75%. The anode would ideally have some intrinsic position-sensitivity with the most conservative number of channels of signal processing required as can reasonably be achieved. In addition, if the enclosure could be made either square or hexagonal, a number of these devices could potentially be tessellated together to form a larger imaging plane if required. Due to the relative simplicity of the proximity focused HPD described earlier, and the problems associated with designing an electrostatically focused HPD having square or hexagonal cross-section, it was decided that the initial phase of this project would consider the design and construction of a square, position-sensitive HPD which uses proximity focusing.

8.5 Anode Structures

Various anode structures that offer the possibility of position-sensitivity have been considered as potential candidates for the proximity focused HPD development. Two basic types of detector are currently available which use different techniques to provide the spatial information. The first employs some configuration of discrete readout elements which could be fabricated on the same wafer, whilst the second uses a continuous readout system based on a resistive charge division method to derive the position of interaction. Ideally, a single position-sensitive diode could be employed as the anode, requiring only readout electronics to drive four position channels, one energy channel of readout electronics, and one biasing contact per device. Assuming that a spatial resolution of 1 mm FWHM can be achieved, a large-area device suitable for applications in nuclear medicine, having dimensions of 50 mm by 50 mm, will be capable of producing approximately 2500 image pixels. This would represent a considerable saving compared with the multi-anode approach adopted by DEP. This compares very well with the number of image pixels currently contributing to the image in nuclear medicine imaging studies of small single organs such as the thyroid gland.

Multi-Pixel Anode Readout

Discrete devices, or arrays of many small diodes can be fabricated on a single wafer to suit the application. Each interaction occurs at a unique address generating a charge signal which is read out from the device, enabling the position of interaction to be identified and reconstructed. Clearly, if many segments are contained on the wafer, many channels of signal processing electronics will be required in order to read out the individual signals from each pixel. However, this problem of having many channels of electronics to enable segmented wafers to be read out might be resolved by using Anger logic to determine the position of interaction. If devices can be fabricated which integrate a resistor divider between adjacent hexagonal pixels of the wafer, the required number of channels of signal processing electronics could be reduced, independently of the number of anode pixels, to only four in order to determine the unique address of the interaction. This is analogous to the technique used in conventional gamma cameras, and was identified because of the visual similarity between the anode structures used in prototype multi-anode HPDs produced by DEP, and the hexagonal PMTs used in gamma cameras. This adaptation of a segmented anode structure to enable the continuous sampling of charge with relatively few channels of electronics was recently suggested by the author in discussions with Canberra and DEP who are currently considering a modification to the design of the 37 element anode structures currently in development. This could offer the first commercially available HPD offering truly intrinsic imaging capability.

Orthogonal Strip Detector Readout

Another example of a detector employing a discrete array of elements is the orthogonal silicon micro-strip detector, where p-type and n-type strips are implanted orthogonal to each other on the upper and lower surfaces of a diode, as shown in Figure 8.5. A pixel is defined where two electrode strips overlap. These devices exhibit spatial resolutions in the range 5 - 25 μm.

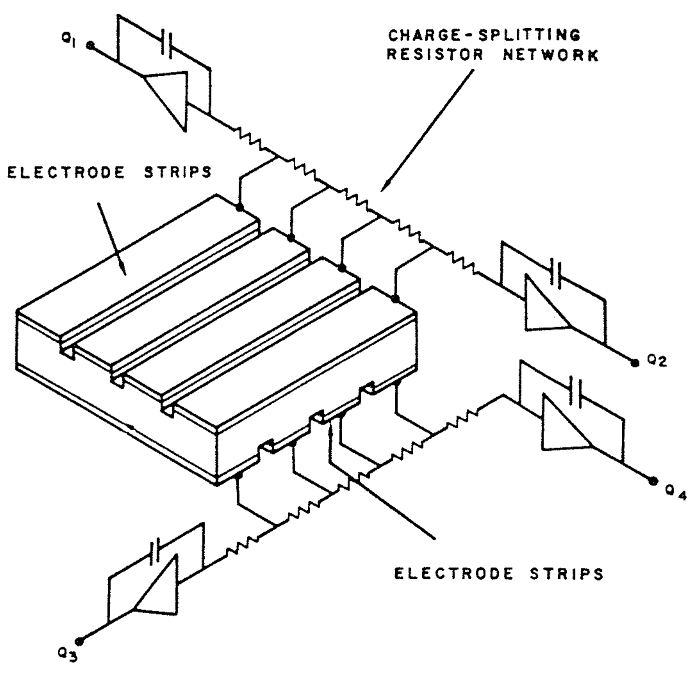

Figure 8.5: *Layout of a silicon micro-strip detector*

The requirement still exists for many channels of readout electronics in order to sample the charge distribution emerging from the strips in either axis. Gerber et al. proposed that a resistive divider can similarly be applied in order to overcome this problem as illustrated in the previous figure which has been taken from Knoll [68]. However, these devices are expensive to fabricate, and demonstrate spatial resolution characteristics which are considerably better than would be required of a small gamma camera. For these reasons, the orthogonal strip configuration is less interesting for the application described earlier.

Wedge and Strip Readout

A novel and potentially interesting position-sensitive anode structure for our HPD development is based upon the wedge and strip anode (WSA), which was first proposed by Anger in 1966, and was later applied by several other authors (Lapington et al. [72], Schwarz et al. [109], and Martin et al. [139]). The principle of the WSA relied upon a position-sensitive pattern of conductors etched upon an insulating substrate in order to sample the charge distribution. Whilst this would not facilitate charge gain in the manner that we have previously described, it might be possible to develop a silicon WSA where the pattern of conductors is fabricated by the implantation regions of the diode.

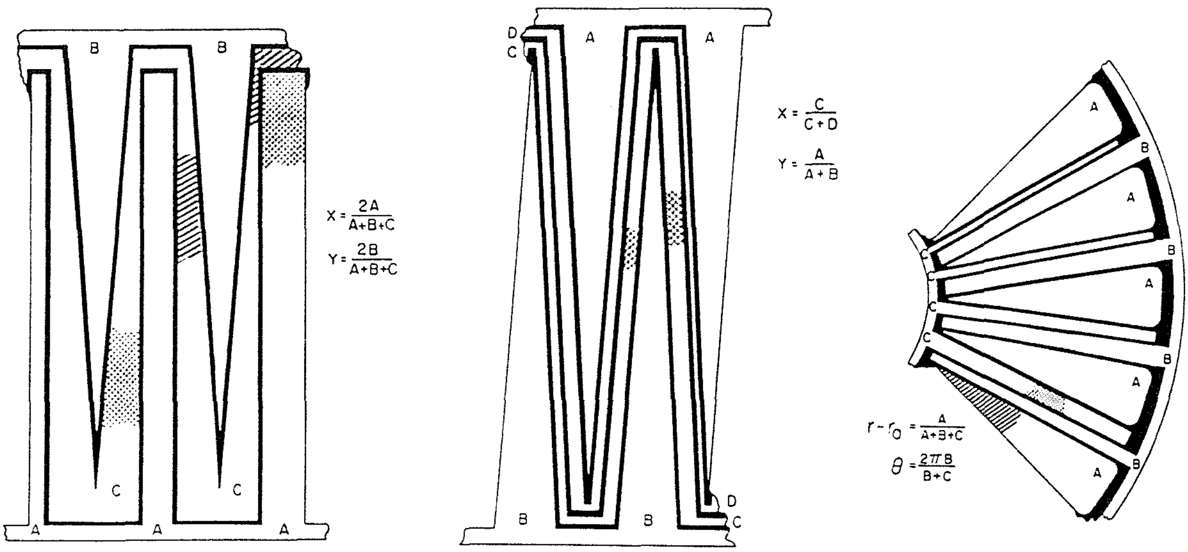

Figure 8.6: *Three typical configurations of wedge and strip detector*

Three simple electrode WSA patterns are shown schematically in Figure 8.6 together with the algorithms that would enable the determination of the spatial co-ordinates of the charge distribution at the anode. It can be seen from this illustration that whilst the area of the wedges remains constant, the area of the strips modulates as a function of position. Thus, for a particular distribution of charge falling upon the WSA, the ratio between the fractional charge sampled by each of the three electrodes as a function of spatial position will yield a unique address. The spatial resolution of the WSA will be dependent upon the area of the anode, the pitch between the wedges, and the modulation of the strips contained within the WSA pattern. Results have been reported where spatial resolution of the order of 75 μm FWHM has been achieved. As the photoelectron distribution varies at the anode, the statistical fluctuations in the charge sampled by each electrode as a function of position cause a variation in the spatial resolution. This has been reported to vary by more than 100% over a 40 mm square area (Schwartz et al. [109]). These anodes have also been shown to suffer considerable spatial distortion of the image. Because the development and fabrication of a custom-made silicon anode based upon the WSA principle would be more expensive than commercially available devices, and such a development would suffer from non-linearity of both spatial resolution and position, the WSA is not considered suitable for inclusion within a position-sensitive HPD.

Position-Sensitive Diode (PSD) Readout

Another technique used to determine the address of the interaction is for a continuously resistive silicon electrode to be implanted into the structure of the diode at the time of fabrication [22]. Several variations of the position-sensitive diode (PSD) are available that enable the detection of photons or charged particles in either one or two dimensions (see Figure 8.7).

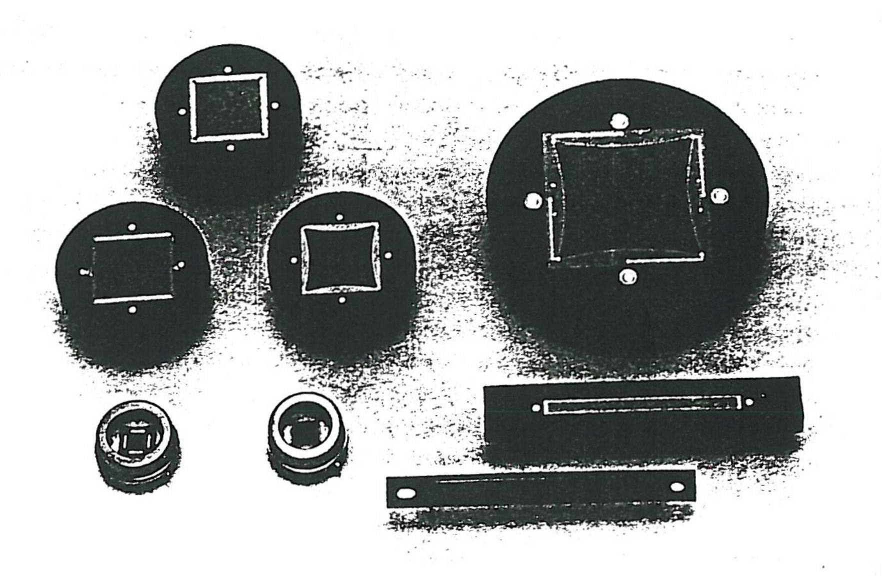

Figure 8.7: *Various one-dimensional and two-dimensional PSDs*

In the last decade, several PSDs have been developed which offer two-dimensional position-sensitivity (Doke et al. [37], Yamamoto et al. [133], and Yanagimachi et al. [135]). Those PSDs that offer two-dimensional capability are fabricated in two basic configurations:

The duolateral PSD has resistive P-type and N-type implantations on the front and rear surfaces of the chip respectively, and two collection electrodes on each side of the device mounted orthogonally (see Figure 8.8).

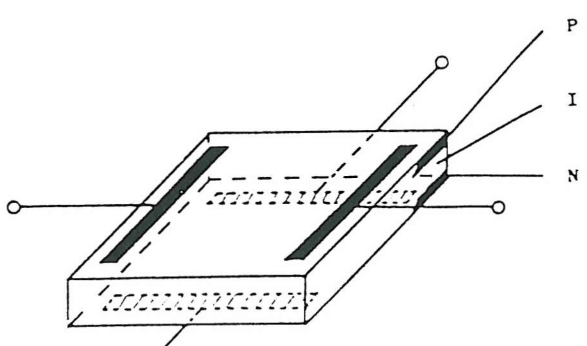

Figure 8.8: *The structure of a duolateral PSD*

The energy signal is therefore derived from the sum of these four channels, whilst the position signal is derived from the centroid of the charge emerging from the two electrodes in each axis. A complete treatment of the mechanism of position sensing by charge division in PSDs is presented by Alberi et al. [1], Kalbitzer et al. [63], Lægsgaard [71], and Radeka [93].

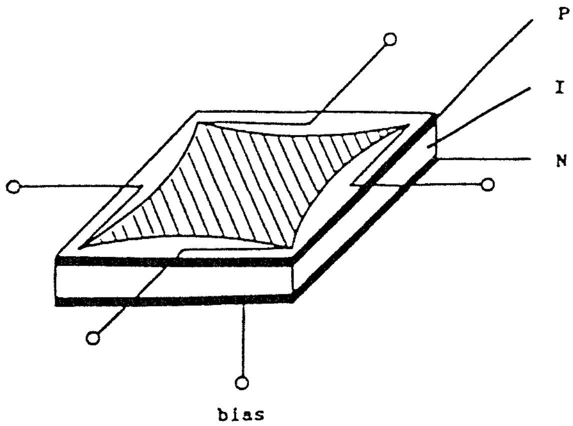

Figure 8.9: *The structure of a tetralateral PSD*

The tetralateral PSD varies from the previous description in that five channels are used in order to sample the charge, and the chip is fabricated with the resistive implantation on the front surface of the chip only (see Figure 8.9). On the front surface of the device, four collection electrodes sample the divided charge which is subsequently used to calculate the centroid, and hence determine the position of interaction. The rear surface of the device collects the total charge deposited, and hence the energy of the event can be determined.

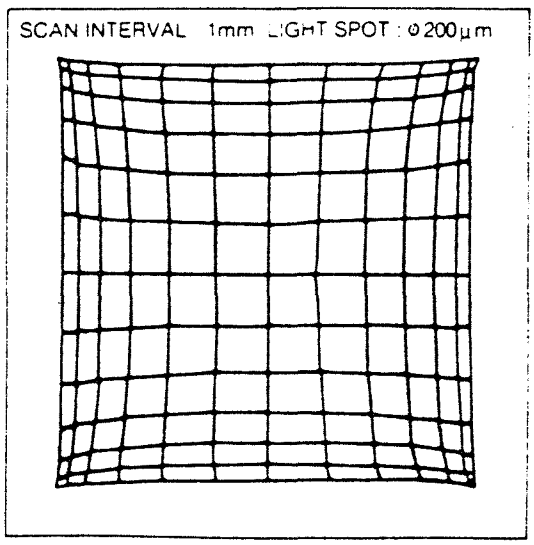

Figure 8.10: *Pin-cushion distortion in the duolateral and tetralateral PSD*

Like many position-sensitive devices discussed in this work, both of these configurations suffer from non-linearity of the position signal (see Figure 8.10). This pin-cushion distortion requires that both the semiconductor material and the resistive layer should be highly uniform and homogeneous, whilst it has been reported that damage caused to the resistive layers by continuous bombardment by alpha-particles significantly increases the amount of distortion observed (Teraoka et al. [120]). Correct shaping of the output signals is also required. If care is taken, non-linearities can be less than 1% of the length of the detector. The intrinsic spatial resolution of these devices is reported to be of the order of 250 μm FWHM when illuminated with optical photons, and is linear as a function of position. However, the intrinsic spatial resolution is not accurately known when the devices are bombarded with alpha-particles. However, since the spatial resolution is determined by the spread of charge-carriers within the device, we can deduce from curves of specific energy loss in silicon (Knoll [68]), that the mean range of 5.5 MeV alpha-particles in silicon is less than 40 μm. The intrinsic spatial resolution for alpha-particles will therefore be be very close to that specified for photons. Recently reported work would suggest that the distortion from the duolateral PSD is considerably less than that from the tetralateral PSD. However, the tetralateral PSD offers the possibility of a rear-bombarded anode for the HPD that would offer some protection to the very thin, and fragile resistive implantation. Both types of PSD described here are readily available in a range of sizes, some employing large sensitive areas approaching 25 cm^2. It was therefore decided that further investigation of the duolateral PSD should be made to determine its suitability for inclusion within an HPD.

8.6 Tests of a 1 cm^2 Duolateral PSD

A small duolateral position-sensitive diode (PSD) was supplied for the purposes of this study by Silicon Sensor GmbH of East Berlin, who have particular expertise in the design and manufacture of custom silicon PiN diodes with the necessary Si_3N_4 passivation. The duolateral PSD was chosen because of its simplicity, availability, low cost, and useful sensitive area compared with alternative smaller devices within the Silicon Sensor product range [115].

8.6.1 Experimental Procedure

Tests were conducted in the laboratory to examine the performance characteristics of a square duolateral position-sensitive PiN photodiode (PSD), having an effective sensitive area of 100 mm^2. An ideal test of the performance of this device for an application such as that which is proposed would be to use a collimated source of pulsed 15 keV electrons incident normally upon the surface of the device. However, no such source was available, and so an alternative means of determining the response of the PSD had to be found. By simulating the photoelectric absorption of a 122 keV (^{57}Co) γ-ray within a CsI(Tl) scintillation crystal optically coupled to the entrance window of the HPD, we were able to determine the equivalent charge produced within the PSD by the impinging electrons. From this we were able to select a suitable alpha-particle source which would simulate this deposited charge. It was found that 5.5 MeV alpha-particles from a 1.7 μCi, metal foil ^{241}Am alpha-particle source produced almost exactly the right amount of charge within the diode. The ^{241}Am source was initially viewed by the duolateral PSD, collimated using a simple aluminium mask. Two 0.5 mm in diameter holes were drilled in the mask on a pitch measuring 5 mm between centres, and the source was placed a few millimetres away from the mask to determine if the system was working. However, ^{241}Am also decays producing 59.5 keV γ-rays, although their interaction efficiency within silicon is perhaps only 1% of that of an alpha-particle. An energy spectrum was obtained to confirm that pulse-height discrimination was not necessary in order that these low-energy deposits could be rejected in favour of the more energetic alpha-particles.

It was clear from this preliminary measurement that stematic uncertainties due to poor collimation was causing off-axis dispersion of the incident alphas, and that this was dominating over the intrinsic resolution of the PSD. A simple calculation revealed that by modifying the test system, and moving the source further away from the detector, the PSF could be reduced by as much as 0.5 mm FWHM. A more sophisticated test system would therefore be required in order that the source could be moved further away from the mask. This would facilitate a reduction in the spatial resolution to a value which approximates to the intrinsic resolution of the PSD when bombarded with normally incident electrons. However, the approximate range of 5.5 MeV α-particles in air is approximately 4 cm. In order to significantly increase the source-detector separation, a test chamber is required which can be maintained at a vacuum whilst the measurements are made. In considering the design for such a chamber, whilst reducing the systematic spread of α-particles as they are incident upon the PSD, it was important to maintain a sufficiently high count rate which would enable the data to be acquired within a reasonably short period of time (overnight for example). It was considered that in order to obtain good statistical certainty of the data, each data set should be composed of 60,000 events within the field-of-view.

In order to estimate the optimum design, further calculations were made that considered the compromise between the count rate, the source-detector distance, and the dimension of the hole or slit used in the mask. For the purposes of this model, a simple mask was chosen that comprised of two small slits separated by some distance, which also separate the source and the detector. The result of this simple simulation demonstrated that for a slit width of 0.5 mm separated by 10 cm, the count rate at the detector will have reduced to 3 counts per second (see Figure 8.11). Therefore, for the required 60,000 events to be collected for each set of data, less than 6 hours would be necessary, which is well within the time available for each set of data.

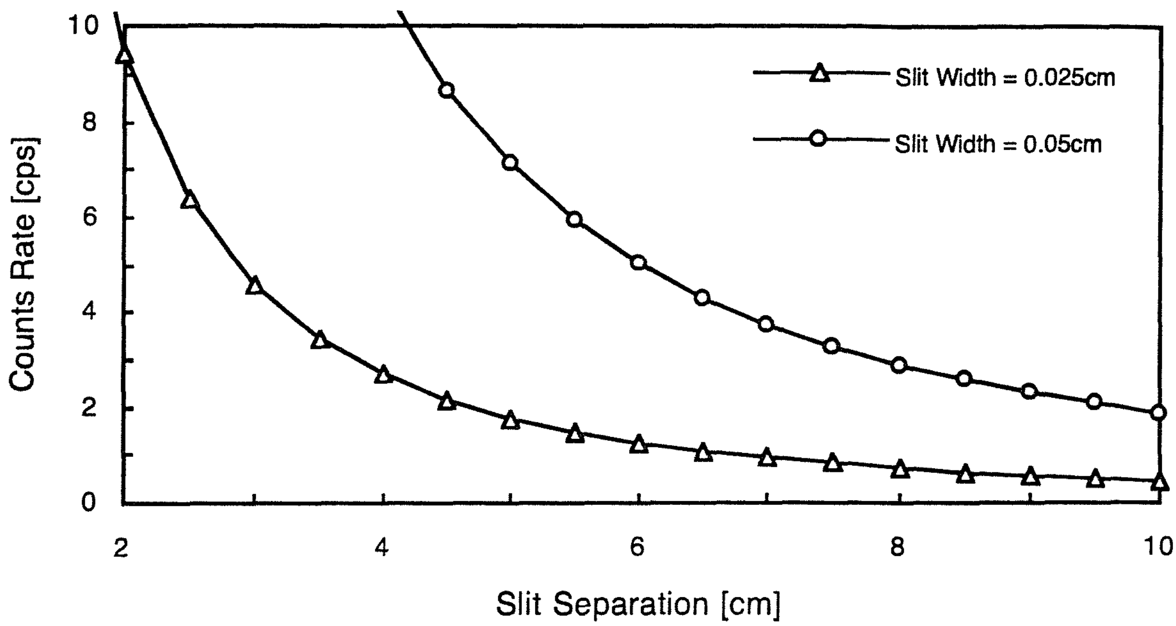

Figure 8.11: *Simulated count rate at detector as a function of source-detector separation*

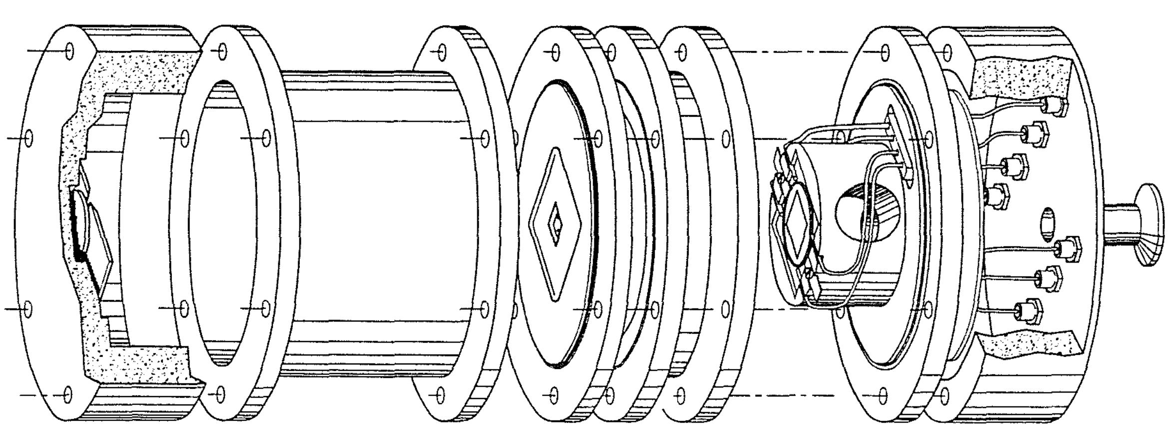

Figure 8.12: *Diagram illustrating the vacuum chamber*

In order that the systematic effects could be identified and reported, it was decided to construct a vacuum test chamber having three interchangeable collars which would enable the distance between the source and the detector to be incrementally increased to a maximum of 10 cm (see Figure 8.12).

8.6.2 Signal Processing

Although the duolateral PSD used in these measurements requires only four channels of signal processing electronics in order to determine the location and energy of the interaction, the test system needed to be easily modified for conducting future tests on tetralateral PSDs. These devices differ from the duolateral PSD in that there is a single channel on the reverse of the chip that is dedicated to the acquisition of the total deposited charge (or energy), whilst four other channels on the front of the chip collect the divided charge which is later used to determine the position of interaction. Therefore, we designed a circuit offering four channels of signal processing, that could be easily adapted for testing tetralateral PSDs by adding a further preamplifier (see Figure 8.13).

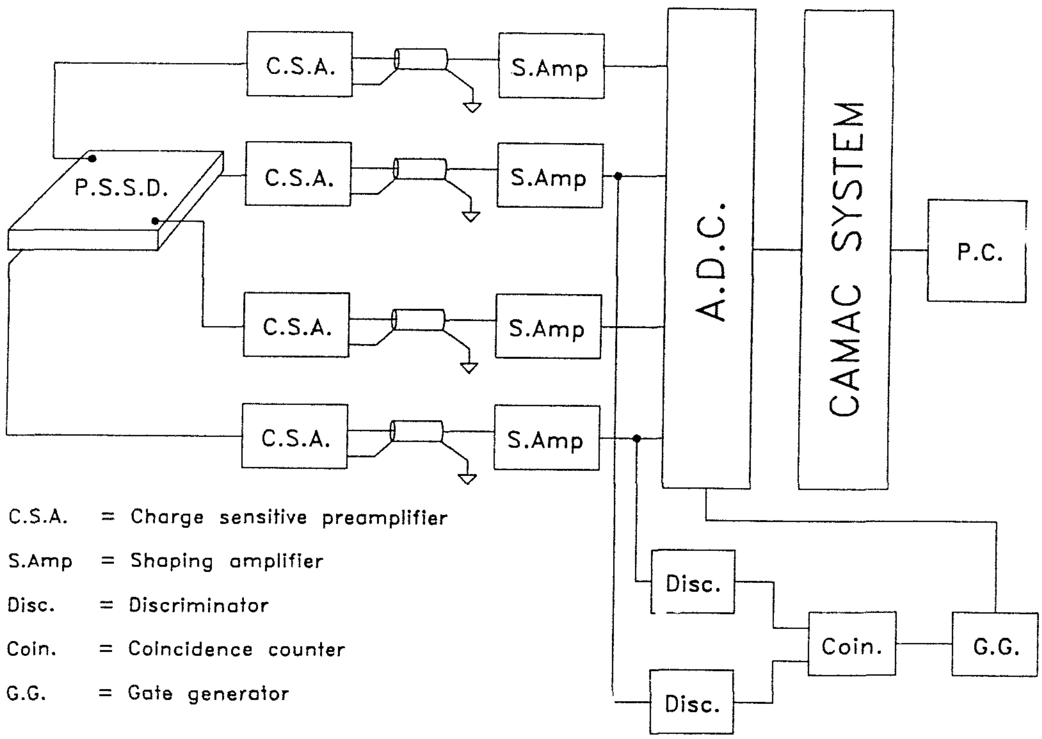

Figure 8.13: *Schematic diagram of the PSD test system*

Since the signal-to-noise ratio from these measurements was expected to be high, four Aurel single-channel hybrid preamplifier chips, each offering modest noise performance of approximately 500 electrons rms were chosen. Initially, a prototype circuit was designed and tested by mounting the components upon vero board which was located within a well screened aluminium box outside of the vacuum chamber.

However, long cables were necessary in order to make the electrical connection with the diode, increasing both the capacitance, and the RF noise picked up by the cables. Therefore, it was decided that a dedicated signal processing board should be fabricated that could be included within the vacuum chamber, connected to the PSD with short flying leads. Such a board was constructed, and is illustrated in Figure 8.14.

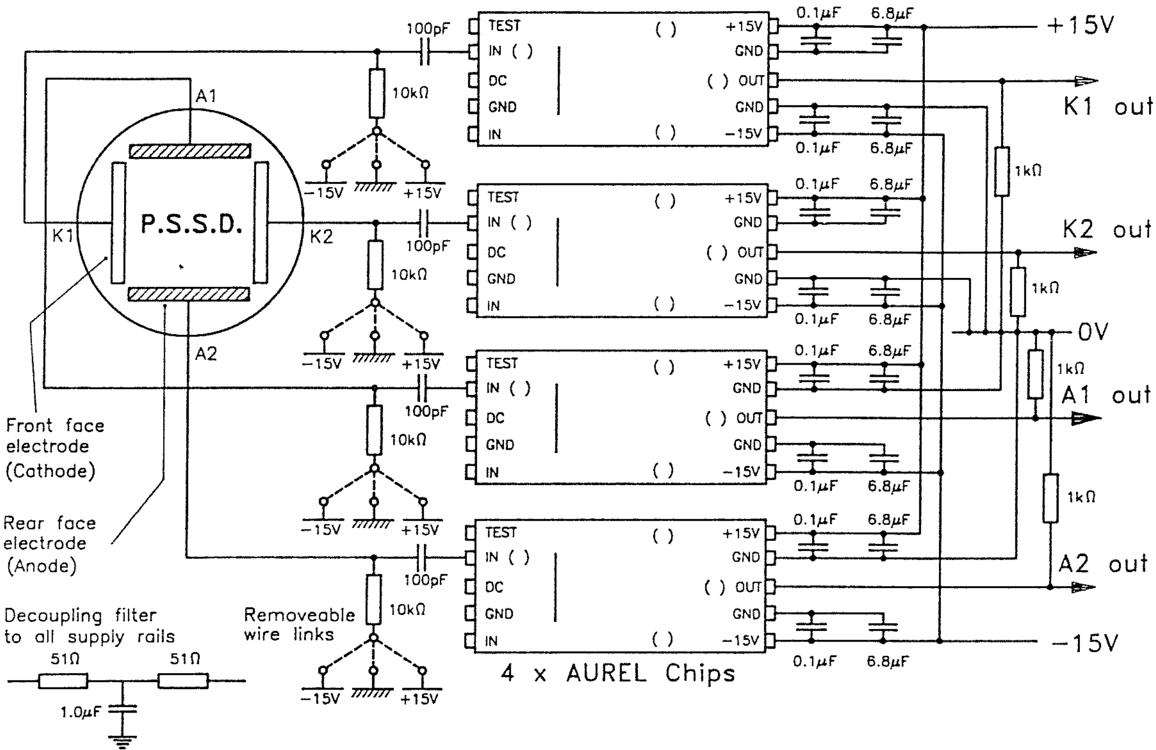

Figure 8.14: *A dedicated four channel signal processing board*

This circuit was subsequently demonstrated to work very effectively, and did not appear to be significantly influenced by external sources of noise. This is perhaps due, at least in part, to the very large ground plane supplied on both sides of the double-sided circuit board, isolating the board very effectively from most sources of electrical interference in the laboratory.

8.6.3 Energy Resolution

The energy deposited within the PSD by the incident α-particles was used to obtain an energy spectrum (see Figure 8.15). Measurements of this spectrum have been made to determine the energy resolution when illuminated with α-particles. This data approximates to the energy resolution expected if the PSD were to be illuminated with photoelectrons inside a position-sensitive HPD. The low energy detection threshold of a position-sensitive HPD based upon the PSD can also be predicted from this result. This value can then be used to predict the largest sensitive area PSD that would yield a resolvable signal above the noise for nuclear medicine applications at 122 keV.

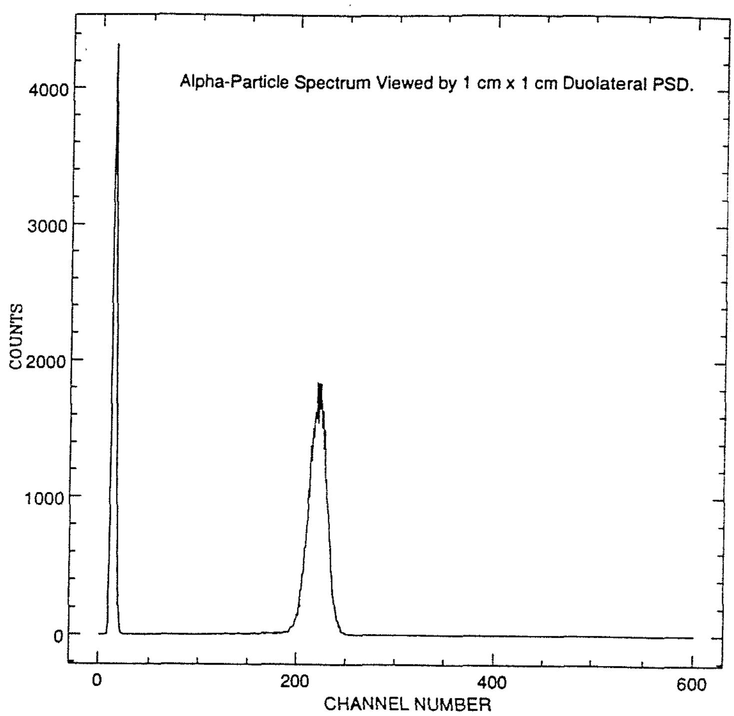

Figure 8.15: *Energy spectrum of ^{241}Am α-particle deposit in a duolateral PSD*

It can be seen from this spectrum that the signal-to-noise ratio is approximately 9:1, whilst the energy resolution of the PSD used to detect 5.5 MeV α-particles is approximately 11% FWHM. Each α-particle directly depositing its energy within the PSD has been calculated to be roughly equivalent to a single 100 keV γ-ray energy deposit within a CsI(Tl) detector crystal, viewed by a position-sensitive HPD. We can therefore use this result to make some positive predictions for a position-sensitive HPD based upon the duolateral PSD.

Theoretically, these values suggest that a position-sensitive HPD based upon the PSD could detect incident γ-ray energies as low as 10 keV. Since both the leakage current and the noise of a PSD scale linearly with surface area, this result more usefully implies that the sensitive area of the device could be increased to approximately 1000 mm^2 for the detection of 122 keV γ-rays. Whilst this is approaching the kind of sensitive area that would be useful for applications in clinical nuclear medicine, we have concluded that this result was either adversely affected by noisy signal processing electronics, or alternatively that the particular device that we used for these measurements was of poor quality. It is possible that α-particle scattering in the thin metal protective layer of the source has broadened the energy spectrum. However, this does not account for the surprisingly low SNR obtained with this detector which is approximately an order of magnitude less than we would have expected to have observed using Aurel hybrid preamplifiers which exhibit approximately 500 electrons rms in noise.

8.6.4 Spatial Resolution

Using the very simple two pinhole mask and test system described previously, the spatial resolution when bombarded with 5.5 MeV α-particles was found to be 1.38 mm FWHM (see Figure 8.16).

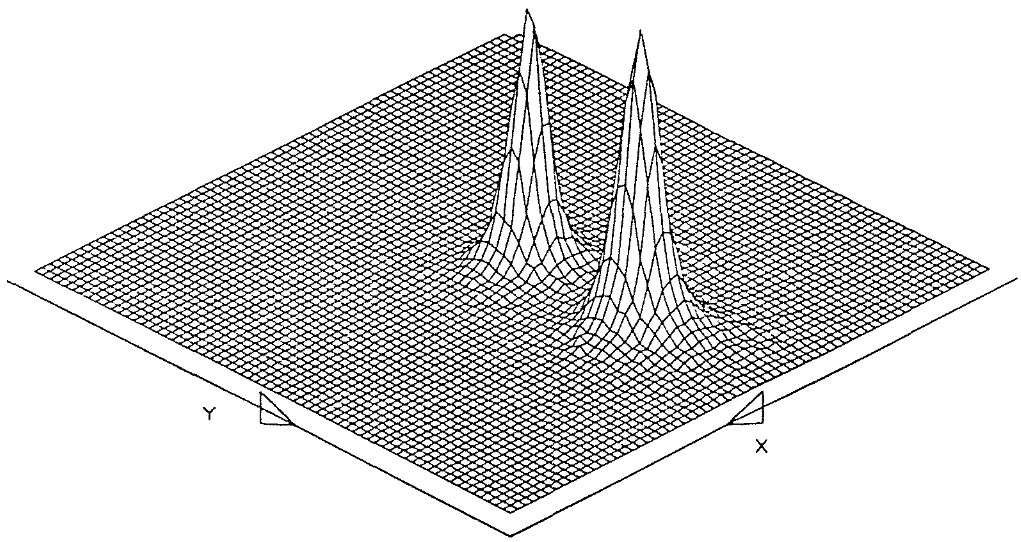

Figure 8.16: *Intensity plot of 5.5 MeV α-particles, source-detector separation = 3 mm*

In principle, by increasing the distance between the source and detector, the solid angle can be reduced, enabling the spatial resolution to be reduced below 1 mm FWHM. It has been demonstrated that the intrinsic spatial resolution can be reduced to only 370 μm FWHM by increasing the source-detector separation to 100 mm(see Figure 8.17).

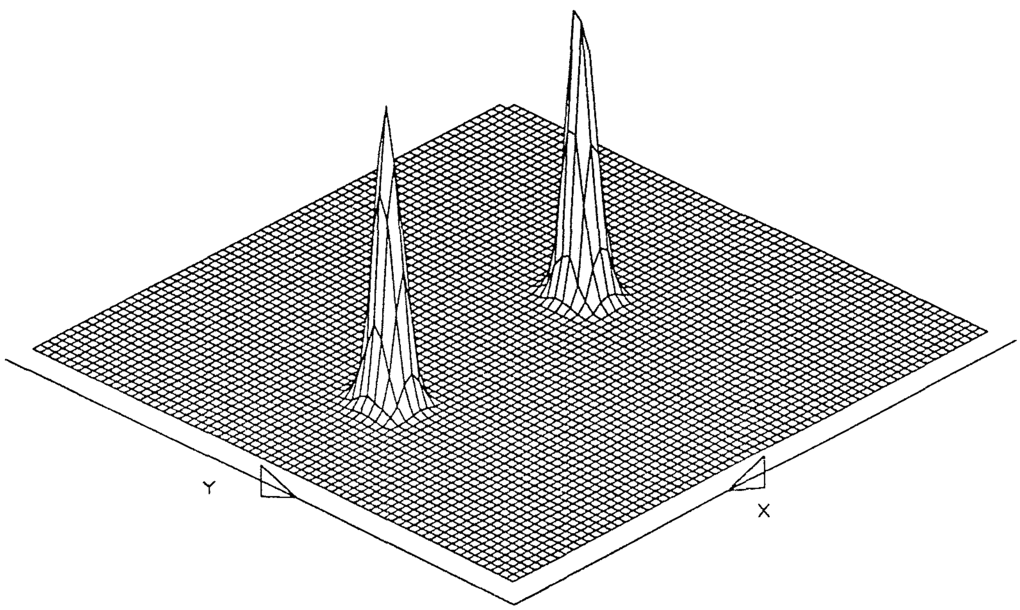

Figure 8.17: *Intensity plot of 5.5 MeV α-particles, source-detector separation = 100 mm*

8.6.5 Position Linearity

Like most other devices which offer the benefit of intrinsic position-sensitivity, the PSD suffers from non-linear position response, resulting in some parts of the image becoming distorted. In the duolateral PSD, this is known as *pin-cushion* distortion, and is most problematic towards the edges and corners of the device where the electric field gradients are most intense. In order that the degree of distortion could be assessed for an ion-bombarded PSD, it was decided that a mask comprised of a matrix of 64 holes, each having a diameter of 0.3 mm, and on a pitch of 1.3 mm between centres be placed between the source and the detector. The resulting plot illustrates the very low degree of pin-cushion distortion when the duolateral PSD is bombarded by ^{241}Am α-particles at equispaced intervals over the area of the device (see Figure 8.18).

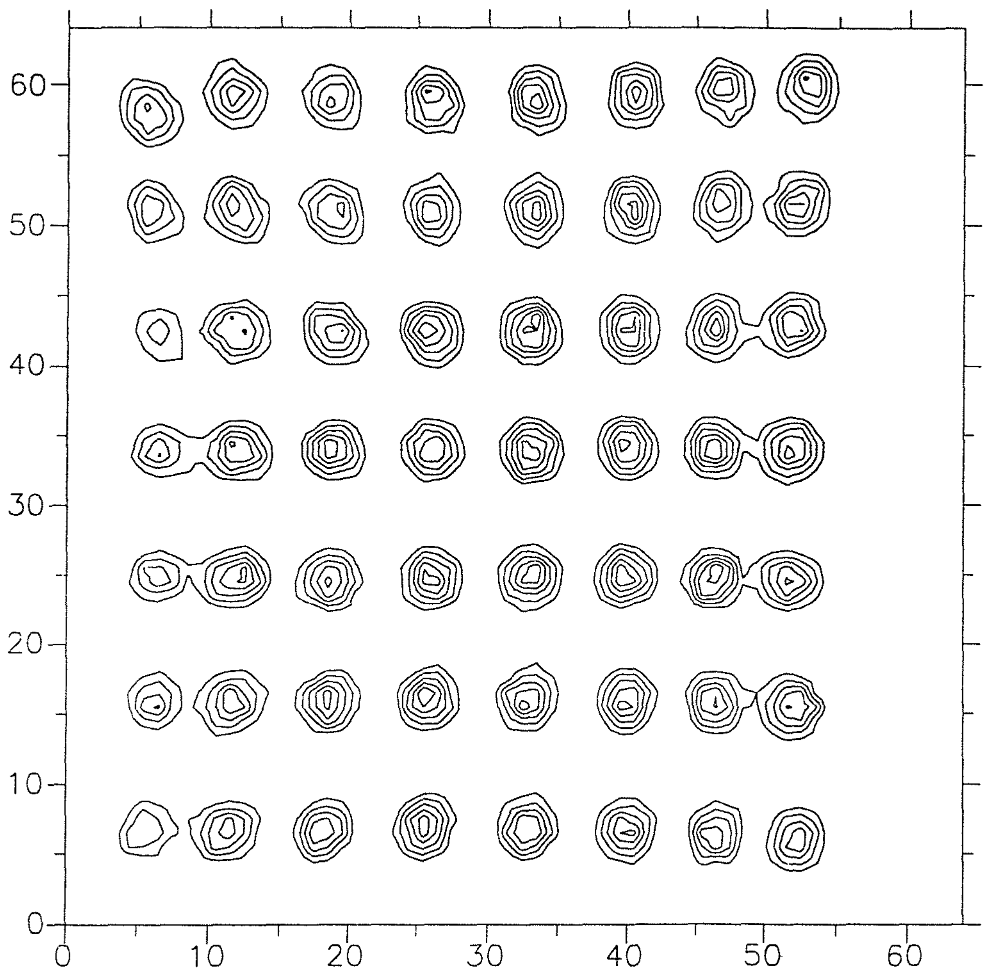

Figure 8.18: *Position linearity of a duolateral PSD*

However, despite careful calibration of the data acquisition system to ensure that each channel provided equal gain, the pitch of these reconstructed positions was clearly different in each axis. By comparing our results with those of Doke et al. [37], and particularly with those of Teraoka et al. [120], it is clear that the charge division should be approximately equal in both axes. After carefully adjusting the data acquisition system in an attempt to identify the cause of the pulse-height difference in two channels, we were unable to determine a cause. We have therefore concluded that this apparent inexplicable and very obvious difference between the way the charge was dividing in the X direction, and the Y direction is a result of the construction of the diode itself. Since once again the quality of the diode had been called into question, it had now become necessary to specifically determine the performance characteristics of the PSD used in our measurements.

8.6.6 Diode Characteristics

In order that accurate measurements could be made of both the diode leakage current, and capacitance as a function of reverse bias voltage, the device was connected to a Hewlet Packard 4145A semiconductor parameter analyser to determine the leakage current. An integration time of 320 ms and a step size of -1 volt was chosen to provide a detailed plot for voltages ranging up to -65 volts (see Figure 8.19).

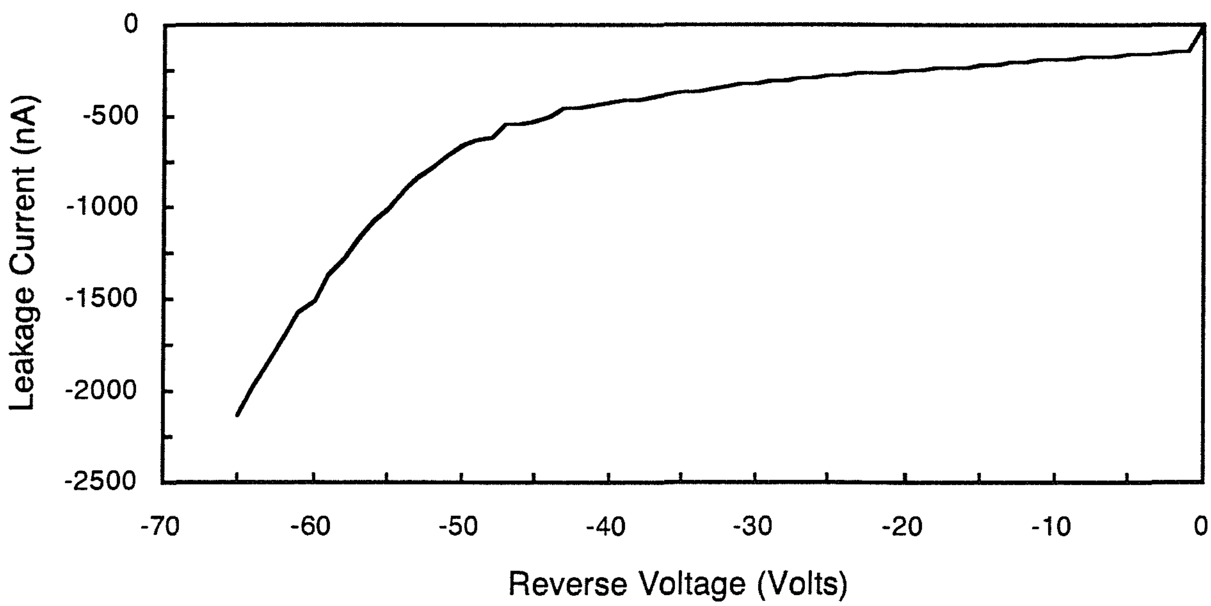

Figure 8.19: *PSD leakage current as a function of reverse bias*

This result confirmed our initial suspicions that the device was indeed not of the very highest quality. We had been operating our diode well within the manufacturers specifications with a reverse bias of -30 volts, at which the leakage current flowing from the device was approaching 500 nA. In a good quality PSD, we might reasonably expect a current of a few nA/cm^2. With this value being so high, it was therefore necessary to ensure that full depletion of the diode was occurring at this voltage.

The changing capacitance of the diode as a function of reverse voltage usually indicates the point where the diode becomes fully depleted, and gives a general indication to the depletion depth. The capacitance of the PSD was therefore measured as a function of reverse bias in steps of -1 volt using a Hewlet Packard capacitance tester, and the plot illustrated in Figure 8.20 obtained.

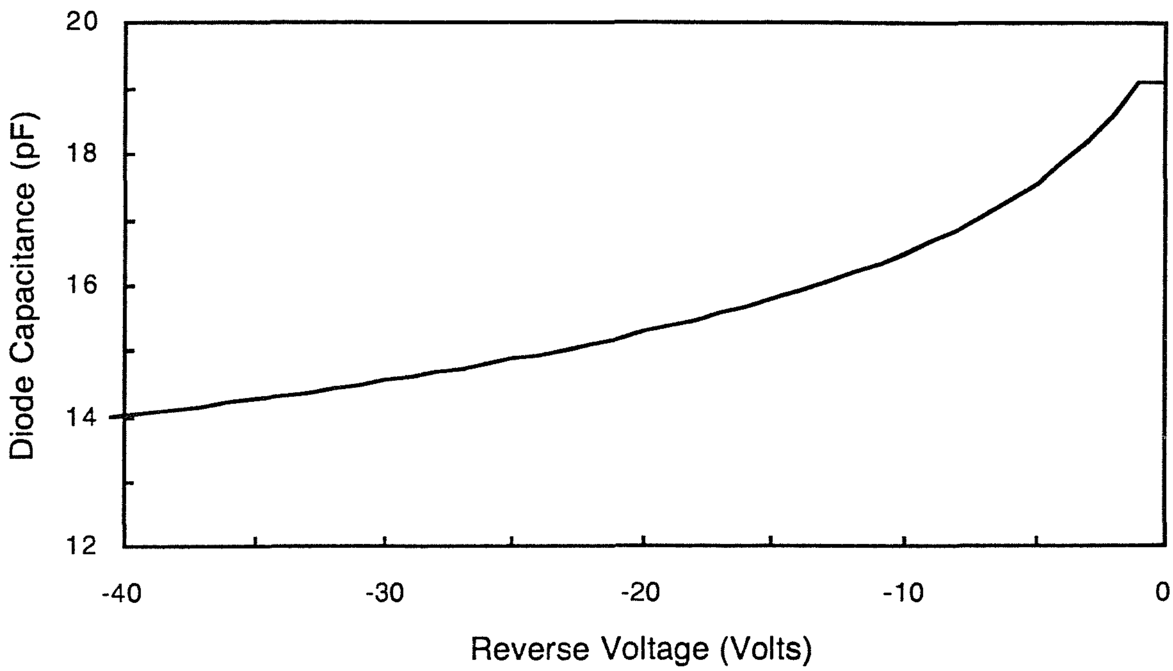

Figure 8.20: *PSD capacitance as a function of reverse bias*

The very low value of capacitance obtained at each step in the plot indicates that the depletion depth for this diode is large, whilst there is no observable and clear transition to a constant value of capacitance. This would imply that at -30 volts bias the device is not fully depleted, and so a higher leakage current might be expected. Since the depletion depth is fixed at the time of wafer fabrication, it would seem reasonable to conclude that the results that were obtained were not adversely affected due to deterioration in the chip through its bombardment by charged particles.

8.6.7 Typical Characteristics of an 'Ideal' PSD

In order to test the claim that the PSD used in our measurements was not of typical quality, it was necessary to compare its performance characteristics with another device of similar dimensions. For the purposes of this comparison the Hamamatsu S1300 PSD was chosen because of its comparable sensitive area [44], and the same leakage current and capacitance measurements made. These results are presented in Figure 8.21.

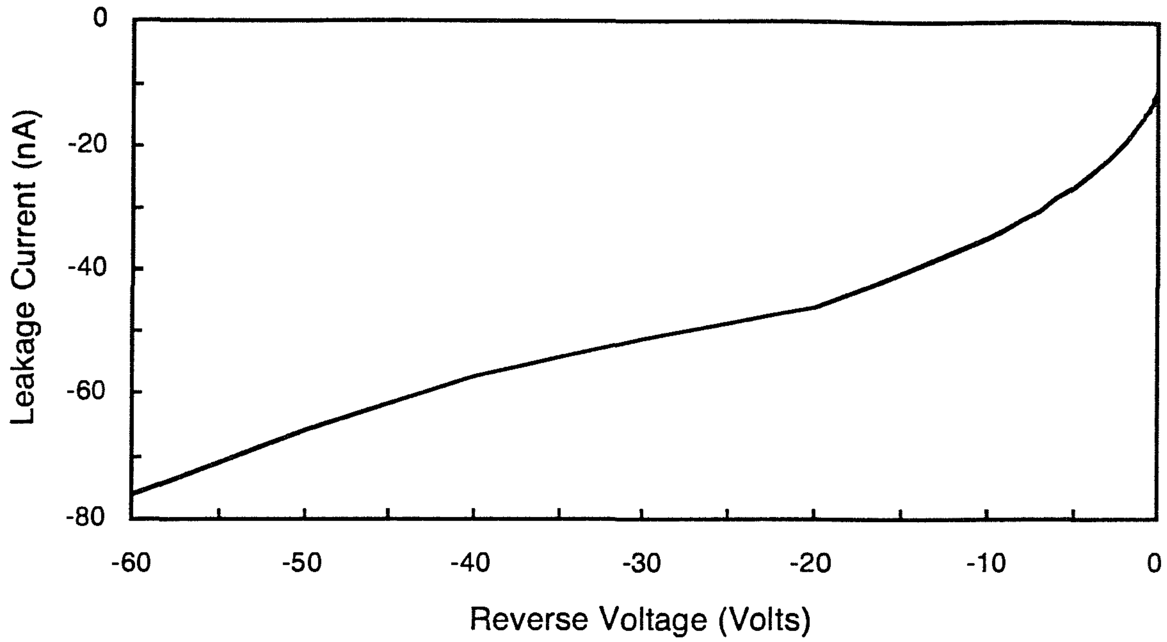

(a) PSD leakage current as a function of reverse bias

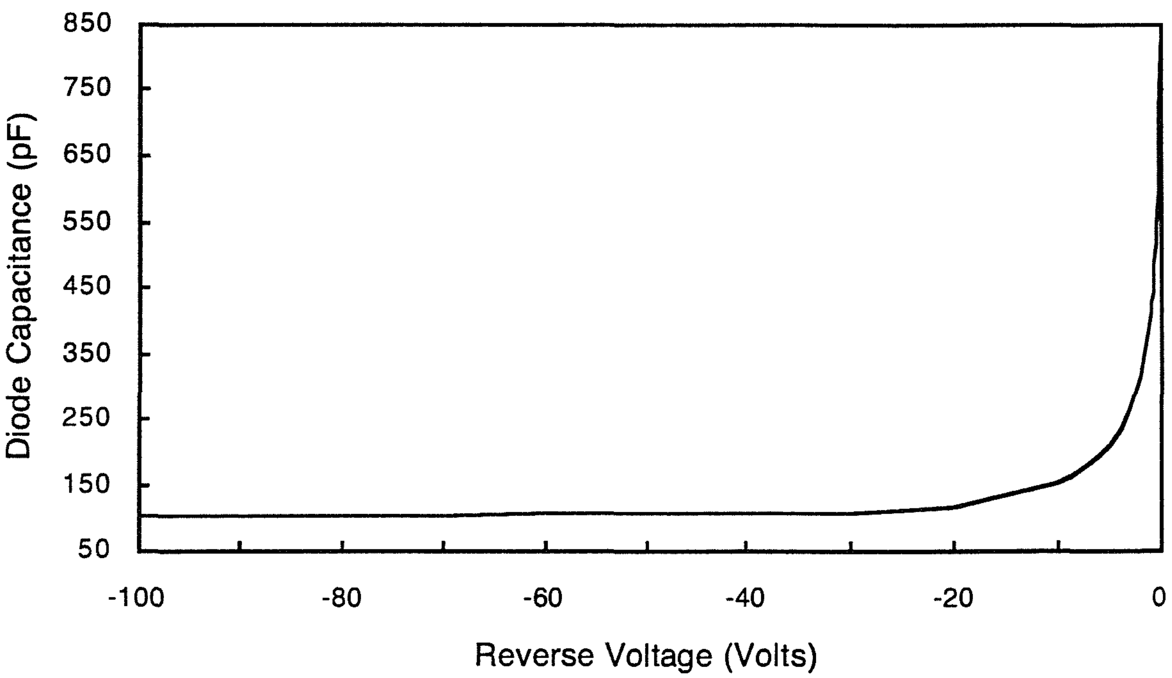

(b) PSD capacitance as a function of reverse bias

Figure 8.21: *Characteristics of an 'ideal' PSD*

The most noticeable result of these measurements is that the leakage current per cm^2 at -30 volts bias is almost an order of magnitude improved over the Silicon Sensor device. Plotting capacitance as a function of reverse voltage yields capacitance values ranging between 836 pF and 106 pF, and at approximately -20 volts bias there is a clearly visible transition where full depletion has occurred. At full depletion the capacitance of the Hamamatsu device is an order of magnitude greater than the Silicon Sensor diode, implying a considerably reduced depth of depletion region for this PSD. It would also appear from these results that there are clearly constructional differences between the two devices that enable the Hamamatsu PSD to offer excellent performance. It would appear that the higher resistivity silicon used by Hamamatsu is partly responsible for this improved response.

8.7 Design Considerations for the HPD

In parallel with this study of the PSD, we conducted a design study for a new generation of hybrid photodiode for the detection and imaging of x-rays and γ-rays for nuclear medicine imaging applications. This project was carried out in close collaboration with Electron Tubes Limited (ETL), who made their technical expertise, vacuum photocathode deposition process, production and test equipment available to us.

8.7.1 Development of a single-pixel 'Flip-Chip' PiN Diode for the HPD

Once fabricated, in order that silicon devices can survive in the presence of the alkali photocathode materials Caesium and Antimony, an impervious barrier must be formed to protect the diode from contamination in the presence of alkali metals. In order to guarantee the performance of the semiconductor devices, a semiconductor manufacturer was therefore chosen that had experience of using silicon nitride in addition to the standard silicon dioxide wafer passivation. Discussions with Silicon Sensor GmbH., of Berlin, Germany, led us to feel confident in their capability to develop a custom 'flip-chip' device in which connections to both the ohmic and junction sides of the diode would be made on the rear surface only (see Figure 8.22).

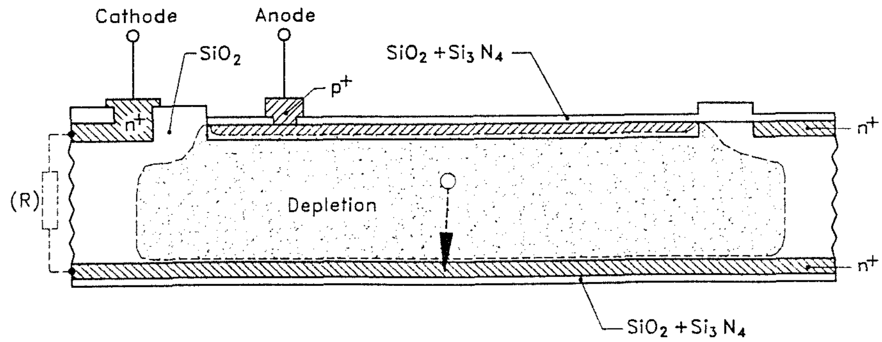

Figure 8.22: *The structure of a 'flip-chip' silicon PiN photodiode*

Such a design would require no wire bonding to the upper surface of the diode, and enables the device to be soldered onto a ceramic header substrate of the same dimensions as the device itself. Since these connections would be made under the diode itself, it would therefore be possible to increase the surface-area of the diode, and reduce the amount of *dead space* which would otherwise have been occupied by bond pads. It was agreed that we should work with Silicon Sensor to develop at least twenty hexagonal silicon nitride passivated 'flip-chip' devices each having active dimensions of 11 mm A/F which were required for another project running in parallel.

8.7.2 Development of the Ceramic Enclosure

Initial discussions between the author, Dr. David Ramsden, Electron Tubes Limited (ETL), and the precision ceramics supplier Morgan Matroc Ltd., led to the design of a ceramic enclosure which was both practical and cost-effective (see Figure 8.23).

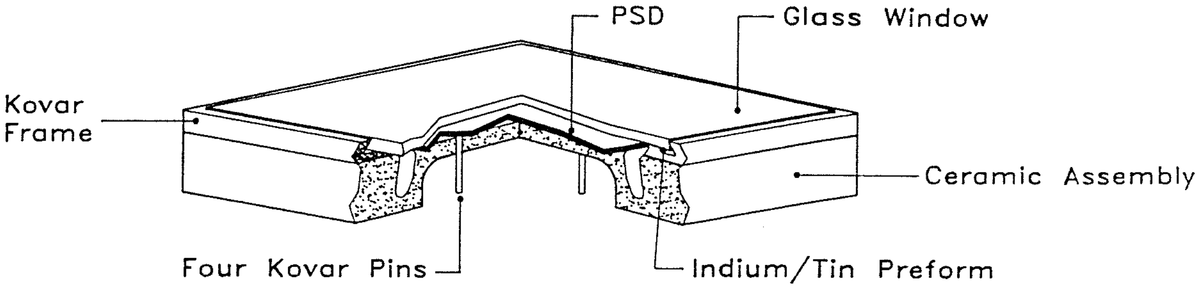

Figure 8.23: *Design of the ceramic enclosure*

This design of ceramic enclosure had a square cross-section, and outside dimensions of 62 mm x 62 mm x 10 mm. Within the package a position-sensitive silicon PiN diode having dimensions of 50 mm x 50 mm could be located in close proximity to the planar glass window. This dimension was chosen in order to moderate development costs by selecting the largest single position-sensitive PiN diode that can be fabricated from a standard 3" diameter silicon wafer. Such a design would provide an HPD having a fractional sensitive area of 65% which is considerably higher than the existing circular devices manufactured by DEP Instruments of Roden in the Netherlands, but more importantly, being square these new HPDs will offer excellent tessellation properties.

An initial batch of five ceramic assemblies were produced by Morgan Matroc to this specification. It was proposed that the integrity of these assemblies would be verified using the newly developed 11 mm A/F hexagonal 'flip-chip' diodes from Silicon Sensor. Theoretically, these innovative devices could be biased through electrical connections to one side of the diode only. Although they possess no intrinsic position-sensitivity, they were thought to provide an excellent test of both the assembly process, and the 'flip-chip' concept, without requiring any further financial commitment to develop a large-area position-sensitive device based upon this technique. There still remains five partially completed assemblies at the factory, awaiting our instructions for the artwork pattern that we require in order to connect the large-area position-sensitive anodes. It was planned that this information would be given once the initial investigation had been completed successfully.

8.7.3 The Assembly Process

Before developing an expensive position-sensitive solution, each stage in the assembly process needed to be evaluated. In particular, the integrity of the hermetic seal between the square kovar/indium frame, and the chrome-plated edge of the glass entrance window. In addition, the photocathode survivability after the vacuum sealing process, and the subsequent stability of the photodiode are also very important elements of the design which needed to be confirmed. All assembly work, together with the deposition of photocathodes using the transfer process took place at ETL.

Assembly was carried out under hard vacuum conditions using specially made jigs and tools manufactured by the mechanical workshop in the Department of Physics at Southampton. Vacuum sealing of each assembly was achieved by heating an indium-tin preform washer in a vacuum using an RF furnace through several cycles to remove impurities. The window-frame/preform assembly was then removed, and profiled using NC milling techniques to provide the optimum shape for wetting to the glass window whilst at the same time minimising the undesirable capillary effect experienced during the final wetting process during manufacture. Final assembly of window and photocathode to window frame, ceramic carrier and diode is done under hard vacuum conditions and the whole assembly is heated to 160° C in a furnace. Despite having carefully profiled the indium preform to remove excess material, after the wetting process we observed that *wicking* of the indium along the inner surface of the glass had occurred. Upon further investigation, we found that a graphite stopping compound applied to the inner surface of the window overcame this problem.

Following the successful completion of this initial stage of the project, it was proposed that the next step be the incorporation of a position-sensitive PiN diode as the anode of the device. Silicon Sensor GmbH located in Berlin, Germany, again agreed to undertake the development and fabrication of a new type of rear-illuminated tetra-lateral PSD which would incorporate the 'flip-chip' technique. This configuration, as well as protecting the front surface resistive layer from electron bombardment, also avoids having to make fragile wire bond connections to the top surface of the diode which is in a high field region. Once again, all assembly work would take place at ETL together with the vacuum deposition of photocathodes using the transfer process. All assembly would be carried out under hard vacuum conditions using the same jigs and techniques used in the first phase of the project.

8.8 Outcome of Investigation

The outcome of this project clearly depends upon achieving competence in all of the stages in the production process previously mentioned. The fabrication of both a photodiode employing the 'flip-chip' technique, and high quality ceramic assemblies which form a hermetically sealable enclosure, are each pivotal to the success of the development of the position-sensitive scintillation counter that has been proposed.

8.8.1 Development of the 'Flip-Chip' Silicon PiN Diode

We have attempted to operate the devices supplied to us from Silicon Sensor in our standard laboratory test configuration with flying lead connections made to the solderable contacts. Two means of connecting the leads were tested:

(a) Silver-loaded epoxy contacts

(b) Direct soldered contacts

Neither method provided a working detector, and unfortunately it was not possible to determine whether the failure was due to a faulty chip, contamination or heat damage. Measurements have been made of two early devices which were supplied by Silicon Sensor for testing. The first device, labelled Diode 1, failed to work at all, and provided no observable signal.

The second device, labelled Diode 2, worked well initially. Performance was judged to be typical of that observed for standard Hamamatsu devices having dark currents ~1 nA. However, the diode rapidly became more noisy, and after one hour was no longer usable. This behaviour implies that perhaps there could be some form of damage occurring, probably as a result of the connections. It was felt that this was not due to heat damage, which would be immediately apparent, but more probably due to contamination from the solder.

A Hewlett Packard 4145 picoammeter was used to measure the leakage current for a random sample of the photodiode chips. A standard prober system was used to make contact with the chips in order to avoid the problems associated with making permanent connections.

Diode Number	Leakage Current (nA)	Reverse Voltage (Volts)	Breakdown Potential (Volts)
Scheibe 42/9 #1	23	-30	-50
Scheibe 42/9 #2	32	-30	-50
Diode #1	85	-30	-50
Diode #2	4	-20	-30

Table 8.1: *Leakage current characteristics when probed at Southampton*

The results of these measurements are illustrated in Table 8.1 where it can be seen that each device appeared to be exhibiting either soft breakdown, or high leakage currents. Measurements of the dark current of the devices were made at intervals up to 100V bias, which subsequent tests at Southampton have indicated may be too high for optimum operation of the devices. Subsequent discussions between ourselves, DEP, and Canberra, indicated that the failure of these diodes was a consequence of providing inadequate protection of the high resistivity silicon against contamination from the solder. Some of the devices were retested and further examined to try to identify the problem in more detail, and a number were supplied to ETL for these purposes (see Table 8.2).

Diode Number	Specified Leakage Current (nA)	Measured Leakage Current (nA)
1	12	55
2	12	70
3	12	30
4	12	40
5	12	30
6	1	10,000

Table 8.2: *Leakage current measurements performed at ETL*

The measured leakage current from each of these devices was thus independently assessed, and demonstrated to be inferior to the manufacturers stated specifications in every case (R M^{c}Alpine [79]). In addition, five further diodes were investigated by plotting their I-V characteristics within the Microelectronics Department at Southampton using the Hewlet Packard 4145A picoammeter (see Figure 8.24).

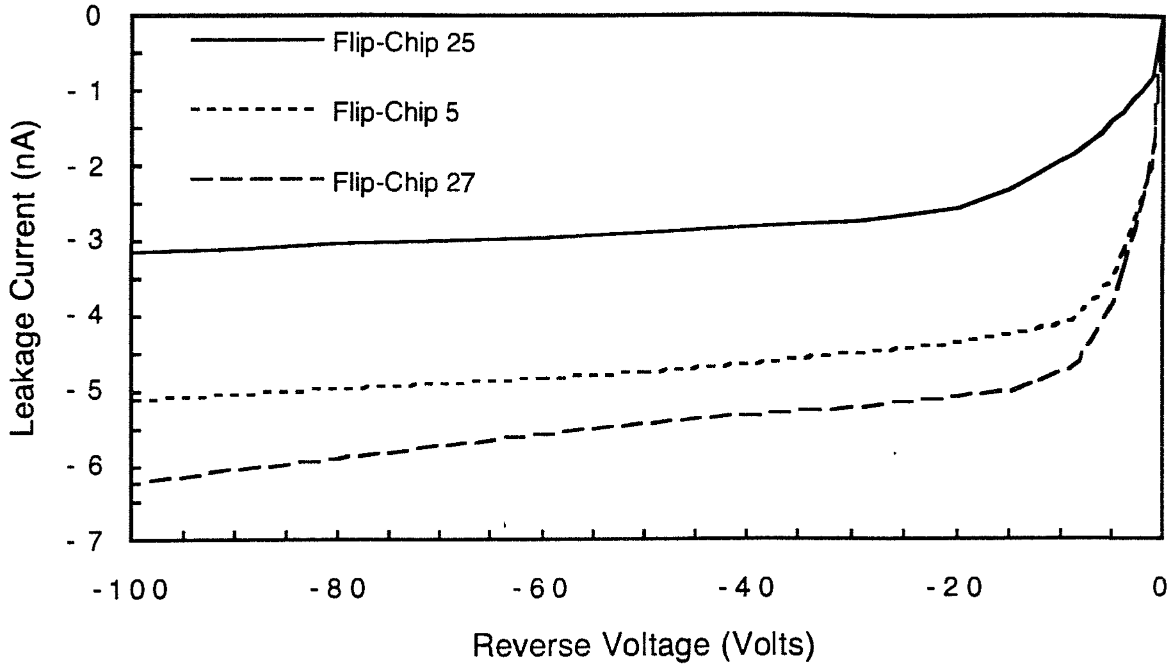

(a) Leakage current characteristics of the best three 'flip-chip' diodes

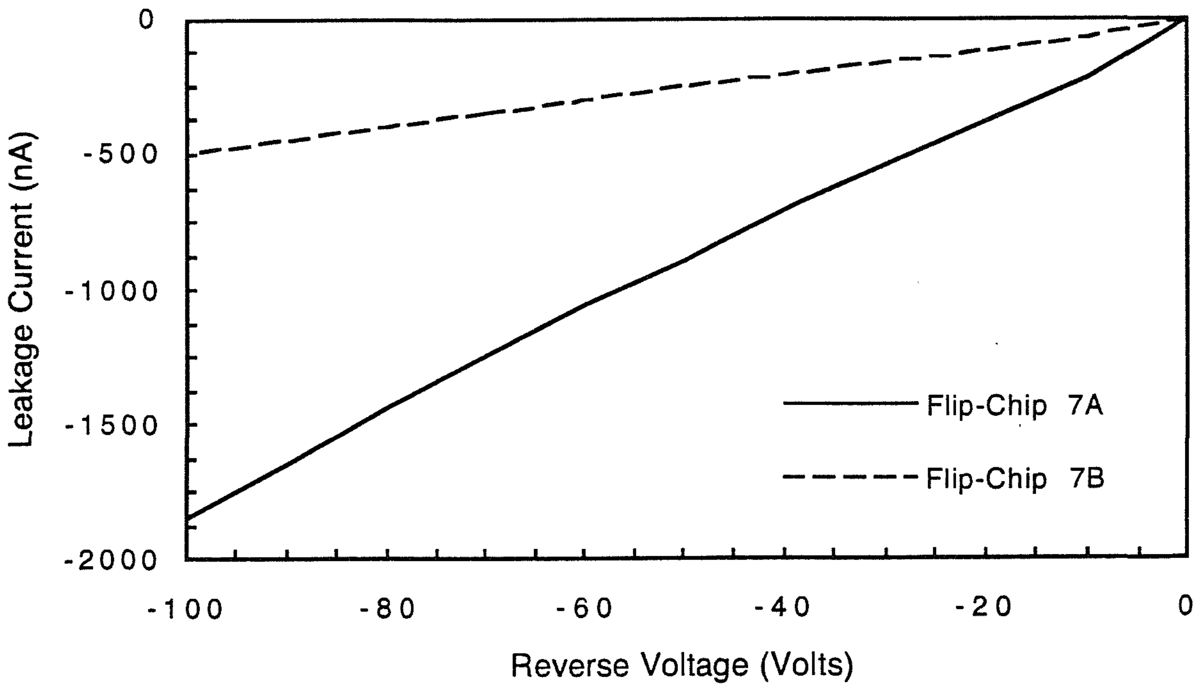

(b) Leakage current characteristics of two 'improved' flip-chip diodes

Figure 8.24: *Performance characteristics of the 'flip-chip' diode*

These results demonstrate the best and the worst of the diodes that were received. The two *improved* diodes were fabricated using high resistivity silicon in order to attempt to reduce the bulk leakage current in the device. Finally, discussions with the manufacturer led to their admission that the whole batch of devices that we had received from them were in fact shorting out when connected, and could not be remedied without remasking and redesigning the chips. Silicon Sensor have subsequently abandoned the concept of a solderable 'flip-chip' device in favour of more conventional technology.

8.8.2 Development of the Ceramic Enclosure

In addition to the problems associated with the fabrication of flip-chip devices described previously, the development of the ceramic enclosures also failed to proceed as smoothly as we had expected. Once again there were two principal problems associated with the development of the square ceramic structures that we had not envisaged at the initial discussion stage. The first was that of achieving an adequate hermetic seal on each of the four gold-plated kovar leadthroughs. Difficulties were experienced at Morgan Matroc in brazing the pins into the through-plated laser drilled holes. This ultimately led to the delivery of ceramic assemblies which when tested further at ETL proved each assembly to have a leak on at least one pin. A single ceramic assembly was thought not to have any leaks, and was used to construct a prototype HPD. Once sealed, the photocathode was monitored visually for a period of 48 hours. Unfortunately at the location of one of the leadthroughs, the photocathode was observed to disappear, indicating the presence of a small leak at this location (see Figure 8.25).

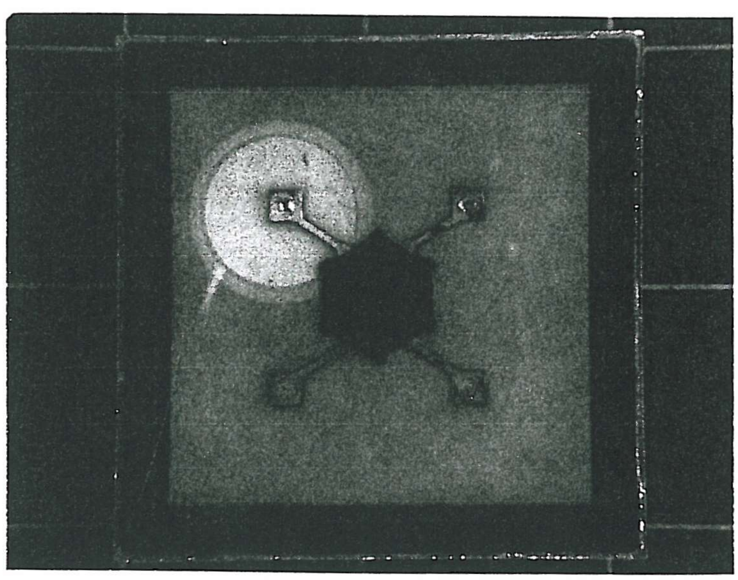

Figure 8.25: *A leak on one of the leadthroughs of an assembled HPD*

The second problem was that of micro-cracking on the inside corners of the ceramic assemblies (see Figure 8.26). This was believed to be less serious than the leaks which were detected from the leadthroughs, but if these cracks were to propagate further then the hermetic integrity of the enclosures could potentially be compromised.

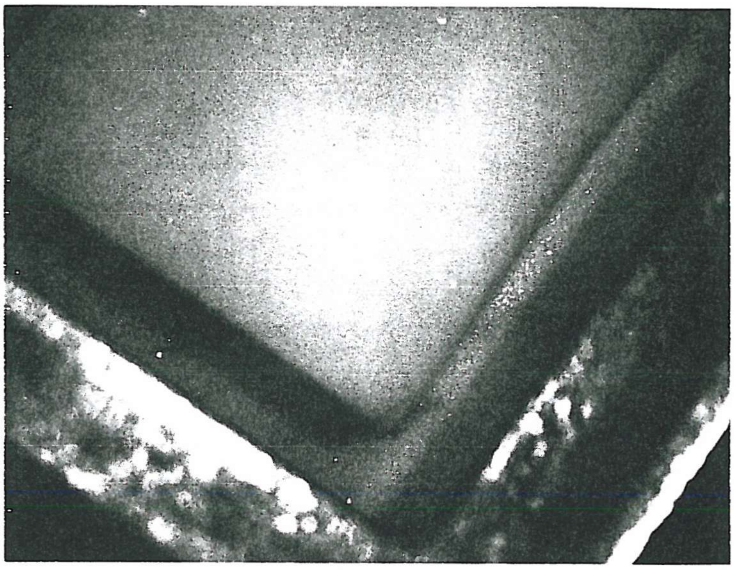

Figure 8.26: *Micro-cracking in the corners of the ceramic assemblies*

Both of these problems were believed not to be helped by the move of the ceramics division of Morgan Matroc from London to Rugby part way through the project, with the associated delays caused by moving the production equipment. These problems remain unresolved at the time of writing, although Morgan Matroc have given their assurance that further enclosures will maintain their high vacuum integrity.

8.9 Conclusions & Future Work

The case for a position-sensitive hybrid photodiode has been introduced in this chapter, and offers some performance advantages over conventional photon counting devices for new applications in nuclear medicine and auroral imaging where high signal-to-noise ratios and excellent low energy threshold are important. However, the development of such a device is non-trivial, and certain problems exist that remain to be overcome.

The performance of a duolateral PSD used to detect charged particles has been measured, and its suitability for inclusion within a position-sensitive HPD considered. This work suggests that a modestly proportioned PSD shows excellent potential for inclusion within such a device, offering both excellent spatial resolution, and position linearity for low cost. Since the PSD has demonstrated greater position resolution than would be required of a practical gamma camera system, an electrostatically focused HPD with a small PSD anode could achieve a larger field-of-view whilst preserving detail in the image.

The newly fabricated 'flip-chip' devices suffered from two serious flaws which prevented successful operation in the manner for which they were intended. Firstly, the devices when characterised were found to be outside of the specified range of leakage current as stated by the manufacturer. Secondly, and more importantly, the devices were found not to be solderable, but instead shorted due to an error in the design and construction of the chips which remains to be resolved. Therefore, this novel concept has for the moment been abandoned in favour of more conventional diode structures and contacting techniques. It remains an excellent idea in principle, and will most likely be of interest for some future application in physics.

Whilst the successful development of these components is pivotal in achieving the stated objective of a position-sensitive HPD based upon the proximity focused technique, a large area 'flip-chip' would not be necessary for an electrostatically focused tube such as those that have been developed by DEP in parallel with this research. The measurements made with the duolateral PSD from Silicon Sensor are encouraging and have proved that in principle this diode would offer excellent performance if included within an HPD tube. Therefore, it would appear that an electrostatically focused position-sensitive HPD based upon conventional PSD technology would at the present time offer the highest probability of success. This configuration is currently being considered by the collaboration between DEP and Canberra, and an analysis of the production requirements suggest that by utilising existing windows and enclosures, the costs involved in such a development could be kept to a minimum.

At the begining of this chapter, we stated the requirement for a large ratio between sensitive and total areas, and the need to develop a device capable of tessellating together with other similar devices. It has been suggested that a multi-pixel silicon device could be bump-bonded to a ceramic header and mounted within a thin glass envelope of either square or hexagonal geometry to provide a tube that offers intrinsic position-sensitivity. Clearly it would be a relatively straightforward development to include a PSD within the same glass enclosure. In conclusion, the work conducted at Southampton in the last three years has undeniably contributed to an improved understanding of the problems associated with the fabrication of a new position-sensitive HPD, and through our collaborations we have been in part responsible for influencing future developments in this field.

Chapter 9

A Single-Anode Hybrid Photodiode for Scintillation Counting.

9.1 Introduction

In the preceding chapter, the development of a position-sensitive hybrid photodiode for scintigraphic applications in nuclear engineering and nuclear medicine was discussed. Many design and manufacturing difficulties were experienced which has ultimately precipitated the withdrawal of the principal industrial sponsor's support for the project. Despite these problems, the development demonstrated several key principles, and proved that the objective of a continuously position-sensitive HPD will shortly be achieved. Since there was little that could further be demonstrated by continuing with the development beyond this initial phase, it was decided that further work on this project should be temporarily suspended until alternative ceramic and silicon suppliers could be found. However, during the development of this detector, two other manufacturers were also considering the benefits offered by such a device for a range of applications. With the suspension of our own development project, a collaboration was sought between ourselves, DEP, Canberra, and Dr. Riccardo DeSalvo. This collaboration, using new funding made available from the EC Human Capital and Mobility Programme, has enabled us to further pursue our ideas for a position-sensitive scintillation counter based upon a HPD. The links and trust that we have built as a direct result of this collaboration have enabled us to make considerable steps towards this goal, and a number of prototype devices have been made available to us for these purposes. This chapter describes the results of measurements made using these recently available prototype devices for γ-ray scintillation counting.

9.2 The HPD Development

A continuing close collaboration between DEP, the silicon diode manufacturer Canberra, and Dr. Riccardo DeSalvo who is currently working on the development of the gravity wave experiment at INFN Pisa has resulted in the currently available hybrid photodiode tubes. The resurrection of the HPD electron multiplier was catalysed by the ideas and efforts of Dr. DeSalvo who, having secured significant funding from INFN as part of the CERN-LAA project, approached DEP with his proposals for a new type of electron multiplier tube. These first generation tubes were therefore specifically designed for particle-beam calorimetry experiments based at CERN, where immunity to the very high magnetic fields which are a product of both the charged particle beam confinement process, and the superconducting magnets used to bend the beam, are required. When the LAA project later stalled, the uncertain future for these novel devices has encouraged the collaboration between DEP and the University of Southampton in an attempt to identify suitable applications in nuclear medicine and other fields where the HPD might prove advantageous.

A variety of commercially available HPDs are now manufactured by DEP [35]. Recent additions to the product range are devices which have segmented anode structures, providing some limited position-sensitivity. Currently available tubes have 7 hexagonal diodes grouped concentrically, although two prototype HPD tubes are currently being tested at Southampton which have 19 hexagonal diodes grouped concentrically. All HPDs fabricated at the present time fall into one of two generic groups, either electrostatically or proximity focused.

9.2.1 Electrostatically Focused

Electrostatically focused tubes use a spherically ground glass or fibre window upon which the photocathode has been deposited using the transferable process. A series of electrodes maintained at negative potentials enable the photoelectron charge to be focused onto a silicon diode inside a hard vacuum enclosure. Photoelectrons are focused onto the imaging plane in either a *fountain-tube* or *cross-focused* arrangement. Here, depending upon the ratio of the high potentials applied to the photocathode and field rings, the photoelectrons either converge to form a small spot which is then read out by a small non position-sensitive PiN diode, or cross over to form a minified image which can be read out by a single large non position-sensitive PiN diode, or by an array of small PiN diodes if position-sensitivity is desired.

9.2.2 Tube Characteristics

The electrostatic focusing described previously enables a reduction in the size of the photoelectron distribution to correspond with a silicon anode of very modest dimensions. Because each anode element is only required to cover a much smaller area, both the diode capacitance and leakage current will be reduced, since these quantities scale in direct proportion to the surface area of the device. The resulting reduction in electronic noise enables this variant of the HPD to offer a very modest low energy detection threshold, and excellent signal-to-noise ratio (SNR). However, as one might expect, non-uniformities are introduced as a direct result of the spherically ground entrance window, and in order to reduce aberration due to light spread in the entrance window, a fibre-optic entrance window is usually chosen. In addition, there will be some non-uniformities introduced by the electrostatic focusing process itself. These non-uniformities have yet to be demonstrated in an HPD developed specifically for imaging applications, but would certainly have to be corrected for if this device were to be used for nuclear medicine imaging.

9.2.3 Proximity Focused

Proximity focused HPD tubes use a planar glass or fibre window upon which the photocathode has been deposited using the transferable process. The entrance window is held in close proximity (a millimetre or so) to a planar anode inside a hard vacuum. A high potential is applied between these two surfaces and the photoelectrons follow short rigid paths forming a 1:1 image which is then read out by an array of small PiN diodes to provide some limited position resolution (see Figure 9.1).

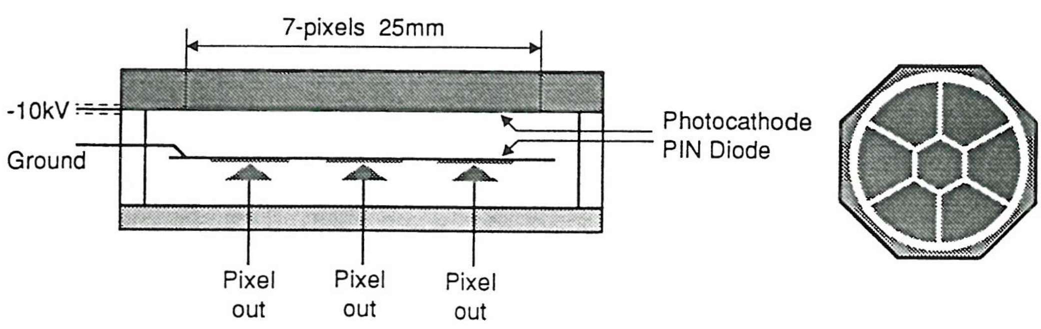

Figure 9.1: *Schematic representation of a 7 segment anode HPD*

Recently, a variation of the proximity focused technique using an Avalanche Photodiode (APD) has been developed by Advanced Photonix Inc., in California. This tube has been named the Vacuum Avalanche Photodiode (VAPD), and has been demonstrated to offer gains as high as 1.5×10^6 for applications where position-sensitivity is not required (Szawlowski et al. [119]). Although research in this area is moving apace there remains considerable scope for development and further specific improvement in design to facilitate a much wider adoption of this technology for scintillation detectors for nuclear medical imaging applications such as γ-ray scintigraphy, and PET.

9.2.4 Tube Characteristics

The proximity focused HPD described previously was primarily developed for operation in extremely high magnetic field environments such as particle beam calorimetry. These devices were originally designed to provide larger area coverage with some limited position-sensitivity by adopting a segmented anode structure. However, because of the requirement for a 1:1 ratio between the light spread function at the detector crystal, and the photoelectron distribution at the anode, the silicon anode structure out of necessity covers a much larger area than does the anode in an electrostatically focused tube. The choice is therefore between having many silicon anode elements of very modest dimensions, or fewer elements each having larger surface area. Since both the diode capacitance and leakage current scale in direct proportion to the surface area of the device, it is possible to select the size of anode elements according to the SNR required for a particular application. If a segmented detector crystal is chosen, the anode elements may also be chosen to match the size of the detector crystal elements. The maximum number of pins which can successfully be taken outside of the vacuum enclosure whilst preserving a hermetic seal also influences the choice of anode element size, as does the number of channels of signal processing electronics which will be required in order to read out the device. The resulting device offers the benefit of position-sensitivity and uniform response with either a planar or fibre-optic entrance window, and are certainly of interest for applications in nuclear medicine imaging.

9.3 Tests of an Electrostatically Focused Single-Pixel HPD

Tests have been made using four single-pixel electrostatically focused HPD tubes from DEP, and have yielded mixed results. Initial testing of the first device when used to view a large CsI(Tl) detector crystal, optically bonded to the entrance window of the tube, and illuminated by a ^{137}Cs source yielded no visible signal above the oscillator noise induced by the internal power supply of the device. Upon return to the manufacturer, it was subsequently found that the diode when fully depleted permitted an excessive leakage current to flow. Unfortunately, the replacement tube, when subjected to the same test yielded equally disappointing results, although a further test using a ^{90}Sr β-particle source to illuminate a small disk of plastic scintillator viewed by the HPD and directly coupled to a fast Tektronix 2235 100 MHz oscilloscope fitted with an image intensifying screen did permit a series of fast pulses to be observed, proving that it was operating. The problem of the oscillator noise still remained, and upon consultation with DEP removal of the power supply was advised as several other customers had identified the same problem. The final replacement tube provided by DEP had the power supply removed from within the enclosure of the device. This device, together with a fourth tube which has a EURORAD R304 preamplifier included within the enclosure of the device, have been tested, and these results are presented in the sections which follow.

9.3.1 Experimental Procedure

The HPD is a very sensitive photodetector which offers the possibility of counting individual optical photons. Stray light falling upon the photocathode will contribute to the signal produced at the anode resulting in a decrease in the spectral resolution. The HPD was therefore operated in a light-tight box placed within a dark-room for the purpose of the tests described in this section.

Various inorganic scintillator crystals were wrapped in white Millipore paper and white PTFE tape, and optically coupled to the entrance window of the tube. The signal from the first tube was amplified using a Amptek A250 preamplifier with a feedback capacitor of 0.3 pF, and a feedback resistor of 1 GΩ. The output of the preamplifier was coupled to the input of a EG&G Ortec 575A shaping amplifier with a shaping time of 1.5 μs. The shaped signal was monitored using a Philips PM3355 60 MHz digital oscilloscope, and the pulse-height spectra collected with a Compusys 286 SX personal computer fitted with a EG&G Ortec 916A PHA card, and loaded with EG&G Maestro II PHA software. Energy spectra were taken at various energies using a range of laboratory calibration radioactive point sources, and the measurements repeated for each scintillator material.

9.3.2 Charge Gain

Unfortunately, difficulties were experienced when attempting to apply the high voltage bias to the photocathode. The glass entrance window appeared to be acting as a capacitor with a glass dielectric, and showed signs that it was charging up due to the application of the high voltage to the inside surface of the window. These problems persisted, getting worse at increasing photocathode potential, until the tube could be heard to crackle as the acquired charge gradually *leaked away* into the surrounding atmosphere. The result was that neither HPD could be operated beyond -10 kV potential, with an associated reduction in gain from the -15 kV which was specified as the operating range of each device. In addition, a distinct peak could be identified on each spectra which we attributed to small fluctuations associated with this leakage of charge from the glass window causing electrons to be incident upon the silicon anode, and false events to be registered. Knowing this, we believe that the results of energy resolution obtained have also been adversely affected by the additional fluctuations caused by this charge leakage, and that the uncertainty for each spectrum obtained could be further improved. We approached DEP to discuss our difficulties, and were told that they were aware of the problem, and that all of their tubes are now fitted with quartz entrance windows which do not exhibit the problems that we have experienced.

9.3.3 Energy Resolution

Tests were performed to determine the energy resolution characteristics of the HPD used as a scintillation counter with a range of scintillation materials suitable for applications in nuclear medicine (see Table 9.1).

Scintillator	Energy Resolution (%FWHM)			
Material	59.5 keV	122 keV	511 keV	662 keV
CsI(Na)	20.3	15.3	10.7	9.4
NaI(Tl)	32.6	21.7	12.4	9.8
CsI(Tl)	24.3	17.6	11.3	10.6
GSO	38.8	25.9	12.3	11.1
LSO	45.6	32.0	17.5	16.9
YAP(Ce)	47.4	33.9	Compton	Compton

Table 9.1: *Spectral performance of the HPD with quartz entrance window*

Illustrated in Figure 9.2 are two sample spectra taken using the HPD to view a CsI(Na) detector crystal having dimensions of 15 mm x 15 mm x 30 mm.

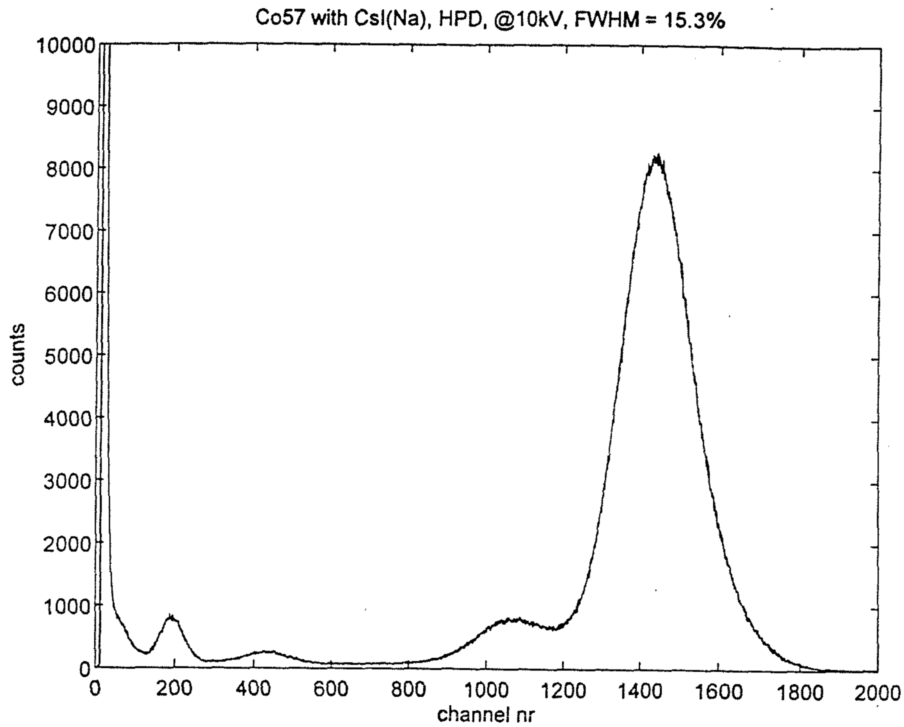

(a) ^{57}Co source

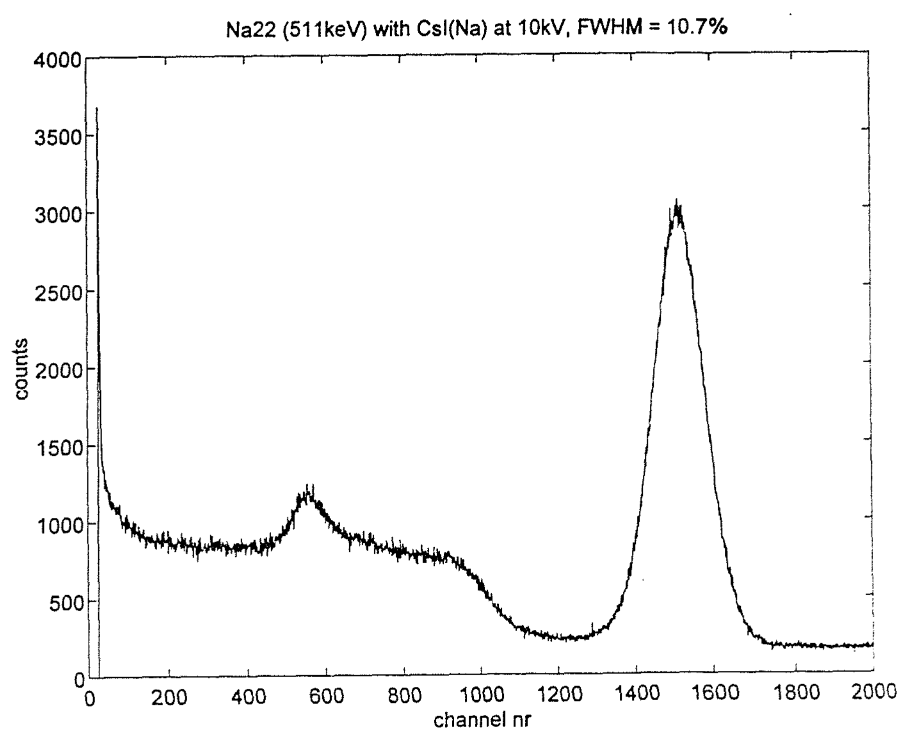

(b) ^{22}Na source

Figure 9.2: *Energy spectra of CsI(Na) viewed by HPD*

These results were then compared with those obtained from other devices commonly used for scintillation counting in order to determine the relative ability of the HPD to resolve sources of the same energy (see Table 9.2).

Detector Type	Energy Resolution (%FWHM) 59.5 keV	122 keV	511 keV	662 keV
Photodiode [1]	40.0	21.0	7.2	6.0
APD [2]	44.9	21.1	9.3	8.1
Photomultiplier [3]	15.0	15.0	11.0	7.0
HPD [4]	32.6	21.7	12.4	9.8

1 Viewing CsI(Tl) (A.J.Bird et al. [15]), 2 Viewing CsI(Tl) (C.Lawton [73]),
3 Viewing NaI(Tl) (values taken from Harshaw Q&S [49]), 4 Viewing NaI(Tl)

Table 9.2: *Relative spectral performance of the HPD compared with other scintillation counting devices*

It can clearly be seen from these results that the HPD compares very favourably with the performance characteristics of both photodiodes and APDs when coupled to a suitable scintillator material, illuminated by γ-rays of 122 keV or less. As expected, at higher energies than this both the photodiode and the APD offer superior spectral resolution due to their higher quantum efficiency. However, it can be seen that at the present time the spectral response of the HPD compares rather poorly with the best resolution that can currently be achieved with conventional PMTs over the entire energy range. We would usually expect very similar performance characteristics from each of these devices. It should be noted here that the sample of NaI(Tl) used to obtain these measurements was of extremely poor quality, since the mechanical encapsulation had deteriorated permitting the ingress of moisture to affect the crystal. The detector crystal had already started to show signs of discoloration due to this deterioration. Indeed, Table 9.1 demonstrates that superior results were obtained with a crystal of CsI(Na) which has only 85% of the total light output of NaI(Tl). Therefore, this result demonstrates better potential if one were to consider the superior result obtained with the crystal of CsI(Na). Once the problems associated with the charging up of the glass entrance window have been resolved, it is expected that the accompanying improvement in energy resolution which will be achieved will demonstrate the HPD to be a very useful alternative photodetector to the PMT for applications where position-resolution combined with excellent spectral resolution are required over a broad range of energies.

9.3.4 Optical Photon Counting

The unusually low noise associated with the HPD, combined with a modest gain, and a fast response enable the detection of very low energy γ-ray photons when used as the photodetector for scintillation counting applications. These same characteristics also enable the detection of individual optical photons which are incident upon the photocathode of the device (D'Ambrosio et al. [32]). However, since the quantum efficiency of even the best photocathode does not usually exceed 25%, and in our device does not exceed 16%, the overall detection efficiency will always be low. Nevertheless, we have confirmed the practical ability to count individual optical photons with an HPD (see Figure 9.3).

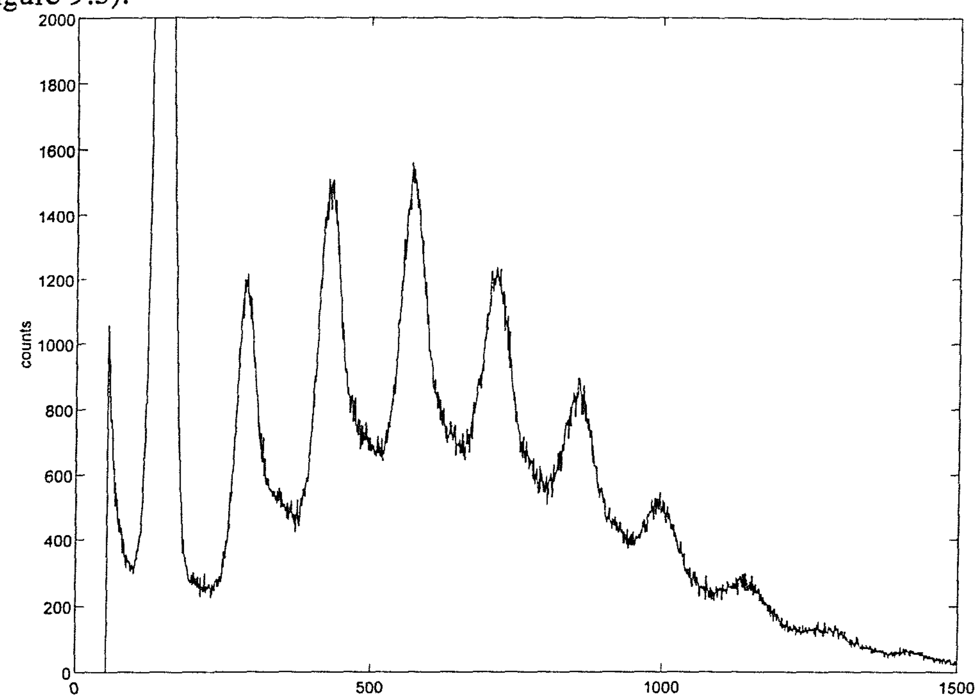

Figure 9.3: *Spectra demonstrating single optical photon counting ability of an HPD*

The above spectra was obtained by using the output of a precision pulse generator to provide a series of fast, low amplitude pulses which were used to illuminate an LED placed directly in the field-of-view of the HPD which was placed within a dark box. The output of the pulse generator was used in coincidence with the output of the shaping amplifier to trigger the PHA. Whilst monitoring the output from the HPD on both a CRO, and using the PHA software, the amplitude of the output from the pulse generator was adjusted until the spectra illustrated was observed. Clearly a device such as the HPD, which can identify individual optical photons in this way would be extremely useful for applications where the optical signal from the scintillator is small, either due to the size of the energy deposit, or due to the intrinsic light yield from the scintillator being low.

9.3.5 Low Energy Detection Threshold

The low energy detection threshold of the HPD was estimated experimentally by using a 5.9 keV ^{55}Fe laboratory calibration γ-ray source to illuminate a CsI(Tl) detector crystal coupled to the HPD. Due to relatively high levels of systematic electronic noise from both the HPD and the preamplifier, the 5.9 keV photopeak can only be partially resolved (see Figure 9.4).

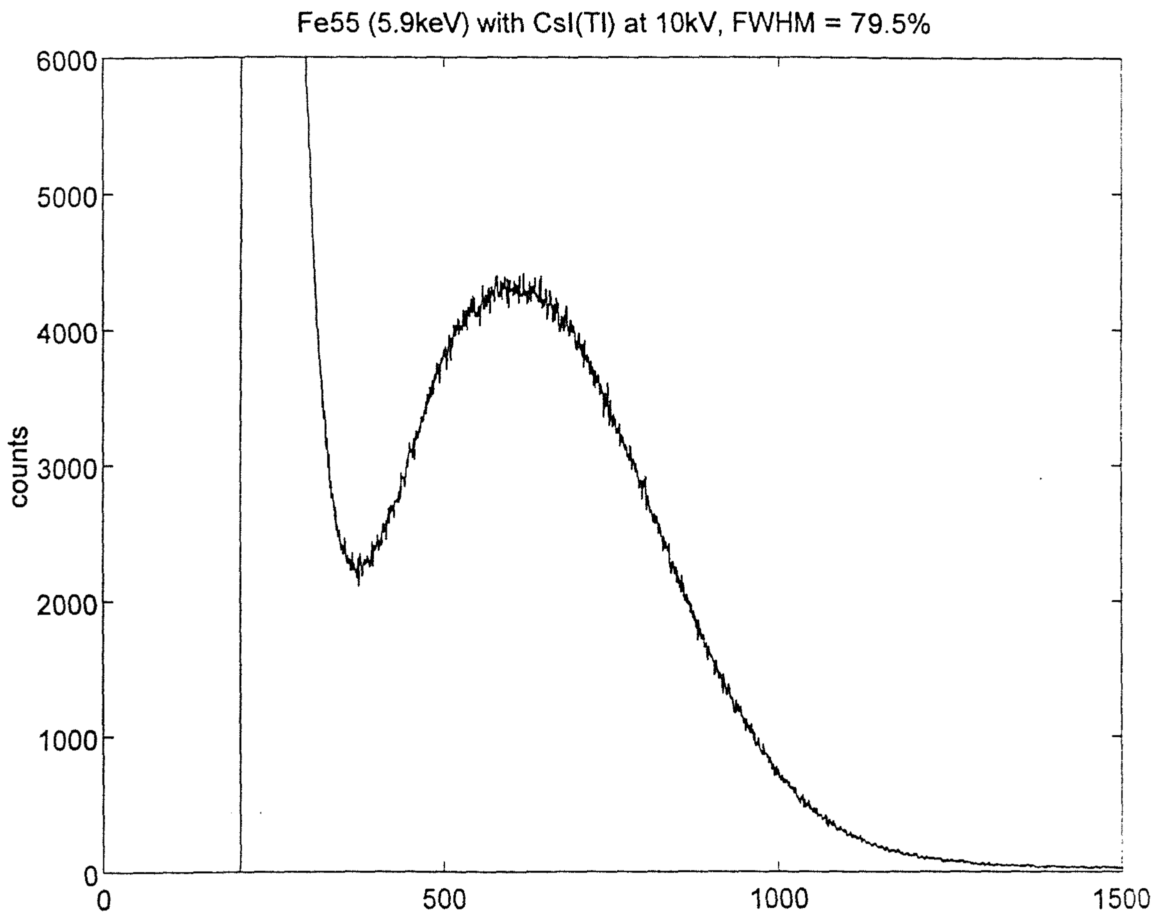

Figure 9.4: *Energy spectrum of ^{55}Fe with CsI(Tl) coupled to HPD*

From this an estimate of the low energy detection threshold of the HPD used as a scintillation counter was determined to be approximately 3.5 keV. This is higher than the theoretically predicted 5σ threshold of 2 keV, but with better optimised electronics, and a higher quantum efficiency photocathode (Schomaker [107]), it is expected that this figure could be reduced still further to approximate to the predicted value. In order to determine the noise which could be attributed to the HPD alone, it was decided that it would be useful to characterize the silicon diode. Measurements have therefore been made of both the leakage current and diode capacitance as a function of diode bias potential (see Figure 9.5).

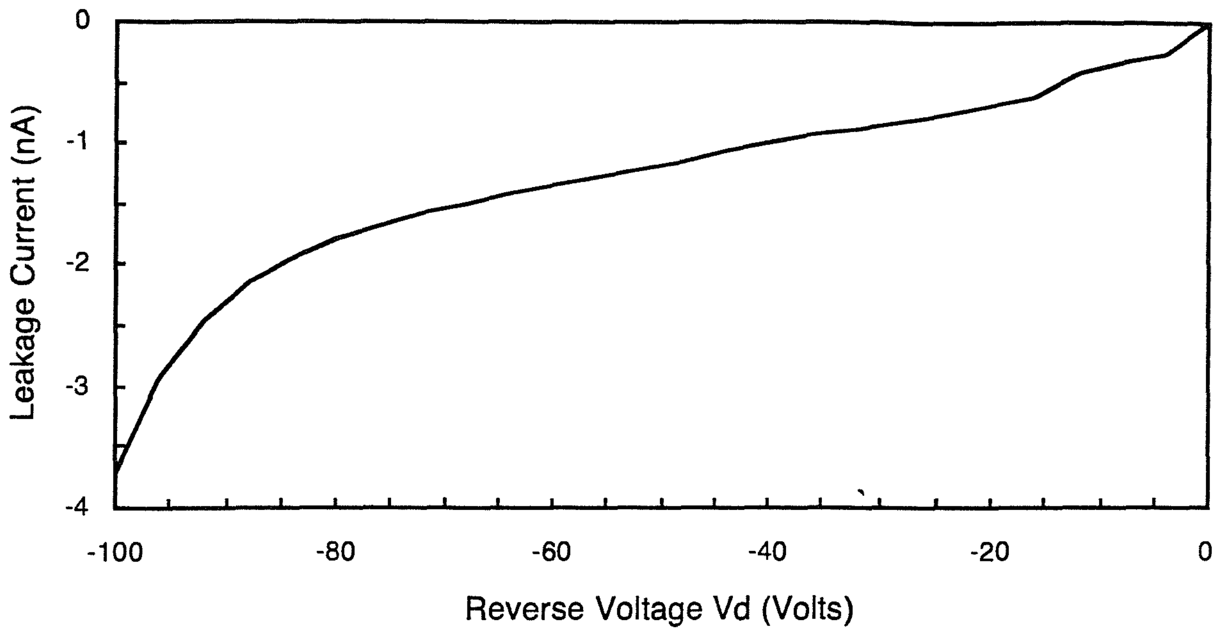

(a) Hybrid photodiode leakage current as a function of reverse bias

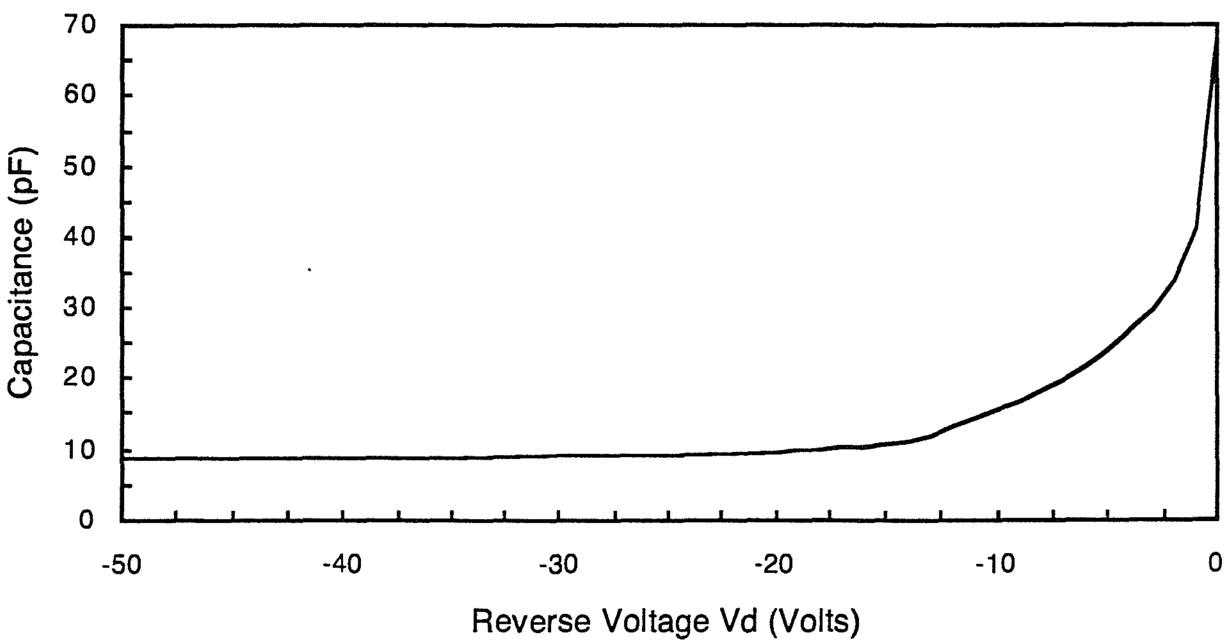

(b) Hybrid photodiode capacitance as a function of reverse bias

Figure 9.5: *Hybrid photodiode silicon PiN diode characteristics*

The results of these measurements showed that the silicon diode used in our HPD became fully depleted at approximately -20 Volts bias, at which potential the leakage current flowing in the device was less than 1 nA. We can therefore conclude from this that the diode supplied by Canberra that is used in this tube is of very high quality.

Since the noise in the HPD is dominated by the leakage current which flows in the silicon diode, and this has been determined to be very small, the major source of noise observed to be contributing to our measured signal must be primarily due to electronic noise from the preamplifier.

9.4 Applications of the HPD

The hybrid photodiode is a concept which has taken many years to mature into a commercially available device. Because of the development input of Dr. DeSalvo, these first generation tubes have been developed with the specific application of charged particle beam calorimetry in mind, and at the present time very few alternative applications have been identified for these interesting devices. However, it is the author's view that if devices could be produced which offer both intrinsic position-sensitivity and a usable sensitive area of the order of 40 cm^2 (100 mm diameter), the HPD will provide a competitive alternative, offering much better photocathode uniformity than the PSPMT for many applications in nuclear medicine.

9.4.1 Gamma-Ray Spectroscopy

Earlier in this chapter we demonstrated the capability of the HPD to offer excellent spectroscopic resolution, almost equalling the best results that can presently be achieved with all but the most recent advances in expensive semiconductor detectors such as CdZnTe. The HPD offers the combination of photomultiplier and photodiode technology within a single device which is capable of offering modest gain, and could be advantageous for some low energy spectroscopic applications, or for veto counting.

9.4.2 Gamma Camera Probe with Hybrid Photodiode Readout

Recently we have considered the application of newly emerging multi-anode HPDs as the photodetector for a compact clinical gamma camera (Durrant et al. [48]). The visual similarity of the anode structure of a multi-anode HPD to the arrangement of the photomultiplier tubes in an Anger Camera (Anger [3]), has given us the idea of applying a centroiding method of interpolation similar to that used in conventional clinical gamma cameras (see Figure 9.6).

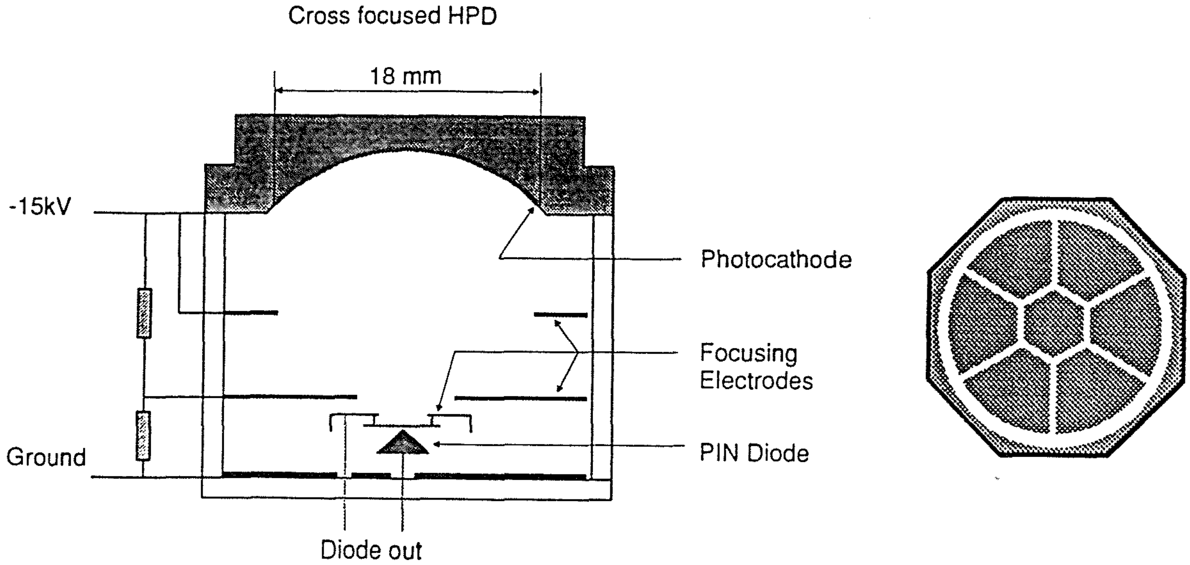

Figure 9.6: *Anode structure of the multi-anode HPD*

The advantages of this technique are those of continuous position-sensitivity combined with a spatial resolution that is considerably smaller than the size of each anode element. An optimised design for a compact clinical gamma camera has been proposed, which uses the prototype 40 mm diameter active area, nineteen anode-element HPD based upon both electrostatically focused, and proximity focused tube types. This design comprises a segmented CsI(Na) detector crystal with 2 mm x 2 mm x 4 mm elements, optically coupled to a 5 mm thick lightguide which in turn is coupled to the entrance window of the HPD. A non-linear resistive divider or delay line circuit is used to weight and combine the signals from each anode element to produce four outputs which correspond to an orthogonal set of co-ordinates. These outputs are then digitised and an interpolating algorithm used to determine the centroid of the light-spread function which accurately describes the position of interaction within the detector crystal. The expected intrinsic resolution of this camera is 2 mm at 140 keV, with both detection efficiency and energy resolution comparable to the conventional Anger Camera. This work is still developmental, and it is hoped that results using this small camera to image tumours will be reported shortly.

9.4.3 Miniature SPECT

Depending upon the outcome of the development discussed previously, it might be possible to integrate such a compact gamma camera into a modular SPECT system such as that proposed by Rogers [101]. Recent authors have proposed very compact CT systems based upon the PSPMT (Matthews et al. [78], and Watanabe et al. [129]).

Clearly, a very compact SPECT system which employs a small camera based upon the development of a position-sensitive HPD would have particular application for nuclear medicine studies involving the investigation of the wrist, elbow, ankle, and knee, in patients experiencing some degree of restricted movement in these joints. The combination of millimetric spatial resolution and the ability to reduce the radial distance of the camera from the patient could offer significant advantages over conventional SPECT systems for diagnosing the cause of restricted mobility in these patients.

9.5 Conclusions & Future Work

Clearly the hybrid photodiode is a very interesting device which offers some performance advantages over alternative devices which are commonly used for scintillation counting. In this chapter we have demonstrated the performance of the HPD through the operation of an electrostatically focused single-pixel tube in both scintillation counting mode, and to count individual optical photons.

We have demonstrated the operation of an electrostatically focused, single-pixel HPD used in scintillation counting mode. Whilst the signal processing electronics were far from optimised, we have been able to achieve spectroscopic resolution measurements for various scintillation materials over a range of energies of interest for nuclear medicine studies, which compare favourably with other devices commonly used in scintillation counting. It has been demonstrated that the single-pixel HPDs used in our measurements exhibit a very low detection threshold of the order of 3.5 keV, which through a process of optimisation could be improved still further, offering excellent potential for auroral imaging. One of the HPDs used in these measurements has been characterized in order to determine the principal sources of electronic noise contributing to the signal, and we have shown that the silicon device employed in this HPD contributes very little to the overall electronic noise of our prototype experimental system. However, both HPDs demonstrated an unexpectedly high dark-count rate at the single photoelectron level. During the spectroscopic measurements described earlier, the leakage of charge due to the charging of the entrance window was presenting problems in operating these devices within the manufacturers specified operating range of high voltage [35]. Even with quartz entrance windows, the tube still generates a high number of dark-counts. The only entrance window where the dark-counts do not increase as a function of the high voltage applied to the tube is the fibre window. The single photoelectron dark-count rate for this tube is very low, but it instead exhibited a sensitivity to the presence of almost any material (including scintillation materials) in close proximity to the entrance window. Obviously a considerable amount of work remains to be done both by ourselves, and the manufacturer in overcoming these problems.

In addition to this, we were plagued by ripple on the high voltage bias to each tube. Attempts were made to overcome this through the application of a three stage RC filter which offered some improvement. However, a small ripple on the output is still present, limiting the single photon resolution to approximately 24%, where a resolution of 10% should be achievable. It is felt that with a more stable high voltage, and better optimisation of the preamplifier stage, both improved spectroscopic data and reduced low energy detection threshold could be achieved.

For this device to remain interesting for applications in nuclear medicine, the proposed development of an HPD capable of exhibiting some degree of position-sensitivity will first need to be demonstrated. This development is currently near completion, and results are expected within the next few months which will hopefully confirm the imaging capability of multi-anode HPD's used as the photodetector in position-sensitive scintillation counters. Meanwhile, alternative anode structures are currently under investigation together with Canberra, who plan to integrate the resistor divider onto the silicon wafer using resistive polycrystalline silicone between each anode element during the fabrication process. A further possibility is to use a position-sensitive diode (PSD), as proposed in Chapter 8, as the continuously position-sensitive anode structure within a vacuum enclosure developed by DEP.

Appendix A

The Interaction of Gamma-Rays with Matter

A.1 Introduction

Complementary to the specific design requirements for new detector developments discussed in previous chapters, it is necessary to understand the nature of the interaction of γ-rays within the detector. This appendix to the work discussed previously presents in greater detail the principles which underly the most important mechanisms relevant for the imaging of x-rays and γ-rays within a range of energies from a few keV to several hundred keV.

In the context of γ-ray detection, the primary interaction mechanisms result in the liberation of energetic electrons which either partially or completely carry away the energy of the incident γ-ray photon. These electrons in turn transfer all of their energy to the surrounding matter through subsequent atomic interactions, yielding a signal which can be detected either optically or electronically. Photons interact with matter to produce energetic electrons through three principal processes:

- The Photoelectric Effect
- The Compton Effect
- Pair Production

For the range of energies experienced in both nuclear medicine (typically $\leq$ 511 keV), and auroral imaging, pair production cannot occur, and photoelectric absorption and Compton scattering dominate (see Figure A.1).

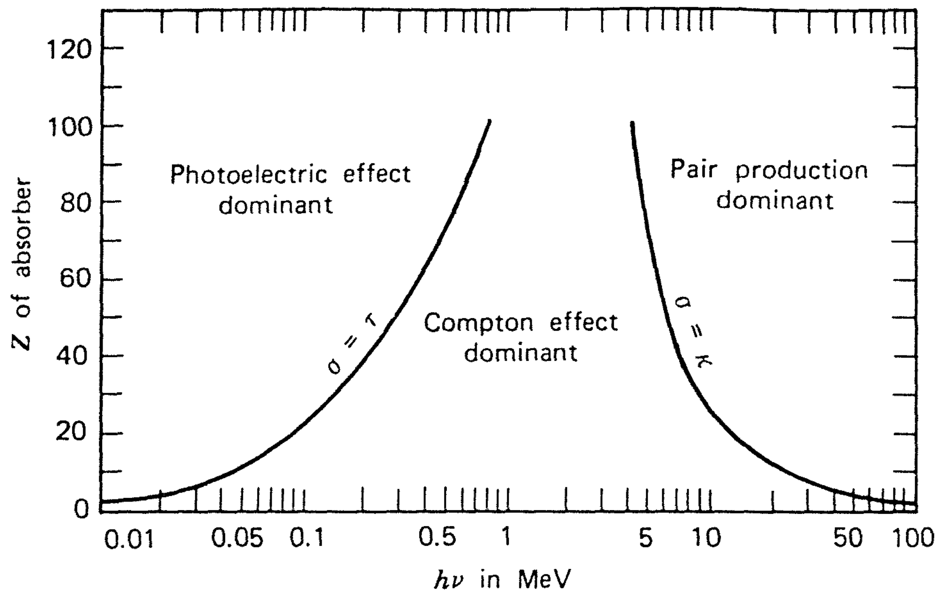

Figure A.1: *Relative contribution of gamma-ray interaction processes*

Here, the relative contribution as a function of energy of the three principal mechanisms by which γ-rays interact with matter is illustrated. Each curve plotted on this graph represents the values of atomic number and photon energy for which the two neighbouring effects have the same cross-section of interaction.

The statistical probability of an incident γ-ray photon interacting with an atom of a particular material by one of these three processes is often described as its interaction cross-section. This statistical cross-section can be represented graphically as the change in *linear attenuation coefficient* as a function of γ-ray energy. The linear attenuation coefficient, μ, is defined as the product of the total cross-section per atom of a particular material, and the number of atoms per unit volume. The linear attenuation of the incident γ-rays is represented by:

$$I = I_0 \, e^{-\mu x} \qquad \text{A.1}$$

Here x is the thickness of the absorber through which the γ-rays pass, and μ is strongly energy dependent (see Figure A.2). However, since linear attenuation coefficient itself depends upon the *mean free path*, λ, of the γ-ray before it interacts, μ will vary as a function of density for absorbers of the same atomic number. This limits the usefulness of μ, and is the reason why mass attenuation coefficient is occasionally preferred, where:

$$\text{Mass attenuation coefficient} = \frac{\mu}{\rho} \qquad \text{A.2}$$

For γ-rays of a given energy, the mass attenuation coefficient is measured in cm^2/g and is independent of density. However, when calculating the shielding requirements of detectors, or the stopping efficiency of a particular scintillator material, linear attenuation is the more intuitive of the two, and usually is the parameter which is most commonly used.

As previously mentioned, the three interaction cross-sections can be represented graphically and is illustrated by Figure A.2 for sodium iodide.

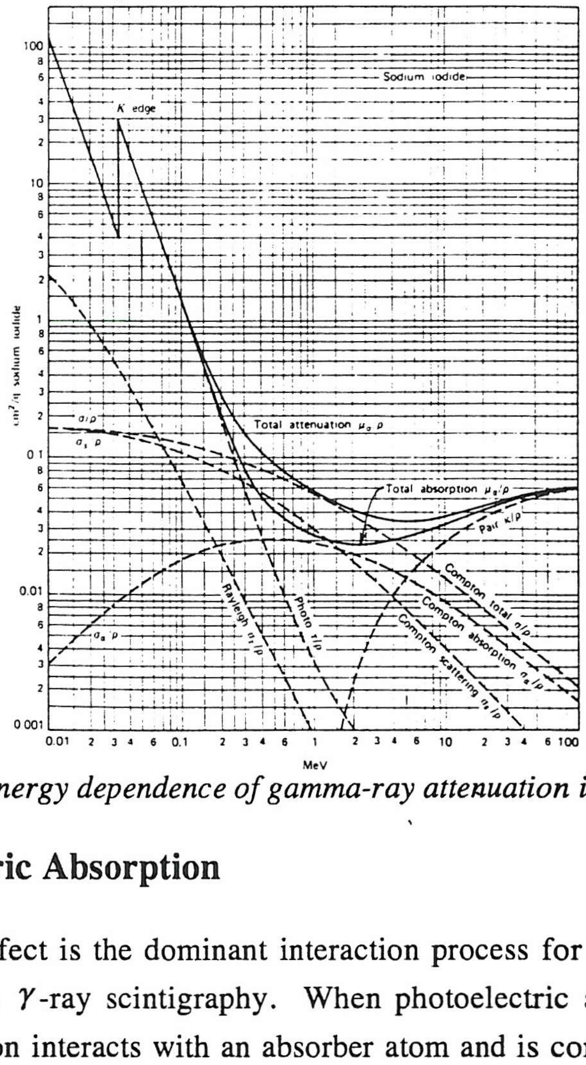

Figure A.2: *Energy dependence of gamma-ray attenuation in sodium iodide*

A.2 Photoelectric Absorption

The photoelectric effect is the dominant interaction process for the range of energies commonly found in γ-ray scintigraphy. When photoelectric absorption occurs, an incident γ-ray photon interacts with an absorber atom and is completely absorbed. A recoil electron, or *photoelectron* is liberated from one of the bound atomic shells (usually the K or L shell) as a consequence of this interaction, and has an energy which is given by:

$$E_{e^-} = h\upsilon - E_b \qquad \text{A.3}$$

where E_b represents the binding energy of the photoelectron in its original shell. For energetic incident γ-rays having $h\upsilon >> E_b$, that is energies greater than a few hundred keV, the photoelectron carries off most of the original photon energy. The ionized absorber atom has a vacancy in one of its bound shells which is quickly filled through free electron capture and/or rearrangement of electrons from other bound shells. Hence, one or more characteristic x-ray photons may also be generated (see Figure A.3). Occasionally, the characteristic x-ray may be substituted by the emission of an Auger electron which will carry away the atomic excitation energy.

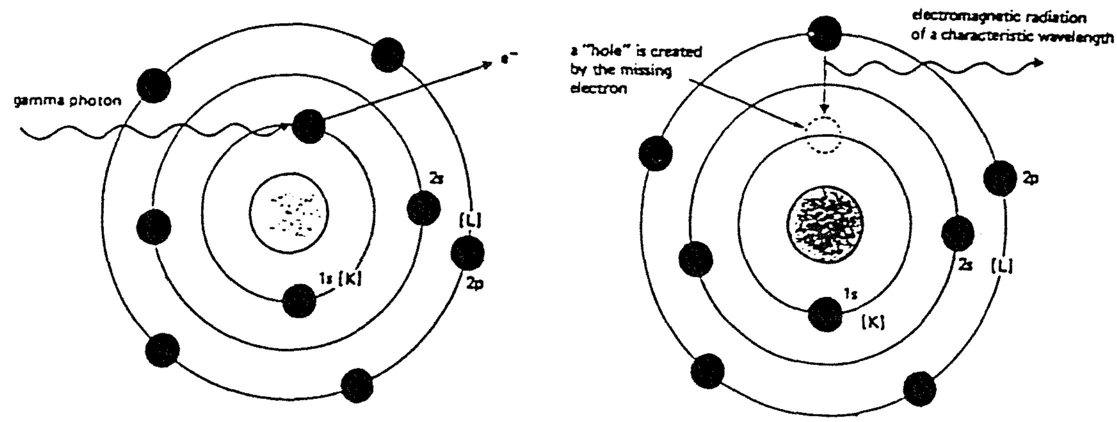

Figure A.3: *The photoelectric absorption process*

The cross-section for photoelectric absorption of a γ-ray photon approximates to the expression:

$$\sigma_{pe} \cong \text{Constant x } \frac{Z^n}{E_\gamma^3} \qquad \text{A.4}$$

where E_γ represents incident photon energy, Z represents the atomic number of the absorber, and n varies between 4 and 5 over the γ-ray region of interest. The strong dependence of the photoelectric absorption probability upon the absorber atomic number explains why lead and tungsten make excellent detector shielding materials. By reducing the background flux, high-Z shielding materials can be used to improve the sensitivity of most detector systems at energies where photoelectric absorption dominates. The density of the scintillator will also have a considerable effect upon the detector sensitivity by increasing the photoelectric interaction cross-section, and materials which have a high atomic number are favoured.

Whilst the graph of interaction cross-section for sodium iodide in Figure A.2 follows the general form of equation A.4, there are additional sharp discontinuous features known as *absorption edges*. These sudden transitions are due to the quantised energy level structure of the atom, and correspond to the binding energies of electrons in various shells of the absorber atom. As the incident photon energy increases, it becomes possible to ionise each of the bound electrons from its orbital shell in turn, from the least tightly bound electrons through to the most tightly bound K electron. As the photon energy exceeds the binding energy of one of these electrons, there is a sudden increase in the number of electrons that can be ionized, and hence a corresponding discontinuity in the probability of photoelectric interaction.

A.3 Compton Scattering

Compton scattering occurs between an incident γ-ray photon and a loosely bound electron in the absorber atom. It is often a dominant interaction mechanism for γ-ray energies typical of radioisotope sources and is well understood. If the binding energy of the electron is low compared to that of the incident photon, it may be considered to be a free electron, and the interaction between the photon and the electron can essentially be regarded as an elastic collision (see Figure A.4).

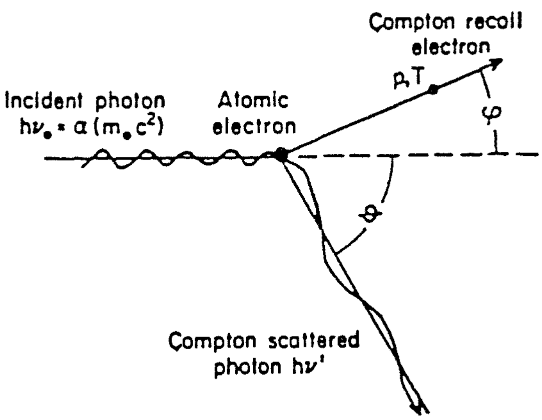

Figure A.4: *The Compton scattering process*

The incident γ-ray photon is scattered through an angle θ relative to its original direction, and in doing so has its energy reduced from $h\nu$ to $h\nu'$. The electron carries away the difference between the incident and scattered photon energies, and is known as a *recoil electron*. The relationship between incident and scattered photon energies, and scattering angle is given by the solution of simultaneous equations for the conservation of energy and momentum, resulting in the expression:

$$h\upsilon' = \frac{h\upsilon}{1+\alpha(1-\cos\theta)} \qquad \text{A.5}$$

where $\alpha = h\upsilon/m_0c^2$ and m_0c^2 is the rest mass of the electron. The energy transferred from the incident γ-ray photon to the electron is given by:

$$E_{e^-} = h\upsilon - h\upsilon' \qquad \text{A.6}$$

which can also be expressed as:

$$E_{e^-} = h\upsilon\frac{\alpha(1-\cos\theta)}{1+\alpha(1-\cos\theta)} \qquad \text{A.7}$$

The energy of the recoil electron varies from zero to a large fraction of the incident γ-ray energy, making scattering possible for angles between $\theta=0$ to $\theta=\pi$. For $\theta=0$, the energy transferred to the electron is negligible, whilst maximum energy transfer occurs for scattering angles of $\theta=\pi$, where equation A.7 becomes:

$$E_{e^-_{MAX}} = h\upsilon\frac{2\alpha}{1+2\alpha} \qquad \text{A.8}$$

This implies that a continuum of recoil electron energies can be created up to a maximum value known as the *Compton edge*, which is a function of the incident γ-ray energy.

The probability of Compton scattering per absorber atom depends upon the number of bound electrons with which the incident γ-ray photon can interact, increasing linearly with atomic number. However, since there is a higher probability of a photoelectric absorption taking place in high Z materials compared with low Z materials, the fraction of the total incident γ-rays that lose energy by the Compton effect is greatest in low Z elements. In fat and muscle for example, the Compton effect is more probable than the photoelectric effect at energies above about 30 keV, and in bone it is more probable above about 100 keV. This dependence of interaction cross-section upon incident γ-ray energy is illustrated in Figure A.2 for sodium iodide.

The angular distribution of scattered γ-rays illustrated in Figure A.5(a), shows the number of scattered photons against scatter angle for a range of energies. This polar distribution taken from Cho et al. [28], illustrates the predominance of forward scatter for high incident γ-ray energies. The values presented are those for the differential cross-section, σ_e', per electron per solid angle (cm²/electron/Ω). Illustrated in Figure A.5(b) is the total cross-section, σ_e, of the interaction, derived by integrating the differential cross-section over all possible angles to yield an expression which is a function of energy only.

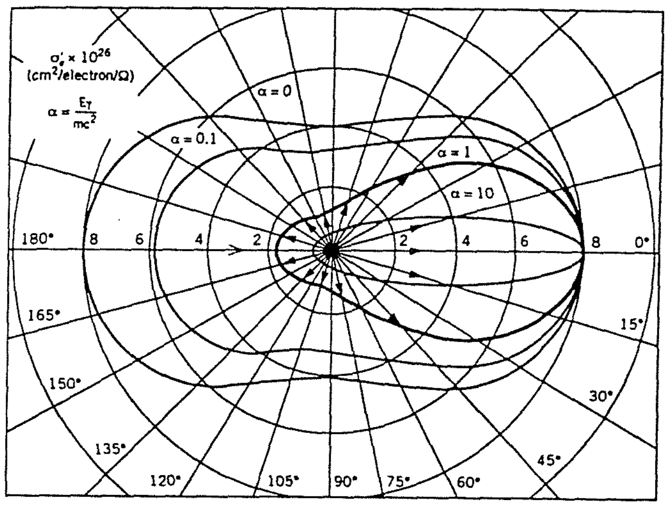

(a) Dependence of Compton scatter cross-section upon scatter angle

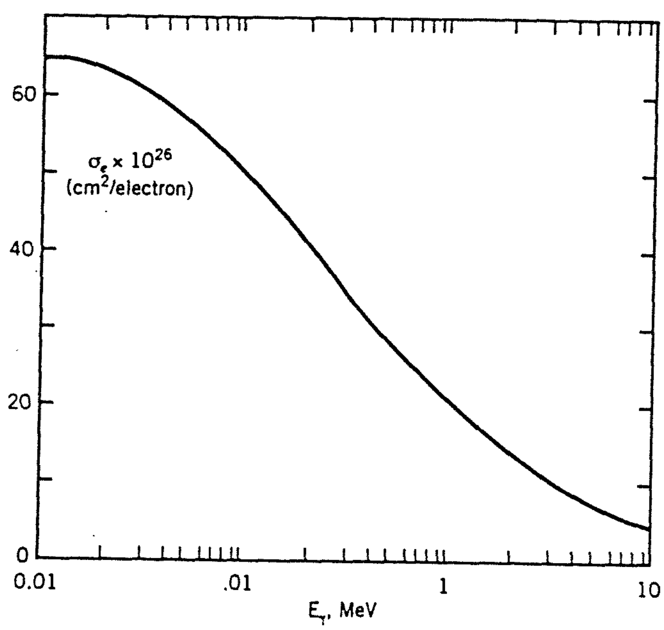

(b) Dependence of Compton scatter cross-section upon energy

Figure A.5: *Some cross-sections for Compton scatter*

A.4 The Scintillation Process

Strictly speaking the scintillation process is not an interaction mechanism in the same sense as the photoelectric and Compton effects. However, each imaging system discussed in previous chapters relies upon the prompt conversion of γ-ray energy into scintillation light before being converted into an electronic signal by the photodetector. An appreciation of the underlying principles is therefore desirable.

The group known as organic scintillators are aromatic hydrocarbon compounds containing linked or condensed benzene-ring structures. The scintillation mechanism in organic molecules arises from the energy level structure of molecules with certain symmetrical properties giving rise to what is known as a π - *molecular orbital* structure. These π - electronic energy levels for an organic molecule are illustrated in Figure A.6.

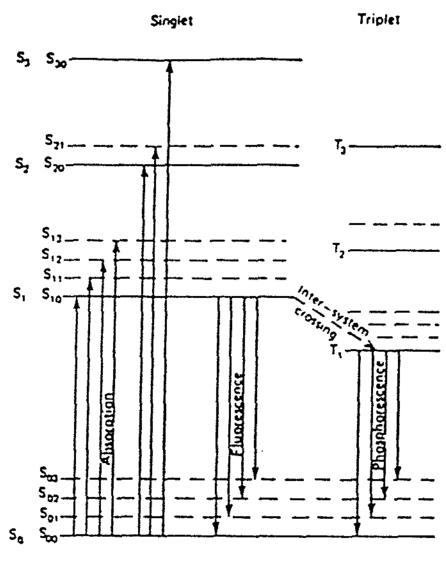

Figure A.6: *π-electron energy structure of an organic molecule*

Interactions between incident γ-ray photons and the scintillator liberate electrons through photoelectric absorption and Compton scattering. These delocalized electrons are dissociated from any particular atom in the molecule, yet remain associated with the molecule from which they were liberated, subsequently occupying π - molecular orbitals around the molecule. Absorption of kinetic energy from passing energetic electrons leads to the promotion of π - electrons from their vibrational ground state at room temperature (labelled S_{00}) into any one of a number of excited singlet states labelled (S_0, S_1, S_2, S_3), with spin 0. Typical organic scintillators require 3 or 4 eV to promote electrons between S_0 and S_1, and for higher excited states less energy than this is required. Following this brief excitation, the molecules immediately de-excite to the S_{10} vibrational state within a few picoseconds ($\leq$10 ps) through non-radiative internal conversion known as *internal* *degradation*, and a population of excited molecules in the S_{10} state is produced. The principal component of the scintillation light, known as *prompt fluorescence*, is emitted when the electrons return from the S_{10} vibrational state to one of the S_0 vibrational states of the ground electronic state. The time taken for this fluorescence to decay in intensity is typically of the order of a few nanoseconds. A transition known as *intersystem crossing*, allows excited electrons in the S_{10} vibrational state to be converted into triplet states with spin 1, which are characterised by much longer lifetimes than their corresponding singlet state. The lifetime of T_1 states may be as much as 10^{-3} seconds, delaying the de-excitation from T_1 to one of the S_0 vibrational states, and consequently the light emission which is known as *phosphorescence*. Because of this late decay, phosphorescence is an undesirable feature of organic scintillators. However, since T_1 lies at a lower potential than S_1, the wavelength of this phosphorescence will be longer than that of normal fluorescence. In addition, there is some probability that whilst in the T_1 state further excitation of the molecule by energetic electrons can induce a return to the S_{10} state where subsequent decay will be through prompt fluorescence. Also illustrated in Figure A.6 is the energy difference between the fluorescent photon and that required to promote electrons into one of the higher singlet states. For this reason organic scintillators are transparent to their own scintillation light.

The scintillation mechanism in inorganic scintillators is determined by the crystalline structure of the material which, as with semiconductors, allows electrons only in discrete bands of energy (see Figure A.7).

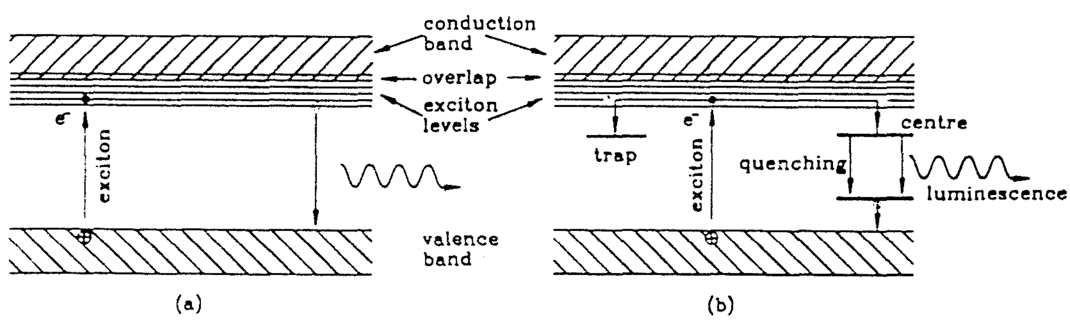

Figure A.7: *Luminescence in (a) a pure alkali halide crystal, (b) a crystal with added impurity*

In this model taken from Michette and Buckley [81], an insulating crystal such as sodium iodide has a filled valence band and an empty conduction band separated by an energy gap E_g. The absorption of a γ-ray can result in electrons being promoted into the conduction band from the valence band where they are free to move through the crystal lattice of the scintillator. Alternatively, an electron can be raised from the valence band to an exciton state. Excitons are electron-hole pairs which remain associated with each other through the Coulomb interaction. They can move throughout the crystal but there is no resulting current since no net charge moves. The higher levels of the exciton band overlap the conduction band, and the lowest excitons can decay to the valence band with the emission of a photon. However, this emission process is highly inefficient since self-absorption often occurs due to the energy of these photons lying within the optical absorption band of the bulk crystal. Furthermore, since $E_g \approx 5$-10 eV for most insulators, these photons fall within the ultraviolet region of the spectrum which is incompatible with common photodetectors, and so are extremely difficult to detect. In order for a 'free' electron in the conduction band to enter an exciton state and decay, it must lose energy by thermal collisions, which can only happen if the crystal is cooled. Thus cooled pure crystals are sometimes used if high counting rates are required, since electrons quickly transfer to the lowest exciton state giving a short decay time. At room temperature however, the performance of pure alkali halides is extremely poor, and for this reason, a small amount of impurity, known as an *activator*, is usually introduced. If an activator impurity, such as thallium to give NaI(Tl), is introduced so that it causes inclusions in the lattice, crystals can be made to emit in the visible range. Exciton energy states are created within the forbidden gap of the scintillator through which the electron can de-excite to the ground state of the activator.

Incident γ-ray photons interact within the scintillator crystal through photoelectric absorption and Compton scattering producing energetic electrons which subsequently generate many electron-hole pairs by Coulomb interactions. Electrons are promoted from the valence band into the conduction band, and the holes will quickly drift towards activator sites which become ionized since their ionization energy is below that of the surrounding crystal lattice. Meanwhile, electrons in the conduction band migrate until they encounter these newly ionized activators, recombine with the impurity site, and form an excited energy state of the neutral activator. The excited electrons subsequently de-excite by returning to the activator ground state with the emission of scintillation light. It is also possible for electrons in the conduction band to recombine with an impurity to produce excited states whose de-excitation to the ground state is forbidden. These electrons become trapped, and may subsequently absorb thermal energy promoting them to higher excited states where transition to the ground state is allowed. This produces extremely long-lived phosphorescence and is a source of unwanted background light or *afterglow* in inorganic scintillators. Another possibility is that electrons captured by an activator site undergo radiationless transitions between some excited states formed by electron capture and the ground state, in which no radiation results. These processes are known as *quenching*, and represent loss mechanisms in the conversion of particle energy to scintillation light. The light conversion efficiency, η, is the fraction of absorbed incident γ-ray photon energy that appears as optical scintillation photon energy. The most commonly used scintillators have values of absolute scintillation efficiency shown in Table A.1.

Material	**Conversion Efficiency[1] η (%)**	**Peak Emission (nm)**	**Average Energy[1] ω_s (eV)**
CsI(Tl)	11.9	550	19.23
NaI(Tl)	11.3	415	26.31
CsI(Na)	11.4	420	25.64

1 Values taken from Radiation Detection and Measurement by Knoll [68]

Table A.1: *Properties of scintillators at 20° C*

The average energy ω_s required to produce one optical photon is expressed as:

$$\omega_s = \frac{E_s}{\eta}$$

where E_s is the average energy of optical emission. The efficiency of conversion varies considerably as a function of temperature which is well illustrated by Figure A.8 taken from Leo [75].

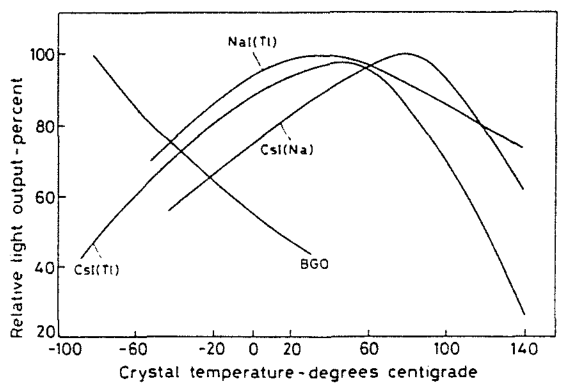

Figure A.8: *Temperature dependence of light output from inorganic crystals*

Bibliography

[1] Alberi JL et al., 'Position Sensing by Charge Division', IEEE Transactions on Nuclear Science, Vol. NS-23(1), pp 251-258, (1976).

[2] Anderson I, Aspergen K, Janzow L, et al., 'Mammographic Screening and Mortality from Breast Cancer', The Malmo Mammographic Screening Trial, British Medical Journal, Vol. 297, pp 943-948, (1988).

[3] Anger HO, 'Scintillation Camera', Review of Scientific Instruments, Vol. 29, pp 27-33, (1958).

[4] Anger HO, 'Scintillation Camera with Multichannel Collimators', Journal of Nuclear Medicine, Vol. 5, pp 515-531, (1964).

[5] Anger HO, 'Sensitivity, Resolution, and Linearity of the Scintillation Camera', IEEE Transactions on Nuclear Science, Vol. NS-13(3), pp 380-392, (1966).

[6] Arnaudon H et al., 'Proximity Focused Hybrid Photo Diode Characteristics Evaluations', Nuclear Instruments and Methods in Physics Research, Vol. A342, pp 558-570, (1993).

[7] AURIO Auroral Imaging Observatory, Phase-A Report, NSC Report (92)9.

[8] AURIX-H Phase-A Study Report, February 1992.

[9] Baccaro S et al., 'Scintillation Properties of YAP:Ce', Nuclear Instruments and Methods in Physics Research, Accepted for Publication, (1995).

[10] Barone et al., 'Toward a Nuclear Medicine with Sub-Millimiter Spatial Resolution', Nuclear Instruments and Methods in Physics Research, Vol. A360, pp 302-306, (1995).

[11] Basa S et al., 'Test Results of the First Proximity Focussed Hybrid Photodiode Detector Prototypes', Nuclear Instruments and Methods in Physics Research, Vol. A330, pp 93-99, (1993).

[12] Bicron Scintillation Products Catalogue.

[13] Bird AJ, Ramsden D, 'Images Obtained with a Compact Gamma Camera', Nuclear Instruments and Methods in Physics Research, Vol. A299, pp 480-483, (1990).

[14] Bird AJ, PhD Thesis, University of Southampton, England, (1990).

[15] Bird AJ, Carter T, Dean AJ, Ramsden D, Swinyard BM, 'The Optimisation of Small CsI(Tl) Scintillators', IEEE Transactions on Nuclear Science, Vol. NS-40(4), pp 395-399, (1993).

[16] Bird AJ, He Z, Ramsden D, 'Multi-Channel Readout of Crossed Wire Anode Photomultipliers', Nuclear Instruments and Methods in Physics Research, Vol. A348, pp 668-672, (1994).

[17] Bird AJ, Carter T, He Z, Dean AJ, Ramsden D, 'Pulse-Shape Analysis of Signals from a CsI/PD Detector', Nuclear Instruments and Methods in Physics Research, Vol. A353, pp 46-49, (1994).

[18] Bird AJ, Carter T, Dean AJ, Ramsden D, Swinyard BM, 'Small CsI(Tl) Detectors for the INTEGRAL Mission', In 'Heavy Scintillators for Scientific and Industrial Applications', Paris.

[19] Blasse G, 'Scintillator Materials' Chemistry of Materials, Vol. 6(9), pp 1465-1475, (1994).

[20] Boutot JP, Lavoute P, Eschard G, 'Multianode Photomultiplier for Detection and Localization of Low Light Level Events', IEEE Transactions on Nuclear Science, Vol. NS-34(1), pp 449-452, (1987).

[21] Cameron JR, Skofronick JG, 'Medical Physics', John Wiley & Sons.

[22] Canberra, Ion Implanted Position-Sensitive Photodiode Products Catalogue (1995).

[23] Carrier C, LeComte R, 'Recent Results in Scintillation Detection with Silicon Avalanche Photodiodes', IEEE Transactions on Nuclear Science, Vol. NS-37(2), pp 209-214, (1990).

[24] Carswell H, 'Small Cameras Launch Intraoperative Imaging', Diagnostic Imaging Europe, September/October, pp 23-24, (1995).

[25] Carter T, Bird AJ, Dean AJ, Ramsden D, 'The Optimisation of CsI(Tl)-PIN Photodiode Detectors', Nuclear Instruments and Methods in Physics Research, Vol. A348(2-3), pp 567-571, (1994).

[26] Carter T, PhD Thesis, University of Southampton, England, (1995).

[27] Chen C-T et al., 'Radionuclide Probes for Tissue Damage in Electrical Injury', NYAS Annals, Vol. 720, pp 181-191.

[28] Cho Zhang-Hee, Jones JP, Singh M, 'Foundations of Medical Imaging', John Wiley & Sons.

[29] Cormack AM, 'Representation of a Function by its Line Integrals, with Some Radiological Applications', American Journal of Radiology, Vol. 34, pp 2722-2727, (1963).

[30] Cox PH, Belfer AJ, van der Pompe WB, 'Thallium 201 Chloride Uptake in Tumours, a Possible Implication in Heart Scintigraphy', British Journal of Radiology, Vol. 49, pp 767-768, (1976).

[31] Daghighian F et al., 'Intraoperative Beta Cameras', Journal of Nuclear Medicine, June, p 110P, (1995).

[32] D'Ambrosio C et al., 'Photon Counting with a Hybrid Photomultiplier Tube', Nuclear Instruments and Methods in Physics Research, Vol. A338, pp 389-397, (1994).

[33] Dean AJ et al., 'A Position Sensitive Gamma-Ray Detector which Employs Photodiode and CsI(Tl) Crystals', IEEE Transactions on Nuclear Science, Vol. NS-34(4), pp 1089-1092, (1987).

[34] Day DS, Telfer J, Hilger Analytical, Private Communications.

[35] Delft Electronische Producten, Hybrid Photomultiplier Tubes (HPMT) Products Catalogue (1995).

[36] DeSalvo R et al., 'First Results on the Hybrid Photodiode Tube', Nuclear Instruments and Methods in Physics Research, Vol. A315, pp 375-384, (1992).

[37] Doke T et al., 'A New Two-Dimensional Position Sensitive Detector with a Good Linear Response', Nuclear Instruments and Methods in Physics Research, Vol. A261, pp 605-609, (1987).

[38] Durrant PT, Truman A, Datema C, Ramsden D, 'A Gamma Camera Probe with Hybrid Photodiode Readout', Conference Proceedings of the 1995 IEEE Nuclear Science Symposium and Medical Imaging Conference, San Fransisco, CA.

[39] Fessler JA, Rogers WL, Clinthorne NH, 'Robust Maximum-Liklihood Position Estimation in Scintillation Cameras', Conference Proceedings of the 1991 IEEE Nuclear Science Symposium and Medical Imaging Conference, Vol. 3, pp 1851-1855.

[40] Gong WG et al., 'Quality Tests of CsI(Tl) Scintillators', Nuclear Instruments and Methods in Physics Research, Vol. A287, pp 639-641, (1990).

[41] Grassman H, 'Properties of CsI(Tl) - Renaissance of an Old Scintillation Material', Nuclear Instruments and Methods in Physics Research, Vol. A228, pp 323-326, (1985).

[42] Grassman H et al., 'Improvements in Photodiode Readout for Small CsI(Tl) Crystals', Nuclear Instruments and Methods in Physics Research, Vol. A234, pp 122-124, (1985).

[43] Groom D, 'Silicon Photodiode Detection of Bismuth Germanate Scintillation Light', Nuclear Instruments and Methods in Physics Research, Vol. A219, pp 141-148, (1984).

[44] Hamamatsu Technical Data Sheet - Position-Sensitive Diodes, Hamamatsu Photonics K.K., Japan, (1994).

[45] Hamamatsu Technical Data Sheet - R2487 PSPMT, Hamamatsu Photonics K.K., Japan, (1986).

[46] Hamamatsu Technical Data Sheet - R3292 PSPMT, Hamamatsu Photonics K.K., Japan, (1988).

[47] Hamamatsu Technical Data Sheet - R5900 PSPMT, Hamamatsu Photonics K.K., Japan, (1994).

[48] Hamamatsu Technical Data Sheet - Hybrid Photo-Detector, Tentative Data, Hamamatsu Photonics K.K., Japan, (1994).

[49] Harshaw Q &S Radiation Detectors Catalogue, (1992).

[50] Hayashi T, 'New Photomultiplier Tubes for Medical Imaging', IEEE Transactions on Nuclear Science, Vol. NS-36(1), pp 1078-1083, (1989).

[51] He Z, Bird AJ, Ramsden D, Meng Y, 'A 5 Inch Diameter Position-Sensitive Scintillation Counter', IEEE Transactions on Nuclear Science, Vol. NS-40(4), pp 447-451, (1993).

[52] He Z, Truman A, Guru SV, Wehe DK, Knoll GF, Ramsden D, 'Portable Wide-Angle γ-Ray Vision Systems', IEEE Transactions on Nuclear Science, Vol. 42(4), pp 668-674, (1995).

[53] He Z, PhD Thesis, University of Southampton, England, (1993).

[54] 'Heavy Scintillators', Proceedings of the Crystal 2000 International Workshop.

[55] Hilger Analytical Scintillation Products Catalogue.

[56] Hisada K, Tonami N, Miyamae T, et al., 'Clinical Evaluation of Tumor Imaging with 201Tl Chloride', Radiology, Vol. 129, pp 497-500, (1978).

[57] Houndsfield GN, British Journal of Radiology, Vol. 46, p 1016, (1973).

[58] INTEGRAL, ESA SCI(93)1, April 1993.

[59] Ito M et al., 'CsI(Na) Scintillation Plate with High Spatial Resolution', IEEE Transactions on Nuclear Science, Vol. NS-34(1), pp 401-405, (1987).

[60] Johansen GA, PhD Thesis, University of Bergen, Norway, (1990).

[61] Johansen GA, Stadsnes J, 'A New Detector Concept for Energetic Auroral X-Ray Imaging', Proceedings of an ESA Symposium on Photon Detectors for Space Instrumentation, ESA SP-356, December 1992.

[62] Johansen GA, Johnson CB, 'Operational Characteristics of an Electron-Bombarded Silicon-Diode Photomultiplier Tube', Nuclear Instruments and Methods in Physics Research, Vol. A326, pp 295-298, (1993).

[63] Kalbitzer S, Melzer W, 'On The Charge Dividing Mechanism in Position Sensitive Detectors', Nuclear Instruments and Methods in Physics Research, Vol. A56, pp 301-304, (1967).

[64] Kalibjian R, 'A Phototube using a Semiconductor Diode as the Multiplier Element', IEEE Transactions on Nuclear Science, Vol. NS-13(3), pp 54-62, (1966).

[65] Kawarabayashi J et al., 'New Array Type Electron Multiplier as a Two Dimensional Position Sensitive Detector', Nuclear Instruments and Methods in Physics Research, Vol. A353, pp 172-175 (1994).

[66] Khalkhali I, Mena I, Jouanne E, et al., 'Prone Scintimammography in Patients with Suspicion of Breast Cancer', Journal of the American College of Surgeons, Vol. 178, pp 491-497, (1994).

[67] Kilgus U, 'Prospects of CsI(Tl)-Photodiode Detectors for Low-Level Spectroscopy', Nuclear Instruments and Methods in Physics Research, Vol. A297, pp 425-440, (1990).

[68] Knoll GF, 'Radiation Detection and Measurement', John Wiley & Sons.

[69] Kotthaus R, 'CsI(Tl)-Photodiode Detectors for Spectrometry at Low Radiation Levels', Nuclear Instruments and Methods in Physics Research, Vol. A329, pp 433-439, (1993).

[70] Kume H, Muramatsu S, Iida M, 'Position-Sensitive Photomultiplier Tubes for Scintillation Imaging', IEEE Transactions on Nuclear Science, Vol. NS-33(1), pp 448-452, (1986).

[71] Lægsgaard E, 'Position-Sensitive Semiconductor Detectors', Nuclear Instruments and Methods in Physics Research, Vol. A162, pp 93-111, (1979).

[72] Lapington JS et al., 'Microchannel Plate Pore Size Limited Imaging with Ultra-Thin Wedge and Strip Anodes', IEEE Transactions on Nuclear Science, Vol. NS-34(1), pp 431-433, (1987).

[73] Lawton C, 'Avalanche Photodiode Results', Reported July 1995.

[74] Lecoq P, Schussler M, 'Progress and Prospects in the Development of New Scintillators for Future High Energy Physics Experiments', Nuclear Instruments and Methods in Physics, Vol. A315, pp 337-343, (1992).

[75] Leo WR, 'Techniques for Nuclear and Particle Physics Experiments', Springer-Verlag.

[76] Lewis RA, PhD Thesis, University of Southampton, England, (1984).

[77] Limber MA et al., 'Direct Reconstruction of Functional Parameters for Dynamic SPECT', Conference Proceedings of the 1994 IEEE Nuclear Science Symposium and Medical Imaging Conference, Norfolk, VA, pp 1207-1211.

[78] Matthews KL, Aarsvold JN, Mintzer RA, Ordonez CE, Pan X, Yasillo NJ, Chen J, Chen C-T, Beck RN, 'Tomographic Imaging with a Miniature Gamma Camera', Conference Proceedings of the 1994 IEEE Nuclear Science Symposium & Medical Imaging Conference, pp 1292-1296.

[79] McAlpine R, Boardman RJ, Wilde B, Electron Tubes Ltd., Private Communications.

[80] Melcher CL, 'Cerium-Doped Lutetium Oxyorthosilicate: A Fast, Efficient New Scintillator', IEEE Transactions on Nuclear Science, Vol. NS-39(4), pp 502-505, (1992).

[81] Michette AG, Buckley CJ, 'X-Ray Science and Technology', Institute of Physics Publishing Ltd., (1993).

[82] Milliare A et al., 'A Miniature Caesium Iodide-Photodiode Detector for Ambulatory Monitoring of Left Ventricular Function', Medical Physics, Vol. 21(55), pp 683-689, (1994).

[83] Moisan C et al., "Design Studies of a Depth Encoding Large Aperture PET Camera', TRIUMF Preprint TRI-PP-94-81.

[84] Moore R, Alpert M, Strauss HW, 'A Handheld, Low Power, Gamma Camera: Design Considerations and Initial Results', Journal of Nuclear Medicine, Vol. 29(5), p 832, (1988).

[85] Mullerworth S, Ramsden D, 'A Silicon Diode Array for Hard X-Ray Imaging Applications', Nuclear Instruments and Methods in Physics Research, Vol. A310, pp 179-183, (1991).

[86] Pani R et al., 'Very High Resolution Gamma Camera Based on Position Sensitive Photomultiplier Tube', Physica Medica, Vol. 9(2-3), pp 233-236, (1993).

[87] Pani R et al., 'Multi-Crystal YAP:Ce Detector System for Position Sensitive Measurements', Nuclear Instruments and Methods in Physics Research, Vol. A348, pp 551-558, (1994).

[88] Parker SH, Lovin JD, Jobe WF, Luethke JM, et al., 'Stereotactic Breast Biopsy with a Biopsy Gun', Radiology, Vol. 176, pp 741-747, (1990).

[89] Philips Photonics Product Catalogue (1994).

[90] Physics in Medicine and Biology Encyclopedia.

[91] Poulsen JM, Verbeni R, Frontera F, 'Position-Sensitive Scintillation Detector for Hard X-Rays', Nuclear Instruments and Methods in Physics Research, Vol. A310, pp 398-402, (1991).

[92] Radeka V, 'Signal, Noise and Resolution in Position-Sensitive Detectors', IEEE Transactions on Nuclear Science, Vol. NS-21, pp 51-64, (1974).

[93] Radeka V, 'Semiconductor Position-Sensitive Detectors', Nuclear Instruments and Methods in Physics Research, Vol. A226, pp 209-218, (1984).

[94] Radon J, 'Über die Bestimmung von Funktionen durch ihre Integralwerte längs gewisser Manningfaltigkeiten', Berichte Saechsische Ahademie der Wissenschaften, Vol. 69, pp 262-277, (1917).

[95] Redus RH et al., 'Intraoperative Nuclear Imaging Probe', Conference Proceedings of the1991 IEEE Nuclear Science Symposium & Medical Imaging Conference, Vol. 3, pp 1887-1891.

[96] Redus RH et al., 'A Combined Video and Gamma Ray Imaging System for Robots in Nuclear Environments', Nuclear Instruments and Methods in Physics Research, Vol. A353, pp 324-327, (1994).

[97] Roche CT, Strauss MG, Brenner R, 'Resolution and Linearity of Anger-Type Neutron-Position Detectors as Simulated with Different Signal Processing Optics', IEEE Transactions on Nuclear Science, Vol. NS-32(1), pp 373-379, (1985).

[98] Röentgen WK, 'On a New Kind of Rays' (translated by A Stanton), Nature, Vol. 53, pp 274-276, (1896).

[99] Rogers JG et al., 'Design of an Efficient Position Sensitive Gamma Ray Detector for Nuclear Medicine', Physics in Medicine and Biology, Vol. 31(10), pp 1061-1090, (1986).

[100] Rogers JG, 'A Method for Correcting the Depth-of-Interaction Blurring in PET Cameras', IEEE Transactions on Medical Imaging, Vol. 14(1), (1995).

[101] Rogers WL, Clinthorne NH, Shao L, Koral KF, 'Experimental Evaluation of a Modular Scintillation Camera for SPECT', IEEE Transactions on Nuclear Science, Vol. NS-36(1), pp 1122-1126, (1989).

[102] Rossner W, Grabmaier BC, 'Phosphors for X-Ray Detectors in Computed Tomography', Journal of Luminescence, Vols. 48 & 49, pp 29-36, (1991).

[103] Roziere H et al., 'Large Field-of-View Image Intensifier Gamma-Camera Detectors Using a Silicon XY Scintillation Localizer', IEEE Transactions on Nuclear Science, Vol. NS-28(1), pp 60-63, (1981).

[104] Saffer JR et al., 'Surgical Probe Design for a Coincidence Imaging System Without Collimator', Image and Vision Computing, Vol. 10(6), pp 333-341, (1992).

[105] Schmidt JG, 'The Epidemiology of Mass Breast Cancer Screening - A Plea for a Valid Measure of Benefit', Journal of Clinical Epidemiology, Vol. 43, pp 215-225, (1990).

[106] Schmidt-Ott WD et al., 'PIN Diodes for Electron Detection', Nuclear Instruments and Methods in Physics Research, Vol. A285, pp 459-463, (1989).

[107] Schomaker R, DEP, 'Spectral response curves for a high quantum efficiency photocathode', Private Communication, (1993).

[108] Schotanus P et al., 'Scintillation Characteristics of Pure and Tl-Doped CsI Crystals', IEEE Transactions on Nuclear Science, Vol. NS-37, pp 177-182, (1990).

[109] Schwarz HE, Lapington JS, 'Optimisation of Wedge and Strip Anodes', IEEE Transactions on Nuclear Science, Vol. NS-32(1), pp 433-437, (1985).

[110] Scionix Information Sheet.

[111] Sclar N, 'Electron Bombarded Semiconductor as a Circuit Element', Conference Proceedings of the Electron Devices Conference, Washington, DC, (1957).

[112] Short MD, 'Gamma Camera Systems', Nuclear Instruments and Methods in Physics Research, Vol. A221, pp 142-149, (1984).

[113] Sickle WA, 'Mammographic Features of 300 Consecutive Nonpalpable Breast Cancers', American Journal of Radiology, Vol. 146, pp 661-663, (1986).

[114] Siegel S et al., 'Development of Continuous Detectors for a High Resolution Animal PET System', Conference Proceedings of the 1994 IEEE Nuclear Science Symposium and Medical Imaging Conference, pp 1662-1666.

[115] Silicon Sensor, Position-Sensitive Photodiode Products Catalogue (1992).

[116] Singh M et al., 'Physics of Electronic Collimation for Single photon Transaxial Tomography', Medical Physics, Vol. 4, p 350, (1977).

[117] Suyama M et al., 'Fundamental Investigation of Vacuum PD Tube', Conference Proceedings of the 1993 IEEE Nuclear Science Symposium and Medical Imaging Conference p 641.

[118] Suzuki H, 'Light Emission Mechanism of $Lu_2(SiO_4)O$:Ce', IEEE Transactions on Nuclear Science, Vol. NS-40(4), pp 380-383, (1993).

[119] Szawlowski M et al., 'Performance of the Vacuum Avalanche Photodiode', Advanced Photonix, Camarillo, CA 93012, (1993).

[120] Teraoka H et al., 'Radiation Damage Test of Position Sensitive Silicon Detectors', Nuclear Instruments and Methods in Physics Research, Vol. A324, pp 276-283, (1993).

[121] Thomas S, Electronics Division, DRAL, Chilton, Didcot, England, private communication.

[122] Thompson CJ, Murthy K, Weinberg IN, Mako F, 'Feasibility Study for Positron Emission Mammography', Medical Physics, Vol. 21(4), pp 529-538, (1994).

[123] Tornai MP et al., 'Development of a Small Area Beta Detecting Probe for Intra-Operative Tumor Imaging', Journal of Nuclear Medicine, June, p 109P, (1995).

[124] Truman A, Bird AJ, Ramsden D, He Z, 'Pixellated CsI(Tl) Arrays with Position-Sensitive PMT Readout', Nuclear Instruments and Methods in Physics Research, Vol. A353, pp 375-378, (1994).

[125] Truman A, Ramsden D, 'A Portable High Resolution Gamma Camera System', Conference Proceedings of the 1995 Canadian Organisation of Medical Physicists AGM, pp 59-60, Montréal, June 4-7.

[126] Truman A, Palmer MJ, Durrant PT, Bird AJ, Ramsden D, Stadsnes J, 'A PSPMT Based Auroral X-Ray Imager', Nuclear Instruments and Methods in Physics Research, Accepted for publication (1995).

[127] van Geest LK, Stoop KWJ, 'Hybrid Phototube with Si Target', Nuclear Instruments and Methods in Physics Research, Vol. A310, pp 216-266, (1991).

[128] Visser R, 'Photostimulated Luminescence and Thermoluminescence of LSO Scintillators', IEEE Transactions on Nuclear Science, Vol. NS-41(4), pp 689-693, (1994).

[129] Watanabe M, Omura T, Kyushima H, Hasegawa Y, Yamashita T, 'A Compact Position-Sensitive Detector for PET', Conference Proceedings of the 1994 IEEE Nuclear Science Symposium and Medical Imaging Conference, Norfolk, VA, pp 1652-1656.

[130] Waxman AD, Ramanna L, Memsie LD, et al.,'Thallium Scintigraphy in the Evaluation of Mass Abnormalities of the Breast', Journal of Nuclear Medicine, Vol. 34, pp 18-23, (1993).

[131] Webb S, 'The Physics of Medical Imaging', Adam Hilger.

[132] Wolfgang JG et al., 'Hybrid Photomultiplier Tubes Using Internal Solid State Elements', IEEE Transactions on Nuclear Science, Vol. NS-13(3), pp 46-53, (1966).

[133] Yamamoto K et al., 'New Structure of Two-Dimensional Position Sensitive Semiconductor Detector and Application', IEEE Transactions on Nuclear Science, Vol. NS-32(1), pp 438-442, (1985).

[134] Yamashita T, Watanabe M, Shimizu K, Uchida H, 'High Resolution Block Detectors for PET', IEEE Transactions on Nuclear Science, Vol. NS-37(2), pp 589-593, (1990).

[135] Yanagimachi T et al., 'New Two-Dimensional Position Sensitive Silicon Detector with Good Position Linearity and Resolution', Nuclear Instruments and Methods in Physics Research, Vol. A275, pp 307-314, (1989).

[136] Yasillo NJ et al., 'Design Considerations for a Single Tube Gamma Camera', IEEE Transactions on Nuclear Science, Vol. NS-37(2), pp 609-615, (1990).

[137] Yasillo NJ et al., 'A Single-Tube Miniature Gamma Camera', Conference Proceedings of the 1993 IEEE Nuclear Science Symposium & Medical Imaging Conference, Vol. 2, pp 1073-1076.

[138] Yasillo NJ et al., 'A Clinical Miniature Gamma Camera', Journal of Nuclear Medicine, Vol. 34(5), p 112P.

[139] Martin C et al., 'Wedge-and-Strip Anodes for Centroid-Finding Position-Sensitive Photon and Particle Detectors', Review of Scientific Instruments, Vol. 52(7), pp 1067-1074, (1981).

Appendix to Chapter 6

Analysis of Test Images Acquired with a Compact Gamma Camera

A.1 Introduction

The uncorrected images presented throughout Chapter 6 have qualitatively confirmed the ability of these new compact gamma cameras to provide images of comparable quality to commercial gamma cameras for the clinical investigation of a relatively small region of interest (ROI). In order to identify possible areas where either the camera design or data acquisition system employed might be further improved, a more detailed analysis of these images was performed using the General Electric Optima image processing system at the UCL Middlesex Hospital.

Several of the images that were acquired with the camera described in section 6.5 have been analysed in order to determine the total number of counts that were acquired, and "binned", within particular regions of interest. From these data an indication of the statistical errors present within each image has been estimated. In addition, profiles have been made which intersect several prominent features within each image. If the separation of these features within the object and their apparent separation in the image is measured, an estimate of the distortion in each axis of the image can be determined.

A.2 Flat-Field Response

Whilst the intrinsic spatial resolution of the compact gamma camera without the collimator attached was measured to be 2.9 mm FWHM, the extrinsic spatial resolution of the compact gamma camera complete with collimator was found to be much poorer at approximately 5.0 mm FWHM. Despite this undesirable reduction in spatial resolution, clinical gamma cameras require a parallel-hole collimator in order to accurately localize the origin of the incident γ -rays within the patient, and it is therefore appropriate to consider the extrinsic performance limitations of the compact gamma camera.

The uncorrected extrinsic response has been investigated when the camera is uniformly irradiated by an extended ^{57}Co flood radiation source of the type used to calibrate clinical gamma cameras. The number of counts which have been incorrectly binned due to the centroiding algorithm employed, relative to those correctly binned within the central uniform field of view (UFOV) has been studied.

Three horizontal profiles, and one vertical profile were obtained which intersect the image presented in Figure 6.7. These data were acquired from a 10 minute exposure to a uniform field of radiation from an extended ^{57}Co source placed in intimate contact with the collimator of the camera. The statistical significance of the resulting binning errors as a function of position across the sensitive area of the camera, and their affect upon the overall performance of the compact gamma camera could then be studied (see Figure A.1 and Figure A.2).

The width of a single channel in each of these profiles was estimated to be approximately 0.67 mm which, being considerably smaller than the demonstrated spatial resolution of the gamma camera, would usually be considered to be more than adequate to provide accurate binning of detected counts. Whilst acquiring data for a longer period of time would reduce the relative significance of errors present in the image that are due to Poisson statistics, large fluctuations are present in the profiles which cannot be attributed to counting statistics alone. The periodic nature of these fluctuations together with their spatial separation suggests the possibility that unwanted electronic noise charge originating from the anode wires of the PSPMT is contributing to the image data. Longer acquisition times would therefore only serve to increase this unwanted noise contribution from the PSPMT. However a regular pattern of binned events correlating to the anode structure of the PSPMT was not observed in any of the images that were acquired and evaluated in previous chapters. The more probable explanation of these effects is a combination of counting statistics, and random systematic electronic noise from the PSPMT and associated amplifiers. Also, since the source to collimator distance was so small, it is possible that the collimator could have contributed to such an effect.

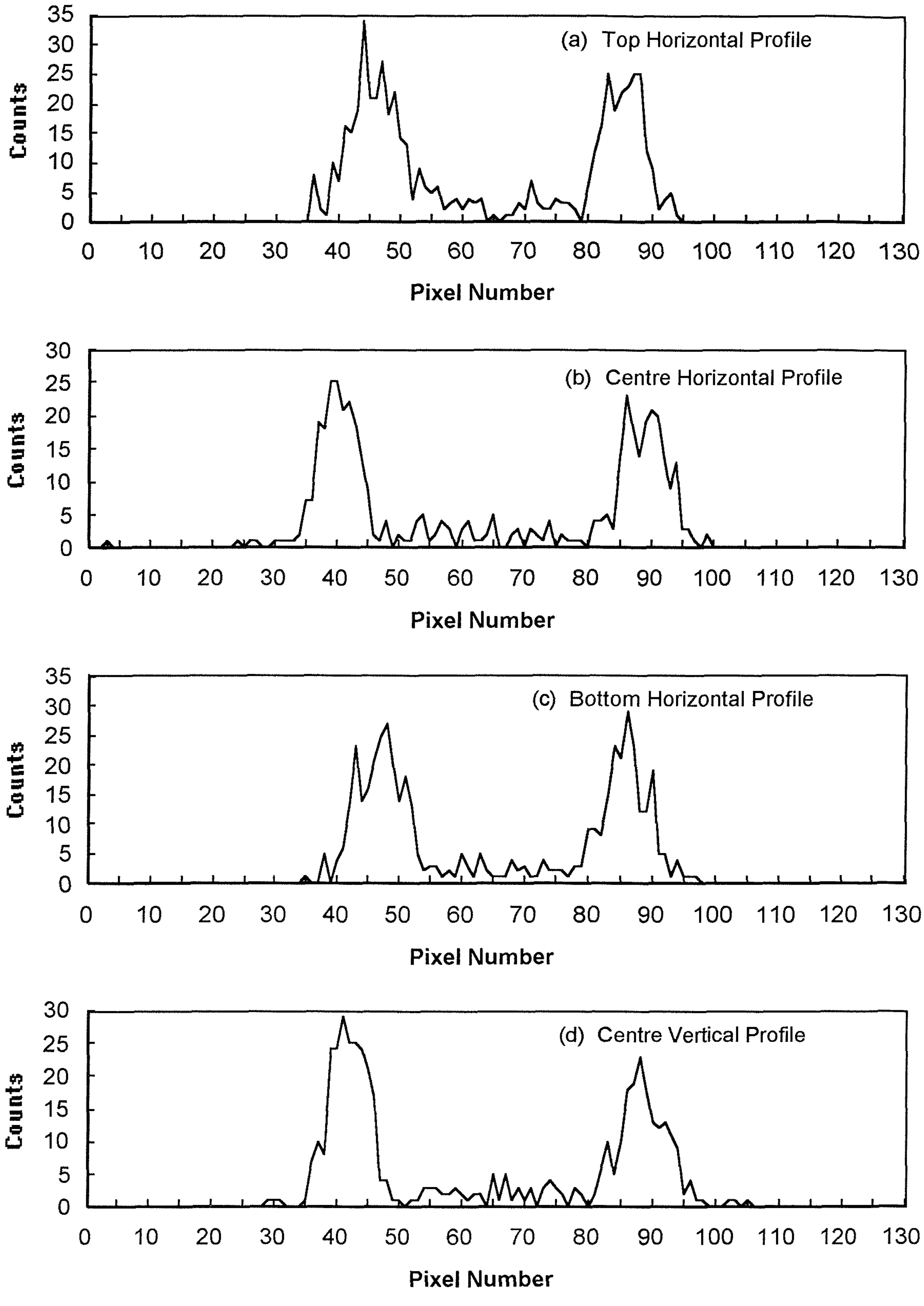

Figure A.1: *Profiles through flat-field image without black annular mask.*

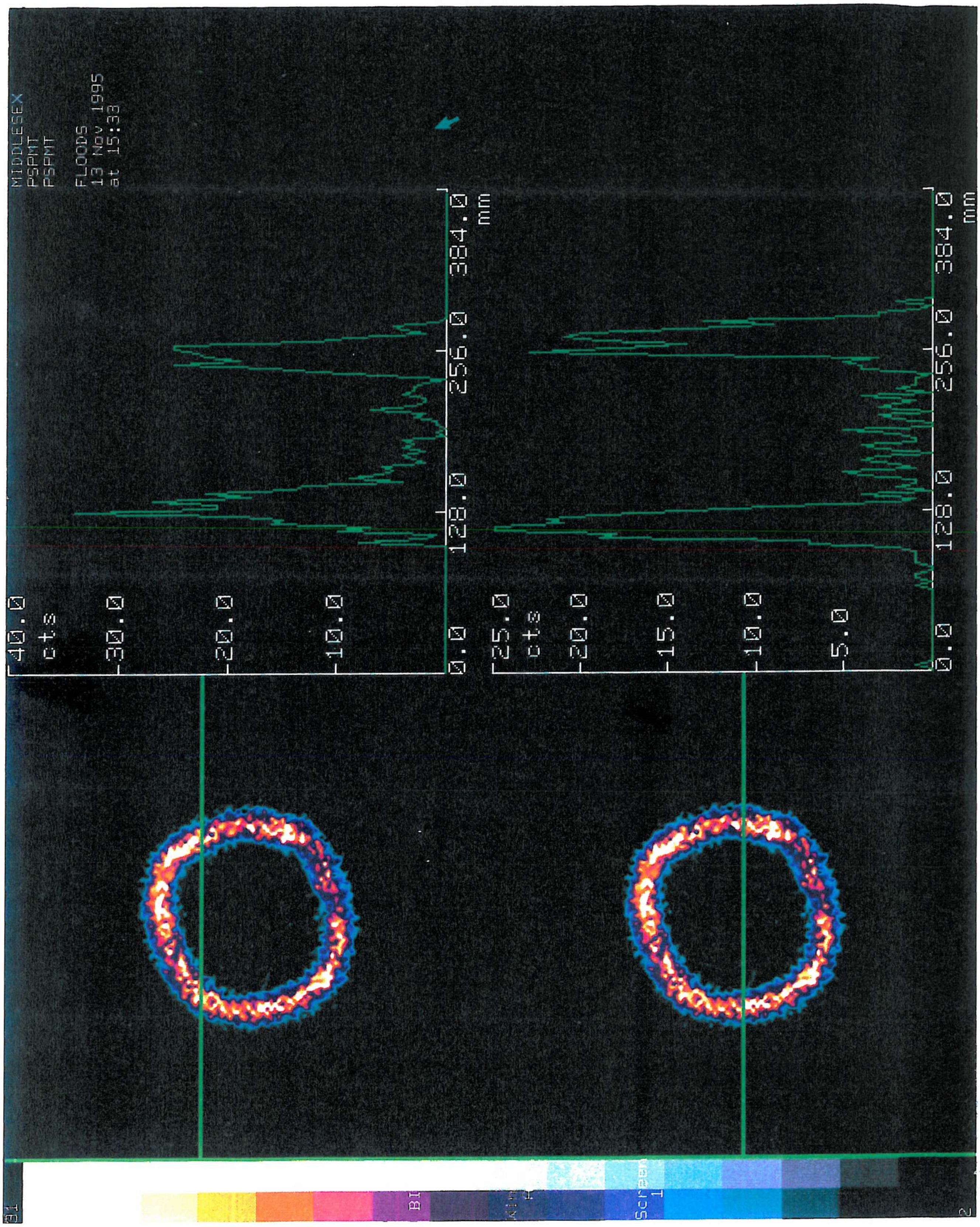

Figure A.2(a): *The GE Optima image processing system was employed to obtain profiles through a flood-field image of an extended ^{57}Co radiation source prior to modifying the gamma camera with the addition of the black annular mask described previously.*

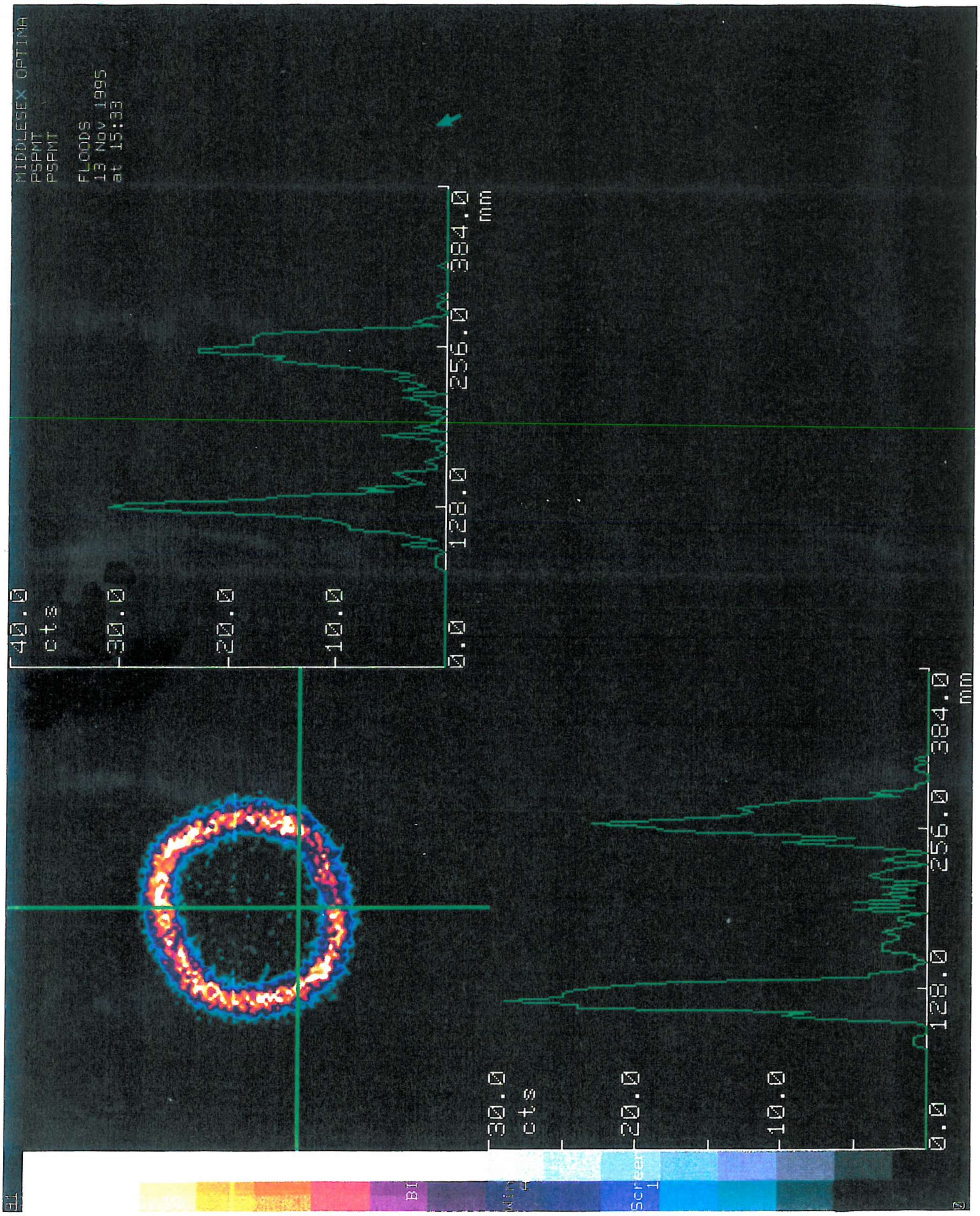

Figure A.2(b): *The GE Optima image processing system was employed to obtain profiles through a flood-field image of an extended ^{57}Co radiation source prior to modifying the gamma camera with the addition of the black annular mask described previously.*

When employing a centroiding algorithm, interactions within a region approximating to the outer 50% of the field of view of the PSPMT are reconstructed having been shifted slightly towards the centre of the field of view. From these data it can clearly be seen that whilst very few counts were binned towards the edge of the field of view (represented by pixel numbers 0 to 30, and pixel numbers 100 to 130), the resulting "pile up" of counts between pixel numbers 30 to 50, and pixel numbers 80 to 100, in the original image has produced a peak-to-valley ratio of approximately 5:1. Since almost all of the total number of events recorded by the camera were binned within this very narrow band, other prominent features which might under normal circumstances be observable from the reconstructed image were clearly unresolvable.

The undesirable effects attributable to the centroiding algorithm used were overcome by employing a similar technique to that used by manufacturers of clinical gamma cameras. The outer 50% of the sensitive area of the photomultiplier tube was masked resulting in a much improved flat-field response function over the central 80 mm diameter uniform field of view (UFOV) such as that presented in Figure 6.8. Taking a horizontal profile through the centre of this image, reveals that the number of pixels containing counts within 2 sigma of the mean does not exceed that which would typically be expected within a sample size of approximately 120 pixels (see Figure A.3 and Figure A.4).

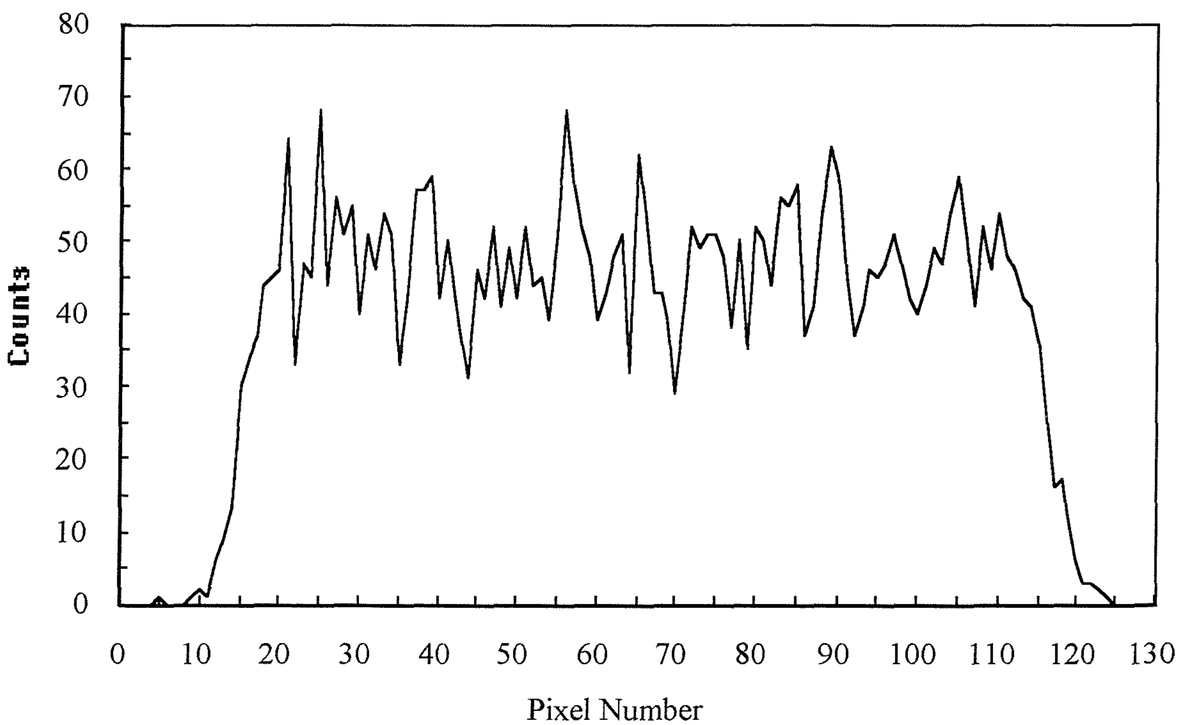

Figure A.3: *Profile illustrating the 'improved' flat-field response function*

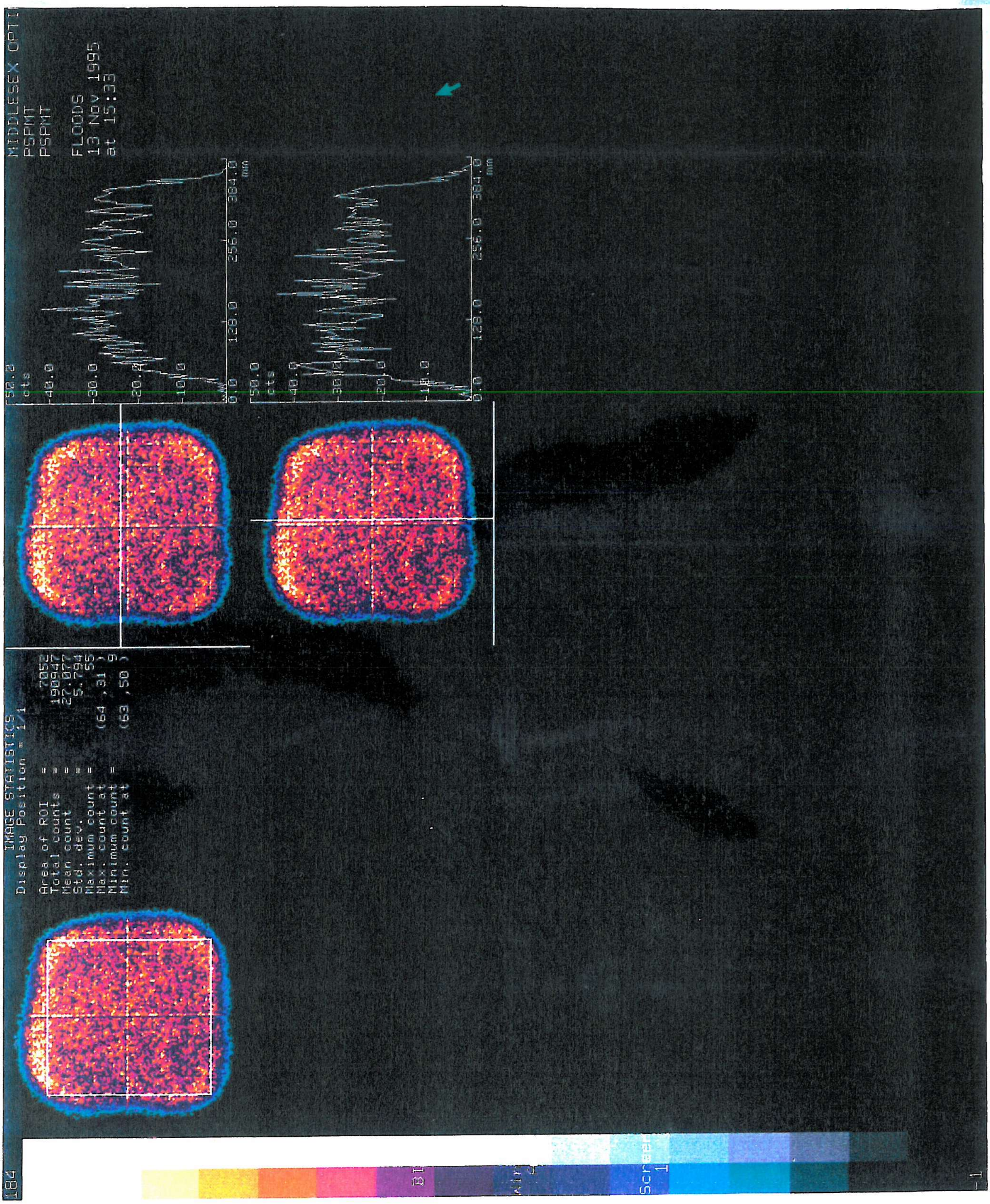

Figure A.4: *Profiles through a flood-field image of an extended* ^{57}Co *radiation source together with associated image statistics after the gamma camera had been modified with the addition of the black annular mask.*

A.3 Imaging Characteristics

Image quality and clarity are general terms which are often used to refer to the degree of visibility of important information within some region of interest in an image. It is often necessary however to use more quantitative descriptions when considering image quality. More specific image attributes such as spatial resolution, image contrast, background counts, and image noise are all terms which are used to describe the quality of an image for a particular nuclear medicine application. Whilst all of these quantities are used to specify the quality of an image, when considered independently, each term reduces to a simple relationship between the signal and the noise present within the image considered.

Unsharpness and resolution usually refers to the degree of blurring along the boundaries between adjacent regions which represent different anatomical features within the image, or in the case of nuclear medicine imaging, different radiopharmaceutical uptake distributions (see Figure A.5).

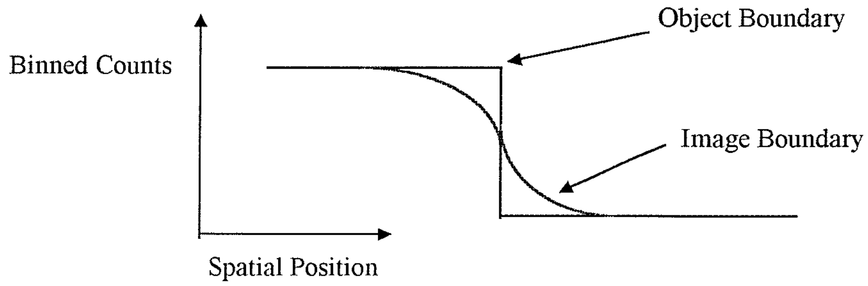

Figure A.5: *Blurring of the image due to the edge response of the detector*

Several methods are employed in practice to determine the extrinsic resolution of a gamma camera. Spatial resolution, or resolving power can be easily determined by moving two point sources of the same isotope and equal activity towards each other and measuring the spatial separation when each point-spread function (PSF) can no longer be separately distinguished from the other (see Figure A.6).

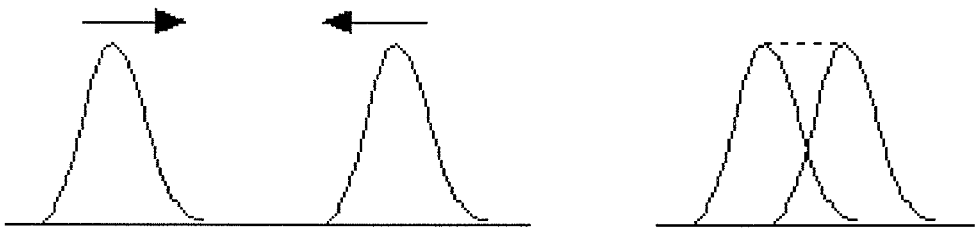

Figure A.6: *Limit of spatial resolution of a detection system*

The metric for spatial resolution in an image is well described by the Rayleigh Criterion, and the two images will completely merge at a separation which is approximately equal to the full-width at half maximum (FWHM) of the image of the point sources. The spatial resolution is generally specified as a single number which refers to the FWHM (measured in mm) of the PSF from a point-source image. The PSF taken from an image of a point source is usually represented in two-dimensions for planar imaging, and in three-dimensions for tomographic SPECT or PET imaging.

Similarly, the line-spread function (LSF) is the one-dimensional response of a gamma camera used to view a narrow capillary line source. This is the convolution of the PSF described previously with a line source of infinite length (see Figure A.7).

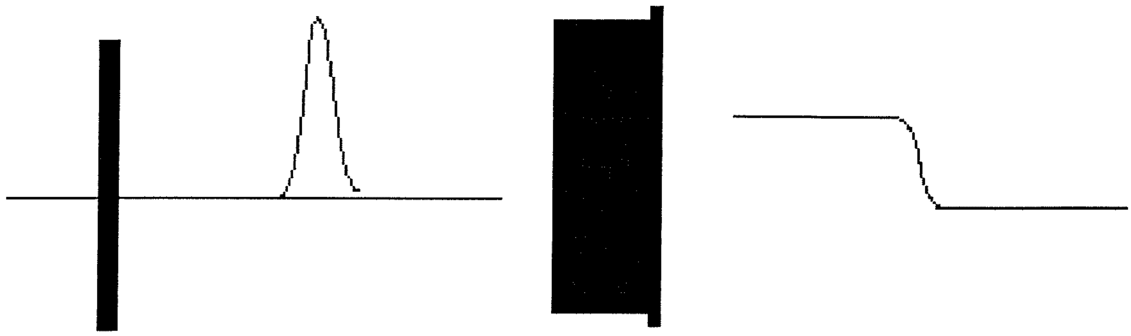

Figure A.7: *The line-spread function (LSF), and the edge response function (ERF)*

The edge-response function (ERF) is the one-dimensional response of a gamma camera used to view a perfectly straight boundary between two regions of different activity, and infinite length. This is the convolution of the LSF described previously with a step function (see Figure A.7).

Each of these techniques used to determine the extrinsic spatial resolution of a gamma camera will of course be affected by the size of each aperture forming the collimator. Whilst the intrinsic spatial resolution of the PSPMT used as the photodetector in the compact gamma camera is specified by the manufacturer to be of the order of 0.3 mm FWHM, the extrinsic spatial resolution of the compact gamma camera was determined to be approximately 5 mm FWHM. This difference between the theoretical resolution limit set by the photodetector, and the practical resolution of the camera is principally due to poor collimator resolution. In most commercially available clinical gamma cameras, the collimator resolution lies somewhere between 8 mm and 25 mm FWHM, and varies as a function of the distance of the source away from collimator (see Figure A.8).

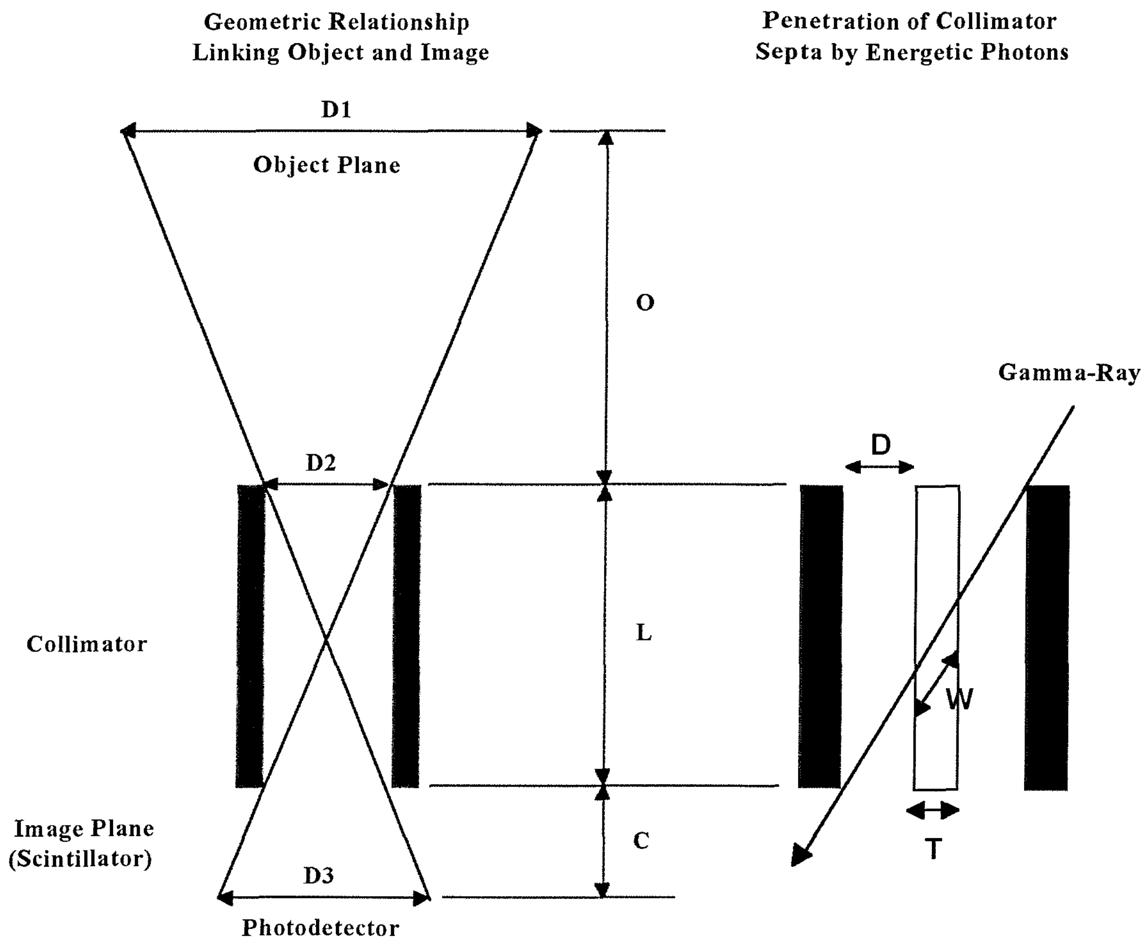

Figure A.8: *Collimator resolution*

The actual extrinsic spatial resolution of a clinical gamma camera will therefore be determined by a combination of the collimator resolution and the intrinsic spatial resolution of the gamma camera itself, with both the object and the image related by a simple geometric expression such as that illustrated by Figure A.8:

By similar triangles:-

$$\frac{D1}{O+(L/2)}=\frac{D2}{(L/2)}=\frac{D3}{C+(L/2)}\Rightarrow\frac{D1}{D3}=\frac{C+(L/2)}{O+(L/2)}$$

Similarly, geometrical relationships can be used to determine the effective shielding provided by the septa when considering the problem of septal penetration in the detector:

$$\frac{W^2}{T^2}=\frac{\{(2D+T)^2+1\}^2}{(2D+T)^2}\Rightarrow W=\frac{LT}{2D}$$

However, for source distances greater than a few centimetres away from the collimator, the spatial resolution of the gamma camera system will be dominated by the collimator effects described previously. Typical values of spatial resolution for a conventional gamma camera range from approximately 4 mm FWHM at the surface of the collimator to approximately 15 mm FWHM when the source is placed 15 cm away from it.

In addition, the Compton scatter of photons interacting within a patient will significantly affect the shape of the spectrum at the full-width at tenth maximum (FWTM) level by broadening the observed spectra (see Figure A.9)

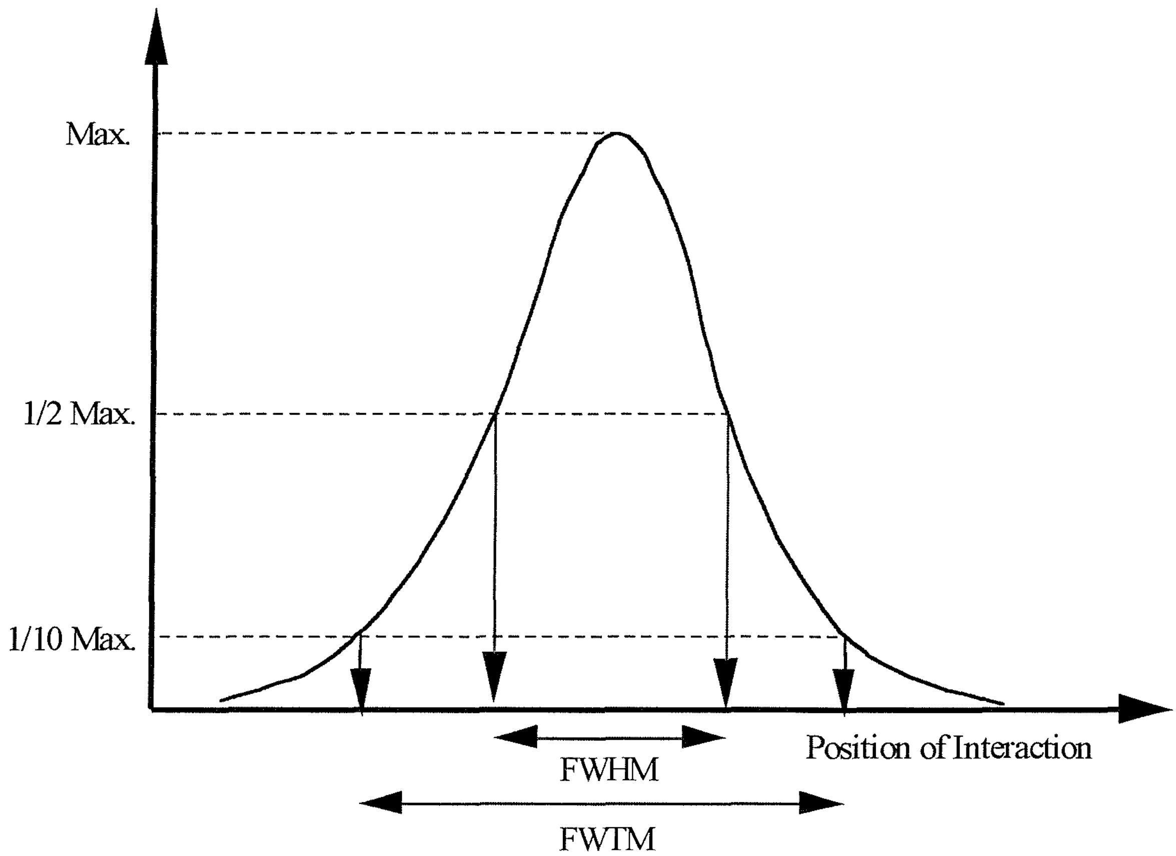

Figure A.9: *The effect of internal Compton scatter upon the spatial resolution*

The extrinsic spatial resolution of the compact gamma camera has been quantitatively estimated by using the line-spread function (LSF) technique described previously to repeat several lines of known width across the field of view. Seven capillary line sources each measuring 2 mm in diameter, and containing approximately 15 MBq of ^{99m}Tc were placed at regular intervals within the field of view in intimate contact with the collimator of the gamma camera. The sources were separated by 10 mm in both the horizontal and vertical axis, and counts were acquired for 10 minutes in each view. Three count profiles were obtained from each view, and in turn measurements were made of each line-spread function. This technique determined a mean value of the extrinsic spatial resolution for the compact gamma camera of approximately 5 mm FWHM.

A.3.1. Spatial Linearity

The extrinsic spatial linearity of the compact gamma camera has been determined both quantitatively and qualitatively. A visual inspection of the line source image provided an indication of the degree of distortion present. The image presented in Figure 6.11 demonstrated a slight outward bowing of the capillary line sources towards the left-hand edge of the field of view. This "pin-cushion" distortion was confirmed quantitatively by analysing the count profiles, first estimating the apparent mean line separation in the central linear region of the field of view (UFOV), and subsequently determining the deviation from this mean value beyond the UFOV (see Figure A.10 and Figure A.11).

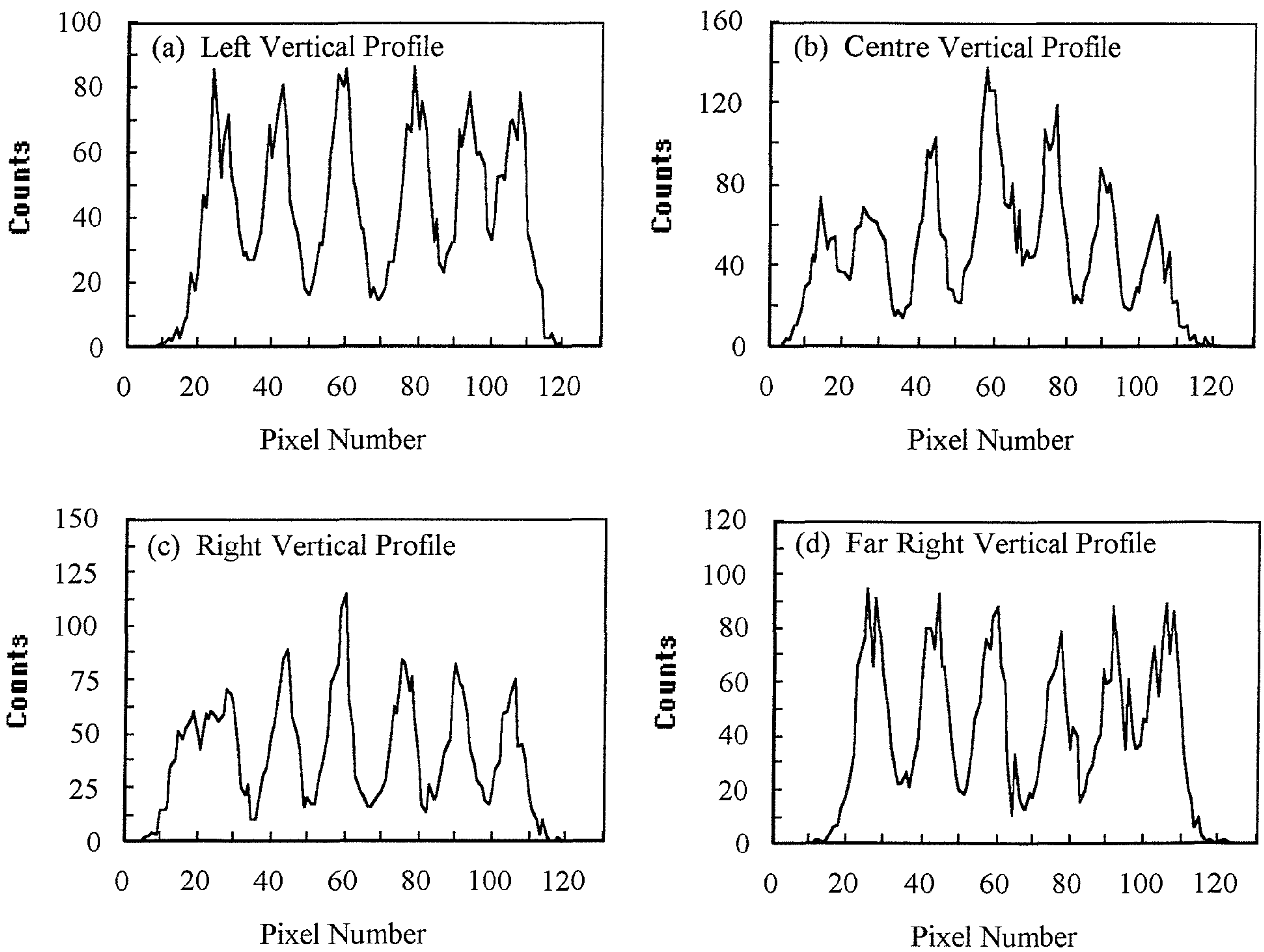

Figure A.10: *Pin-cushion distortion demonstrated by ^{99m}Tc filled capillary line sources*

The mean line separation at the centre of the FOV is approximately 16 pixels. The mean line separation at both edges of the centre vertical profile is reduced by 18.75% from this value. The mean line separation at the upper edge of the left vertical profile is increased by 14.6% from this value, whilst at the lower edge a reduction of 12.5% is observed.

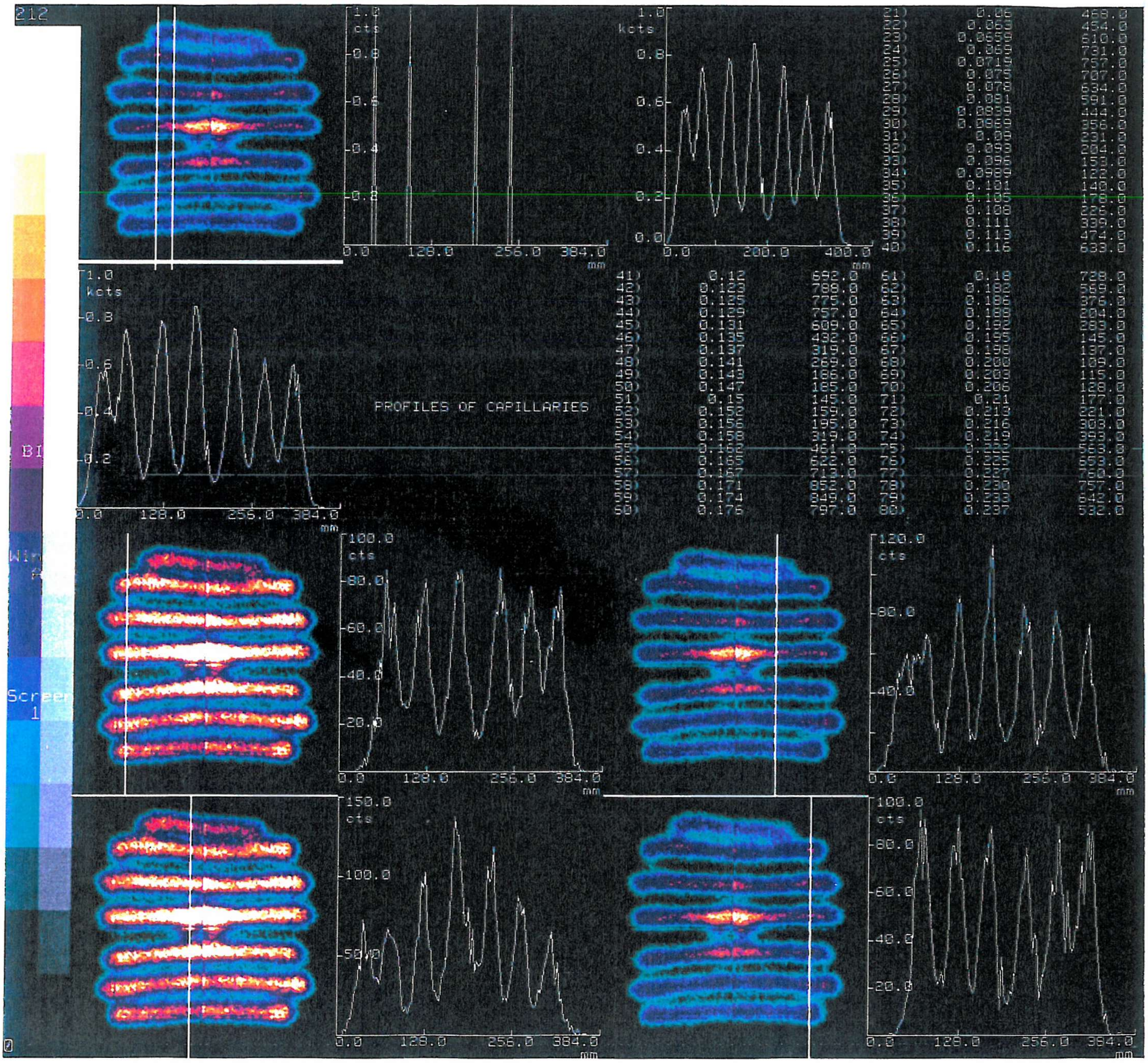

Figure A.11: *Profiles were taken through an image of seven capillary line sources that were each filled with* ^{99m}Tc.

The mean separation of both the right, and far right vertical profiles is approximately equal to that at the centre of the FOV. Clearly the majority of the distortion is exhibited towards the left of the compact gamma camera and, as discussed in previous chapters, is principally attributed to photocathode non-uniformity.

The fidelity with which object information is transferred to the image as a function of spatial frequency in the object is described by the Modulation Transfer Function (MTF). The MTF can be derived from the Fourier transform of the PSF obtained earlier, or can be measured experimentally by imaging a series of bar patterns with different spatial frequencies. In order to evaluate the imaging fidelity of the compact gamma camera, a commercially available bar phantom was used to provide a variety of line-spread functions over the entire diameter of the detector crystal. This phantom contains four quadrants, each containing bars of a different size, and each containing a different bar spacing with the bars oriented orthogonally to each adjacent quadrant. The bar phantom is placed above the collimator, and a uniform flood source is used to uniformly illuminate the entire field of view of the camera. Images are subsequently acquired which should be examined for the appearance of unusual wavy lines and local losses in spatial resolution (i.e. localised inability to resolve the bars). This routine test is conducted on both a daily and a weekly basis on clinical gamma cameras in order to verify the quality of images that have been acquired, and enabling timely servicing in the event of problems.

Bar phantom images can also provide some limited indication of the extrinsic spatial resolution of a camera. If, for example, a set of 2.5 mm bars for a particular phantom cannot be well resolved but a set of 4 mm bars are resolved, then the extrinsically resolvable bar size lies somewhere between these two values. The relationship between the spatial resolution, expressed as the full width at half maximum (FWHM) of the profile of a line-spread function, and the particular bar size that is just barely resolvable is given by the relationship:

$$\text{FWHM (in mm)} = 1.7 \times \text{bar size (in mm)}$$

This is the standard test which is applied to conventional gamma cameras on a weekly basis to estimate the distortion present in the image which might indicate, at least qualitatively, that the camera is suffering from position non-linearity effects, most probably caused by photomultiplier tube drift. The benefit of this technique is that a single acquisition yields many data sets from which accurate average line-spread functions can be derived through analysis of the count-profile. It is evident from the results illustrated in Figures A.12 and A.13 that through visual inspection of bar-phantom images one can qualitatively identify the effects of both pin-cushion and barrel distortion.

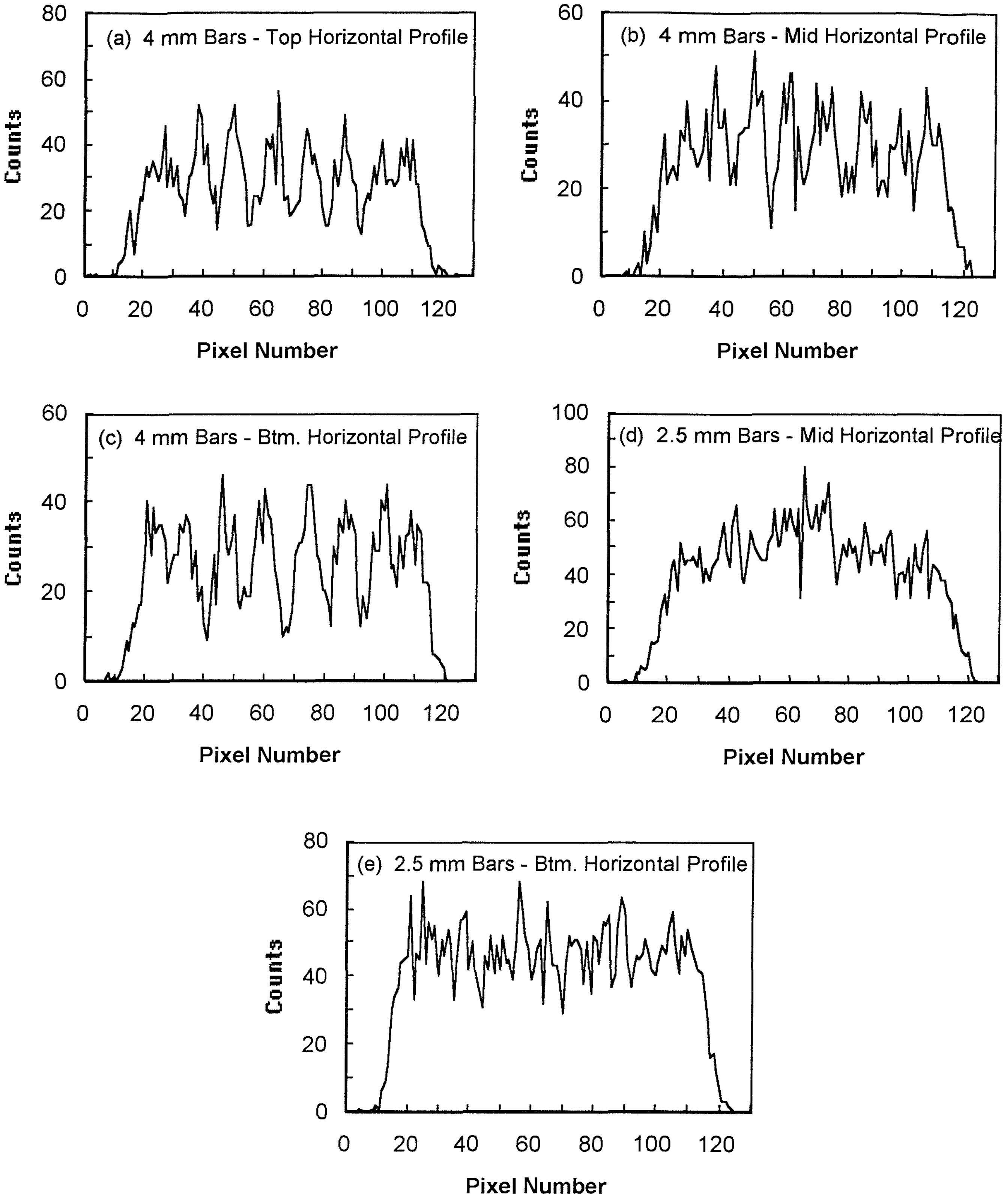

Figure A.12: *Profiles through 4 mm and 2.5 mm bar transmission phantom images*

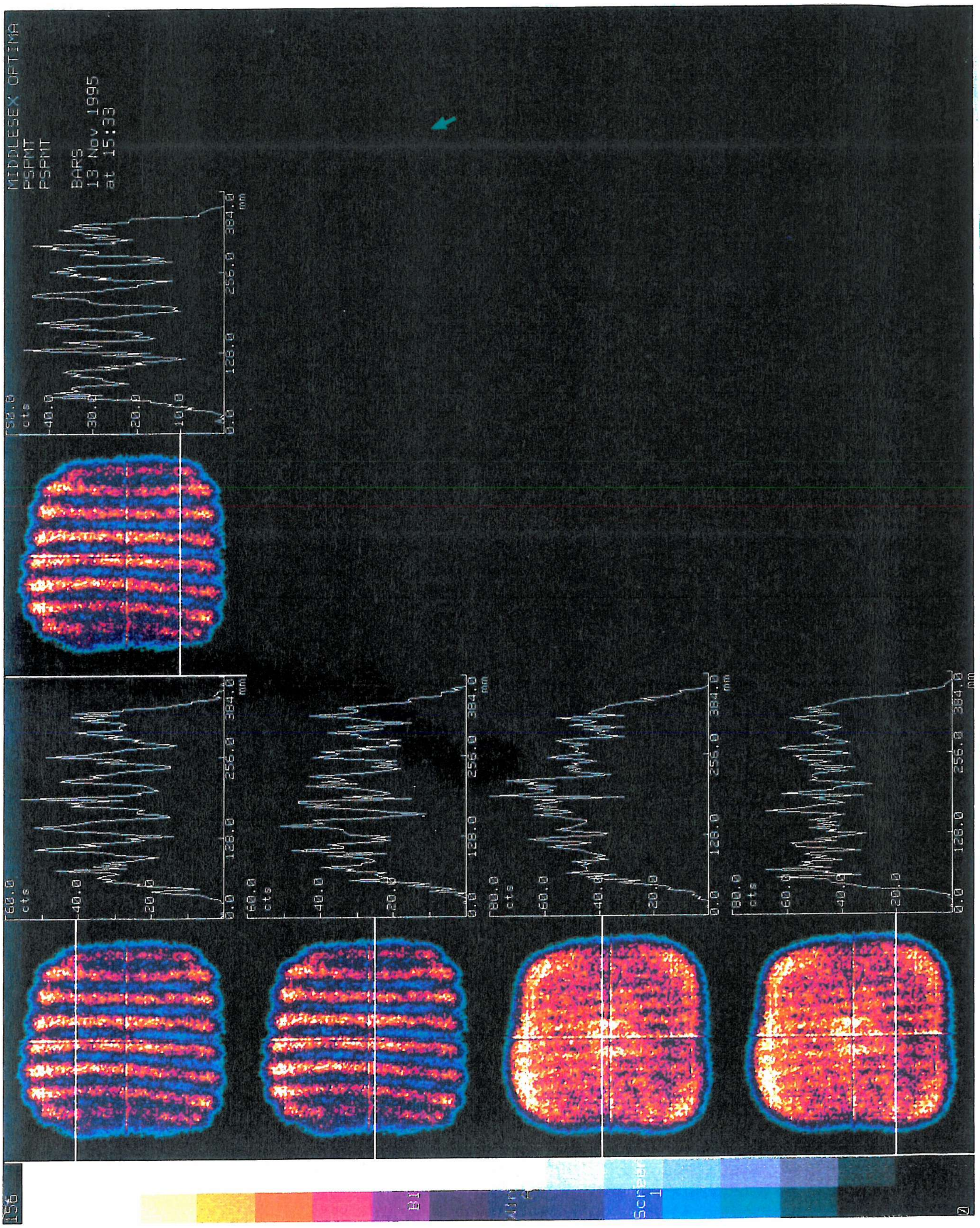

Figure A.13: *The GE Optima system was employed to obtain profiles through two images that were acquired from a bar-transmission phantom using the modified gamma camera.*

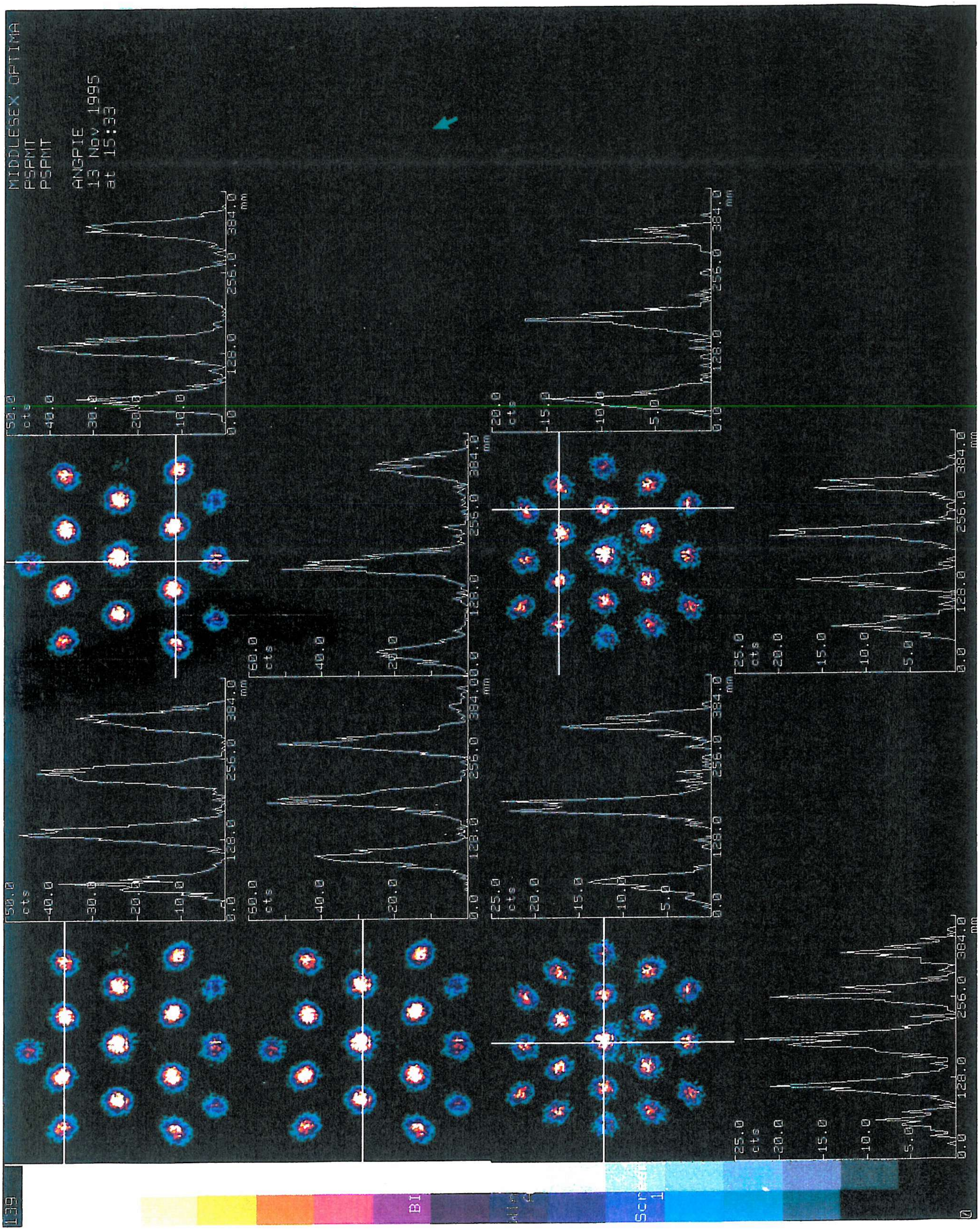

Figure A.14: *Profiles through various pie-transmission phantom images that were obtained using the modified gamma camera.*

The images presented in Figure 6.9 demonstrate that the 2.5 mm bars viewed by the compact gamma camera are clearly resolvable. The expression for the determination of spatial resolution was used to estimate a value of FWHM, and from these profiles of count data the mean extrinsic spatial resolution has been determined to be approximately 4.25 mm FWHM. Profiles obtained from pie-transmission phantom images can similarly be used to determine the spatial resolution of a gamma camera (see Figure A.14).

A.3.2 Uniformity Measurements

The "uniformity" characteristic of a gamma camera is a measure of the amount of noise that is present in the image which is produced as a result of fluctuations in the binned pixel values caused by the statistical nature of radioactive decay and detection processes. This characteristic can best be described by acquiring an image of a uniform flat-field source with a gamma camera. Whilst an ideal gamma camera with perfect uniformity and efficiency will demonstrate very low intrinsic image noise due to systematic effects, the number of counts detected in all pixels of the image will not be the same due to counting statistics (see Figure A.15).

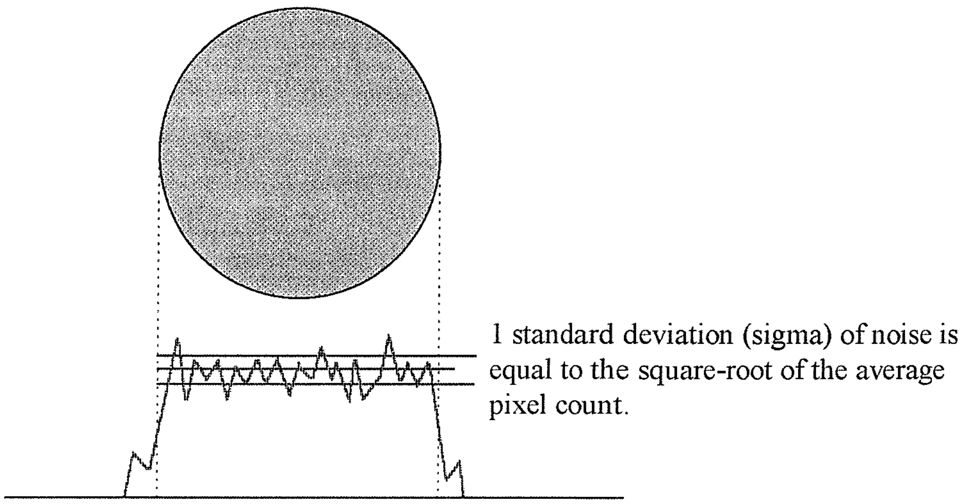

Figure A.15: *Non-uniformity in detector response due to Poisson statistics*

In an ideal clinical gamma camera used in nuclear medicine, the counting noise will be set by Poisson statistics. This means that the variance in the number of counts binned in each of a number of different image pixels will be equal to the mean number of counts expected within a given region of the image. The standard deviation for such a region of the image will be the square-root of this variance. If a feature or lesion is present, the signal-to-noise ratio (SNR) of the image becomes a measure of the significance (in units of standard deviations of noise) with which the extrinsic signal from that feature or lesion can be observed above or below this intrinsic background level. For example, a SNR of around 2 would be marginally detectable, whilst a SNR of 3 would be easily detectable. Clearly, in order to easily determine small features present within a region of interest, one would always prefer as many counts as possible in order to reduce the percentage contribution due to image noise which can be defined as:

$$\text{ImageNoise (\%)} = \frac{100 \text{ sigma}}{\text{N}} = \frac{10}{\sqrt{\text{N}}}$$

The practical limitations for imaging systems used in nuclear medicine are those of relatively short acquisition time, and low patient dose. It therefore becomes necessary to optimise their design, reducing the amount of noise present in the acquired image, and demonstrating as uniform a response function as can be achieved.

The extrinsic spatial uniformity was determined by placing an extended ^{57}Co flood field uniform radiation source, having a half-life of 270 days and a photopeak of 122 keV, within the field of view of the compact gamma camera. The detector crystal was uniformly illuminated and 30 million counts were acquired in order to reveal any accidental damage to the collimator, and any subtle alteration in the camera's energy response. These subtle changes are more easily visualised by acquiring a large number of counts (typically of the order of 30 million), than with images containing only 2 to 5 million counts. Rather than rely upon a visual assessment of flood images in evaluating flood uniformity, two kinds of flood-uniformity parameters of clinical gamma cameras are generally determined. The first of these, known as "integral uniformity", is a measure of contrast over a large area of the detector, and is expressed as:

$$\text{Integral Uniformity (\%)} = 100 \times \frac{\text{Max - Min}}{\text{Max + Min}}$$

where “Max” is the maximum count and “Min” is the minimum count found in any pixel within the specified area. The second parameter, known as “differential uniformity”, is derived for small neighbourhoods of pixels as:-

$$\text{Differential Uniformity (\%)} = 100 \times \frac{\text{Largest Slice Deviation (High - Low)}}{\text{High + Low}}$$

where "High" and "Low" are the maximum and minimum pixel counts, respectively, in any five-pixel row or column of the digital image. Integral uniformity is therefore a global parameter whilst differential uniformity is a local measurement and is more representative of the rate of change of local non-uniformities.

A flood-field image was acquired with the compact gamma camera as described previously, and the image data was subsequently binned as a matrix of 128 x 128 pixels in order to accurately determine the location of counts within the field of view. Since no energy correction algorithm was employed that would usually compensate for photocathode non-uniformities, an energy window was not applied. All events from the edges of the field of view therefore contributed equally in order that the resulting statistics were unaffected. Clearly, since the map of the photocathode response has been shown to vary considerably across the sensitive area of the PSPMT, the application of both an energy correction algorithm, and an energy window to reject Compton scattered events would be a highly desirable feature that would be incorporated into any future versions of the compact gamma camera.

Values of the integral uniformity were determined for the useful field of view (UFOV), which is usually considered to be the central 50 percent to 60 percent of the detector area (see Table A.1).

Uniformity Characteristic	Measurement
Area of Region of Interest (Pixels)	7,052
Total Counts	190,947
Mean Counts	27.077
Standard Deviation Counts	5.794
Integral Uniformity (%)	+11.350
Maximum Count	55
Minimum Count	9

Table A.1: *Uniformity characteristics for the UFOV of the compact gamma camera*

Typically, the standard deviation from the mean value of counts from a conventional gamma camera should not exceed 4 percent above or below that which would normally be expected by simple Poisson statistics, and would usually never exceed 10 percent above or below the expected value. Clearly, the compact gamma camera demonstrated an integral uniformity which is just outside of this margin of error with a value of standard deviation which is 11.35% above that which would be expected by Poisson statistics alone.

A.3.3 Sensitivity Measurements

The extrinsic sensitivity of the compact gamma camera was determined by recording the acquisition time for a 2 million count exposure to a flood field source of known activity. The standard test for the extrinsic sensitivity of a gamma camera uses a 10 cm diameter Petri dish, filled with 20 ml of water and approximately 60 MBq of ^{99m}Tc to provide a count rate of 10 kcps. The syringe used to convey the ^{99m}Tc was assayed before and after delivery of the radioactivity to the vessel, and the times noted to enable decay correction. One minute count rates for this source were then used to determine the extrinsic sensitivity for the compact gamma camera in terms of counts per minute per MBq. By measuring the activity of the source used for obtaining the intrinsic flood field with a dose calibrator, it is possible to compute detector sensitivity, expressed in terms of counts per minute per MBq per meter from the centre of the camera detector:

$$\text{Sensitivity} = \frac{C}{(A.t.d)^2}$$

where C is the count rate, t is the time of acquisition, A is the activity, and d is the source-to-detector distance. Whilst sensitivity should not vary by more than a few percent from one day to the next, such flood field instabilities can be caused by drift in the voltage supplied to the PSPMT. This drift causes the current produced by the tube to vary with time, causing the data acquisition software to reject more events than usual, which results in an overall decrease in detector sensitivity. This technique was employed in order to determine the extrinsic sensitivity of the compact gamma camera to a ^{57}Co radioactive source, and a value of 32,400 CPM/MBq was determined. This compares well with commercially available gamma cameras which demonstrate significantly higher sensitivity due to their thicker detector crystals and dedicated signal processing electronics which have in most cases been developed to handle much higher count rates than our electronics were able to handle.

A.3.4 Summary of Results

Performance Characteristic	Measured Value
Extrinsic FWHM (mm)	5.00
Spatial Non-Linearity (%)	+/-15.3
Sensitivity (CPM/MBq)	32,400
Integral Uniformity (%)	+11.35

All measurements are mean extrinsic values

Table A.2: *Operational performance of the compact gamma camera*

A.3.5 Image Contrast

Contrast is a measure of differences in brightness, counts, or optical density in adjacent regions of the image:

$$\text{Image Contrast (C)} = \frac{(D_1 - D_2)}{1/2(D_1 + D_2)} = \frac{(D_1 - D_2)}{D_2}$$

Displayed contrast will vary according to the means used to capture and display the latent image information. For computer displays, the displayed contrast will therefore depend upon the type of grayscale or colorscale used to transform the counts in each pixel to luminance on the display monitor. This transformation can also be changed with the "window" and "level" (or contrast and brightness) computer controls. The total range of counts that can be recorded between the minimum and maximum displayable brightness is often referred to as the dynamic range of the imaging system. Display devices with wide dynamic range are usually better able to represent image features with poorer contrast than narrow dynamic-range systems. For small lesions, the peak lesion contrast may also be reduced by the system's spatial resolution (see Figure A.16).

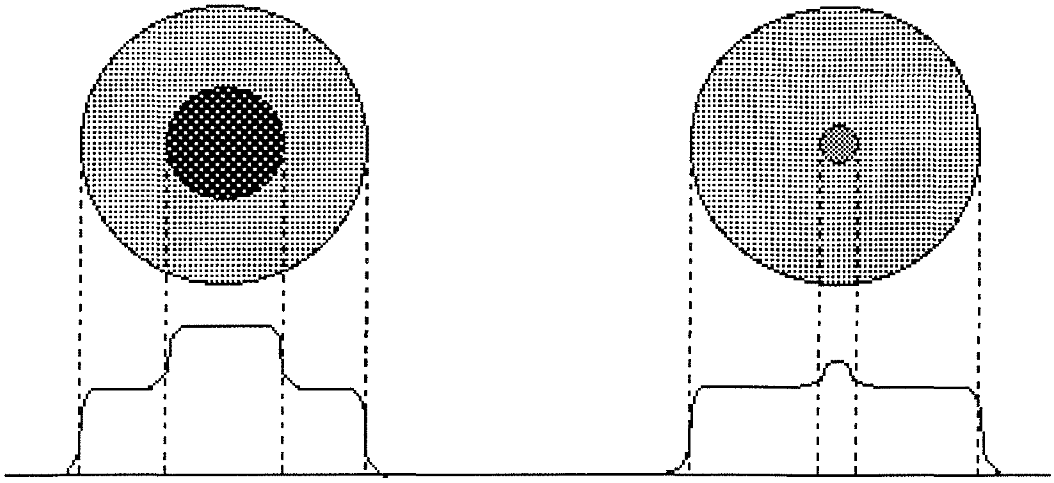

Figure A.16: *The effect of lesion or tumour size upon contrast*

For all lesion sizes, contrast is reduced by Compton scatter from within the patient, and from adjacent materials, producing a measured increase in the FWTM of the PSF. This causes a broad, uniform scatter background which is added to the image of primary unscattered photons (see Figure A.17). This effect is perhaps the most significant contributor to reducing the contrast present within a nuclear medicine image.

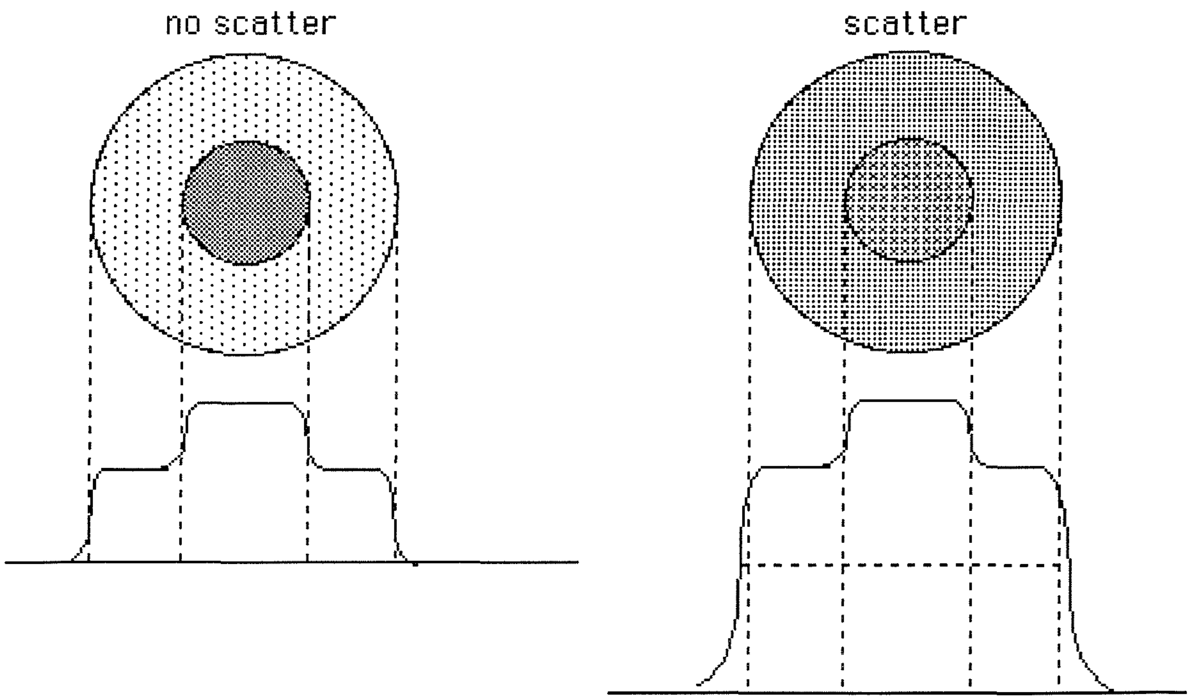

Figure A.17: *The effect of Compton scatter upon contrast*

In addition to the qualitative results described in the previous sections, a quantitative investigation of the planar imaging performance of this gamma camera has been performed using a ^{57}Co thyroid contrast phantom (Figure A.18).

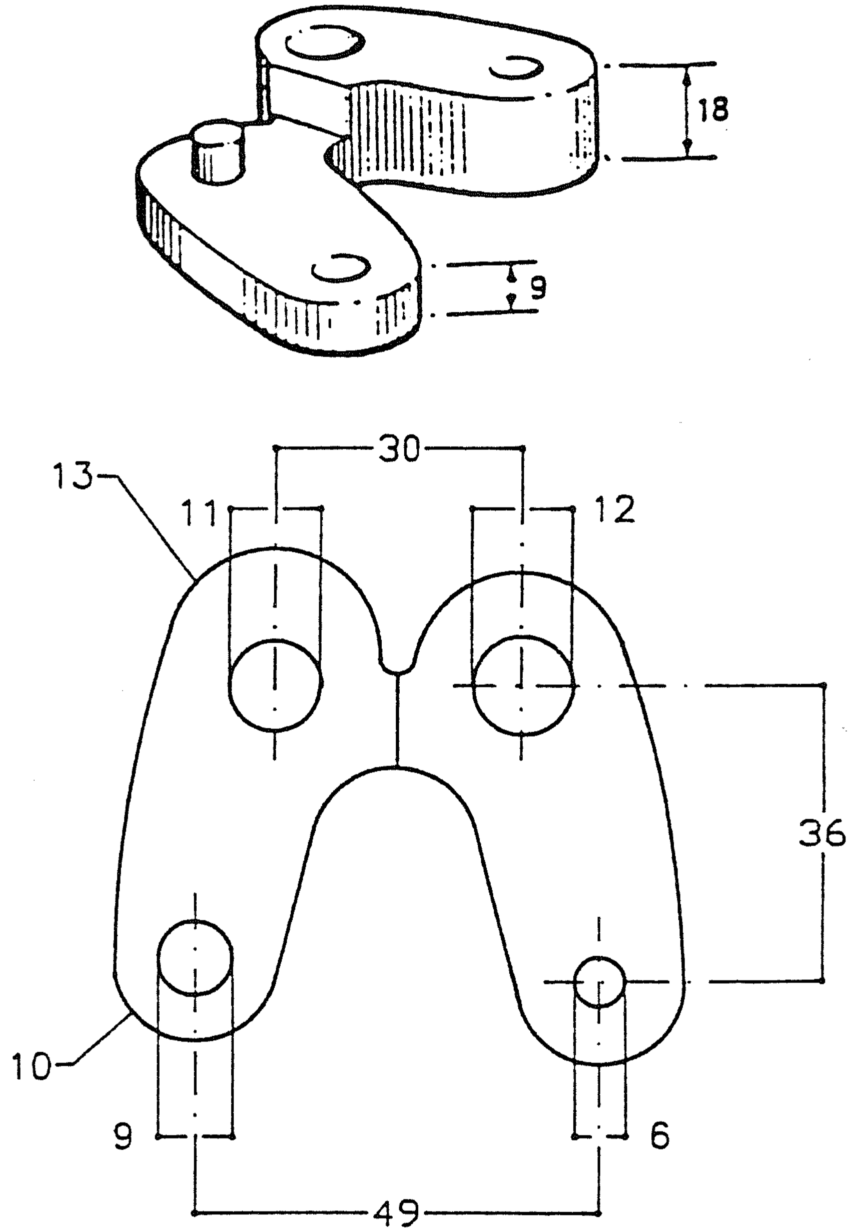

Figure A.18: *The thyroid contrast phantom.*

The gamma camera was used to acquire a single view of the thyroid contrast phantom using an exposure time of 10 minutes which would be the longest practicable clinical exposure. It is apparent from this study that in terms of visual image quality there is little difference between images acquired with the compact gamma camera and similar images acquired using conventional gamma cameras (see Figure A.19 and Figure A.20).

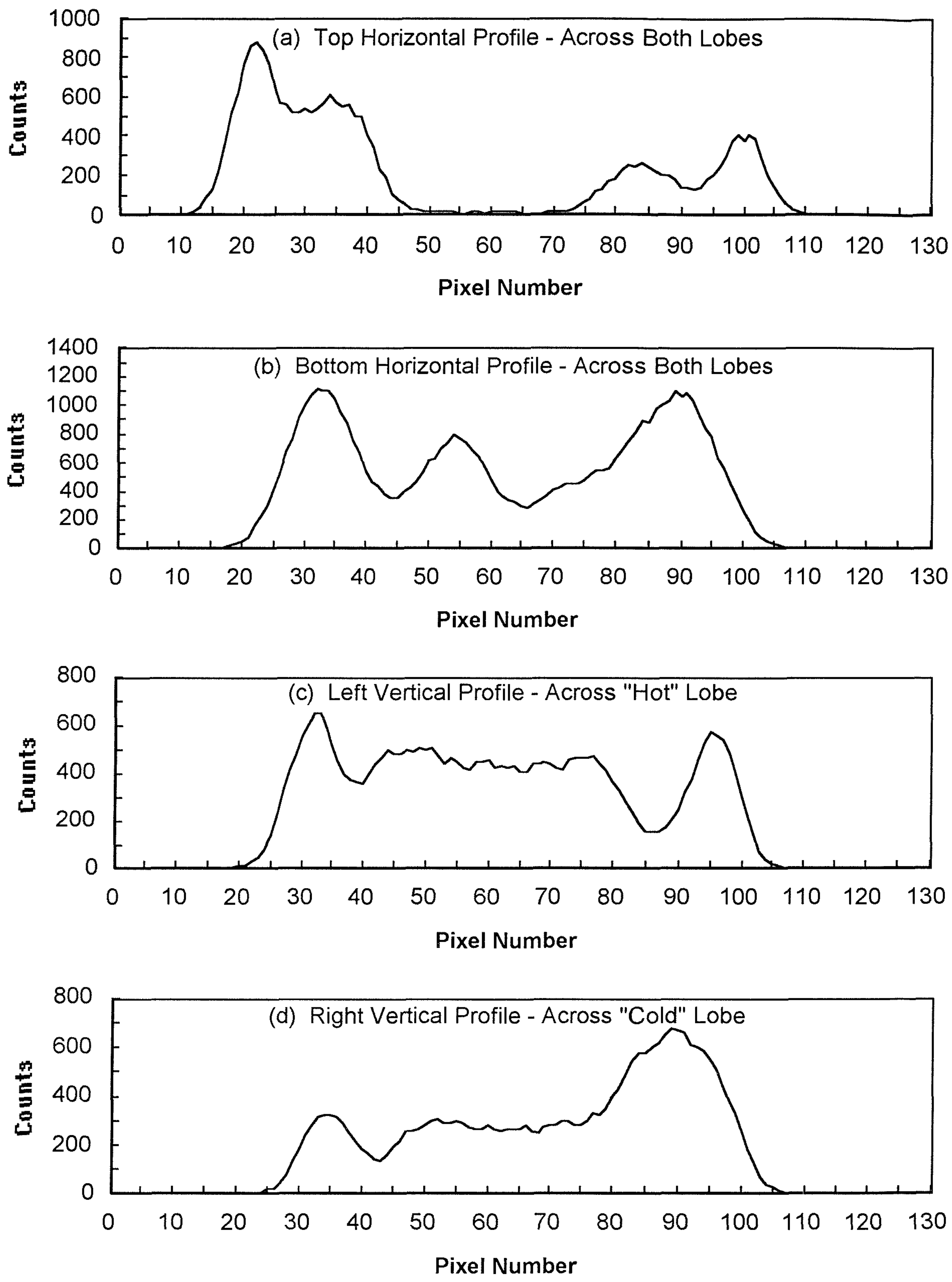

Figure A.19: *Profiles through thyroid contrast phantom image*

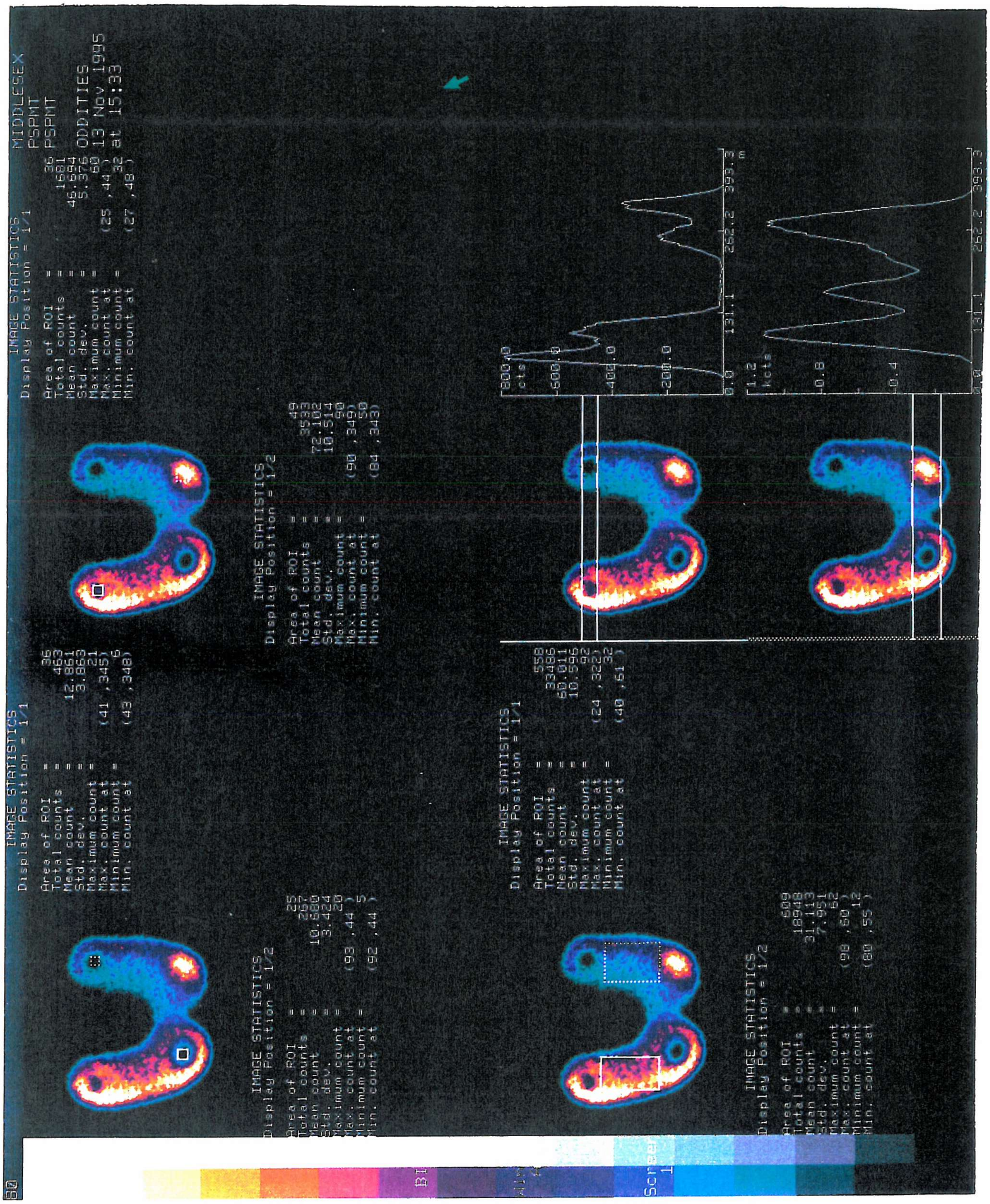

Figure A.20(a): *The GE Optima system was employed to obtain profiles which intersect prominent features from a* ^{57}Co *thyroid contrast phantom image. Regions of interest were also specified from which associated image statistics could be derived.*

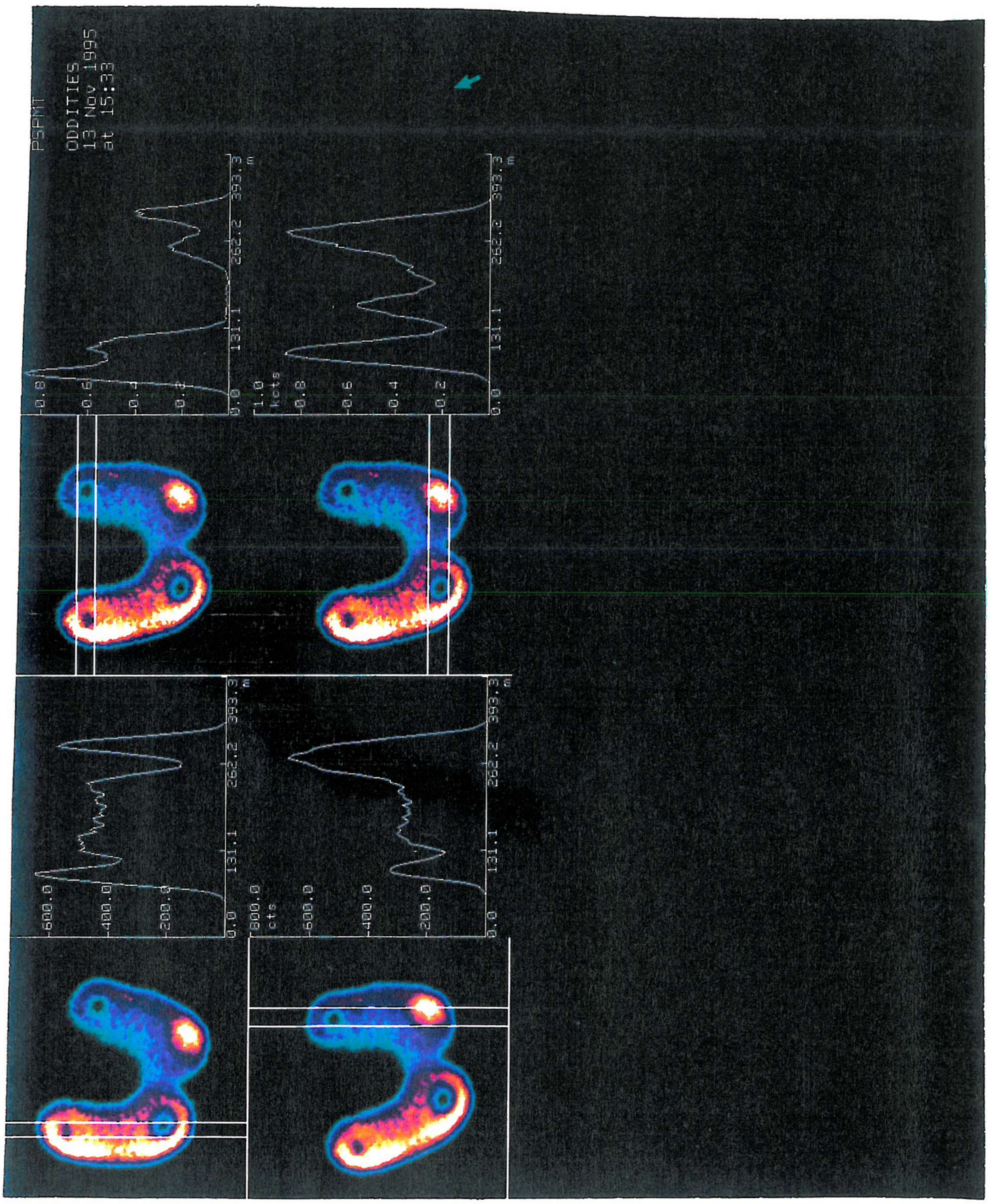

Figure A.20(b): *The GE Optima system was employed to obtain profiles which intersect prominent features from a ^{57}Co thyroid contrast phantom image. Regions of interest were also specified from which associated image statistics could be derived.*

From each of these profiles it is clear that both active and inactive regions of the thyroid phantom are well resolved. However, it is apparent that the contrast has been adversely affected by both the size of the regions themselves, and by the level of activity that surrounds both "hot" and "cold" regions in the image. The number of counts binned within regions of higher activity is approximately double that of the region which represents a source which is approximately half as active. We may therefore conclude that the number of events binned within the whole image is representative of the source being imaged. In addition to these profiles, six regions of interest were specified in order to determine the uniformity of the counts binned across the image (see Table A.3).

Uniformity Characteristic	"Hot" Lobe	"Cold" Lobe	Top LH Hole	Bottom LH Hole	Top RH Hole	RH "Hot Spot"
Area of ROI (Pixels)	558	609	36	36	25	49
Total Counts	33,486	18,948	1,681	463	267	3,533
Mean Counts	60.011	31.113	46.694	12.861	10.680	72.102
Standard Deviation Counts	10.596	7.951	5.376	3.863	3.424	10.514
Integral Uniformity (%)	+ 36.78	+ 42.55	- 21.33	+ 7.72	+ 4.77	+ 23.82
Maximum Counts	92	62	60	21	20	90
Minimum Counts	32	12	32	6	5	50

Table A.3: *Uniformity of counts binned within thyroid contrast phantom image*

A.3.6 Conclusions

Whilst the measurements of the spatial resolution of the compact gamma camera were within acceptable limits, the proposed limits for integral uniformity of ± 5% were not achievable by this camera. In addition, the degree of pin-cushion distortion demonstrated was considerably worse than that which might be expected from a conventional clinical gamma camera.

The results obtained for both the spatial linearity, and the spatial uniformity of the compact gamma camera have shown the need for further development in order to meet the very exacting standards imposed by both the clinical and manufacturing communities. Research is continuing at the Middlesex Hospital, led by Dr. Ian Cullum, and a practical "real time" energy correction algorithm is expected to be completed very shortly. It is anticipated that this single advance will yield improvements in the performance characteristics of the second generation camera that will demonstrate a much improved response, and will enable the compact gamma camera to compare more favourably with conventional clinical gamma cameras that are currently commercially available.

The clearly defined objective of this first generation design of compact gamma camera was to determine its feasibility for use in a variety of applications in nuclear medicine. This has very emphatically been achieved and demonstrated through the results presented in both this appendix and in the preceding chapter. The reader is reminded that the compact gamma camera is primarily a development tool, and a single step leading towards a more clinically useful imaging system for some nuclear medicine procedures. Considerable effort has been made to demonstrate the potential performance of this newly emergent technology as a possible alternative to more expensive, larger, and heavier conventional imaging systems that are currently commercially available.